Archean sulfur reservoirs of the Kaapvaal Craton

Perinne Victoria Chole Tyler

October 2019

A thesis submitted for the degree of Doctor of Philosophy of The Australian National University

Declaration

This thesis contains the results of research done in the Research School of Earth Sciences, The Australian National University, between 2016 and 2019. I certify that this thesis contains no material which has been accepted or submitted for the award of any other higher degree or graduate diploma in any tertiary institution. All work is my own and to the best of my knowledge and belief, the thesis contains no material previously published or written by another person, except where otherwise acknowledged. Word count: 55 144 (excluding abstract).

Perinne Victoria Chole Tyler

Port Macquarie

October 2019

Acknowledgements

Firstly, I would like thank the members of my supervisory panel: Trevor Ireland, Vickie Bennet and Paulo Vasconcelos. Trevor, my primary supervisor, has been particularly helpful, from contributing to numerous discussions about my data, to providing encouragement whenever I felt stuck, and giving helpful feedback on drafts of this thesis. I would also specifically like to thank Vickie for her support and the excitement and enthusiasm she has shown for my project and its results.

The majority of the data for this thesis has been collected using the machines within the SHRIMP Lab at RSES and so I would also like to thank the staff of that lab. In particular, I would like to thank Peter Holden and Peter Lanc for their help and support. Both have provided a large amount of help and been extremely patient in teaching me how to use the various machines within that lab and the associated software. Peter Holden, in particular, has been helpful and supportive and has endured many late night and weekend phone calls when there have been machine problems. In addition to Pete and Pete, I would also like to thank the other users of the SHRIMP Lab, including Richard Armstrong, Mark Fanning, Ian Williams and Bin Fu, for their support and advice.

Several people have provided technical support in other labs around RSES: Morgan Williams and Melanie Sieber with the SEM and James Tolley and Laura Crisp with the LA-ICP-MS. I am grateful for all the assistance they have provided, in particular to Laura, who spent a lot of time showing me how to use the machine and how to process my data. Additionally, Shane Paxton has provided an incredible amount of assistance with sample preparation, something which without this thesis would not have been possible.

Thank you to Josephine Magro, Maree Coldrick and Virginia Riddle for their administrative support over the years. Additionally, Josephine and Maree have been extremely kind and supportive and always made me feel very welcome. Virginia also helped with some administrative difficulties and was very prompt in replying to my somewhat panicked emails, which I would like to acknowledge.

Finally, from RSES, I would like to thank my previous office mates, Li Liu and Liane Loiselle, and my other close friends. Li provided not just emotional support and friendship but

also a large amount of helpful advice regarding my project, which I am extremely grateful for. Liane made me feel extremely welcome at RSES and played a large role in helping me to settle in, which I am also very grateful for. My friends, Suzette Timmerman, Hannah James, Bethany Ellis and Chris Mathews, have provided much love, support and advice over the years, which I am very appreciative of. Many days, Suzette's encouraging messages and postcards have been the only things motivating me to keep writing.

I would also like to thank those from other universities which have helped me throughout the completion of this thesis. Firstly, thank you to Axel Hofmann, Andrea Agangi and Dora Paprika, from the University of Johannesburg, who helped me with my fieldwork and made me feel extremely welcome during my time in South Africa. I would also like to thank them for the opportunities they have provided to continue our collaboration. Thank you, also, to Barry Maynard, now retired, formerly from the University of Cincinnati, who gifted me some of the paleosol samples that were analyzed for Chapter 4 of this thesis.

Outside of academia, my friend Grace Katuzans, has incredibly supportive and encouraging and I would not have been able to complete my thesis without her. I would also like to thank her parents, Nancy and Eve, for their support and encouragement.

Most importantly, I would like to thank my father, Stephen Tyler, for his unwavering love and support. He has not only endured many phone calls consisting of me complaining about my thesis but has also let me live in his house whilst I was finishing writing. I can never say thank you enough. I would also like to thank my brother, Clay, for his support and encouragement, which has been similarly invaluable.

Finally, I would like to acknowledge the financial support I have received during my candidature. The Australian Government Research Training Program Scholarship (formerly the Australian Postgraduate Award) and the Australian National University Supplementary Scholarship have covered my university fees and living costs, for which I am very grateful. Additionally, my travel to the AGU 2018 Fall Meeting was covered by the D. A. Brown travel award, for which I am also very appreciative.

Abstract

Archean sulfur minerals typically display anomalous isotopic signatures where $\Delta^{33}S$ and $\Delta^{36}S \neq 0$ and $\Delta^{36}S/\Delta^{33}S = \sim -0.90$. However, the current data record is composed predominantly of data collected from marine sedimentary rocks and only a very small amount of data has been collected from terrestrial sedimentary rocks. Additionally, the data available from terrestrial sedimentary rocks suggests that these rocks preferentially preserve sulfur from different sources than the sulfur preserved in the equivalent marine rocks. Therefore, it is the main objective of this thesis to explore the isotopic composition of sulfur minerals hosted by terrestrial sedimentary rocks and determine if and why terrestrial and marine sedimentary environments would preserve different forms of sulfur. A secondary objective is to re-examine the Mesoarchean sulfur isotope record, where the magnitude of $\Delta^{33}S$ and $\Delta^{36}S$ values are observed to be muted and the $\Delta^{36}S/\Delta^{33}S$ slope steepened in comparison to the rest of the Archean. For this study, the majority of samples are aged between 3100 Ma and 2700 Ma.

The South African Witwatersrand and Pongola supergroups are the primary study areas for this thesis. Both are Mesoarchean in age and contain well-preserved sedimentary sequences. Additionally, they contain a wide variety of lithostratigraphic occurrences of pyrite. For this thesis, samples were collected from glacial diamictites, paleosols and fluvial and marine clastic sedimentary rocks. Prior to sulfur isotope analysis, the paragenesis of sulfide mineral grains was determined through textural and morphological studies and LA-ICP-MS trace element analysis. In-situ four sulfur isotope analysis was then completed using the SHRIMP-SI.

Detrital and diagenetic pyrite from glacial diamictites returned mostly negative $\Delta^{33}S$ and $\Delta^{36}S$ values, in the ranges of -0.43 – +0.09 ‰ and -1.95 – +0.15 ‰, respectively. The $\delta^{34}S$ values showed a range of -6.09 – +11.7 ‰. Deviation in $\Delta^{36}S$ from the atmospheric $\Delta^{36}S/\Delta^{33}S$ array and variation in $\delta^{34}S$ is consistent with microbial sulfate reduction of atmospheric sulfate. The restricted $\delta^{34}S$ values observed in one sample set may represent input of mass-dependent crustal sulfur.

Paleosol-hosted sulfide minerals had negative or near-zero $\Delta^{33}S$ values, with a range of -0.50 – +0.17 ‰, and near-zero $\Delta^{36}S$ values, with a range of -0.99 – +0.52 ‰. The $\delta^{34}S$ values showed a range of -8.88 – +6.87 ‰. In samples where both $\Delta^{33}S$ and $\Delta^{36}S$ were ~0 ‰, the sulfur is likely magmatic sulfur inherited from the igneous parent rocks. Samples with small

negative $\Delta^{33}S$ values likely preserve a mixture of atmospheric sulfate and inherited magmatic sulfur.

Detrital and diagenetic pyrite from fluvial rocks typically returned negative $\Delta^{33}S$ and $\Delta^{36}S$ values, with the majority of data falling in the ranges of -0.72 – +0.10 ‰ for $\Delta^{33}S$ and -0.98 – +0.34 ‰ for $\Delta^{36}S$. The $\delta^{34}S$ values typically fell within the range of -3.21 – +9.65 ‰. The muted negative $\Delta^{33}S$ values and small $\delta^{34}S$ values are consistent with a mixture of atmospheric sulfate and mass-dependent crustal sulfur. The consist deviation in $\Delta^{36}S$ from the atmospheric $\Delta^{36}S/\Delta^{33}S$ array suggests microbial sulfate reduction.

Diagenetic pyrite from shallow marine samples returned variable isotopic signatures. Several samples showed $\Delta^{36}S/\Delta^{33}S$ = ~6.9, consistent with microbial sulfate reduction. These samples showed $\Delta^{33}S$ values of -0.18 – +0.51 ‰, $\Delta^{36}S$ values of -2.05 – 0.02 ‰ and $\delta^{34}S$ values of -15.8 – +8.53 ‰. These signatures, coupled with observed elevated concentrations of selenium, provide new evidence for a period of elevated atmospheric oxygen during the Mesoarchean. Other samples showed $\Delta^{36}S/\Delta^{33}S$ = ~-2, with $\Delta^{33}S$ values of +0.11 – +0.80 ‰ and $\Delta^{36}S$ values of -2.04 - -0.25 ‰. The $\delta^{34}S$ values showed a range of -1.17 – +7.74 ‰. Data from individual samples were observed to show consistent $\Delta^{33}S$ but variable $\Delta^{36}S$, forming steep arrays extending downwards from the atmospheric $\Delta^{36}S/\Delta^{33}S$ array. This was interpreted to represent microbial fractionation of atmospheric elemental sulfur, suggesting that steepening of the $\Delta^{36}S/\Delta^{33}S$ array during the Mesoarchean is due to microbial activity.

These results indicate that terrestrial sulfide minerals preserved a mixture of atmospheric sulfate and mass-dependent sulfur species. In contrast, marine sulfide minerals preserved atmospheric elemental sulfur, confirming that the different environments preserved different forms of sulfur. It was also confirmed that Mesoarchean samples preserved muted $\Delta^{33}S$ and $\Delta^{36}S$ signatures and it is suggested that this has been caused by both a period of elevated atmospheric oxygen and dilution of atmospheric sulfur species by mass-dependent sulfur species mobilized during oxidative weathering.

Contributions

The key contributions made by thesis are as follows:

- Identification of the isotopic composition of Archean terrestrial sedimentary sulfur reservoirs.
- Confirmation that Archean terrestrial and marine sedimentary environments preferentially preserved different forms of sulfur and a discussion of why this would occur.
- New isotopic and trace element evidence for a period of increased atmospheric oxygen during the Mesoarchean.
- New isotopic evidence that the steepened $\Delta^{36}S/\Delta^{33}S$ array observed for Mesoarchean samples is due to microbial activity.

Table of Contents

List of Figures

List of Tables

List of Equations

Chapter 1: Overview

The stable isotopes of sulfur have become an important tool for determining the surficial oxidation conditions of the early Earth. These insights come from variation in the isotopic composition of sulfur minerals, which is caused by preferential partitioning of the different stable isotopes of sulfur into various sulfur compounds under specific environmental conditions or during certain chemical reactions (this is known as fractionation). As specific chemical reactions produce sulfur compounds with characteristic isotopic compositions, this allows these reactions to be recognized and placed in the rock record. When the reduction-oxidation (redox) conditions these reactions occur under are known, the redox conditions of that environment can therefore be inferred from the sulfur isotope composition of the available sulfur minerals.

As mentioned above, this approach has become useful for examining samples from the Archean Eon (4000 – 2500 Ma). During this time, the sulfur cycle is believed to have been dominated by atmospheric reactions occurring under anoxic conditions (Farquhar et al., 2000, 2001; Pavlov and Kasting, 2002). These reactions produced sulfur compounds with anomalous minor isotopic compositions and the presence of these unusual signatures within the rock record is a major indicator of anoxic surficial conditions. Variations in these signatures and the timing of their disappearance from the rock record are commonly used to examine changes in Archean atmospheric chemistry and determine the timing of the Great Oxidation Event (GOE) (eg. Farquhar et al., 2001; Holland et al., 2002; Bekker et al., 2004; Guo et al., 2009; Philippot et al., 2018).

However, a distinct bias towards marine sedimentary rocks within the current data record is restricting our understanding of the Earth's early sulfur cycle and the various sulfur reservoirs and chemical reactions involved. Additionally, the restricted amount of high resolution four sulfur isotope data collected from Mesoarchean samples has hindered attempts to interpret unusual trends observed within the data record from that era.

This thesis is primarily concerned with determining the isotopic composition of Mesoarchean terrestrial sedimentary sulfur reservoirs and determining if and why the isotopic composition of those reservoirs differed from the equivalent marine reservoirs. The current data set is heavily biased towards marine sedimentary samples, with very few analyses having been completed on sulfur minerals hosted by terrestrial sedimentary rocks. Consequently, the

isotopic composition of terrestrial sedimentary sulfur reservoirs and the mechanisms by which sulfur species are being preserved within them are largely unknown. Additionally, the limited amount of data available from terrestrial sedimentary samples indicates that sulfur minerals from these samples show different isotopic compositions to those from marine sedimentary samples. This suggests that there is a gap in the current understanding of the Earth's early sulfur cycle and the mechanisms by which atmospherically-derived sulfur species were preserved in the rock record. Therefore, it is the primary objective of this thesis to explore the isotopic composition of sulfur minerals from Mesoarchean terrestrial sedimentary rocks and examine if and why terrestrial and marine sedimentary reservoirs would have different isotopic compositions.

A secondary objective of this thesis is to re-examine the Mesoarchean sulfur isotope record. Within the current data record, it is observed that Mesoarchean sulfur minerals show isotopic compositions which differ from those of sulfur minerals from the Eo-, Paleo- and Neoarchean eras. However, due to only a limited amount of four sulfur isotope data collected from Mesoarchean sulfur minerals and inadequate constraints being placed on paragenesis of sulfide minerals prior to analysis, these deviations remain largely unexplained. Therefore, this thesis aims to collect high-resolution four sulfur isotope data from Mesoarchean samples in order to re-examine these deviations and explore possible causes.

This introductory chapter begins with an overview of sulfur isotope geochemistry. This is followed by a description of the fractionation processes believed to be active within the Archean sulfur cycle and the isotopic signatures produced by each process. Next is a discussion of the isotopic composition of the different sulfur reservoirs and the mechanisms by which sulfur was preserved within those reservoirs. Discussion of the Archean sulfur cycle concludes with a description of temporal and secular trends observed with the current Archean sulfur isotope data record, with particular attention paid to trends observed within data from Mesoarchean samples. Following is a description of the approach used in this thesis and justifications of this approach. The chapter concludes with the research questions and structure of the thesis.

1.1 Sulfur isotope geochemistry

Sulfur has four stable isotopes: ^{32}S, ^{33}S, ^{34}S and ^{36}S, with the approximate terrestrial abundances of 95.03 %, 0.7487 %, 4.197 % and 0.01459 %, respectively (Ding et al., 2001).

The isotopic composition of sulfur compounds is expressed in delta (δ) notation, as parts per thousand variation relative to a reference material:

$$\delta^{3X} = \left[\frac{(^{3X}S/^{32}S)_{sample}}{(^{3X}S/^{32}S)_{standard}} - 1\right] \times 1000 \quad (1.1)$$

Where 3X may refer to 33, 34 or 36 and δ^{3X} has units of per mil (‰). Historically, the reference material for sulfur isotope analyses was Canyon Diablo Troilite (CDT), However, it has been proven that CDT is slightly heterogenous in sulfur isotope composition, with a variation in $\delta^{34}S$ values of ~0.4 ‰ (Gonfiantini et al., 1993; Robinson, 1993; Beaudoin et al., 1994; Ono et al., 2006a, 2007; Wing and Farquhar, 2015). Due to this heterogeneity, an international reference material, a silver sulfide IAEA-S-1, was adopted and the isotopic composition of this standard was used to define the new Vienna Canyon Diablo Troilite (VCDT) scale. It has also been recognized that CDT shows heterogeneity in $\delta^{33}S$ and $\delta^{36}S$ (Ding et al., 2001; Ono et al., 2007). In order for there to be consistency between the VCDT and CDT scales, measurements of IAEA-S-1 relative to CDT from fifteen individual laboratories were averaged to define the $\delta^{34}S$ value for IAEA-S-1 at -0.3 ‰ relative to VCDT (Robinson, 1995; Krouse and Coplen, 1997). A similar exercise is yet to be undertaken to define the $\delta^{33}S$ and $\delta^{36}S$ values for IAEA-S-1 relative to VCDT.

For the majority of fractionation processes within the sulfur isotope system, fractionation is mass-dependent, where the different isotopic ratios vary systematically in proportion to the mass differences between the isotopes (Urey, 1947; Hulston and Thode, 1965a, b). For example, variations in the $^{33}S/^{32}S$ ratio of a sample will be approximately half that of the $^{34}S/^{32}S$ ratio as the mass difference between ^{33}S and ^{32}S is approximately half that of the mass difference between ^{34}S and ^{32}S. This produces the following linear fractionation trends, commonly known as the terrestrial mass fractionation lines (TMFL) (Figure 1.1):

$$\delta^{33}S = 0.515 \times \delta^{34}S \quad (1.2)$$

$$\delta^{36}S = 1.91 \times \delta^{34}S \quad (1.3)$$

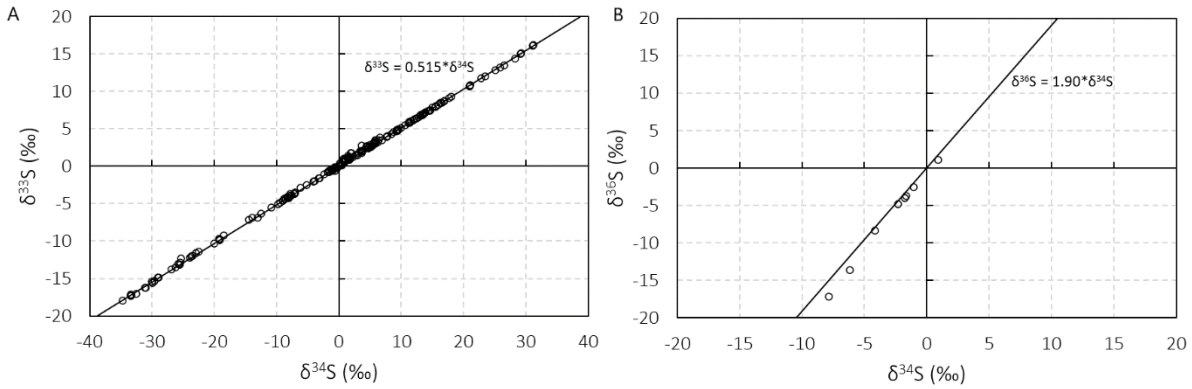

Figure 1.1. The terrestrial mass fractionation lines (TMFL) for the sulfur isotope system. A. Relationship between $\delta^{33}S$ and $\delta^{34}S$. B. Relationship between $\delta^{36}S$ and $\delta^{34}S$. Data from Ono et al. (2006a); Bekker et al. (2004); Papineau et al. (2005, 2007).

Historically, it was not expected that deviations from these trends would be observed within the rock record. Due to this, the majority of sulfur isotope studies measured only ^{32}S and ^{34}S and the multiple sulfur isotope analyses necessary to confirm mass-dependent fractionation (MDF) rarely occurred. More recently, however, multiple sulfur isotope studies have become common. This in part due to advances in analytical capabilities and in part due to the experiments of Farquhar et al. (2000, 2001) which showed that photolysis reactions could produce sulfur compounds with isotopic compositions which deviated from the TMFL. These deviations reflect non-mass dependent or mass-independent (MIF) fractionation processes and are expressed in terms of $\Delta^{33}S$ and $\Delta^{36}S$, where:

$$\Delta^{33}S = \delta^{33}S - 1000 \times \left[\left(1 - \frac{\delta^{34}S}{1000}\right)^{0.515} - 1\right] \quad (1.4)$$

$$\Delta^{36}S = \delta^{36} - 1000 \times \left[\left(1 - \frac{\delta^{34}S}{1000}\right)^{1.91} - 1\right] \quad (1.5)$$

$\Delta^{33}S$ and $\Delta^{36}S$ values also have units of per mil (‰). A positive $\Delta^{3x}S$ value indicates that a compound is anomalously enriched in that isotope and a negative value indicates that a compound is anomalously depleted. MIF processes were particularly important during the Archean, as will be discussed in the following section.

More detailed reviews of the fundamentals of sulfur isotope geochemistry and the systematics of mass-dependent and mass-independent fractionation can be found in Farquhar and Wing (2003) and Seal (2006).

1.2 Fractionation processes involved in the Archean sulfur cycle

As different fractionation processes produce sulfur compounds with different isotopic compositions, the combination of the measured $\delta^{34}S$, $\Delta^{33}S$ and $\Delta^{36}S$ values and the $\Delta^{36}S/\Delta^{33}S$ ratio can be used to identify action of those processes within the rock record. Below is a description of a portion of the fractionation processes believed to have been involved in the Archean sulfur cycle, the isotopic signatures produced by those processes and how they can be recognized in the rock record. Whilst other fractionations processes may be believed to have been active within the Archean sulfur cycle (eg. photoexcitation of SO_2 (Whitehall and Ono, 2012)), the discussion below covers those which are most relevant to this thesis.

Atmospheric processes

Archean sulfur minerals typically show non-zero $\Delta^{33}S$ and $\Delta^{36}S$ values, where $\Delta^{36}S/\Delta^{33}S$ = ~-0.90 and $\Delta^{33}S/\delta^{34}S$ = ~0.90 (Figure 1.2; Farquhar et al., 2001; Ono et al., 2003). These are commonly referred to MIF signatures, despite other fractionation processes in the sulfur isotope system also causing mass-independent fractionation (eg. microbial sulfate reduction (Johnson et al., 2005b, 2007; Ono et al., 2006a), photoexcitation of SO_2 (Whitehall and Ono, 2012) and certain pathways of thermochemical sulfate reduction (Watanabe et al., 2009)). The characteristic $\Delta^{36}S/\Delta^{33}S$ and $\Delta^{33}S/\delta^{34}S$ arrays observed for Archean samples are frequently referred to as the Archean reference arrays (ARA, Figure 1.2).

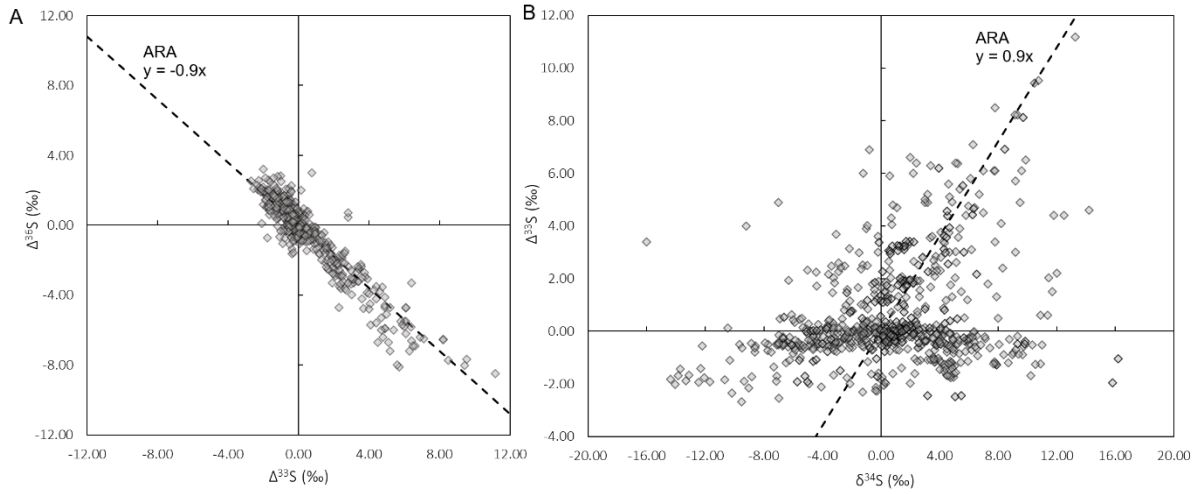

Figure 1.2. Isotopic relationships typically observed for Archean sulfur minerals. A. $\Delta^{36}S$ vs. $\Delta^{33}S$ plot, showing data lying on the Archean reference array of $\Delta^{36}S/\Delta^{33}S$ = ~-0.90, B. $\Delta^{33}S$ vs. $\delta^{34}S$ plot, showing data lying on the Archean reference array of $\Delta^{33}S/\delta^{34}S$ = 0.90. Data from Mojzsis et al. (2003); Ono et al. (2003, 2009); Whitehouse et al. (2005); Ohmoto et al. (2006); Kaufman et al. (2007); Patridge et al. (2008); Shen et al., (2009); Thomazo et al. (2009); Zerkle et al. (2012); Farquhar et al. (2013); Kurzweil et al. (2013); Zhelezinskaia et al. (2014); Izon et al. (2015); Muller et al. (2016, 2017); Mishima et al. (2017); Eickmann et al. (2018).

Experiments have demonstrated that similar isotopic signatures are produced through photolysis reactions involving SO and SO_2 and ultraviolet (UV) radiation at wavelengths of 190 – 220 nm (Farquhar et al., 2000, 2001; Pavlov and Kasting, 2002). Further evidence for an atmospheric origin is provided by the observation of similar isotopic signatures in modern atmospheric sulfate aerosols and in sulfate produced from volcanogenic SO_2 preserved in Antarctic ice cores and firn (Romero and Thiemens, 2003; Savarino et al., 2003; Baroni et al., 2007). Based on this evidence, photolysis of SO and SO_2 is the most widely accepted cause of the Archean MIF signatures, although investigation continues into other possible causes (e.g. Lasaga et al., 2008; Watanabe et al., 2009; Whitehall and Ono, 2012).

The products of these photolysis reactions, which carry the MIF signatures, are a reduced and an oxidized sulfur aerosol. The reduced aerosol, believed to be elemental sulfur (in the form of S_8 molecules, which are believed to form through a pathway involving S^0 and other intermediates) carries positive $\Delta^{33}S$ values and negative $\Delta^{36}S$ signatures. In contrast, the oxidized aerosol, believed to be sulfate (SO_4^{2-}), carries negative $\Delta^{33}S$ values and positive $\Delta^{36}S$ values (Figure 1.3; Farquhar et al., 2001).

MIF signatures as a proxy for anoxic conditions

As mentioned at the beginning of this chapter, the observation of MIF signatures within sulfur minerals is a major indicator for anoxic surficial conditions. This is due to both the specific wavelengths of UV radiation required for the production of these signatures and the low atmospheric oxygen concentrations required for the effective transport of both the reduced and oxidized sulfur aerosols to the Earth's surface.

First, ozone, and to a lesser extent, oxygen are the primary atmospheric constituents which absorb UV radiation of wavelengths <300 nm, including the wavelengths involved in the photolysis reactions described above (~190 – 220 nm; Farquhar et al., 2000, 2001). Atmospheric ozone is produced through reactions which involve atmospheric oxygen. Therefore, observation of MIF signatures implies that the atmosphere was transparent to short wavelength UV radiation and that atmospheric oxygen concentrations were not high enough to facilitate the formation of an ozone UV shield.

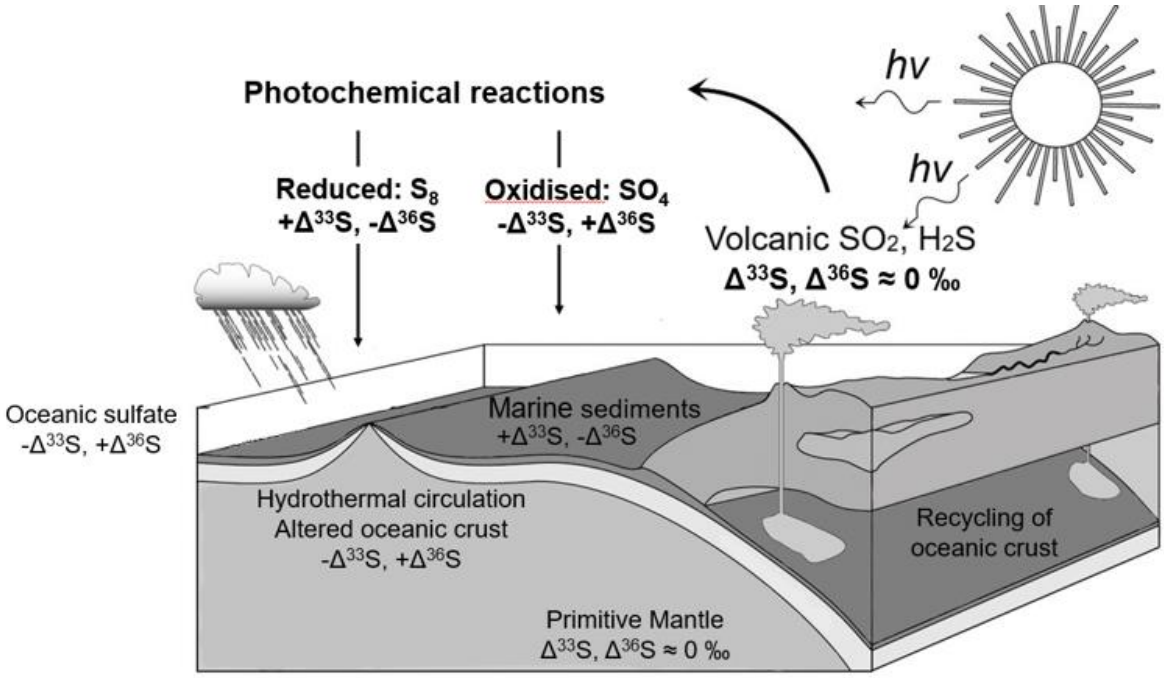

Figure 1.3. Schematic illustration of the Archean sulfur cycle. Figure modified from Farquhar and Wing (2003).

Second, the effective transfer of both a reduced and an oxidized sulfur aerosol from the atmosphere to the Earth's surface requires an atmosphere with a low oxidative capacity. Using a one-dimensional model of Archean atmospheric chemistry, Pavlov and Kasting (2002) determined that effective transfer occurs only when oxygen levels are $<< 10^{-5}$ present atmospheric levels (PAL). Only at these low oxygen concentrations do oxidized sulfur species carrying negative $\Delta^{33}S$ and positive $\Delta^{33}S$ signatures and reduced sulfur species carrying positive $\Delta^{33}S$ and negative $\Delta^{36}S$ signatures exit the atmosphere in sub-equal proportions. Due to these two factors, observation of MIF signatures signals that the sulfur minerals formed under anoxic surficial conditions.

Additionally, other processes dependent on the availability of oxygen, such as oxidative weathering of sulfide minerals, can help to remove the MIF signatures from the rock record. In this situation, oxidative weathering of crustal sulfide minerals which do not carry an MIF signature, e.g. igneous sulfides, produces sulfate which then dilutes and essentially overwhelms the MIF signature (e.g. Romero and Thiemens, 2003).

Biological processes

Various sulfur metabolisms are proposed to have been active during the Archean, due to observation of specific isotopic signatures and other evidence (e.g. Shen et al., 2001, 2009;

Philippot et al., 2007; Wacey et al., 2010; Guy et al., 2012; Eickmann et al., 2018). These include sulfate reducers and sulfur disproportionators.

Microbial sulfate reduction

Sulfate reducing microbes metabolize sulfate, producing sulfide as a product. Their metabolism can be described by the general reaction:

$$2\ CH_2O + SO_4^{2-} \rightarrow H_2S + 2HCO_3^- \quad (1.6)$$

Where CH_2O represents generic organic matter (Berner, 1985). These microbes preferentially metabolize ^{32}S relative to ^{34}S, resulting in negative fractionations in $\delta^{34}S$ in the product sulfide (Thode et al., 1951; Jones and Starkey, 1957; Harrison and Thode, 1958). Within modern environments, these fractionations can be quite large (up to ~50 ‰; Harrison and Thode, 1958; Goldhaber and Kaplan, 1975; Canfield and Teske, 1996; Canfield, 2001b) and sulfide minerals containing sulfide produced through microbial sulfate reduction (MSR) can have extremely negative $\delta^{34}S$ values. Within Archean environments, however, fractionation in $\delta^{34}S$ is typically <20 ‰ (Sim et al., 2019).

The minor isotope fractionations produced by MSR are also relatively well studied (e.g. Johnston et al., 2005b, 2007; Ono et al., 2006a). This process is known to concentrate ^{33}S in the product sulfide, resulting in small positive $\Delta^{33}S$ values, and to discriminate against ^{36}S, resulting in negative $\Delta^{36}S$ values in the product sulfide relative to the reactant sulfate. Here, the $\Delta^{36}S/\Delta^{33}S$ ratio is ~-6.9 (Ono et al., 2006a; Johnston et al., 2007). The magnitude of the changes in $\Delta^{33}S$ and $\Delta^{36}S$ values are also largely observed to scale with degree of fractionation in $\delta^{34}S$ (Johnston et al., 2007).

The magnitude of fractionation produced by MSR has been shown to depend on various factors, including sulfate concentration (eg. Canfield et al., 2000; Habicht et al., 2002), environmental conditions at the time of reduction (eg. Jorgensen, 1977) and sulfate reduction rates (Canfield, 2001b; Demeter et al., 2001; Habicht and Canfield, 2001).

Within modern environments, the steep negative $\Delta^{36}S/\Delta^{33}S$ produced through MSR typically passes through the origin of a $\Delta^{36}S$-$\Delta^{33}S$ plot due to modern oceanic sulfate having $\Delta^{33}S$ and $\Delta^{36}S$ values of ~0 ‰ (Figure 1.4A). However, within Archean oceans, the $\Delta^{33}S$ and $\Delta^{36}S$ values of oceanic sulfate are ≠ 0 ‰ due to input of atmospheric MIF sulfate with non-zero $\Delta^{33}S$ and $\Delta^{36}S$ values (Ono et al., 2003; Ueno et al., 2008; Shen et al., 2009; Zhelezinskaia et al., 2014). For various sets of Archean samples, the MSR $\Delta^{36}S/\Delta^{33}S$ array has been observed

to extend downwards from the left-hand side of the ARA in $\Delta^{36}S$-$\Delta^{33}S$ space, representing reduction of sulfate with an isotopic composition lying on the ARA (Figure 1.4B). This deviation from the ARA in $\Delta^{36}S$ is a key indicator of MSR within Archean samples.

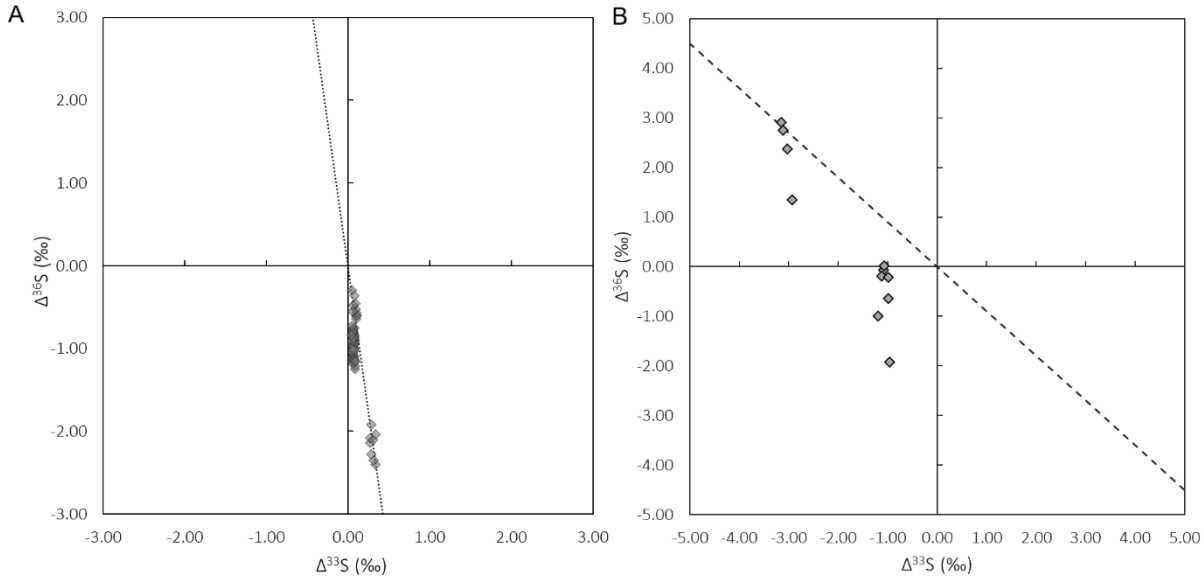

Figure 1.4. Isotopic signatures produced by microbial sulfate reduction. A. Post-Archean isotopic signatures where the $\Delta^{36}S/\Delta^{33}S$ array of ~-6.9 (represented by the dotted line) passes through the origin. Data from Ono et al. (2006a); Johnston et al. (2007). B. Archean isotopic signatures where data deviate from the Archean reference array (represented by the dashed line) in $\Delta^{36}S$. Data from Zhelezinskaia et al. (2014); Mishima et al. (2017).

Microbial sulfur disproportionation

Microbial sulfur disproportionators metabolize sulfur intermediate compounds, such as elemental sulfur (S_0) and sulfite (SO_3^{2-}) and produce both sulfide and sulfate as a product (Bak and Pfennig, 1987; Canfield and Thamdrup, 1994; Thamdrup et al., 1994; Canfield and Teske, 1996; Finster et al., 1998; Cypionka et al., 1998; Habicht et al., 1998). General forms of these metabolisms are provided in equations 1.7 and 1.8:

$$4S_0 + 4H_2O \rightarrow 3H_2S + SO_4^{2-} + 2H^+ \quad (1.7)$$

$$4SO_3^{2-} + 2H^+ \rightarrow H_2S + 3SO_4^{2-} \quad (1.8)$$

In regards to elemental sulfur disproportionation, culture studies have shown that this process typically concentrates ^{32}S in the product sulfide, resulting in negative $\delta^{34}S$ fractionations of between 5.5 – 11.3 ‰ (Canfield et al., 1998; Johnston et al., 2005b). However, a culture study of elemental sulfur disproportionators from Gulfo Dolce, Costa Rica by Johnston et al. (2005b) shows that the opposite can also be true, with ^{34}S being concentrated in the product sulfide, resulting in positive $\delta^{34}S$ fractionation of ~4 ‰. In contrast, ^{34}S is consistently concentrated in the product sulfate, producing positive fractionations in $\delta^{34}S$ of between 17.1 -

33.9 ‰ (Canfield et al., 1998; Johnson et al., 2005b). There is only limited information available concerning how this process fractionates the minor isotopes, however, initial results indicate that the $\Delta^{33}S$ values of the product sulfate are more positive than that of the reactant sulfur by ~0.06 – 0.09 ‰, and that negligible changes are produced in $\Delta^{33}S$ value of the product sulfide relative to the reactant (Johnston et al., 2005b).

Studies of sulfite disproportionators have similarly shown that the product sulfide is depleted in ^{34}S and the product sulfate is enriched in ^{34}S. The sulfide shows positive fractionations in $\delta^{34}S$ of between ~20.5 – 45.2 ‰ and the sulfate shows negative fractionation in $\delta^{34}S$ of ~6.9 – 12.0 ‰ (Habicht et al., 1998; Johnson et al., 2005b). The limited amount of multiple sulfur isotope data available indicates that the $\Delta^{33}S$ values of both the sulfide and sulfate are increased relative to the reactant sulfur, in the order of ~0.10 – 0.16 ‰ (Johnston et al., 2005b).

Within the Archean rock record, action of microbial sulfur disportionation (MSD) is typically recognized through sulfide minerals carrying positive $\Delta^{33}S$ values and relatively large positive or negative $\delta^{34}S$ values, where the isotopic composition of these minerals deviates from the ARA in $\Delta^{33}S$-$\delta^{34}S$ space (Figure 1.5; Philippot et al., 2007; Wacey et al., 2010).

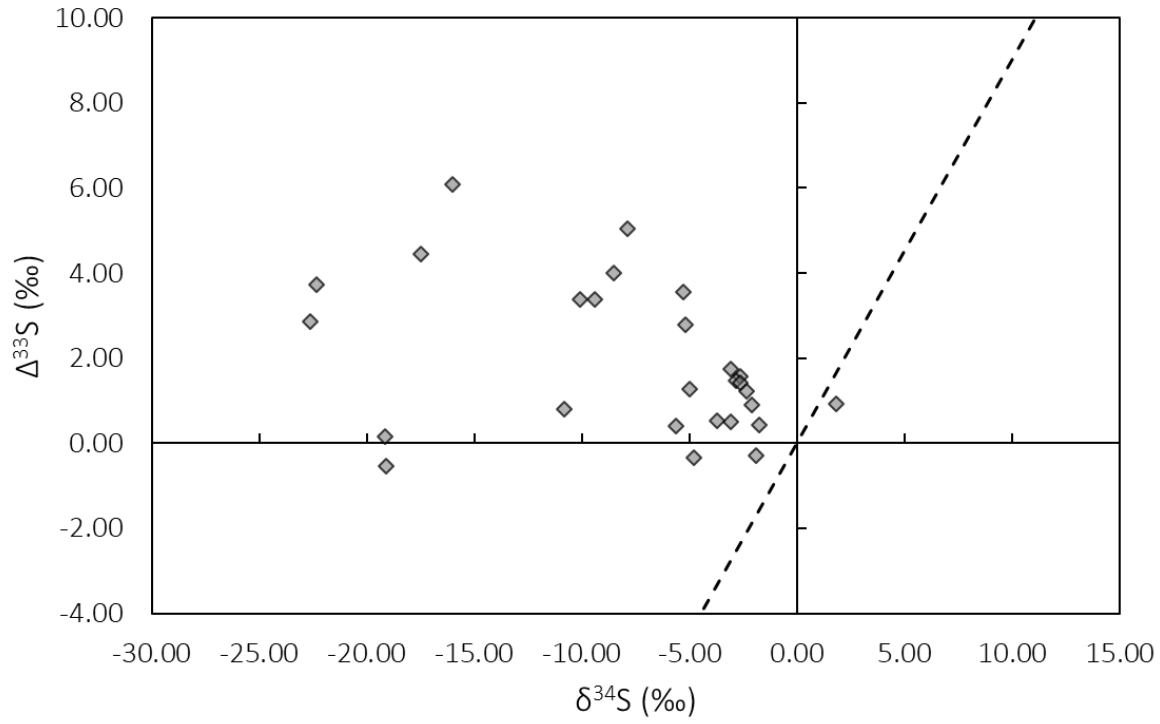

Figure 1.5. Isotopic signatures produced by microbial sulfur disproportionators during the Archean. Here, sulfide minerals show positive $\Delta^{33}S$ signatures but deviate from the Archean reference array (represented by the dashed line) in $\delta^{34}S$. Data from Philippot et al. (2007); Wacey et al. (2010).

Abiotic processes

Thermochemical sulfate reduction (TSR) is also believed to have been an active fractionation process within the Archean sulfur cycle (e.g. Bekker et al., 2009; Watanabe et al., 2009; Jamieson et al., 2013). TSR reduction may refer to either abiotic reduction of sulfate where ferrous iron (Fe^{2+}) acts as a reductant or abiotic reduction of sulfate where organic matter acts as a reductant. These reactions occur at higher temperatures than MSR, which is typically active between 0 – 110 °C but has an optimal temperature range between ~20 – 40 °C (Jørgensen et al., 1990; Sagemann et al., 1998; Canfield et al., 2001b). Both forms of TSR have been proposed to have been involved within the Archean sulfur cycle.

TSR reduction involving Fe^{2+} proceeds via equation 1.9 and occurs at temperatures of ~200 – 350 °C (Trudinger et al., 1985). The isotopic fractionations produced by this process are not well defined but modelling completed by Janecky and Shanks (1988) showed that it concentrates ^{34}S in the product sulfide, resulting in positive fractionations in $\delta^{34}S$ of ≥ 5 ‰. How this process fractionates the minor isotopes of sulfur is yet to be investigated. Within the rock record, this process is usually recognized where sulfide minerals carrying negative $\Delta^{33}S$ values (which requires reduction of MIF sulfate) occur within high-temperature deposits or environments, such as volcanogenic massive sulfide (VMS) deposits (e.g. Jamieson et al., 2006, 2013; Bekker et al., 2009).

$$8Fe^{2+} + 10H^{+} + SO_4^{2-} \rightarrow 8Fe^{3+} + H_2S + 4H_2O \quad (1.9)$$

TSR involving organic matter commonly occurs at temperatures of ~100 – 140 °C, but can be observed at temperatures up to 180 °C (Machel, 1998; Claypool and Mancini, 1989). Its mechanism is similar to that provided in equation 1.6. Experimental results indicate that this process concentrates ^{32}S in the product sulfide and produces negative fractionations in $\delta^{34}S$ of between ~0 – 10 ‰ (Kiyosu, 1980). It has also been shown that the $\Delta^{33}S$ values of the product sulfide are ~0.1 – 2.1 ‰ higher than that of the reactant sulfate (Watanabe et al., 2009). The $\Delta^{36}S$ values of the product sulfide are variable and may be either more positive or more negative than those reactant sulfate; Watanabe et al. (2009) observed changes between -1.1 - +1.1 ‰. Whilst this process has been proposed to be active within the Archean sulfur cycle, it is yet to be definitively recognized.

Now that these fractionation processes are familiar, they can be placed within the context of the Archean sulfur cycle.

1.3 Systematics and sulfur reservoirs of the Archean sulfur cycle

Figure 1.3 provides a schematic illustration of the Archean sulfur cycle. Volcanic sulfur gases were introduced into the atmosphere during volcanic eruptions and periods of quiescent degassing. These sulfur gases were then involved in the photolysis reactions described in the previous section, producing reduced and oxidized sulfur aerosols carrying MIF signatures (Farquhar et al., 2001). The aerosols were then preserved, via abiotic and biotic mechanisms, within sediments and altered oceanic crust. A large portion of the oxidized aerosol is also believed to have resided within the ocean (Farquhar and Wing, 2003; Ono et al., 2003; Zhelezinskaia et al., 2014; Eickmann et al., 2018). It is expected that some sulfur was introduced into the oceans via weathering of the continents but this amount was likely small compared to the modern flux due to lack of oxidative weathering. Currently the isotopic composition of this terrestrial sulfur is poorly defined. Finally, sulfur within marine sediments and altered oceanic crust were subducted, to begin the cycle again (Farquhar et al., 2002; Farquhar and Wing, 2003).

A discussion of the isotopic composition of the different sulfur reservoirs within this cycle and the fractionation processes active within the reservoirs is provided below.

Mantle and igneous reservoirs

Sulfur within the mantle was traditionally believed to be unfractionated and similar in composition to meteoritic sulfur, where $\delta^{34}S = 0 \pm 2$ ‰ (Thode et al., 1961) and $\Delta^{33}S$ and $\Delta^{36}S = \sim 0$ ‰ (Farquhar and Wing, 2003). More recently, however, evidence for isotopic heterogeneity has been discovered. Sulfide minerals within mantle xenoliths ($\delta^{34}S = 1.3 \pm 3.8$ ‰) and primitive igneous rocks (mid-ocean ridge basalts: $\delta^{34}S = -0.3 \pm 3.8$ ‰, ocean island basalts: $\delta^{34}S = 1.0 \pm 1.9$ ‰) and sulfide inclusions within diamonds ($\delta^{34}S = -0.8 \pm 5.0$ ‰) all show variability in $\delta^{34}S$ (Sakai et al., 1984; Chaussidon et al., 1987, 1989; Torssander, 1989; Eldridge et al., 1991; Farquhar et al., 2002; Thomassot et al., 2009; Cabral et al., 2013). Sulfide inclusions within diamonds also indicate that the mantle shows isotopic heterogeneity in $\Delta^{33}S$ ($\Delta^{33}S = -0.5$ - $+1$ ‰; Farquhar et al., 2002; Thomassat et al., 2009; Cabral et al., 2013). The $\Delta^{36}S$ values of sulfur within the mantle is yet to be investigated.

The isotopic composition of Archean igneous sulfur is less studied and sulfur isotope data from Archean igneous rocks is scarce. Igneous sulfur is typically expected to have $\Delta^{33}S$ and $\Delta^{36}S$ values of ~0 ‰, as the majority of processes which cause variation in $\Delta^{33}S$ and $\Delta^{36}S$ are either surficial (e.g. SO-SO_2 photolysis) or occur at lower temperatures than found within

igneous systems (e.g. MSR). Sulfur isotope measurements made on an Archean granite and diabase by Maynard et al. (2013) returned $\Delta^{33}S$ values of -0.072 ‰ and -0.076 ‰, respectively, consistent with this hypothesis. However, analysis of pyrrhotite hosted by the ca. 2700 Ma Abitibi granite-greenstone returned mean $\Delta^{33}S$ and $\Delta^{36}S$ values of -0.96 ± 0.04 ‰ and 1.02 ± 0.27 ‰, respectively (LaFlamme et al., 2016), providing evidence against this hypothesis. Additionally, as mentioned above, studies of sulfide inclusions within diamonds have shown heterogeneity in $\Delta^{33}S$ for sulfur within the mantle (Farquhar et al., 2002; Thomassot et al., 2009; Cabral et al., 2013) and incorporation of crustal sulfur carrying non-zero $\Delta^{33}S$ and $\Delta^{36}S$ values would also have the potential to result in variability in $\Delta^{33}S$ and $\Delta^{36}S$. Therefore, further analysis of Archean igneous sulfides may reveal non-zero $\Delta^{33}S$ and $\Delta^{36}S$ values. The $\delta^{34}S$ values of Archean igneous sulfides can be estimated to some degree from the composition of post-Archean igneous rocks to be between ~-5 – 10 ‰ (Ueda and Sakai, 1984; Chaussidon et al., 1987; Rye et al., 1984; Ohmoto and Goldhaber, 1997; Luhr and Logan, 2002). The limited measurements completed on Archean igneous sulfides fall within this range (Maynard et al., 2013; LaFlamme et al., 2016).

Similar to both mantle sulfur and igneous sulfides, the volcanic sulfur gases involved in photolysis reactions within the Archean sulfur cycle are traditionally expected to have $\Delta^{33}S$ and $\Delta^{36}S$ of ~0 ‰. More recently it has also been proposed that, post the start of plate tectonics, these sulfur gases could carry significant non-zero $\Delta^{33}S$ and $\Delta^{36}S$ anomalies due to recycling of MIF sulfur (Gallagher et al., 2017).

Marine reservoirs

Marine sulfur reservoirs can be divided into marine sediments, seafloor hydrothermal environments and seawater sulfate.

Marine sediments

Archean marine sedimentary rocks most often contain pyrite with positive $\Delta^{33}S$ and negative $\Delta^{36}S$ signatures, which indicates that the reduced, MIF elemental sulfur aerosol was preserved within this environment. In particular, these signatures are typically observed within clastic sedimentary rocks such as shales and mudstones, both in shallow and deep marine samples (e.g. Ono et al., 2003; Thomazo et al., 2009; Gregory et al., 2015b; Izon et al., 2015). Currently, however, how the MIF elemental sulfur was converted to sulfide and incorporated into sulfide minerals within these sediments is not well known.

One possible mechanism is microbial disproportionation of elemental sulfur but, whilst believed to have been an active process during the Archean, it does not appear to have been dominant. Evidence for MSD, in the form of pyrite with positive $\Delta^{33}S$ and relatively large $\delta^{34}S$ values, where the isotopic composition deviates from the ARA in $\Delta^{33}S$-$\delta^{34}S$ space, is only rarely observed within the rock record (Philippot et al., 2007; Wacey et al., 2010). A pathway involving microbial oxidation, is also considered unlikely, as it would be expected that if the MIF elemental sulfur was oxidized to sulfate, it would then mix with the MIF sulfate and the $\Delta^{33}S$ and $\Delta^{36}S$ signatures of opposite sign would cancel each other and be essentially erased. Therefore, at least a portion of the MIF elemental sulfur must have been incorporated into sulfide minerals without first being oxidized.

There are three other possible mechanisms which do not involve oxidation: abiotic sulfur disproportionation, microbial reduction of elemental sulfur and reaction with FeS. Abiotic sulfur disproportionation occurs via a similar mechanism to that described in equation 1.7. This process can occur at low temperatures (<200 °C) and, at these temperatures, produces only small fractionations in $\delta^{34}S$ of <3 ‰ in the product sulfide (Smith, 2000). Therefore, this could possibly explain the observation of pyrite with positive $\Delta^{33}S$ signatures with an isotopic composition that does not deviate from the ARA in $\Delta^{33}S$-$\delta^{34}S$ space. Similarly, microbial reduction of elemental sulfur produces only small fractionations in $\delta^{34}S$ in the product sulfide, both positive and negative. The largest observed fractionation produced by this process is ~-5 ‰, with most fractionations being <2 ‰ (Kaplan and Rittenberg, 1962; Tada et al., 2008; Surkov et al., 2012). Finally, MIF elemental sulfur could have been fixated through reaction with FeS (equation 1.10) via polysulfides or other metastable intermediates (Berner, 1970; Rickard, 1975; Luther, 1991; Schoonen and Barnes, 1991).

$$FeS + S_0 \rightarrow FeS_2 \quad (1.10)$$

Here, the FeS could contain sulfide from MSR, MSD or microbial elemental sulfur reduction.

Less typically observed within Archean marine sedimentary rocks are sulfide minerals carrying negative $\Delta^{33}S$ values, indicating that the oxidized MIF sulfate aerosol was also preserved within this environment. These signatures are typically observed within sulfide minerals hosted by sedimentary rocks which precipitate directly from seawater, such as limestones, dolomites, chert and banded iron formations (BIF) (e.g. Mojzsis et al., 2003; Ono et al., 2003; Kaufman et al., 2007; Zhelezinskaia et al., 2014; Muller et al., 2016; Eickmann et al., 2018) or within clastic sedimentary rocks associated with or interbedded with these rock

types (e.g. Kaufman et al., 2007; Ono et al., 2009; Farquhar et al., 2013). Here, the MIF sulfate appears to have been dominantly transformed to sulfide via MSR, as indicated by variable and/or relatively large negative $\delta^{34}S$ values and deviation from the ARA in $\Delta^{36}S$ (e.g. Mojzsis et al., 2003; Zhelezinskaia et al., 2014; Mishima et al., 2017; Eickmann et al., 2018).

Seafloor hydrothermal environments

Sulfide and sulfate minerals present within Archean altered oceanic crust where seawater was circulated through hydrothermal systems (e.g. volcanogenic massive sulfide deposits) typically carry negative $\Delta^{33}S$ values between 0 ‰ and -1 ‰ (e.g. Jamieson et al., 2006, 2013; Bekker et al., 2009). Within these environments, MIF sulfate present within seawater is believed to be transformed into sulfide through TSR where Fe^{2+} acts an oxidant, with the Fe^{2+} being present within hydrothermal fluids and having likely been sourced from the surrounding rock (Farquhar and Wing, 2003; Jamieson et al., 2006, 2013; Bekker et al., 2009). The magnitude of the negative $\Delta^{33}S$ values is typically low and this has been attributed mixing with hydrothermal sulfide carrying $\Delta^{33}S$ values of ~0 ‰ following TSR (Jamieson et al., 2013). The $\Delta^{36}S$ values of sulfur minerals within these environments is yet to be investigated.

Seawater sulfate

As mentioned above, a significant amount of MIF sulfate is believed to have resided within seawater. Under the low oxygen atmosphere, input of sulfate from the continents is believed to have been negligible due to lack of oxidative weathering, and atmospheric deposition of MIF sulfate is believed to have been the dominant source of seawater sulfate (Farquhar et al., 2000, 2001; Ono et al., 2003). The isotopic composition of seawater sulfate can be estimated from the isotopic composition of sedimentary sulfate minerals and sulfide minerals produced through MSR of seawater sulfate. This produces an estimated range of ~+3 — +16 ‰ for $\delta^{34}S$ (Lambert et al., 1987; Canfield and Raiswell, 1999; Ono et al., 2003), ~-1 — -2 ‰ for $\Delta^{33}S$ (Farquhar et al., 2000; Ono et al., 2003; Ueno et al., 2008; Shen et al., 2009; Zhelezinskaia et al., 2014) and ~+1 — +2 ‰ for $\Delta^{36}S$ (Ueno et al., 2008; Shen et al., 2009). More recent measurements made on sedimentary barite by Muller et al. (2016, 2017), however, indicate that the $\Delta^{33}S$ and $\Delta^{36}S$ values of seawater sulfate may have been more variable.

Terrestrial reservoirs

Here ‘terrestrial sulfur reservoirs’ refer to sulfur contained within terrestrial sedimentary rocks. It does not include sulfur contained within igneous rocks that formed part of the continents, as this has already been discussed.

In comparison to the marine sulfur reservoirs, there is only a limited amount of data available from terrestrial sedimentary sulfide minerals and, consequently, the isotopic composition of terrestrial sulfur reservoirs is poorly defined (Figure 1.6). The small amount of data available from sulfide minerals hosted by terrestrial sedimentary rocks (e.g. fluvial sandstones and conglomerates, paleosols, glacial diamictites), including both diagenetic grains and detrital grains of sedimentary origin, shows that these minerals typically show small negative $\Delta^{33}S$ values (Guy et al., 2012, 2014; Maynard et al., 2013). This implies that the MIF sulfate aerosol was being preserved within these environments but the small magnitude of the negative $\Delta^{33}S$ values suggests that it may be being mixed with some form of sulfur carrying $\Delta^{33}S$ values of ~0 ‰, similar to what occurs within seafloor hydrothermal environments. It has previously been suggested that this sulfur with $\Delta^{33}S$ of ~0 ‰ has been sourced from subaerial volcanism (Kump and Barley, 2007; Gaillard et al., 2011; Guy et al., 2012), and/or low temperature geothermal systems (McCarthy et al., 1990; Myers et al., 1990; Falconer, 2003; Guy et al., 2012) and/or weathering of reactive sulfide minerals present in igneous rocks in the surrounding areas (Reinhard et al., 2009; Lefticariu et al., 2010; Wacey et al., 2011; Guy et al., 2012) and/or otherwise inherited from igneous rocks (Maynard et al., 2013). Variable and/or relatively high magnitude negative $\delta^{34}S$ values and negative $\Delta^{36}S$ values observed for some sulfide minerals (e.g. Guy et al., 2012; Nabhan et al., 2016, 2018) suggests that the MIF sulfate was being transformed to sulfide via MSR. Note that this contrasts to the isotopic composition of marine clastic sediments, which preferentially preserve MIF elemental sulfur and where MSR was not a dominant process. Therefore, examining the isotopic composition of terrestrial sulfur reservoirs is of interest not only because it remains largely undefined but also because the sulfur being preserved within these environments, and the methods by which it is being preserved, appear different from that preserved within the equivalent marine reservoirs.

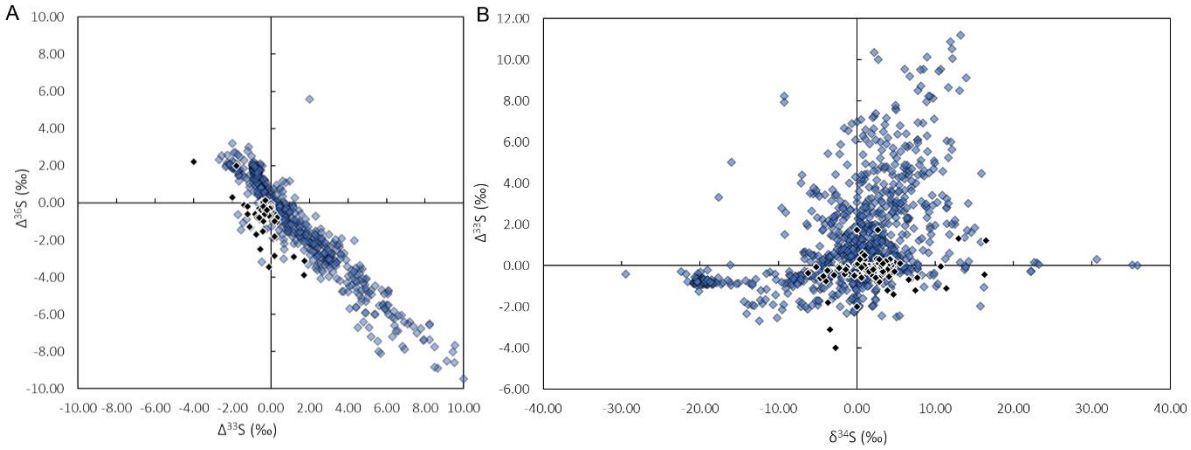

Figure 1.6. Sulfur isotope data from marine and terrestrial sedimentary rocks. Filled blue diamonds represent marine data, filled black diamonds represent terrestrial data. A. $\Delta^{36}S$ vs. $\Delta^{33}S$, B. $\Delta^{33}S$ vs. $\delta^{34}S$. Data from Mojzsis et al. (2003); Ono et al. (2003, 2009); Whitehouse et al. (2005); Ohmoto et al. (2006); Kaufman et al. (2007); Patridge et al. (2008); Hofmann et al. (2009); Shen et al., (2009); Thomazo et al. (2009); Guy et al. (2012, 2014); Zerkle et al. (2012); Farquhar et al. (2013); Kurzweil et al. (2013); Maynard et al. (2013); Zhelezinskaia et al. (2014); Izon et al. (2015); Muller et al. (2016, 2017); Mishima et al. (2017); Eickmann et al. (2018).

The exception to this is pyrite from shales of the ~2730 Ma Tumbiana Formation. Here, $\Delta^{33}S$ values are typically small and positive. Bulk analysis of pyrite returned $\delta^{34}S$ values of -5.73 — 2.75 ‰ (mean of -0.36 ‰), $\Delta^{33}S$ values of -0.25 — 1.64 ‰ (mean of 0.47 ‰) and $\Delta^{36}S$ values of -1.89 — 0.84 ‰ (mean of -0.46 ‰) (Thomazo et al., 2009). Secondary ion mass spectrometry (SIMS) analysis returned similar values: $\delta^{34}S$ values of -8.80 — 3.02 ‰ (mean of -0.90 ‰) and $\Delta^{33}S$ values of -0.31 — 0.91 ‰ (mean of 0.52 ‰) (Wiliford et al., 2016). These signatures have been interpreted to represent biological sulfur cycling in a low sulfate environment where there was input of MIF elemental sulfur (Thomazo et al., 2009; Wiliford et al., 2016). However, the depositional environment of the Tumbiana Formation is heavily disputed. The upper Mingah Member has varyingly been interpreted to represent fluvial (Packer, 1990), fluvial and shallow marine (Thorne and Trendall, 2001) and alluvial and shallow marine (Sakurai et al., 2005) depositional environments. Meanwhile, the underlying Meentheena Member has been inconsistently been interpreted to represent marine (Packer, 1990; Thorne and Trendall, 2001; Sakurai et al., 2005) and lacustrine depositional environments (Kriewaldt and Ryan, 1967; Walter, 1983; Buick, 1992; Bolhar and Van Kronendonk, 2007; Awmarik and Buchheim, 2009; Coffey et al., 2013). Therefore, the sulfur isotope signatures of pyrite from the Tumbiana Formation are not included in the discussions in Chapter 7 of the isotopic composition of terrestrial sedimentary sulfur reservoirs.

Non-marine surface waters

Currently, the sulfur isotope composition of sulfate within non-marine surface waters is undefined. However, as the Archean sulfur cycle is believed to have been dominated by photolysis of SO and SO_2 and the low atmospheric oxygen concentrations during the Archean would have limited oxidative weathering of sulfide minerals, the dominant sulfate flux to both non-marine and marine waters would have been atmospheric. Therefore, it could be hypothesized that sulfate in non-marine waters would have a similar isotopic composition to that of seawater sulfate.

1.4 Trends in the Archean sulfur isotope data record

As the Archean sulfur isotope data record has grown, temporal and secular trends have been identified within that record. In particular, it has been noted that Mesoarchean sulfur minerals show isotopic compositions which differ from those of sulfur minerals from the Eo-, Paleo- and Neoarchean eras. More specifically, the magnitude of the $\Delta^{33}S$ and $\Delta^{36}S$ values shown by Mesoarchean minerals are restricted in comparison to the values shown by minerals from the other Archean eras. Additionally, this attenuation in $\Delta^{33}S$ and $\Delta^{36}S$ occurs concurrently with steepening of the slope of the MIF $\Delta^{36}S/\Delta^{33}S$ array.

Outside of the Mesoarchean, similar steepening of the MIF $\Delta^{36}S/\Delta^{33}S$ array is observed during the Neoarchean. Besides this, there is also a consistent bias towards positive $\Delta^{33}S$ and negative $\Delta^{36}S$ signatures observed throughout the entirety of the Archean eon. All of these trends are discussed in further detail below.

Mesoarchean minimum in $\Delta^{33}S$ and $\Delta^{36}S$ values

There is an apparent minimum in the absolute ranges of $\Delta^{33}S$ and $\Delta^{36}S$ values during the Mesoarchean (Figure 1.7). It is observed that Mesoarchean sulfur minerals show a range in $\Delta^{33}S$ values of approximately ~4 ‰, in comparison to range of ~14 ‰ across the other Archean eras. There is less $\Delta^{36}S$ data available, particularly for the early Archean, however, Mesoarchean samples are observed to show a range of ~6 ‰ in comparison to a range of ~14 ‰ displayed by Neoarchean samples. Numerous hypotheses have been proposed the cause of the attenuated signatures, including:

- A transient increase in the oxygen concentrations of the Archean atmosphere (Ono et al., 2006b).

- An oxic atmosphere since ~3800 Ma, where periods of high magnitude $\Delta^{33}S$ and $\Delta^{36}S$ values represent phases of high volcanic activity where sulfur gases where ejected into the atmosphere and underwent photolysis (Ohmoto et al., 2006).
- Variability in the oxidation state of volcanic sulfur volatiles (Halevy et al., 2010).
- Changes in atmospheric chemistry which altered the transparency of the atmosphere to UV radiation and impacted the photolysis reactions which produce MIF signatures (Farquhar et al., 2007; Domagal-Goldman et al., 2008; Thomazo et al., 2009).
- Dilution of the MIF sulfur signal by mass-dependent crustal sulfur (Guy et al., 2012).
- Dominance of the elemental sulfur exit channel (Pavlov and Kasting, 2002; Kurzweil et al., 2013; Izon et al., 2015). Here mass balance demands that if atmospheric sulfur removal is dominated by one exit channel, that species will display lower magnitude $\Delta^{33}S$ and $\Delta^{36}S$ values (Kurzweil et al., 2013; Claire et al., 2014).

Another possibility, not listed above, is that the attenuation in MIF signatures during the Mesoarchean could be due to an increase in the partial pressure of CO_2 (PCO_2). This is because at $PCO_2 > 0.5$ bar, the Rayleigh scattering tail of CO_2 is sufficient to block the UV radiation involved in the photolysis reactions which produce MIF signatures (Shemansky, 1972; Farquhar et al., 2001; Farquhar and Wing, 2003; Mojzsis, 2007).

Despite these numerous hypotheses, the reason for the attenuated Mesoarchean $\Delta^{33}S$ and $\Delta^{36}S$ values remains unclear. This in part due to the restricted amount of four sulfur isotope data available from Mesoarchean samples and in part due to inadequate constraints being placed on paragenesis of sulfide minerals prior to analysis. Here, inadequate restraints on paragenesis can lead to the isotopic signatures of detrital or epigenetic grains being interpreted as representative of the depositional environment, when this is not the case.

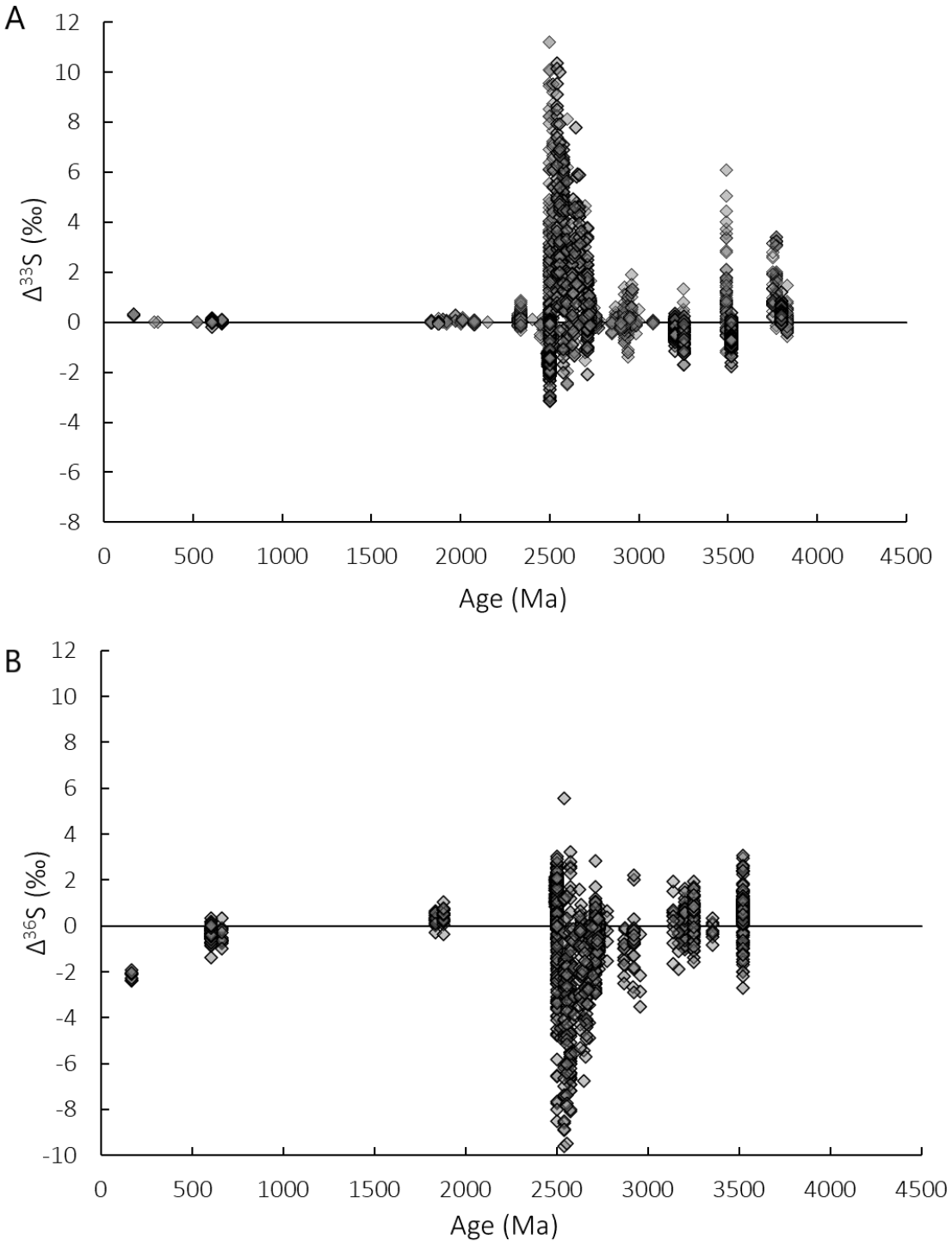

Figure 1.7. Variation in $\Delta^{33}S$ and $\Delta^{36}S$ values with time. A. $\Delta^{33}S$ vs. time, B. $\Delta^{36}S$ vs. time. Data from Mojzsis et al. (2003); Ono et al. (2003, 2006a, 2009) Bekker et al. (2004); Johnston et al., (2005b, 2006); Papineau et al. (2005, 2007); Whitehouse et al. (2005); Cates and Mojzsis (2006); Ohmoto et al. (2006); Farquhar et al. (2007); Kamber and Whitehouse (2007); Philippot et al. (2007); Domagal-Goldman et al. (2008); Patridge et al. (2008); Cates (2009); Hofmann et al. (2009); Thomazo et al. (2009); Guy et al. (2012); Zerkle et al. (2012); Kurzweil et al. (2013); Maynard et al. (2013); Zhelezinskaia et al. (2014); Izon et al. (2015); Crockford et al. (2016); Muller et al. (2016, 2017); Roerdink et al. (2016); Sansjofre et al. (2016); Mishima et al. (2017).

Variation in the MIF $\Delta^{36}S/\Delta^{33}S$ array

Initially, it was identified that Archean sulfur minerals showed isotopic compositions where $\Delta^{36}S/\Delta^{33}S$ = ~-0.90 (Figure 1.2A; Farquhar et al., 2001). However, as more four sulfur isotope data have been collected, it has become apparent that Archean sulfur minerals show variable $\Delta^{36}S/\Delta^{33}S$ arrays.

Within the Neoarchean, $\Delta^{36}S/\Delta^{33}S$ slopes have been observed to vary over short stratigraphic intervals. Time-equivalent 2700 – 2500 Ma sedimentary sequences of South Africa and Australia were observed to display steepening $\Delta^{36}S/\Delta^{33}S$ arrays (from ~-0.90 to ~-1.5) over restricted stratigraphic intervals, where this steepening was accompanied by high magnitude negative $\delta^{13}C_{org}$ values of <-38 ‰ (Zerkle et al., 2012; Izon et al., 2015). These negative $\delta^{13}C_{org}$ values were interpreted to represent periods of enhanced biogenic methane flux, which was hypothesized to have increased the atmospheric CH_4:CO_2 mixing ratios and caused the formation of organic haze. The presence of this organic haze was then proposed to have slowed the atmospheric sulfur cycle and possibly altered the photolysis reactions which produce MIF signatures, resulting in the observed change in the $\Delta^{36}S/\Delta^{33}S$ array (Domagal-Goldman et al., 2008; Haqq-Misra et al., 2008; Izon et al., 2015). Intervening sections within these sedimentary sequences, which showed more positive $\delta^{13}C_{org}$ values and sulfur minerals with isotopic compositions that fell on the typical ARA of $\Delta^{36}S/\Delta^{33}S$ = ~-0.90 were interpreted to represent haze-free background states (Zerkle et al., 2012). Shallower $\Delta^{36}S/\Delta^{33}S$ slopes (~-0.60 and ~-0.80) were also observed within these sequences but remain unexplained (Kurzweil et al., 2013; Izon et al., 2015). These fluctuating $\Delta^{36}S/\Delta^{33}S$ slopes not only suggest that the chemistry of the Neoarchean atmosphere was quite dynamic but also that MIF signatures can be influenced by various atmospheric constituents, not just oxygen.

Variable $\Delta^{36}S/\Delta^{33}S$ arrays have also been observed within Mesoarchean samples, concurrent with the observed attenuation in the magnitude of $\Delta^{33}S$ and $\Delta^{36}S$ values (Farquhar et al., 2007; Guy et al., 2012; Mishima et al., 2017). Farquhar et al. (2007) observed variable $\Delta^{36}S/\Delta^{33}S$ arrays within sedimentary rocks of South Africa, with Guy et al. (2012) also observing a steepened $\Delta^{36}S/\Delta^{33}S$ array within one of the same sedimentary sequences. Mishima et al. (2017) observed a similar steepened array ($\Delta^{36}S/\Delta^{33}S$ = ~1.5) within an Indian sedimentary sequence. Initially, Farquhar et al. (2007) interpreted this to represent variations in atmospheric chemistry which altered the transparency of the atmosphere. This hypothesis was proposed on the basis that the slope of the $\Delta^{36}S/\Delta^{33}S$ array produced by photolysis reactions is wavelength dependent, i.e. the slope of the $\Delta^{36}S/\Delta^{33}S$ array changes depending on the

wavelength of UV radiation involved in the photolysis reactions (Farquhar et al., 2001). Therefore, if the transparency of the atmosphere changed, it may alter the wavelengths of UV radiation that are penetrating the atmosphere and interacting with volcanic sulfur gases, and, as a result, alter the $\Delta^{36}S/\Delta^{33}S$ slope (Farquhar et al., 2007). More recently, the steepened slopes observed for Mesoarchean samples was attributed to the presence of a persistent organic haze (Domagal-Goldman, 2008; Haqq-Misra et al., 2008; Kurzweil et al., 2013; Mishima et al., 2017). However, when the greater Archean data record is examined, it is obvious that there is little four sulfur isotope data available for samples older than ~2700 Ma and that much of this data deviates from this slope of ~-1.50. Therefore, caution should be taken in attempting to determine the state of the Mesoarchean atmosphere until further four sulfur isotope data is gathered.

Bias towards positive $\Delta^{33}S$ and negative $\Delta^{36}S$ signatures

Within the current data record, there is an asymmetry in the $\Delta^{33}S$ and $\Delta^{36}S$ records in terms of both frequency and magnitude. Mass balance of sulfur cycled through the Archean atmosphere dictates that the average $\Delta^{33}S$ and $\Delta^{36}S$ values of all MIF sulfur must be equal to those of primitive sulfur, where $\Delta^{33}S$ and $\Delta^{36}S$ are expected to be ~0 ‰. However, this is not observed. Not only are positive $\Delta^{33}S$ and negative $\Delta^{36}S$ signatures observed more frequently than signatures of the opposite signs but they also extend to much higher magnitudes (Figure 1.7). Positive $\Delta^{33}S$ values of up to +12 ‰ are observed, but negative $\Delta^{33}S$ values are observed to extend down to only ~-4 ‰. Similarly, negative $\Delta^{36}S$ values are observed to extend down to ~-10 ‰, whilst positive values extend upwards to only ~+4 ‰.

Reinhard et al. (2013) proposed that this bias could have been caused by preferential erosion of reservoirs of negative $\Delta^{33}S$, positive $\Delta^{36}S$ sulfur over geologic time. As mentioned above, initial measurements suggest that sulfide minerals within terrestrial sediments do preserve small negative $\Delta^{33}S$ values (Guy et al., 2012, 2014; Maynard et al., 2013) and, as these sediments exist on the continental surface, they were likely more vulnerable to erosion than the marine sediments which preserve positive $\Delta^{33}S$ sulfur. However, oxidative weathering and erosion of the continental surfaces is considered to have been much less active during the Archean, so this may not fully explain the observed bias.

It has also been suggested that the bias is due to a sampling imbalance within the current data record, where reservoirs of negative $\Delta^{33}S$, positive $\Delta^{36}S$ sulfur have been under-sampled and therefore are underrepresented (Farquhar and Wing, 2003; Maynard et al., 2013). Maynard et

al. (2013) has suggested that terrestrial sediments, which are under-sampled within the current record, could contain a large reservoir of negative $\Delta^{33}S$ sulfur capable of balancing the currently observed bias. This hypothesis is supported by the limited amount of data currently available from sulfide minerals hosted by terrestrial samples (Hofmann et al., 2009; Guy et al., 2012, 2014; Maynard et al., 2013). Therefore, further analysis of terrestrial sulfur reservoirs would also be beneficial in testing this hypothesis, in addition to constraining the isotopic composition of terrestrial sulfur reservoirs.

1.5 The approach taken in this thesis

Thus far, this chapter has highlighted that (a) the isotopic composition of terrestrial sulfur reservoirs is poorly constrained, (b) these reservoirs possibly preserve different forms of sulfur and that sulfur is preserved through different mechanisms than within the equivalent marine reservoirs, and (c) further sampling of terrestrial sediments may help to correct the bias positive $\Delta^{33}S$ and negative $\Delta^{36}S$ values within the current data record. Therefore, the primary objective of this thesis is to explore the isotopic composition of terrestrial sulfur reservoirs and determine if and why differences exist between the isotopic compositions of terrestrial and marine reservoirs.

It has also been highlighted that Mesoarchean sulfur minerals show isotopic signatures which differ from those of minerals from the other Archean eras and that interpretation of the causes of these differences is currently hindered by the lack of well constrained four sulfur isotope data collected from Mesoarchean samples. Therefore, it is a secondary objective of this thesis is to re-examine the Mesoarchean sulfur isotope record and explore possible causes of both the apparent minimum in $\Delta^{33}S$ and $\Delta^{36}S$ values and the steepened MIF $\Delta^{36}S/\Delta^{33}S$ array.

Below is a brief description of the approach taken in this thesis, accompanied by justifications of the chosen approach. A more detailed description of the analytical methods used in this thesis is provided in Chapter 2.

Sample selection

The primary sampling areas chosen for this thesis were the Mesoarchean Pongola and Witwatersrand supergroups, both of which occur on the Kaapvaal Craton of South Africa. These were chosen as they both contain well-preserved sedimentary sequences which are relatively unaltered and have largely experienced only low grades of metamorphism (Watchorn and Armstrong, 1981; Hegner et al., 1984; Phillips, 1987; Wronkiewicz and Condie, 1989; Frimmel et al., 1993). Therefore, the sulfur isotope data collected from

minerals within these sequences should be representative of Mesoarchean sequences. Additionally, within these sequences, sulfide minerals occur within a wide range of rock types, including glacial diamictites, paleosols and both fluvial and marine clastic sedimentary rocks. This allows for analysis of sulfide minerals from a range of different types of terrestrial sedimentary rocks, providing a more complete inspection of the isotopic composition of terrestrial sulfur reservoirs. Furthermore, the occurrence of terrestrial and marine clastic sedimentary rocks within the same sedimentary sequence allows for a direct comparison of the isotopic composition of the sulfide minerals within those rocks, eliminating any isotopic variation that could have been caused by different local environmental conditions. Finally, the Mesoarchean age of these sequences provides the opportunity to simultaneously re-examine the apparent minimum in $\Delta^{33}S$ and $\Delta^{36}S$ values and steepened $\Delta^{36}S/\Delta^{33}S$ arrays previously observed for this era (Farquhar et al., 2007; Guy et al., 2012; Mishima et al., 2017).

More detailed information regarding the geology of the Pongola and Witwatersrand supergroups is provided in Chapters 3 and 4, respectively.

Sample characterization

Sample characterisation involved detailed morphological and textural studies carried out using reflected light microscopy and back scatter electron imaging (BSE). This was followed by NaOCl etching and trace element analysis, conducted via laser ablation inductively coupled plasma mass spectrometry (LA-ICP-MS). These steps were undertaken in order to determine the paragenesis of sulfide grains, i.e. whether they were detrital, syngenetic/diagenetic or epigenetic origin. This is crucial to ensure that the sulfur isotope data gained from these grains is interpreted in the correct context.

Morphological and textural analysis

Morphological and textural analysis of sulfide mineral grains and examination of the relationships between these grains and the surrounding matrix has long been used to constrain sulfide mineral paragenesis and is still commonly used in modern studies (e.g. Ramdohr, 1958; Saager, 1970; McClay and Ellis, 1983; Craig et al., 1998; England et al., 2002; Guy et al., 2010, 2012, 2014; Philippot et al., 2018). For this thesis, features such as the size, shape, abundance and internal textures of grains, shape and distribution of pores, distribution of grains and association with other minerals were used to determine paragenesis.

Detrital grains are typically recognized by rounded edges, which is an indication of mechanical transport. Additionally, internal textural features will typically be truncated at

these rounded edges (e.g. England et al., 2002; Guy et al., 2014). However, it is important to note that smaller detrital grains may not show rounding and can retain an angular shape (Utter, 1980; Guy et al., 2010). Detrital grains are also commonly observed to be concentrated along sedimentary features, such as scour surfaces, where they occur with other heavy minerals such as zircon and titanium oxides (e.g. England et al., 2002; Guy et al., 2010). The features described above are not necessarily displayed for detrital grains within glacial diamictites, however, which will be discussed in further detail in Chapter 3.

Syngenetic/diagenetic grains can display a wide range of sizes, shapes and textures, from small (<20 μm) euhedral, non-porous grains (e.g. Taylor and Macquaker, 2000; Guy et al., 2010) to large (>500 μm), porous nodules (e.g. Guy et al., 2010; Gregory et al., 2015b, 2019), to highly anhedral, concretionary cements which envelope clasts within clastic sediments (e.g. Carstens, 1986; Salles-Martinez, 1996). Due to this variability, some caution should be used when attempting to determine if a grain is syngenetic/diagenetic solely using morphology and texture. However, reviews of the various morphologies and textures displayed by syngenetic/diagenetic grains are available and can be employed when attempting to identify this grain type (e.g. Saager, 1970; Guy et al., 2010).

Epigenetic grains are commonly recognized due to their frequently large size (>500 μm), euhedral shape, high abundance (presence in aggregates) and either lack or pores, or presence of crystallographically-aligned pores (Ramdohr et al., 1958; Saager, 1970; McClay and Ellis, 1983; Craig et al., 1998; Guy et al., 2010). These grains are also typically observed to overprint the surrounding matrix. Epigenetic grains can also be observed to be replacing matrix minerals, or to be occurring within veins and veinlets or polymineralic aggregates, such as aggregates of chalcopyrite, sphalerite and galena (e.g. Craig et al., 1998; Guy et al., 2010; George et al., 2016; Li et al., 2019; Song et al., 2019).

NaOCl etching

NaOCl etching was employed to further investigate textural features of pyrite grains and to identify where multiple generations of pyrite may occur within a single grain or aggregate. The NaOCl acts as an oxidant for the pyrite and the intensity of tarnish varies with mineral composition and crystal lattice orientation. Therefore, zones of different discolouration reflect compositional differences within grains and aggregates, allowing different generations of pyrite to be recognized (e.g. Fleet et al., 1993; King, 2013; Peterson and Mavrogenesis, 2014; Sykora et al., 2018).

Trace element analysis

Theory and overview

Similar to morphological and textural analysis, trace element analysis of sulfide minerals has a long and well-established history of being used to determine sulfide paragenesis (e.g. Cambel and Jarkovsky, 1969; Price, 1972; Bralia et al., 1979; Bajwah et al., 1987; Meyer et al., 1990; Guy et al., 2010; Gregory et al., 2015a). In particular, the Co/Ni ratio of pyrite has been determined to be indicative of the environment in which a sulfide mineral formed. More recently, studies have also begun to look at other elemental ratios, including Cu/Ni, Zn/Ni, As/Ni, Co/As and Ni/As (Guy et al., 2010; Gregory et al., 2015a).

Syngenetic/diagenetic pyrite typically shows low Co/Ni values of 0.01 — 2.00 (Price, 1972; Bajwah et al., 1987; Guy et al., 2010; Gregory et al., 2015a). A study completed by Gregory et al. (2015a) also showed that syngenetic/diagenetic pyrite typically shows Cu/Ni, Zn/Ni and As/Ni values of 0.01 — 10. However, that study was completed only using pyrite from black shales and therefore those parameters should be applied with some caution to pyrite hosted by other sedimentary rock types, especially since the work of Guy et al. (2010) indicates that the trace element composition of syngenetic/diagenetic pyrite varies with depositional environment.

Hydrothermal or epigenetic pyrite has typically been believed to show high Co/Ni values, which exceed those observed in syngenetic pyrite, however this is not always the case (e.g. Guy et al., 2010). Indeed, even those hydrothermal pyrite grains originally analyzed by Price et al. (1972), which is some of the foundation work this hypothesis is based upon, showed an average Co/Ni value of 1.17, which falls within the range determined for syngenetic/diagenetic pyrite. Hydrothermal pyrite, however, does typically show a high level of variability in Co/Ni values, even within the same sample or grain, which can aid in identification (Bralia et al., 1979). Within the sampling areas chosen for this study, hydrothermal pyrite has also been recognized to contain lower concentrations of trace elements, including Co and Ni, than the co-occurring diagenetic pyrite (Utter, 1978; Meyer et al., 1990; Guy et al., 2010).

Studies have also identified that pyrite from VMS deposits show elevated Co/Ni values of ~5 — 50 (Hawley and Nichol, 1961; Price, 1972; Gehrisch et al., 1975; Bralia et al., 1979) where pyrite shows very low concentrations of Ni (Price, 1972; Gehrisch et al., 1975). The trace element composition of pyrite from igneous rocks is less consistent and appears to be

controlled, at least in part, by the composition of the host rock (Hawley and Nichol, 1961; Loftus-Hills and Solomon, 1967; Price et al., 1972).

Choice of analysis method

For this thesis, trace element analysis was carried out via LA-ICP-MS.

In the past, trace element studies of sulfide minerals have employed a method by which partial digestion is used to dissolve pyrite, followed by analysis of the resultant solution (e.g. Huerta-Diaz and Morse, 1992). However, the reactants used during digestion are not selective, meaning that they could dissolve multiple generations of pyrite at one time. Additionally, they also lack mineral specificity (Martin et al., 1987), which can result in trace elements being leached from multiple other minerals, including other sulfide minerals. Both of these factors can lead to erroneous trace element concentrations being measured. Other studies have manually separated the pyrite prior to digestion and analysis (e.g. Berner et al., 2013) and, whilst this eliminates the problems described above, it is time consuming and can still fail to separate pyrite of different generations.

In contrast, LA-ICP-MS does not suffer from these shortcomings. As it allows for in-situ analysis, it is mineral specific. Additionally, the high spatial resolution (this study employed a 35 µm diameter analysis spot) allows for grains to be analyzed individually, reducing the possibility of multiple generations of pyrite being analyzed together. This also minimizes the chance of analysing inclusions of other sulfide minerals that would result in incorrect trace element concentrations being measured. Finally, examination of time-resolved LA-ICP-MS output graphs can provide insights into how the trace elements occur in pyrite. A consistent Fe to trace element ratio commonly indicates that the trace element is contained within the crystal lattice or as evenly distributed nano-inclusions, whilst a sharply changing Fe to trace element ratio indicates that the trace element is occurring within inclusions of other minerals (Large et al., 2007; Thomas et al., 2011).

Whilst other in-situ techniques are available, such as electron microprobe, the lower detection limits and greater variety of elements that can be analyzed simultaneously by LA-ICP-MS made it the preferred method.

Sulfur isotope analysis

For this thesis, four sulfur isotope analysis was conducted via secondary ion mass spectrometry (SIMS) using the Sensitive High-Resolution Ion Microprobe – Stable Isotope (SHRIMP-SI). In comparison to the traditional fluorination method, which requires samples

to be converted to gaseous form and consumes the entirety of a sample, SIMS allows for in-situ isotopic analysis. This decreases the sample preparation time, as sample crushing, grain picking and multiple steps of sample digestion and purification are not required. Additionally, the high spatial resolution of the SHRIMP-SI (a 35 μm diameter spot was used for this thesis) minimizes the chances of multiple generations of pyrite being analyzed together and allows for identification of isotopic zoning. This is aided by the presence of an in-machine microscope, which permits targeted analysis. Furthermore, as this method is relatively non-destructive, samples can be re-examined and re-analyzed if unusual results are obtained or difficulties are encountered during the initial analysis. Finally, at the time this thesis was written, the analytical precision of the SHRIMP-SI was approaching or equal to that of the fluorination method, making it a viable alternative.

1.6 Research questions and thesis structure

The first research question is: what is the isotopic composition of terrestrial sulfide minerals? To answer this question, detailed morphological, trace element and sulfur isotope studies were completed on sulfide minerals collected from a variety of different types of terrestrial sedimentary rocks. The isotopic results indicated that diagenetic sulfide minerals and detrital sulfide minerals originally of diagenetic origin consistently showed either small negative $\Delta^{33}S$ values consistent with a mixture of MIF sulfate and mass-dependent sulfur carrying $\Delta^{33}S$ and $\Delta^{36}S$ signatures of approximately 0 ‰, or $\Delta^{33}S$ values of approximately 0 ‰, suggesting a solely mass-dependent sulfur source. The majority of these grains also showed negative $\Delta^{36}S$ values, suggesting that MSR was an important process in preserving sulfur within terrestrial environments. This was supported by the observation of variable $\delta^{34}S$ values within numerous samples, where the observed ranges in $\delta^{34}S$ were similar to those previously attributed to MSR within Archean samples. However, within sulfide minerals hosted by paleosols, isotopic indicators of MSR were absent, suggesting that other fractionation processes were also involved in preservation of sulfur within terrestrial sulfur reservoirs. These results also provide new evidence for the hypothesis of Maynard et al. (2013) that terrestrial sediments contain an under-sampled reservoir of negative $\Delta^{33}S$ sulfur potentially capable of balancing the bias towards positive $\Delta^{33}S$ sulfur within the current data record.

The second research question is: do sulfide minerals hosted by marine clastic sedimentary rocks within these same sedimentary sequences show different isotopic compositions to those hosted by terrestrial sedimentary rocks? This was addressed through detailed morphological, trace element and sulfur isotope analysis of sulfide minerals collected from marine sandstones

and shales. The results indicated that a portion of these samples showed isotopic compositions consistent with MSR of mass-dependent sulfate; these samples showed variable and/or relatively high magnitude negative $\delta^{34}S$ values and a steep negative $\Delta^{36}S/\Delta^{33}S$ array similar to those previously observed for MSR. This $\Delta^{36}S/\Delta^{33}S$ array passed approximately through the origin in $\Delta^{36}S$-$\Delta^{33}S$ space, indicating that the reactant sulfate likely had $\Delta^{33}S$ and $\Delta^{36}S$ of ~0 ‰. The remaining samples showed positive $\Delta^{33}S$ values consistent with preservation of MIF elemental sulfur, confirming that terrestrial and marine clastic sedimentary rocks do preferentially preserve different forms of MIF sulfur. However, deviation from the ARA in $\Delta^{36}S$ suggested that sulfur was preserved in these environments through secondary biological fractionation, which is atypical. This research question was then extended to consider the greater isotope record, where it was observed that the results of this thesis were consistent with those previously observed: marine clastic sediments typically preserved MIF elemental sulfur and terrestrial sediments typically preserved MIF sulfate.

The third research question is: why are different forms of MIF sulfur preferentially preserved within different sedimentary environments? Maynard et al. (2013) suggested that differences in the solubility of MIF sulfur aerosols resulted in preferential erosion of the MIF elemental sulfur and consequent preservation of this aerosol in marine environments. However, this was disproved by the results of this thesis, where positive $\Delta^{33}S$ signatures consistent with preservation of MIF elemental sulfur were absent from diagenetic pyrite grains from both diamictite and fluvial samples. It would be expected that if solubility were the only barrier to preservation of MIF elemental sulfur, that it would be able to be preserved within those diagenetic grains named above, as those sedimentary environments would collect sulfur eroded from the continental surface. Instead, the observed dichotomy is proposed to be due to preferential accumulation of the different MIF aerosols within different locations and differences in the mechanisms in which those aerosols are converted to sulfide and incorporated into sulfide minerals. However, further investigation into how MIF elemental sulfur is preserved within sulfide minerals is required.

Concurrently investigated with the first and second research questions was the final research question of this thesis: what was the cause of muted $\Delta^{33}S$ and $\Delta^{36}S$ values and steepened $\Delta^{36}S/\Delta^{33}S$ arrays observed during the Mesoarchean? The isotope data used to investigate these questions came from the same terrestrial and marine samples named above. The data confirmed that both terrestrial and marine samples from this era preserve muted $\Delta^{33}S$ and $\Delta^{36}S$ values compared to samples from other Archean eras. As mentioned above, a portion of

the marine samples preserved a purely biological signature with no evidence for preservation of either MIF sulfur species. This was observed to be coupled with elevated concentrations of selenium, which is mobile under oxidising conditions. Therefore, it seems that likely that, consistent with the hypothesis of Ono et al. (2006b), there was a transient increase in the concentrations of atmospheric oxygen during the Mesoarchean. After oxygen concentrations returned to typical Archean levels, it is possible that mobile mass-dependent sulfur species produced through oxidative weathering of igneous sulfur reservoirs during the period of oxidation, or through some other means, may have continued to dilute the MIF signatures, similar as to proposed by Guy et al. (2012). Within the marine samples, a steepened MIF $\Delta^{36}S/\Delta^{33}S$ array of ~-2 was observed. Close inspection of this array revealed that it was not actually a singular, linear array but rather a series of arrays, where each individual sample showed a consistent $\Delta^{33}S$ composition and variation in $\Delta^{36}S$, where the $\Delta^{36}S$ values deviated downwards from the ARA. This was interpreted to represent secondary biological fractionation, possibly involving a combination of sulfur metabolisms. It is therefore suggested that the steepened MIF $\Delta^{36}S/\Delta^{33}S$ array observed during the Mesoarchean is due to secondary biological activity but further investigation is required to confirm whether this was a localized or global phenomenon.

Structure of this thesis

Following this introductory chapter, Chapter 2 provides a detailed description of the analytical methods employed during this thesis. They are compiled into a single chapter to prevent unnecessary repetition as similar analysis methods were used for each sample set. Where other analysis methods have been employed, they are described within the relevant chapter. The thesis is then organized into four main chapters, each of which considers the isotopic composition of sulfide minerals hosted by a particular sedimentary rock type. Chapters 3 – 5 consider sulfide minerals hosted by terrestrial sedimentary rocks, starting with glacial diamictites, followed by paleosols, followed by fluvial clastic sedimentary rocks. Chapter 6 then considers sulfide minerals hosted by marine clastic sedimentary rocks. Finally, Chapter 7 provides a summary of key findings, together with a synthesis of data and comparison of terrestrial and marine sulfur isotopic signatures. Also provided is a summary of the implications of this research and proposed directions for future work.

Chapter 2: Analytical methods

2.1 Sample characterization

Textural and morphological analysis

Rock samples containing sulfide minerals of interest were sectioned, mounted in epoxy and polished. The mounts were then photographed under reflected light using an automated Leica D6000 microscope in order to perform preliminary mineral identification and an initial examination of the textural and morphological features of the sulfide minerals grains. The relationships between sulfide minerals and host lithologies were also examined. To confirm mineral identification, major element concentrations of the sulfide minerals were measured using a JEOL JSM-6610A Scanning Electron Microscope (SEM) fitted with an Electron Dispersive X-Ray Spectroscopy (EDS) detector. The SEM was also used to produce Back Scatter Electron (BSE) images which were used to further examine the morphological and textural features of the sulfide grains.

NaOCl etching

The mounts were treated with a sodium hypochlorite (NaOCl) solution in order to identify any intragrain variations in composition. Mounts were soaked in an 8 – 12 % available Cl^- NaOCl solution for ~7 minutes, rinsed with miliQ water and then photographed again under reflected light. The photographs were then used to examine any variations in composition present within the grains.

Trace element analysis

Trace element (^{53}Cr, ^{55}Mn, ^{59}Co, ^{60}Ni, ^{63}Cu, ^{65}Cu, ^{66}Zn, ^{69}Ga, ^{75}As, ^{77}Se, ^{82}Se, ^{95}Mo, ^{107}Ag, ^{111}Cd, ^{121}Sb, ^{125}Te, ^{182}W, ^{205}Tl, ^{208}Pb, ^{209}Bi, ^{238}U) compositions of sulfide mineral grains were analyzed via Laser Ablation Inductively Coupled Mass Spectrometry (LA-ICP-MS) at the Research School of Earth Sciences (RSES), the Australian National University (ANU). The system consisted of a 193 nm wavelength ArF excimer laser coupled to an Agilent 7700 ICP-MS via He-Ar carrier gas. A pulse energy of ~80 mJ and pulse repetition rate of 5 Hz were used. Spot diameter was set to ~35 µm. For DN6 samples, each point consisted of 30 seconds of background measurement (20 seconds pre-ablation, 10 seconds post ablation) and 60 seconds of ablation. For all other samples, each point consisted of 60 seconds of background measurement (30 seconds pre- and post-ablation) and 60 seconds of ablation. Analysis of

samples were bracketed by reference materials. STDGL-3 (Danyushevsky et al., 2011) was used as the primary reference material for all measurements. STDGL-1 (Norman et al., 2003) was used as the secondary reference material for DN6 samples and BCR-2G (Rocholl, 1998) was used as the secondary reference material for all other samples. The internal standard was Fe^{57}, with ^{29}Si and ^{43}Ca used to estimate the contribution of matrix in each analysis. Data was processed using the Iolite software (Paton et al., 2011).

2.2 Sulfur isotope analysis

Sulfur isotope (^{32}S, ^{33}S, ^{34}S, ^{36}S) compositions of sulfide mineral grains (predominantly pyrite (FeS_2), with the exception of pyrrhotite (FeS) from the DN6 drill core) were measured using the Sensitive High-Resolution Ion MicroProbe – Stable Isotope (SHRIMP-SI) at the RSES, the ANU. Prior to analysis, mounts were then coated in 0.05 µm of Au in order to dissipate charge build up and stabilize the sample potential during analysis.

Isotope measurements were performed with a Cs^+ ion primary beam of ~2 nA. Cs^+ ions were generated in a Kimball Physics IGS-4 alkali metal ion gun by heating a Cs zeolite cartridge and were accelerated to a potential of +5 kV. Sample potential was held at -10 kV, resulting in an impact energy of 15 keV at the target. An ~35 µm diameter analysis pit was produced at the target via Kohler illumination; a 200 µm diameter Kohler aperture was de-magnified by the final condenser lens operated as an immersion lens (Philippot et al., 2018).

Secondary ions were accelerated to real ground from -10 kV sample potential and focused by quadrupole triplet lenses before passing through the source slit (set at 60 µm) and entering the secondary mass analyser. The low mass, axial low mass, axial and high mass detectors, equipped with Faraday Cups, were used for simultaneous detection of $^{32}S^-$, $^{33}S^-$, $^{34}S^-$ and $^{36}S^-$, respectively. Collector slit widths were set at 300 µm for $^{32}S^-$ and $^{36}S^-$, 150 µm for $^{33}S^-$ and 200 µm for $^{34}S^-$. The $^{32}S^-$, $^{33}S^-$ and $^{34}S^-$ ion currents were measured on iFlex electrometers with high-ohmic resistors; $^{32}S^-$ was collected on a 10^{11} Ω resistor (50 V range) and $^{33}S^-$ and $^{34}S^-$ on 10^{11} Ω resistors (5 V range). The $^{36}S^-$ ion current was measured on an iFlex electrometer operated in charge mode, where the feedback resistor is replaced by a 22 pF capacitor (Ireland et al., 2014), for all samples except the DN6 samples. For the DN6 samples, $^{36}S^-$ was collected on a 10^{12} Ω resistor (5 V range). Potential isobaric interferences on $^{33}S^-$ and $^{34}S^-$ from $^{32}SH^-$ and $^{33}SH^-$, respectively, were well resolved.

Each spot analysis lasted ~26 minutes (1560 seconds). Prior to data collection, the target was pre-sputtered for ~300 seconds; this removed the coating at the analysis spot and ensured that signal was stable before collection began. This delay was required because when analysing sulfide minerals, the secondary ion current increases steadily for approximately 240 seconds, after which the increase slows and the signal becomes more stable. During the initial period of increasing current, the isotope ratios (e.g. $^{33}S^{-}/^{32}S^{-}$, $^{34}S^{-}/^{32}S^{-}$) also increase, impacting the calculated delta values. Monitoring of background count rates for each detector also occurred during this initial 300 second period. Next, there was ~100 seconds of automated steering adjustment within the secondary column and ~5 seconds of automated centering of the secondary ions in the collector slits to maximize secondary ion signal reaching the collectors. Data collection consisted of 4 sets of 10 measurements, where each measurement lasted 20 seconds, with re-optimisation of centering in the collector slits carried out between sets. Typical count rates on $^{32}S^{-}$, $^{33}S^{-}$, $^{34}S^{-}$ and $^{36}S^{-}$ were ~1-2 x 10^{9} cps, ~1-1.5 x 10^{7} cps, ~6-8 x 10^{7} cps and 2-3 x 10^{5} cps, respectively. Background count rates were ~1.5-1.7 x 10^{4} cps, ~1.8-1.9 x 10^{4} cps, ~1.4 x 10^{5} cps and ~30 cps for ^{32}S, ^{33}S, ^{34}S and ^{36}S, respectively.

Analysis of unknown pyrites were bracketed by measurements of the pyrite reference materials Ruttan and Balmat, which were mounted together with the unknowns. Ruttan pyrite ($\delta^{34}S$ = +1.2 ± 0.2 ‰) (Crowe and Vaughan, 1996) has $\Delta^{33}S$ of ~0.00 ‰ and a $\Delta^{36}S$ anomaly of -0.20 ‰ (Holden per. comm.). Balmat pyrite ($\delta^{34}S$ = +15.1 ± 0.2 ‰) (Crowe and Vaughan, 1996) has $\Delta^{33}S$ and $\Delta^{36}S$ of ~0.00 ‰ (Holden per. comm.). Analysis of unknown pyrrhotites were bracketed by measurements of the Anderson pyrrhotite reference material ($\delta^{34}S$ = +1.4 ± 0.2 ‰) (Crowe and Vaughan, 1996) and the Ruttan and Balmat pyrite reference materials. There are currently no conventionally measured $\Delta^{33}S$ and $\Delta^{36}S$ values available for Anderson pyrrhotite.

Data were processed using the POXI software. During data processing, the background counts were subtracted from the total counts. The corrected counts were then used to calculate the isotopic ratios ($^{33}S/^{32}S$, $^{34}S/^{32}S$, $^{36}S/^{32}S$). The ratios were corrected for instrumental bias by applying a bias factor calculated from the analysis of a reference material with known sulfur isotope ratios (see Supplementary Information for example). These ratios were then corrected for the mass-dependent fractionation which occurs during sputtering. This fractionation was corrected by finding the mean $^{34}S/^{32}S$ value, calculating a fractionation in permil (‰) for each $^{34}S/^{32}S$ ratio from this mean value and then using the terrestrial mass fractionation curves to

calculate the corresponding fractionations in $^{33}S/^{32}S$ and $^{36}S/^{32}S$. These fractionation values were then applied as corrections to the $^{33}S/^{32}S$ and $^{36}S/^{32}S$ ratios to essentially flatten the change in $^{33}S/^{32}S$ and $^{36}S/^{32}S$ during analysis, substantially reducing the overall error bar (Mojzsis et al., 2003). The corrected ratios were then expressed in delta notation (δ), where the ratios were given as permil deviations (‰) from the Vienna Canyon Diablo Troilite (VCDT) reference material:

$$\delta^{33}S_{VCDT} = 1000 \times \left[\frac{(^{33}S/^{32}S)_{corrected}}{(^{33}S/^{32}S)_{VCDT}} - 1\right] (‰) \quad (2.1)$$

$$\delta^{34}S_{VCDT} = 1000 \times \left[\frac{(^{34}S/^{32}S)_{corrected}}{(^{34}S/^{32}S)_{VCDT}} - 1\right] (‰) \quad (2.2)$$

$$\delta^{36}S_{VCDT} = 1000 \times \left[\frac{(^{36}S/^{32}S)_{corrected}}{(^{36}S/^{32}S)_{VCDT}} - 1\right] (‰) \quad (2.3)$$

Deviations from the Terrestrial Mass Fractionation Lines (TFL) were expressed in terms of $\Delta^{33}S$ and $\Delta^{36}S$, which were calculated according to Farquhar et al. (2000):

$$\Delta^{33}S = \delta^{33}S - 1000 \times \left[\left(1 + \frac{\delta^{34}S}{1000}\right)^{0.515} - 1\right] \quad (2.4)$$

$$\Delta^{36}S = \delta^{36}S - 1000 \times \left[\left(1 + \frac{\delta^{34}S}{1000}\right)^{1.90} - 1\right] \quad (2.5)$$

The $\delta^{34}S$ values used in Equations 2.4 and 2.5 were calculated using the mean $^{34}S/^{32}S$ value for each analysis calculated during data correction.

The assumption of mass-dependent fractionation during sputtering has been validated via two separate methods. The first of these was by measuring a reference material with known non-zero $\Delta^{33}S$ and $\Delta^{36}S$ values (Maine pyrite: $\Delta^{33}S$ = +0.06, $\Delta^{36}S$ = -0.62; Philippot et al., 2012, 2018); after correcting for mass-dependent fractionation, the correct $\Delta^{33}S$ and $\Delta^{36}S$ values were calculated (Holden per. comm.). Second, as the majority of instrumental mass fractionation occurs at the source slit (Ickert et al., 2008) and is minimized using Helmholtz coils, varying the settings of the Helmholtz coils can be used to observe the effects of instrumental mass fractionation; when the coils were incorrectly set, large fractionations were seen in δ values but Δ values remained unchanged from when the coils were correctly set (Loiselle per. comm.).

As there are no conventionally measured $^{33}S/^{32}S$ and $^{36}S/^{32}S$ values for the Anderson pyrrhotite reference material, the bias factors for these ratios that were applied to the measured pyrrhotite were calculated from the Ruttan pyrite reference material. Assuming that instrumental bias due to matrix effects is mass dependent, the $\Delta^{33}S$ and $\Delta^{36}S$ values should be insensitive to matrix effects. However, it is acknowledged that a matrix matched reference material should have been used to calculate the sulfur isotopic ratios of the pyrrhotite grains. The bias factor for $^{34}S/^{32}S$ was calculated from the known $^{34}S/^{32}S$ value for Anderson pyrrhotite (Crowe and Vaughan, 1996).

Uncertainties on individual analyses (the internal error) were calculated as the standard deviation of the mean (standard error) of the 40 measurements completed for each analysis spot. All of the reported single spot errors provided in the supplementary information are quoted at 95 % confidence limits ($\sigma_{95\%}$), which corresponds to multiplying the standard error by a Student's t-value (n-1 degrees of freedom on a two-sided 95 % confidence distribution) (Philippot et al., 2018). The internal precision of $\delta^{34}S$, $\Delta^{33}S$ and $\Delta^{36}S$ were typically better than 0.10 ‰, 0.05 ‰ and 0.20 ‰ ($\sigma_{95\%}$), respectively.

Chapter 3: Sulfur isotope composition of diamictite-hosted pyrite

Abstract - A detailed morphological, trace element and multiple sulfur isotope study of pyrite hosted by the Odwaleni Formation diamictites of the Pongola Supergroup is presented. Two species of detrital pyrite were recognized, the first, showed elevated Co/Ni ratios, small negative $\Delta^{33}S$ values and a restricted range of small $\delta^{34}S$ values consistent with the grains having formed within a volcanogenic massive sulfide deposit. The second showed trace element compositions consistent with a sedimentary origin. The variable $\delta^{34}S$ values, consistently negative $\Delta^{36}S$ values and small negative to near-zero $\Delta^{33}S$ values are interpreted to represent microbial sulfate reduction of a mixture of the atmospheric sulfate aerosol and mass-dependent crustal sulfate. These signatures are consistent with the results of previous studies and add further evidence to the hypothesis that terrestrial environments preferentially preserved the atmospheric sulfate aerosol over the atmospheric elemental sulfur aerosol. Also recognized were diagenetic grains which displayed similar isotopic signatures to the second species of detrital grains. This was interpreted to represent a significant influx of crustal sulfur during deposition of the diamictite which outweighed the atmospheric sulfur flux.

3.1 Introduction

This chapter focuses on the sulfur isotope composition of pyrite hosted within the Odwaleni Formation diamictites of the Pongola Supergroup, South Africa. In the context of this chapter, a diamictite is defined to be a sedimentary rock composed of the sediment entrained by a glacier as it moved across the continental surface. Diamictites were chosen to examine the sulfur isotope composition of terrestrial environments as the glacier would have sampled the terrestrial surface over a broad region, collecting sulfide minerals from a multitude of environments. Therefore, the detrital sulfide minerals within diamictites should provide a record of the types of sulfur being preserved in terrestrial environments and insight into how sulfur was being preserved within these environments. The Odwaleni Formation diamictites were chosen specifically as they have a well-established glacial origin (Young et al., 1998; Nhleko, 2003).

A number of previous sulfur isotope studies of diamictite-hosted sulfide minerals have been completed and returned variable results. These studies involved diamictites from the West Rand Group of the South African Witwatersrand Supergroup (Guy et al., 2012; Maynard et al., 2013) and from the Turee Creek Group of the Australian Mount Bruce Supergroup (Wiliford et al., 2011; Philippot et al., 2018). Most commonly, the sulfide minerals showed near-zero $\Delta^{33}S$ values, negative $\Delta^{36}S$ values and small, predominantly positive $\delta^{34}S$ values (Guy et al., 2012; Maynard et al., 2013; Philippot et al., 2018). These signatures were largely interpreted to represent microbial sulfate reduction (MSR) in a sulfate-limited environment (Maynard et al., 2013; Philippot et al., 2018). Philippot et al. (2018) also observed sulfide minerals with small positive $\delta^{34}S$ and small, non-zero $\Delta^{33}S$ and $\Delta^{36}S$. Data from these sulfide minerals were observed to fall on the Archean Reference Array (ARA) of $\Delta^{36}S/\Delta^{33}S$ = ~-0.90 and were concluded to have formed through photolysis of SO_2 (Farquhar et al., 2000, 2001; Philippot et al., 2018). However, the studies completed by both Guy et al. (2012) and Philippot et al. (2018) analyzed diagenetic rather than detrital pyrite. Only the study completed by Maynard et al. (2013) analyzed detrital pyrite, however, the paragenesis of these grains does not appear to have been well constrained. If that study is used as a base, however, it may be expected that detrital sulfides from the Odwaleni Formation diamictite may preserve multiple sulfur isotope signatures consistent with MSR.

This chapter presents a detailed study of the morphology, trace element composition and sulfur isotope signatures of pyrite hosted by diamictites within the Mesoarchean Odwaleni

Formation. The trace element composition and isotopic signatures identified two different populations of pyrite, corresponding to the two different sampling sites. Detrital grains from the Mageza Stream sampling site showed trace element compositions consistent with them having been sourced from a sedimentary terrain and isotopic signatures consistent with MSR. Diagenetic grains from these samples showed similar isotopic signatures. The similarities between the data collected from diagenetic grains within this study and from previous studies (Guy et al., 2012; Philippot et al., 2018) suggests that glaciers consistently supplied MDF crustal sulfur to basins during deposition of glacial sediments and that MSR was consistently active within the sediments post-deposition. Notably, neither the detrital nor the diagenetic grains showed positive $\Delta^{33}S$ signatures consistent with preservation of MIF elemental sulfur. Samples from the Madaga Stream sampling site contained only detrital pyrite that showed trace element composition and isotopic signatures consistent with them having been sourced from a volcanogenic massive sulfide (VMS) deposit.

3.2 Geological context

The Odwaleni Formation occurs within the Mozaan Group of the Pongola Supergroup, South Africa. The Pongola Supergroup consists of a succession of supracrustal rocks overlying granite-gneiss basement of the Kaapvaal Craton and is exposed in the east of the Craton (Weilers, 1990) (Figure 3.1). A maximum age for the Pongola Supergroup is provided by the basement, which has been dated at 3107 ± 6 Ma (Kamo et al., 1990). A minimum age of ~2900 Ma is provided by a Pongola rhyolite (2940 ± 22 Ma, U-Pb zircon; Hegner et al., 1984) and the intrusive Usushwana Complex (2871 ± 30 Ma; Hegner et al., 1984). The rocks of the Pongola Supergroup are well-preserved, with mineral assemblages typically reflecting greenschist facies metamorphism (Watchorn and Armstrong, 1981; Hegner et al., 1984; Wronkiewicz and Condie, 1989; Elworthy et al., 2000; Ossa Ossa et al., 2016). The exception to this is some areas in Swaziland, which show high grade metamorphism (Hofmann et al., 2015).

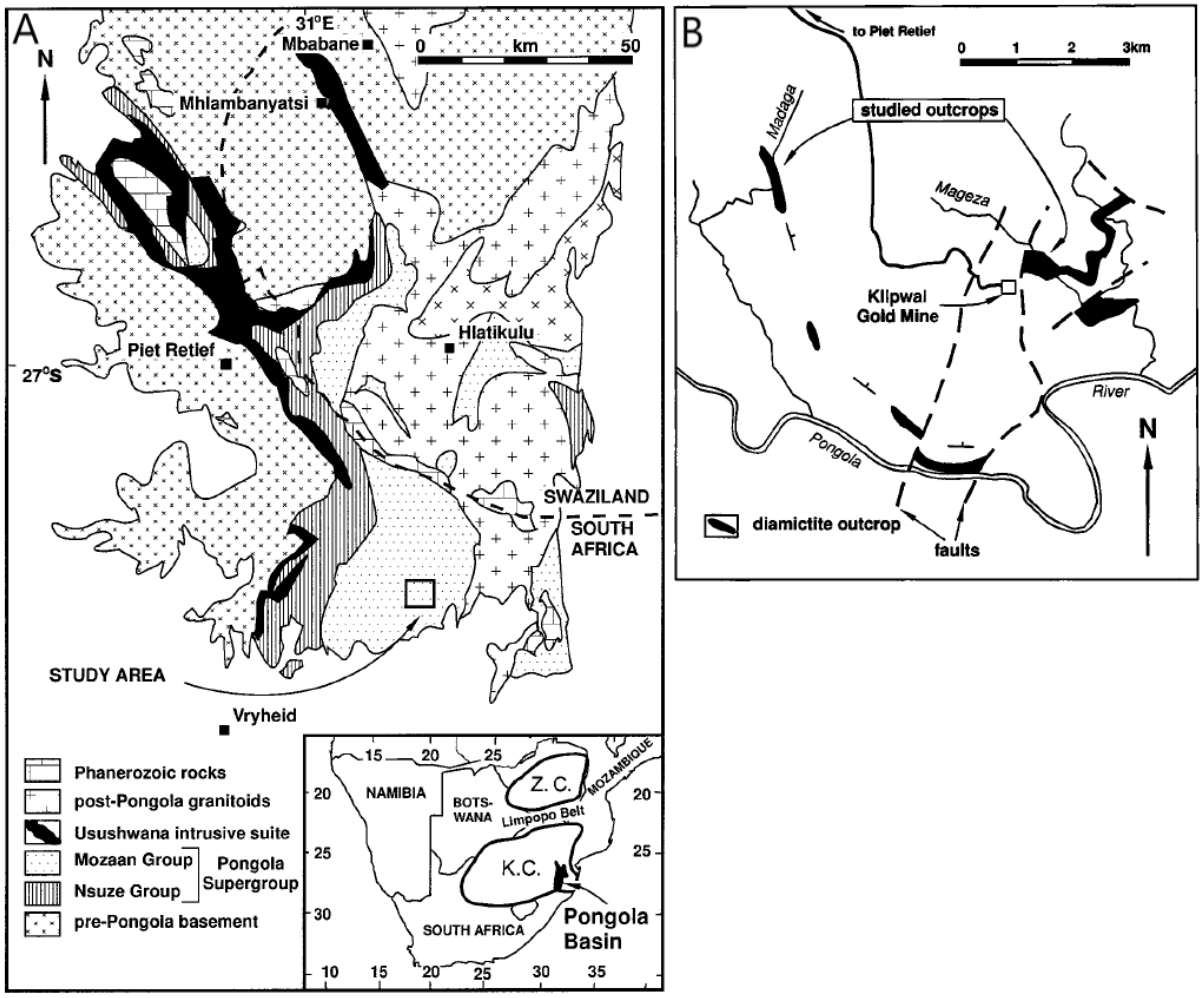

Figure 3.1. A. Geology of the northern Pongola Basin and locality of the study area. Inset shows the regional location of the Pongola Basin in the Kaapvaal Craton. In inset, Z.C. Zimbabwe Craton, K.C. is Kaapvaal Craton. B. Map of the study area shown in A, showing the location of the diamictite outcrops exposed on the banks of the Madaga and Mageza Streams. From Young et al. (1998).

Stratigraphically, from bottom to top, the Pongola Supergroup is divided into the Nsuze and the Mozaan Groups (Figure 3.2). The Nsuze Group is dominated by volcanics, with lesser sedimentary units (Matthews, 1967). The Mozaan Group consists predominantly of alternating sandstone and mudstone units, with lesser amounts of volcanics, pebble conglomerates and iron formation (Matthews, 1967; Beukes and Cairncross, 1991). Sedimentary rocks of the Mozaan Group have been interpreted to represent fluvial, tidal flat and marine shelf depositional environments (von Brunn and Hobday, 1976; Watchorn, 1980).

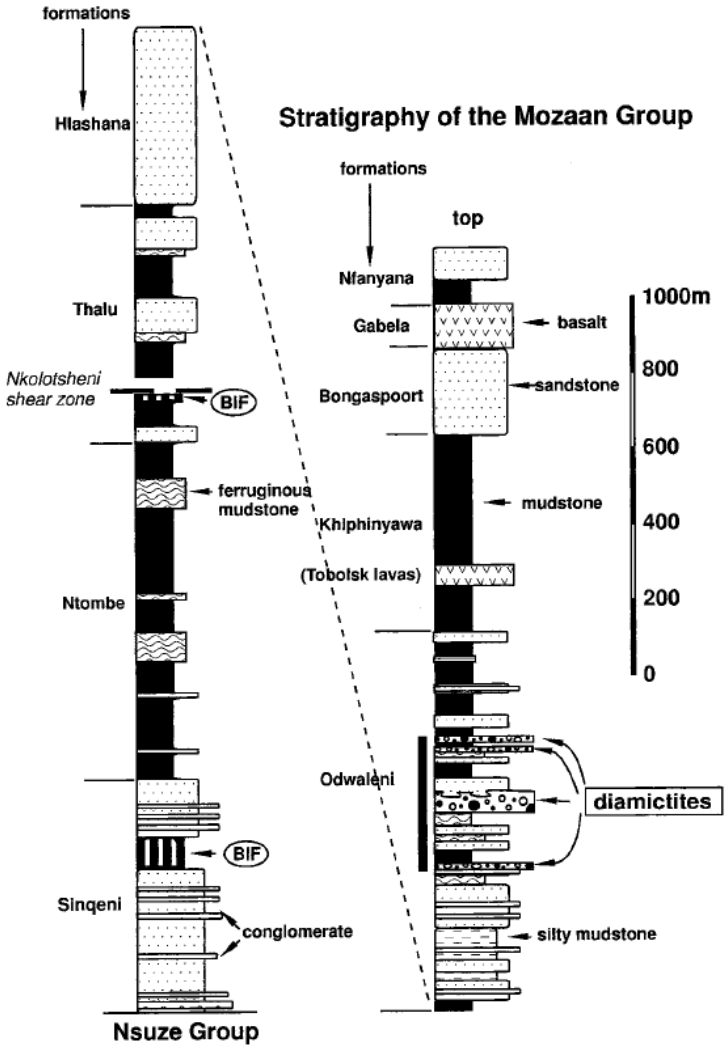

Figure 3.2. Generalized stratigraphy of the Mozaan Group, showing the stratigraphic position of diamictites within the Odwaleni Formation. From Young et al. (1998).

Within the Mozaan Group, the Odwaleni Formation largely consists of interbedded shale and quartzite, with minor diamictite, ferruginous mudstone and volcanics. Four diamictites have been recognized (Figure 3.2; von Brunn and Gold, 1993; Young et al., 1998). Young et al. (1998) determined that the diamictites were of glacial origin based on numerous physical and chemical observations. Physically, the highly varied clast composition, observation of striated and faceted clasts and the presence of dropstones within laminated and finely bedded sequences all indicated a glacial origin. Chemically, when plotted on SiO_2 vs. Al_2O_3 and TiO_2 vs. Al_2O_3 plots, diamictite samples showed similar restricted distributions to modern glacial sediments. Additionally, the calculated Chemical Index of Alteration (CIA) and Plagioclase Index of Alteration (PIA) both suggested low levels of weathering, which is common for ancient glaciogenic materials (Nesbitt and Young, 1982, 1996).

3.3 Sampling information

Samples were collected from the thickest of the diamictite units, in the Klipwal area in the north-east of South Africa, south of the border with Swaziland. Sampling occurred north of the Pongola River, from exposures on the banks of Mageza and Magada streams, at the same locations described by Young et al. (1998). Sampling locations are shown in Figure 3.1. Sample names and sampling localities and depths are provided in Table 3.1.

Table 3.1. Sampling information for the Odwaleni Formation diamictites.

Sample Name	Sampling locality	Sampling depth	Stratigraphic height (m)
KW-C5	Mageza Stream	5 m above base of diamictite	429
KW-C6	Mageza Stream	2 m below top of diamictite	502
KW-A18	Madaga Stream	4 m above base of diamictite	428
KW-A19	Madaga Stream	12.5 m above base of diamicite	436.5

The samples consisted of dark-grey to black, competent rock consisting of rounded clasts of varied composition within a fine-grained, massive matrix.

3.4 Methods

Methods for sample characterisation and sulfur isotope analysis are provided in Chapter 2.

3.5 Results

Sample characterization

Morphology and textural analysis

Pyrite was the dominant sulfide mineral observed within the Odwaleni Formation diamictites. All of the samples were sulfide mineral poor and contained only a limited number of pyrite grains. Sample KW-C5 showed the highest abundance, with the other samples containing lower numbers of sulfide minerals grains.

Four morphologies of pyrite grains were observed within samples from the Odwaleni Formation and will be referred to as KW-SUB-1, KW-SUB-2, KW-AN-1 and KW-AN-2. Backscattered electron (BSE) images of these morphologies are provided in Figure 3.3.

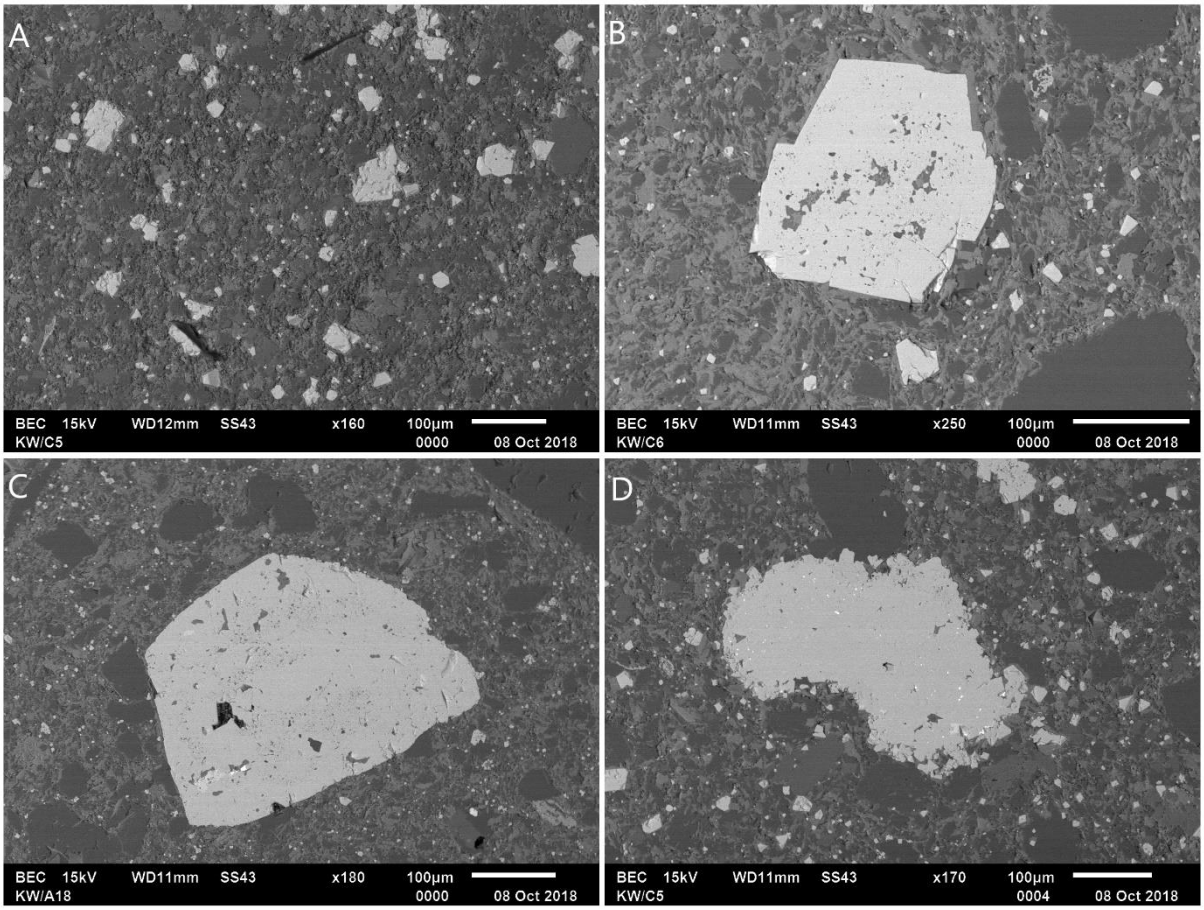

Figure 3.3. BSE photomicrographs of pyrite within the Odlwaleni Formation diamictites. A. KW-SUB-1, B. KW-SUB-2, C. KW-AN-1, D. KW-AN-2.

KW-SUB-1 grains were fine, disseminated subhedral grains, ~10 – 50 µm in diameter, that were observed within samples from the Mageza Stream sampling site. They were non-porous and inclusion-free and were observed to be conformable with the surrounding matrix (they did not overprint the surrounding minerals). KW-SUB-2 grains were subhedral and ~100 – 200 µm in diameter. They showed variable porosity, with randomly distributed pores, and were conformable with the matrix. These grains were observed within samples from both sampling sites.

KW-AN-1 grains were anhedral, porous grains which showed rounding of one or more edges. Pores were randomly distributed and ranged in size, with both very fine pores and larger, irregularly-shaped pores being observed. Also observed within grains were fine, randomly-

distributed blebs of chalcopyrite and galena. Grains ranged in size from ~100 – 500 µm in diameter. They were observed within samples from both sampling sites. KW-AN-2 were nodules, showing variable degrees of rounding and variable porosity. Nodules were typically ~400 µm in diameter and were observed only in samples from the Mageza Stream sampling site.

Trace element composition

A summary of the trace element compositions of pyrite grains from each sample is provided in Table 3.2. The complete data set and maps of the analysis spots are provided in the Supplementary Information.

The following observations can be made regarding the trace element compositions of the different pyrite morphologies observed within the two sampling areas. However, they should be interpreted with some caution, as only a limited amount of data was able to be collected from some morphologies. This was in part due to the limited number of grains of some morphologies present and in part due to a number of the grains being too small to be analyzed via LA-ICP-MS, where a 35 µm diameter spot was used.

For the Mageza Stream samples (KW-C5, KW-C6), it was observed that the different morphologies typically showed overlapping trace element concentrations, with a small number of exceptions (Figure 3.4). The single analysis performed on a KW-SUB-1 grain was observed to return a higher concentration of Ni than observed for KW-SUB-1 and KW-AN-1 grains (Figure 3.4). Additionally, the KW-SUB-1 grain showed a higher Cu concentration than KW-AN-1 grains and a higher As concentration than KW-SUB-2 grains (Figure 3.4). However, as mentioned above, these observations should be interpreted with caution, as only one measurement was completed on KW-SUB-1 grains only two measurements on KW-AN-2 grains and only three measurements on KW-SUB-2 grains (6 measurements were completed on KW-AN-1 grains).

Table 3.2. Summary of the trace element composition of pyrite collected from the Odwaleni Formation diamictites.

Sampling Area	Element	Min (ppm)	Max (ppm)	Median (ppm)	Mean (ppm)	StDev (ppm)
KW-C5 (n = 8)	Co	175	3460	1170	1402	1180
	Ni	132	7400	1073	2320	2630
	Cu	131	4500	1040	1520	1590
	Zn	3.29	25.3	9.45	11.9	6.87
	As	780	5500	3340	3170	1580
	Co/Ni	0.137	26.2	0.906	4.09	8.98
KW-C6	Co	79.0	5080	483	1530	2380
(n = 4)	Ni	366	1260	889	851	413
	Cu	0.530	61.0	25.9	28.3	27.4
	Zn	3.60	4.90	4.25	4.25	0.919
	As	24.1	1980	340	671	895
	Co/Ni	0.216	4.54	0.504	1.44	2.09
KW-A18	Co	4390	9600	7740	7080	1830
(n = 11)	Ni	55.6	640	188	284	210
	Cu	3.10	410	15.7	61.9	119
	Zn	1.13	7.30	4.30	4.49	2.12
	As	281	4500	1360	1610	1400
	Co/Ni	7.07	158	45.2	47.1	43.9
KW-A19	Co	450	9200	1650	2450	2520
(n = 11)	Ni	43.4	1240	148	266	346
	Cu	5.46	267	68.0	91.4	77.8
	Zn	1.38	14.9	4.62	6.19	5.02
	As	67.0	8580	3040	3490	2340
	Co/Ni	0.841	147	9.43	24.3	42.0

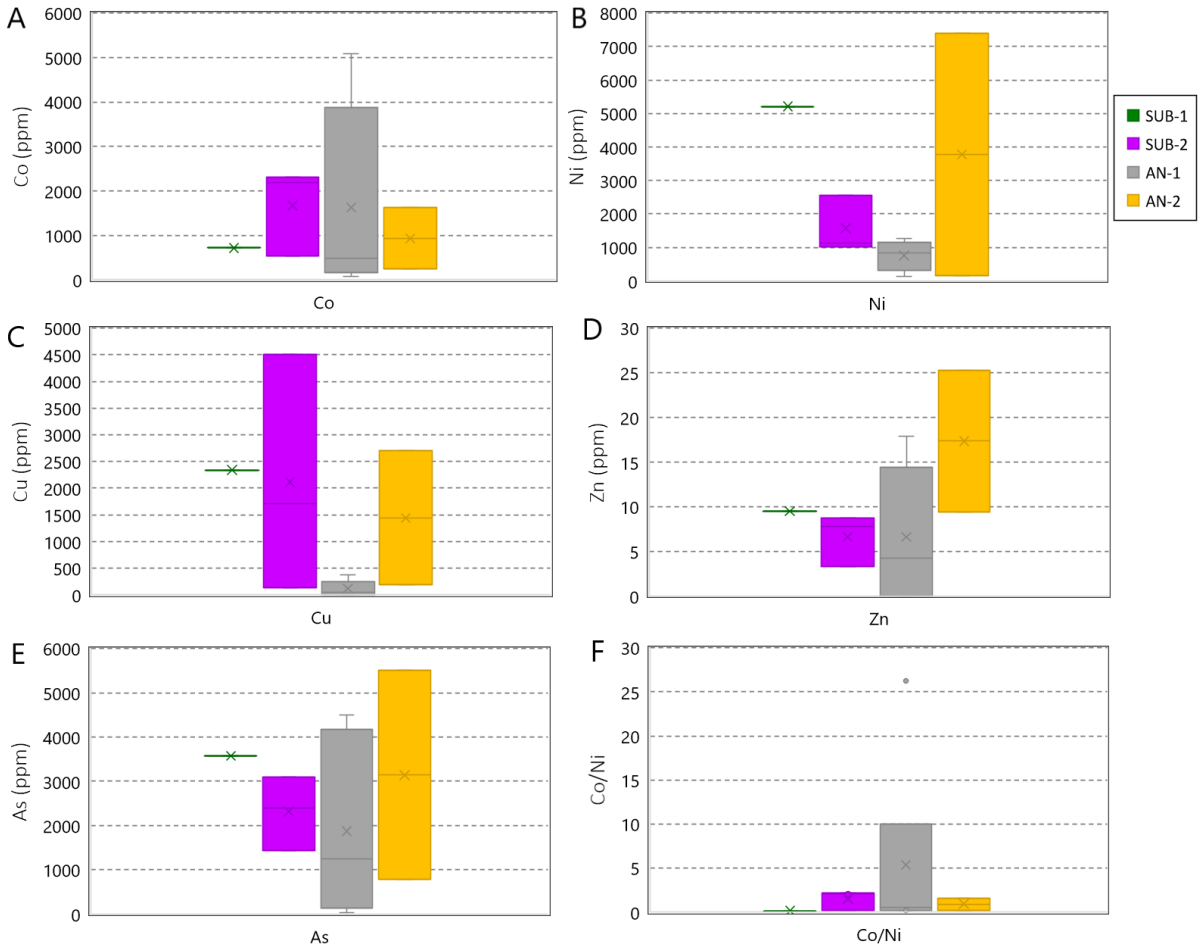

Figure 3.4. Box and whisker plots comparing the trace element compositions of the different morphologies of pyrite observed within the Mageza Stream samples (KW-C5 and KW-C6). A. Co concentrations, B. Ni concentrations, C. Cu concentrations, D. Zn concentrations, E. As concentrations, F. Co/Ni ratios.

For the Madaga Stream samples (KW-A18, KW-A19), the different morphologies consistently showed overlapping trace element concentrations (Figure 3.5). Again, as only one measurement was completed on KW-SUB-2 grains (all other measurements were completed on KW-AN-1 grains), this should be interpreted with caution.

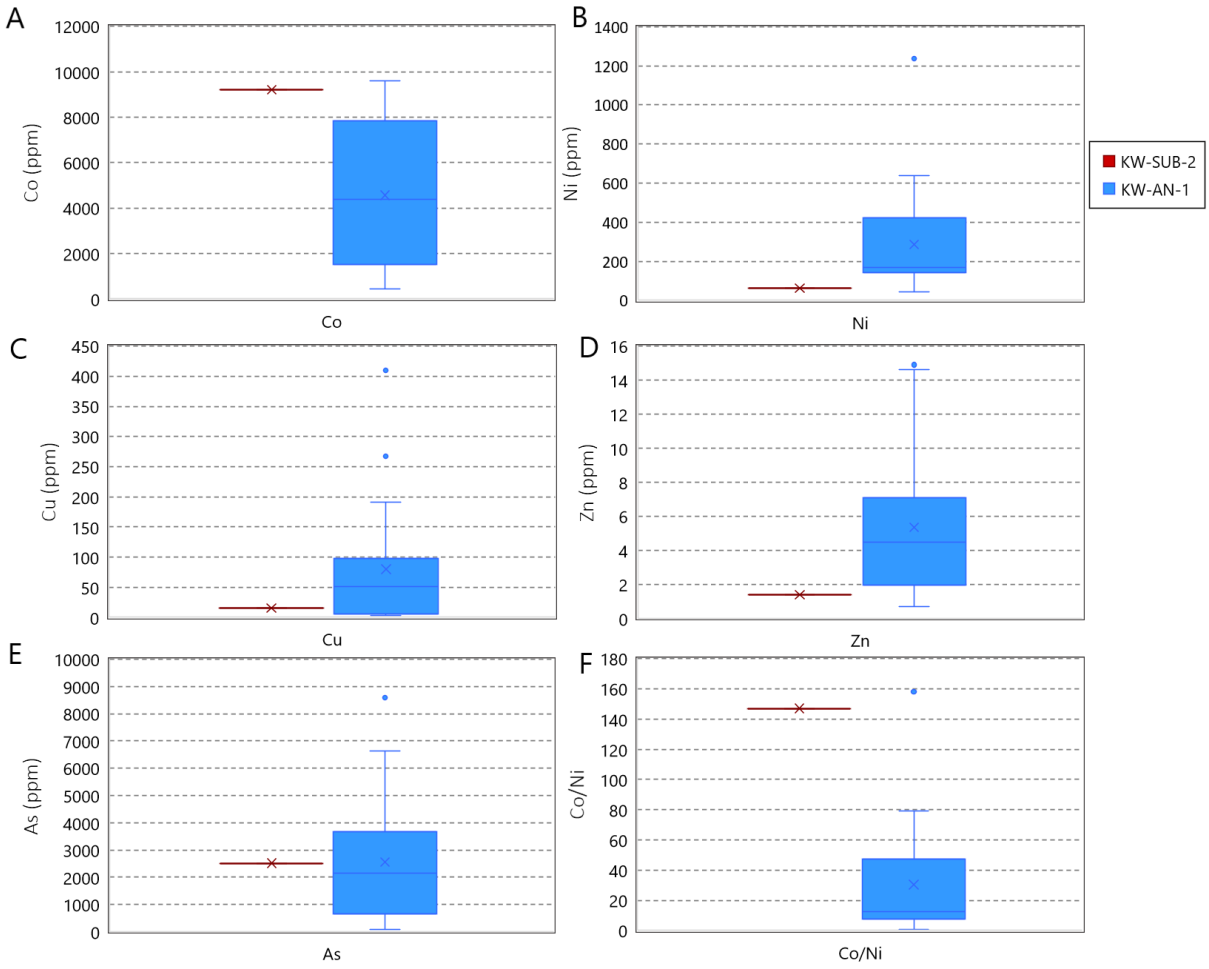

Figure 3.5. Box and whisker plots comparing the trace element compositions of the different pyrite morphologies observed in Madaga stream samples. A. Co concentrations, B. Ni concentrations, C. Cu concentrations, D. Zn concentrations, E. As concentrations, F. Co/Ni ratios.

What could be identified with more certainty, however, is that pyrite collected from the two different sampling sites showed differing concentrations of Co, Ni and Cu and distinct ranges of Co/Ni ratios (Figure 3.6). The pyrite grains collected from the Mageza stream sampling site (KW-C5 and KW-C6) typically returned lower concentrations of Co; range of 79.0 – 5080 ppm, median of 674 ppm and mean of 1450 ± 1560 ppm (1 *SD*, *n* = 12, Figure 3.5). They also typically showed higher concentrations of both Ni and Cu. Ni concentrations showed a range 132 – 7400 ppm, with a median of 1070 ppm and mean of 1830 ± 2230 ppm (1 *SD*, *n* = 12) and Cu concentrations showed a range of 0.530 – 4500 ppm, median of 197 ppm and mean of 1022 ± 1470 ppm (1 *SD*, *n* = 12). As a consequence of lower Co concentrations and higher Ni concentrations, Co/Ni ratios were lower than those observed for the Madaga stream pyrite grains; range of 0.137 – 26.2, median of 0.504 and mean of 3.21 ± 7.36 (1 *SD*, *n* = 12).

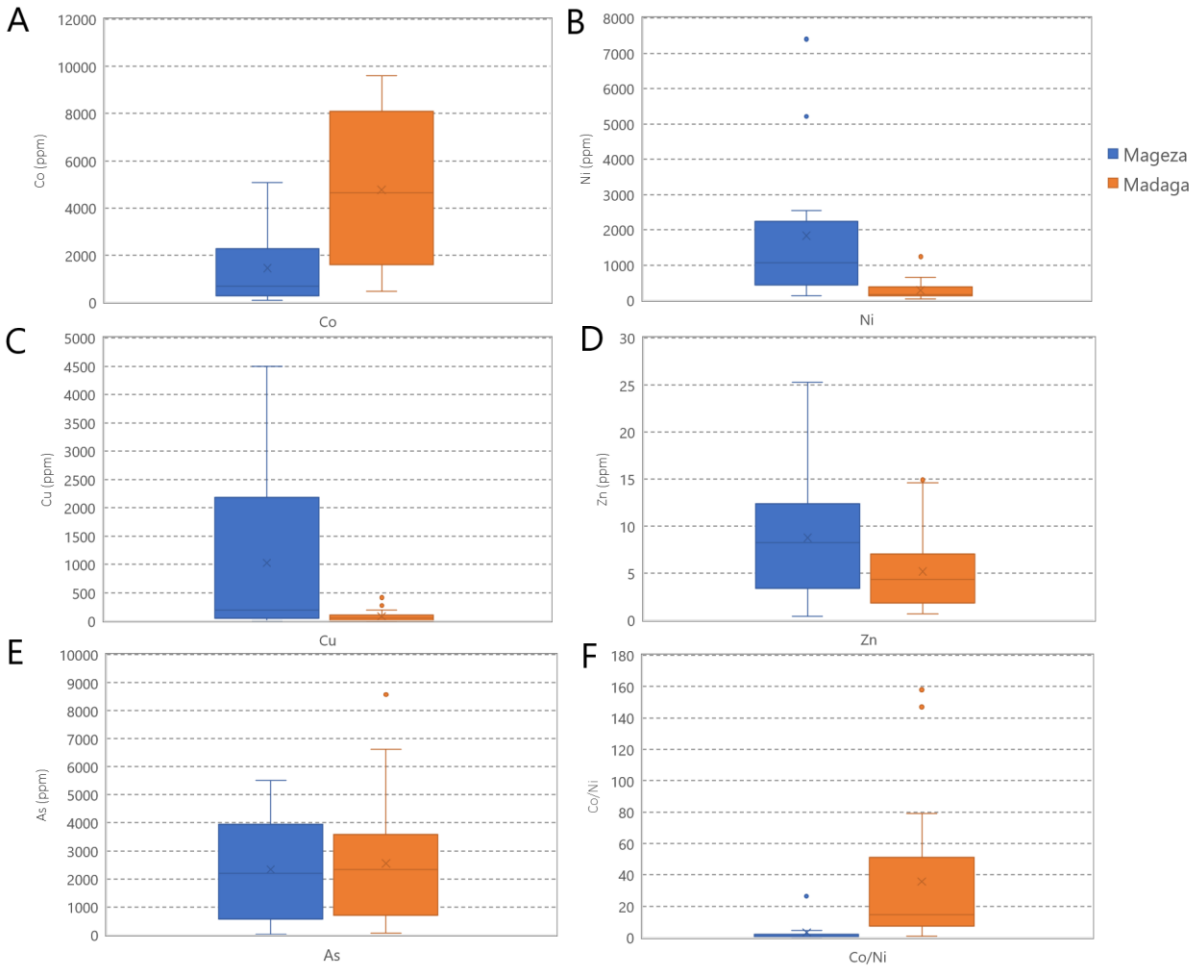

Figure 3.6. Box and whisker plots comparing the trace element composition of samples from the Madaga and Mageza Stream sampling sites. A. Co concentrations, B. Ni concentrations, C. Cu concentrations, D. Zn concentrations, E. As concentrations, F. Co/Ni ratios.

The pyrite grains from the Madaga stream sampling site (KW-A18 and KW-A19) typically showed higher Co concentrations, with a range of 450 – 9600 ppm, median of 4640 ppm and mean of 4770 ± 3200 ppm (1 *SD*, *n* = 22). Ni and Cu concentrations were typically lower; Ni concentrations showed a range of 43.4 – 1240 ppm, with a median of 165 ppm and mean of 275 ± 279 ppm (1 *SD*, *n* = 22) and Cu concentrations returned a range of 3.10 – 410 ppm, with a median of 47.5 ppm and mean of 76.7 ± 99.4 ppm (1 *SD*, *n* = 22). Co/Ni ratios were also typically higher, with an observed range of 0.841 – 158, a median of 14.6 and mean of 35.7 ± 43.5 (1 *SD*, *n* = 22).

The Zn and As concentrations were similar across the two sampling sites (Figure 3.6). Pyrite grains collected from the Mageza stream sampling site showed Zn concentrations of 0.385 – 25.3 ppm, median of 8.25 ppm and mean of 8.75 ± 7.28 ppm (1 *SD*, *n* = 12) and As concentrations of 24.1 – 5500 ppm, median of 2190 ppm and mean of 2340 ± 1820 ppm (1

SD, n = 12). Grains from the Madaga stream site returned Zn concentrations of 0.700 – 14.90 ppm, median of 4.30 ppm and mean of 5.17 ± 3.96 ppm (1 *SD*, n = 22) and As concentrations of 67.0 – 8580 ppm, with a median of 2330 ppm and mean of 2550 ± 2110 ppm (1 *SD*, n = 22).

Sulfur isotope composition

A summary of the sulfur isotope composition of each sample is provided in Table 3.3. The complete data set and maps of analysis spots are provided in the Supplementary Information.

Pyrite collected from the two different sampling sites showed similar isotopic compositions in $\Delta^{33}S$ and $\Delta^{36}S$. However, it was observed that grains from the Mageza stream site showed greater variation in $\delta^{34}S$ compared to those from the Madaga stream site (Figure 3.7). The Mageza stream grains showed a range in $\delta^{34}S$ of -6.09 – 11.7 ‰ (median of 4.90 ‰, mean of 3.55 ± 3.90 ‰ (1 *SD*, n = 36)) compared to a range of 3.06 – 6.06 ‰ for the Madaga stream grains (median of 4.51 ‰, mean of 4.63 ± 0.733 ‰ (1 *SD*, n = 36). Across all samples, $\Delta^{33}S$ values showed a range of -0.430 – 0.093 ‰, with a median of -0.246 ‰ and mean of -0.194 ± 0.122 ‰ (1 *SD*, n = 72). The $\Delta^{36}S$ values showed a range of -1.95 – 0.147 ‰, with a median of -0.653 ‰ and a mean of -0.747 ± 0.425 ‰ (1 *SD*, n = 72). For both $\Delta^{33}S$ and $\Delta^{36}S$, the majority of the variation was contributed by sample KW-C5 (Table 3.3).

Within the Mageza Stream samples, the different morphologies showed similar isotopic compositions (Figure 3.8). Within the Madaga Stream samples, only one data point was able to be collected from KW-SUB-2 grains, however, the isotopic composition of this grain was observed to be similar to that of the analyzed KW-AN-1 grains (Figure 3.9).

Table 3.3. Summary of the sulfur isotope composition of pyrite collected from the Odwaleni Formation diamictites.

Sample name	Isotope ratio	Min (‰)	Max (‰)	Median (‰)	Mean (‰)	StdDev (‰)
KW-C5	$\delta^{34}S$	-1.16	11.7	4.98	4.85	2.72
	$\Delta^{33}S$	-0.430	0.093	-0.185	-0.171	0.144
	$\Delta^{36}S$	-1.95	-0.035	-0.931	-1.00	0.541
KW-C6	$\delta^{34}S$	-6.09	8.44	-0.328	0.196	4.60
	$\Delta^{33}S$	-0.090	0.042	-0.031	-0.029	0.041
	$\Delta^{36}S$	-0.808	0.147	-0.272	-0.268	0.242
KW-A18	$\delta^{34}S$	3.06	6.06	4.92	4.75	0.868
	$\Delta^{33}S$	-0.335	-0.023	-0.266	-0.285	0.068
	$\Delta^{36}S$	-0.798	-0.351	-0.668	-0.652	0.124
KW-A19	$\delta^{34}S$	3.69	5.79	4.37	4.51	0.568
	$\Delta^{33}S$	-0.320	-0.208	-0.254	-0.254	0.031
	$\Delta^{36}S$	-1.15	-0.477	-0.677	-0.741	0.183

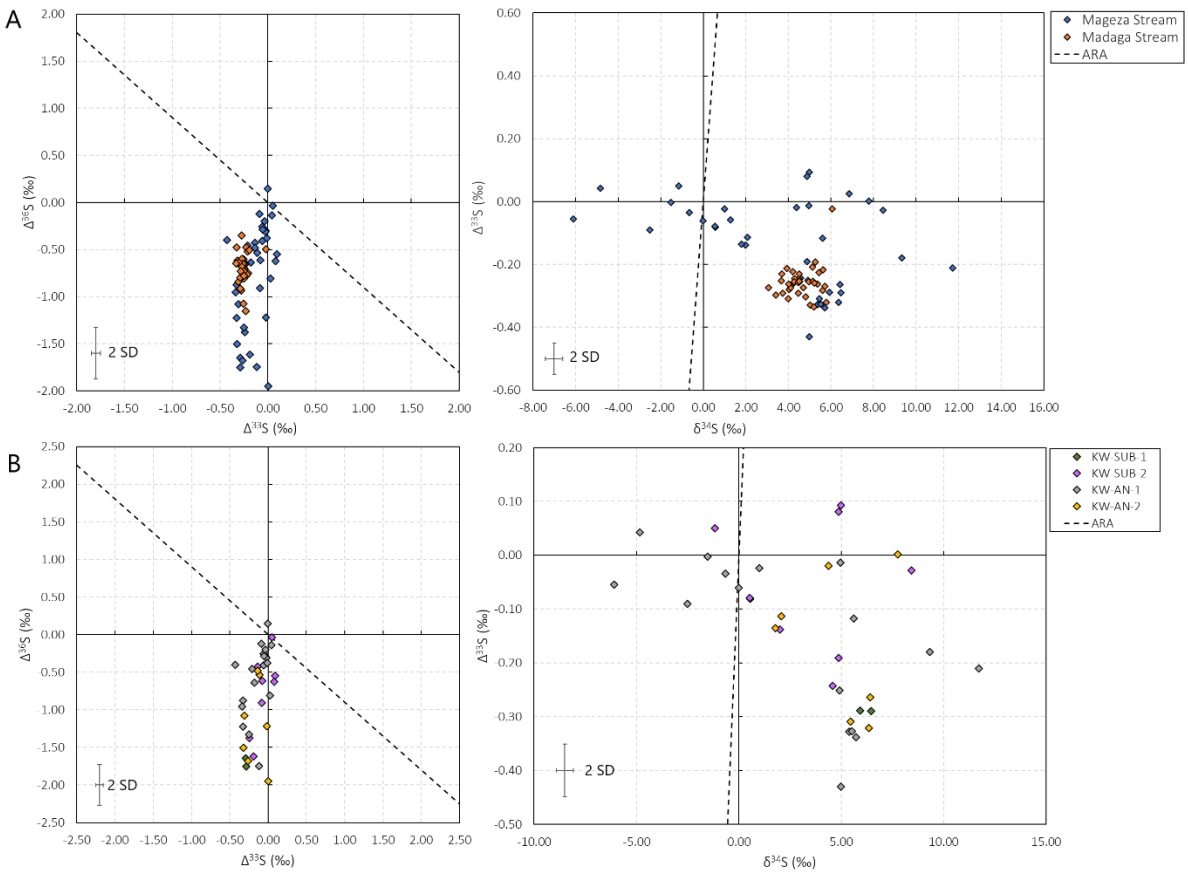

Figure 3.7. Isotopic composition of pyrite within the Odwaleni Formation diamictites. A. Data separated by sampling site. B. Data from the Mageza Stream sampling site, separated by morphology.

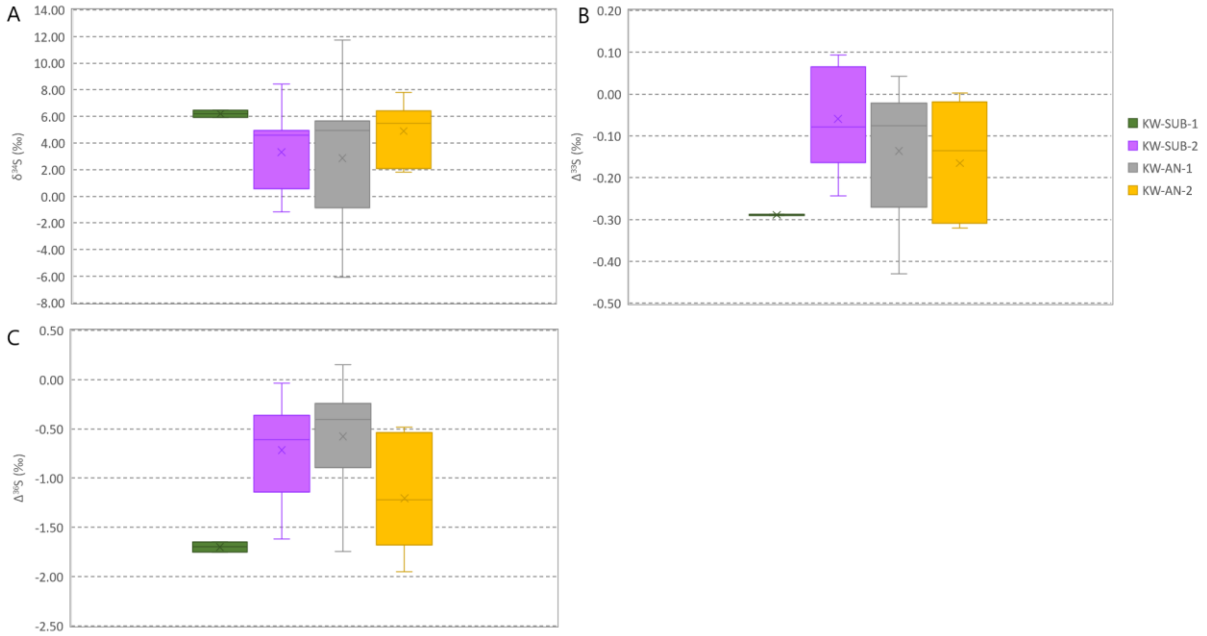

Figure 3.8. Box and whisker plots comparing the isotopic composition of the different pyrite morphologies observed within the Mageza Stream samples. A. $\delta^{34}S$, B. $\Delta^{33}S$, C. $\Delta^{36}S$.

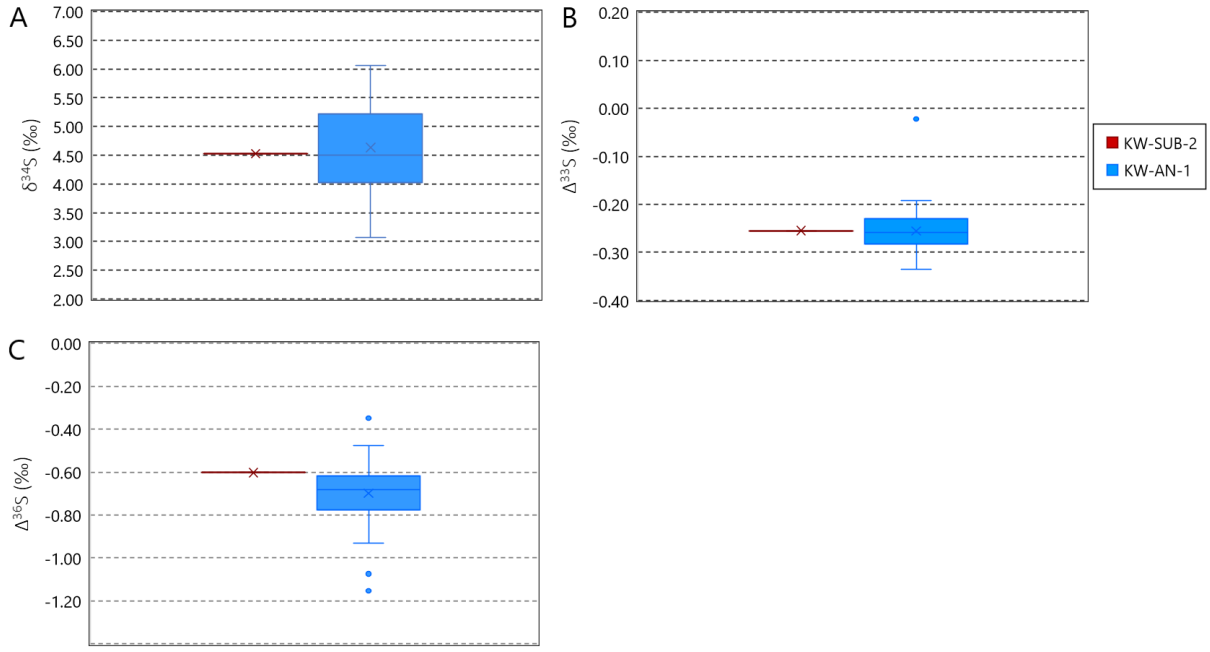

Figure 3.9. Box and whisker plots comparing the isotopic composition of the different pyrite morphologies observed within the Madaga Stream samples. A. $\delta^{34}S$, B. $\Delta^{33}S$, C. $\Delta^{36}S$.

3.6 Discussion

Pyrite paragenesis

Determining the paragenesis of diamictite-hosted pyrite grains proved to be problematic, largely due to difficulties in identifying detrital grains. Previous studies of detrital pyrite have

largely focused on grains which have undergone fluviatile transport (e.g. Utter, 1980; Hoefs et al., 1968; England et al., 2002; Large et al., 2013; Johnson et al., 2014; Guy et al., 2014). During this method of transport grains are predominantly rounded via abrasion which occurs when grains contact the stream or river bed (Füchtbauer and Müller, 1970). In contrast, where grains are transported in sub-glacial sediments, they can experience both abrasion and crushing (Halderson, 1981, 1983; Sharp and Gomez, 1986; Altuhafi and Baudet, 2011). This can result in various morphologies, including angular to sub-angular grain shapes which differ from the traditional rounded shapes expected for detrital grains (e.g. Altuhafi and Baudet, 2011). Additionally, where grains are transported within the ice, the ice shields the grains, preventing both abrasion and crushing, and grains can retain their original shapes. Therefore, identifying detrital pyrite grains within diamictites cannot be completed solely based on morphology.

Trace element compositions should also be interpreted with caution, as a diagenetic trace element composition could represent either a grain which formed during diagenesis of the diamictite or a detrital grain that was originally of diagenetic origin, such as the 'reworked diagenetic pyrite' described by Guy et al. (2014). This is of particular importance to samples from the Odwaleni Formation diamictites, as Young et al. (1998) previously proposed that the glacier which deposited these diamictites incorporated material from sedimentary environments. Certainly, there are sedimentary successions on the Kaapvaal Craton which predate these diamictites and could have contributed diagenetic pyrite e.g. sedimentary units of the Dominion Group and the Nsuze Group.

Taking this into account, trace element measurements and morphological and textural observations were able to be used to identify detrital and diagenetic pyrite species. Additionally, the paragenesis of certain species remain uncertain.

Mageza Stream pyrite

Detrital grains

KW-AN-1 grains typically show rounding on one or more edges, which may indicate that they have undergone transport. Additionally, they are observed to be similar in shape to detrital grains within diamictites that are of similar size (Altuhafi and Baudet, 2011). The difference between the trace element and isotopic composition of KW-AN-1 grains in these samples and the Madaga Stream samples also adds evidence for a detrital origin, as variation between the two sampling sites likely reflects variation in the source rocks (Meyer et al.,

1990; Barton and Hallbauer, 1996; England et al., 2002). The provenance of these detrital grains is discussed in a later section.

Diagenetic grains

KW-AN-2 grains were determined to be displacive nodules, which formed during diagenesis (Salles-Martinez, 1996). Diagenetic nodules of similar morphologies and textures have previously been observed within the Odwaleni Formation diamictites (referred to as framboids, Li et al., 2019) and also within the Tiesi'ao diamictites of the Nanhua Basin, China (Zhang et al., 2015). A diagenetic origin is favoured over a detrital origin as the nodules lack enveloping grain boundaries (the edges of the nodules are quite uneven and the internal textures are not observed to be truncated at grain boundaries (Figure 3.3D)). These features are common in detrital pyrite grains, particularly detrital fragments of nodules (e.g. England et al., 2002; Guy et al., 2014). However, it is acknowledged that, as stated above, detrital grains within diamictites may not show the typical morphological features of detrital grains.

Only two trace element measurements were able to be completed on KW-AN-2 grains, however, both measurements were conclusive with a diagenetic origin. Co/Ni, Cu/Ni, Zn/Ni and As/Ni values were within the ranges previously described for diagenetic pyrite (Table 3.4, Price, 1972; Guy et al., 2010; Gregory et al., 2015a). Concentrations of Co, Ni and As were also observed to fall within ranges previously observed for diagenetic pyrite grains (Guy et al., 2010; Gregory et al., 2015a).

Grains of uncertain paragenesis

The paragenesis of KW-SUB-1 and KW-SUB-2 grains is uncertain. For both of these grain types, the morphological and textural observations and trace element compositions could be representative of either a diagenetic origin or a detrital origin.

Table 3.4. Trace element ratios of the different morphologies of pyrite observed within the Odwaleni Formation diamictites.

Sample Name	Morphology	Co/Ni	Cu/Ni	Zn/Ni	As/Ni
KW-C5	KW-SUB-1	0.137	0.449	0.002	0.685
KW-C5	KW-SUB-2	0.209	1.76	0.001	0.941
KW-C5	KW-SUB-2	2.04	1.52	0.007	2.75
KW-C5	KW-SUB-2	2.14	0.128	0.009	1.41
KW-C5	KW-AN-2	1.59	1.23	0.169	5.20
KW-C5	KW-AN-2	0.219	0.365	0.001	0.743
KW-C6	KW-AN-1	0.216	0.032	0.001	0.484
KW-C6	KW-AN-1	4.53	0.054	0.003	1.77
KW-C6	KW-AN-1	0.502	0.032	0.004	0.398
KW-C6	KW-AN-1	0.506	0.001	0.001	0.037
KW-C6	KW-AN-1	0.173	0.375	0.018	4.20
KW-C6	KW-AN-1	26.2	1.58	0.101	34.1
KW-A18	KW-AN-1	45.2	0.032	0.008	9.73
KW-A18	KW-AN-1	59.4	0.036	0.008	9.13
KW-A18	KW-AN-1	79.0	1.01	0.070	26.9
KW-A18	KW-AN-1	7.64	0.005	0.006	0.673
KW-A18	KW-AN-1	158	0.282	0.013	80.9
KW-A18	KW-AN-1	7.07	0.095	0.011	1.18
KW-A18	KW-AN-1	26.4	0.174	0.023	7.83
KW-A18	KW-AN-1	56.8	0.231	0.032	20.6
KW-A18	KW-AN-1	49.1	0.036	0.021	3.52
KW-A18	KW-AN-1	16.7	0.010	0.012	0.819
KW-A18	KW-AN-1	12.5	0.822	0.015	0.621
KW-A19	KW-SUB-2	147	0.241	0.022	40.1
KW-A19	KW-AN-1	3.16	0.506	0.031	15.9
KW-A19	KW-AN-1	6.45	0.370	0.047	48.0
KW-A19	KW-AN-1	8.86	1.21	0.012	54.3
KW-A19	KW-AN-1	9.43	1.53	0.083	22.1
KW-A19	KW-AN-1	11.6	0.439	0.022	20.5
KW-A19	KW-AN-1	10.4	1.01	0.046	64.5
KW-A19	KW-AN-1	29.7	0.527	0.011	21.4

Sample Name	Morphology	Co/Ni	Cu/Ni	Zn/Ni	As/Ni
KW-A19	KW-AN-1	6.54	0.134	0.029	4.23
KW-A19	KW-AN-1	0.841	0.004	0.008	0.054
KW-A19	KW-AN-1	33.3	1.49	0.071	26.2

The fine subhedral KW-SUB-1 grains are similar in shape and texture to fine diagenetic grains previously observed within the Odwaleni Formation diamictites (Li et al., 2019) and other sedimentary rocks (Guy et al., 2010). However, those grains are typically only a few micrometers in diameter, where the KW-SUB-1 grains are ~10 – 50 µm in diameter (Figure 3.3A), which may indicate they are of a different origin. Detrital grains of similar sizes to the KW-SUB-1 grains are frequently angular (Utter, 1980; Guy et al., 2010; Altuhafi and Baudet, 2011) so a detrital origin cannot be eliminated based on the subhedral shape of the grains. The disseminated occurrence of the grains also does not provide evidence against a detrital origin as density sorting does not occur within diamictites. Therefore, detrital pyrite is not expected to be concentrated in bands or lag deposits with other heavy detrital minerals (e.g. chromite, zircon, uraninite), as is observed in sorted sedimentary rocks (e.g. England et al., 2002; Guy et al., 2010; Johnson et al., 2014). Only one trace element measurement was completed on a KW-SUB-1 grain. The measured Co/Ni, Cu/Ni and As/Ni values were within ranges described for diagenetic grains (Table 3.4, Gregory et al., 2015a), but the author is reluctant to interpret the origin of these grains from a single measurement. Furthermore, as mentioned above, a diagenetic trace element signature could represent either a diagenetic or detrital grain. Consequently, the paragenesis of the KW-SUB-1 grains remains uncertain.

A subhedral porous morphology, such as observed for KW-SUB-2 grains (Figure 3.3B), is common for diagenetic grains (e.g. Guy et al., 2010). Typically, the lack of rounding and angular shape of these grains would indicate that they have formed in situ and not undergone transport. However, this does hold for detrital grains within diamictites, which can be angular to subangular (Altuhafi and Baudet, 2011; Li et al., 2019). Similarly, whilst the trace element compositions of these grains are similar to those of previously measured diagenetic grains (Co/Ni, Cu/Ni, Zn/Ni and As/Ni values are similar to previously observe values (Table 3.4); Price, 1972; Guy et al., 2010; Gregory et al., 2015a), it cannot be conclusively determined whether this represents a diagenetic grain which formed in situ or a detrital grain which was originally of diagenetic origin.

Madaga Stream pyrite

Both KW-AN-1 and KW-SUB-2 pyrite grains within the Madaga Stream samples are interpreted to be of detrital origin. Both morphologies show elevated Co/Ni and As/Ni values which exceed the values previously observed for diagenetic pyrite (Figure 3.5F, Table 3.4, Price, 1972; Guy et al., 2010; Gregory et al., 2015a). This immediately eliminates the possibility that the grains are diagenetic in origin. As the grains are not associated with veins or fractures within the diamictite, it is also unlikely that they are epigenetic in origin. The morphology and texture of both KW-AN-1 and KW-SUB-2 grains is also inconsistent with an epigenetic origin, as epigenetic grains tend to be large (>500 μm), euhedral (except within veins where they may be anhedral) and either non-porous or displaying crystallographically-aligned pores (Ramdohr, 1958; Saager, 1970; McClay and Ellis, 1983; Craig et al., 1998; Guy et al., 2010). Therefore, grains within these samples are interpreted to be detrital in origin. The provenance of these detrital grains is discussed in the following section.

Provenance and isotopic signatures of detrital grains

Mageza Stream samples

Provenance

KW-AN-1 grains within the Mageza Stream samples are interpreted to be re-worked diagenetic grains originating from a sedimentary source. In terms of texture, the shape, size and distribution of pores within these grains is similar to that observed for diagenetic grains (e.g. Guy et al., 2010). The majority of the measured Co/Ni, Cu/Ni and As/Ni values are within the ranges expected for diagenetic grains (Table 3.4, Price, 1972; Guy et al., 2010; Gregory et al., 2015a). Additionally, the variable $\delta^{34}S$ and non-zero $\Delta^{33}S$ and $\Delta^{36}S$ values (Figure 3.7B) are consistent with a diagenetic origin and are discussed in further detail below. When plotted in $\Delta^{33}S$-$\delta^{34}S$ space and $\Delta^{36}S$-$\Delta^{33}S$ space, these grains also show a similar composition to ‘reworked syngenetic/diagenetic grains’ observed by Guy et al. (2014) and ‘sedimentary’ detrital grains observed by Hofmann et al. (2009) within other Archean sedimentary units of the Kaapvaal Craton (Figure 3.10).

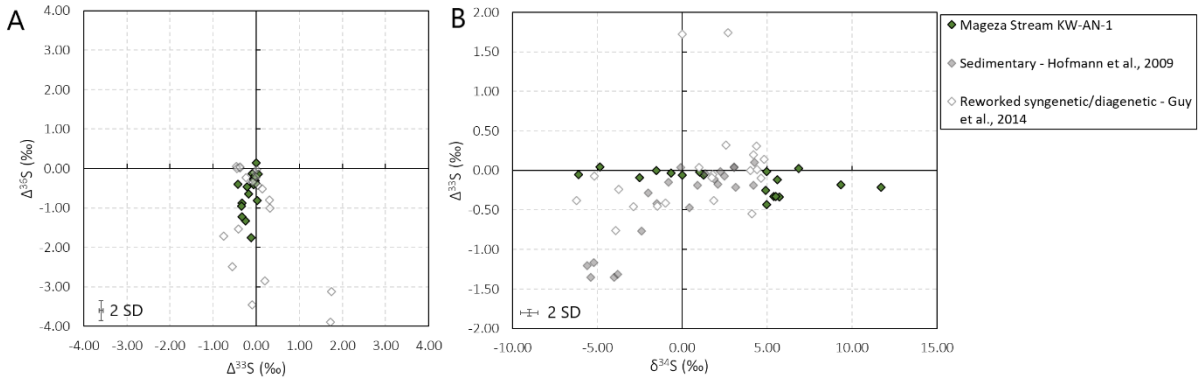

Figure 3.10. Comparison of the isotopic signatures of KW-AN-1 grains from the Mageza Stream samples and detrital grains of sedimentary origin from the Kaapvaal Craton. A. $\Delta^{36}S$ vs. $\Delta^{33}S$ plot comparing Mageza Stream KW-AN-1 grains and 'reworked syngenetic/diagenetic' grains from Guy et al. (2014), B. $\Delta^{33}S$ vs. $\delta^{34}S$ plot comparing Mageza Stream KW-AN-1 grains and 'reworked syngenetic/diagenetic' grains from Guy et al. (2014) and 'sedimentary' grains from Hofmann et al. (2009).

Isotopic signatures

KW-AN-1 grains from the Mageza Stream samples show variable $\delta^{34}S$, small negative or approximately zero $\Delta^{33}S$ values and consistently negative $\Delta^{36}S$ values (Figure 3.7B). Whilst non-zero $\Delta^{33}S$ and $\Delta^{36}S$ values are observed, data do not fall on the ARA in $\Delta^{36}S$-$\Delta^{33}S$ space; there is significant deviation from the ARA in $\Delta^{36}S$ (Figure 3.7B). This suggests that these signatures could not have been produced exclusively through atmospheric photolysis of SO_2. Instead, it may be possible that signatures represent MSR of a mixture of MIF sulfate and MDF sulfur species, or other fractionation processes which are capable of producing negative $\Delta^{33}S$ and $\Delta^{36}S$ values. These possibilities are discussed below.

The first option to be considered is that the signatures represent MSR. KW-AN-1 grains within the Mageza Stream samples show a range in $\delta^{34}S$ of ~16.5 ‰ (Figure 3.7B), which is comparable to ranges previously attributed to MSR within Archean samples (e.g. Shen et al., 2001; Wacey et al., 2010; Guy et al., 2012). Additionally, there is intragrain variability of ~6 ‰ (Supplementary Information), which is also indicative of MSR, as this process can produce $\delta^{34}S$ variation over microscale distances (Wacey et al., 2010). If an estimate of +3 - +16 ‰ is used for Archean seawater sulfate (Lambert et al., 1987; Canfield and Raiswell, 1999; Ono et al., 2003), KW-AN-1 grains preserve fractionations in $\delta^{34}S$ of between ~4.30 ‰ and ~22 ‰ (minimum calculated from maximum estimate for Archean seawater and maximum observed value: +16 - +11.7 = 4.30 ‰, maximum calculated from maximum estimate for Archean seawater and minimum observed value: +16 - -6.09 = 22.09 ‰). Whilst lower than most fractionations observed in post-Archean samples (e.g. Canfield, 2001a; Ono et al., 2006a), the

magnitude of fractionation observed for these grains is similar to that observed within other Archean samples, where fractionations are typically less than 20 ‰ (Sim et al., 2019). Therefore, both the degree of and variation in $\delta^{34}S$ fractionation is consistent with MSR.

In terms of the $\Delta^{33}S$ and $\Delta^{36}S$ values, the consistently negative $\Delta^{36}S$ values show that the grains are depleted in ^{36}S. This is expected for MSR, which discriminates against the heavy isotopes (Ono et al., 2006a; Johnston et al., 2007). Additionally, in $\Delta^{36}S$-$\Delta^{33}S$ space, data show steep $\Delta^{36}S/\Delta^{33}S$ trends similar to the characteristic trend of $\Delta^{36}S/\Delta^{33}S$ = ~-6.9 ‰ produced by MSR (Figure 3.7B; Ono et al., 2006a; Johnston et al., 2007). Further data is required to confirm the exact slope of the observed trends. For those grains which show small negative $\Delta^{33}S$ values, the starting sulfate is interpreted to be a combination of atmospheric MIF and crustal MDF sulfate, where the crustal sulfate carried $\Delta^{33}S$ of approximately zero (Guy et al., 2012). Here, the negative $\Delta^{33}S$ values of the MIF sulfate would be diluted by the MDF crustal sulfate, resulting in the small negative values observed here. Previously, similar small negative $\Delta^{33}S$ values observed within the Witwatersrand Supergroup by Guy et al. (2012, 2014) have been attributed to this mixing. In this scenario, sulfur with $\Delta^{33}S$ of ~0 ‰ may have been sourced from subaerial volcanism (Kump and Barley, 2007; Gaillard et al., 2011; Guy et al., 2012) and/or low temperature geothermal systems (McCarthy et al., 1990; Myers et al., 1990; Falconer, 2003; Guy et al., 2012) and/or weathering of reactive sulfide minerals present in igneous rocks in the surrounding area (Reinhard et al., 2009; Lefticariu et al., 2010; Wacey et al., 201; Guy et al., 2012). Therefore, the observed $\Delta^{33}S$ and $\Delta^{36}S$ values are also consistent with this hypothesis.

The other possibility is that these signatures have been produced without involvement of SO_2 photolysis. Two other processes are known to produce small negative or approximately zero $\Delta^{33}S$ values and negative $\Delta^{36}S$ values. The first of these is photolysis of carbonyl sulfide (OCS). Photolysis reactions involving OCS and UV radiation of wavelengths 200 – 260 nm results in photodissociation of OCS to carbon monoxide and elemental sulfur (Equation 3.1; Sidhu et al., 1966; Rudolph and Inn, 1981).

$$OCS + h\nu \rightarrow S + CO \quad (3.1)$$

This process causes small, typically negative fractionations in $\Delta^{33}S$ and $\Delta^{36}S$ of ~-0.20 - +0.05 ‰ for $\Delta^{33}S$ and ~-1.40 – 0.20 ‰ for $\Delta^{36}S$, where the fractionations in $\Delta^{33}S$ are considered to fall within limits for mass-dependent fractionation (Lin et al., 2011). These are similar to the fractionations observed for KW-AN-1 grains within the Mageza Stream samples (Figure

3.11). Additionally, it has previously been proposed that OCS was an abundant atmospheric sulfur species prior to the Pongola glaciations which deposited these diamictites (Ueno et al., 2009), meaning that OCS may have been available for photolysis at the time and locality at which these detrital grains were forming. However, OCS photolysis produces a narrow range of fractionations in $\delta^{34}S$ (between -2 ‰ and -7 ‰) that is unlike the relatively wide range of $\delta^{34}S$ fractionations observed here. Additionally, questions are raised as to why the elemental sulfur produced through this process would have been preserved when the elemental sulfur produced through SO_2 photolysis was not (positive $\Delta^{33}S$ values are absent from all grains analyzed within this study). This could be explained if OCS photolysis was the dominant photolysis reaction occurring at this locality prior to glaciation. However, sedimentary sulfides from older units of the Mozaan Group show isotopic signatures consistent with SO_2 photolysis (Ono et al., 2006b), so this seems unlikely. Because of this and the inconsistency between the observed $\delta^{34}S$ values and those produced by OCS photolysis, this process is considered unlikely to have produced the isotopic signatures observed for KW-AN-1 grains from the Mageza Stream samples.

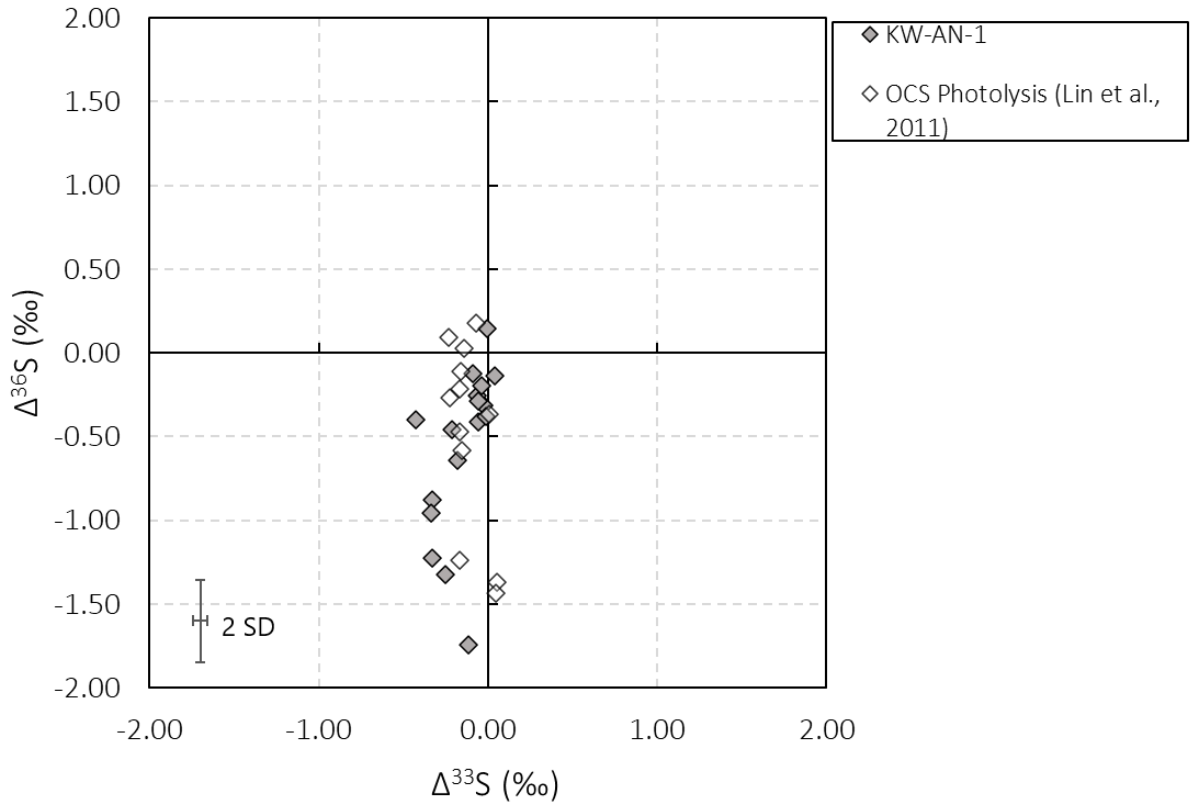

Figure 3.11. $\Delta^{33}S$ vs. $\Delta^{36}S$ plot comparing the isotopic signatures of KW-AN-1 grains from the Mageza Stream samples with the isotopic signatures produced through photolysis of OCS. Data from Lin et al. (2011).

The other process which has been observed to produce sulfur species with small negative to approximately zero $\Delta^{33}S$ values and negative $\Delta^{36}S$ values is biomass burning. Primary sulfate produced during burning of biomass has been observed to carry $\Delta^{33}S$ values of ~-0.23 – 0.03 ‰ and $\Delta^{36}S$ values of ~-2.06 - -0.54 ‰ (Shaheen et al., 2014). However, biomass burning is unlikely to have occurred during the Archean due to both the limited amount of biomass present and low atmospheric oxygen concentrations, which likely would have prevented combustion. On this basis, this process is considered to be irrelevant for Archean samples and not a viable option for explaining the isotopic signatures observed within KW-AN-1 grains from the Mageza Stream samples.

Madaga Stream samples

Provenance

KW-AN-1 and KW-SUB-1 grains from the Madaga Stream samples are interpreted to represent reworked grains from a volcanogenic massive sulfide (VMS) deposit. The elevated Co/Ni values (Table 3.2, Figure 3.5F) are similar to values previously observed for sulfides of this origin, which typically show Co/Ni values of 5 – 50 (Hawley and Nichol, 1961; Price, 1972; Gehrisch et al., 1975; Bralia et al., 1979). Additionally, the high concentrations of Co and low concentrations of Ni (Figure 3.5A, B) are similar to those previously observed within pyrite from VMS deposits (Hawley and Nichol, 1961; Price, 1972; Gehrisch et al., 1975; Bralia et al., 1979). The observed isotopic signatures are also consistent with a VMS source, as sulfides from Archean VMS deposits typically show small $\delta^{34}S$ values and small negative $\Delta^{33}S$ values (Shanks and Seyfried, 1987; Farquhar and Wing, 2005; Jamieson et al., 2006, 2013). Additionally, when compared to the isotope data previously collected from Archean VMS deposits, the isotopic signatures of the KW-AN-1 and KW-SUB-2 grains from the Madaga Stream samples are observed to fall within the range of the previously collected data (Figure 3.12). Furthermore, a VMS deposit has previously been suggested to be the source of detrital grains within sedimentary units of the Kaapvaal Craton (Hofmann et al., 2009).

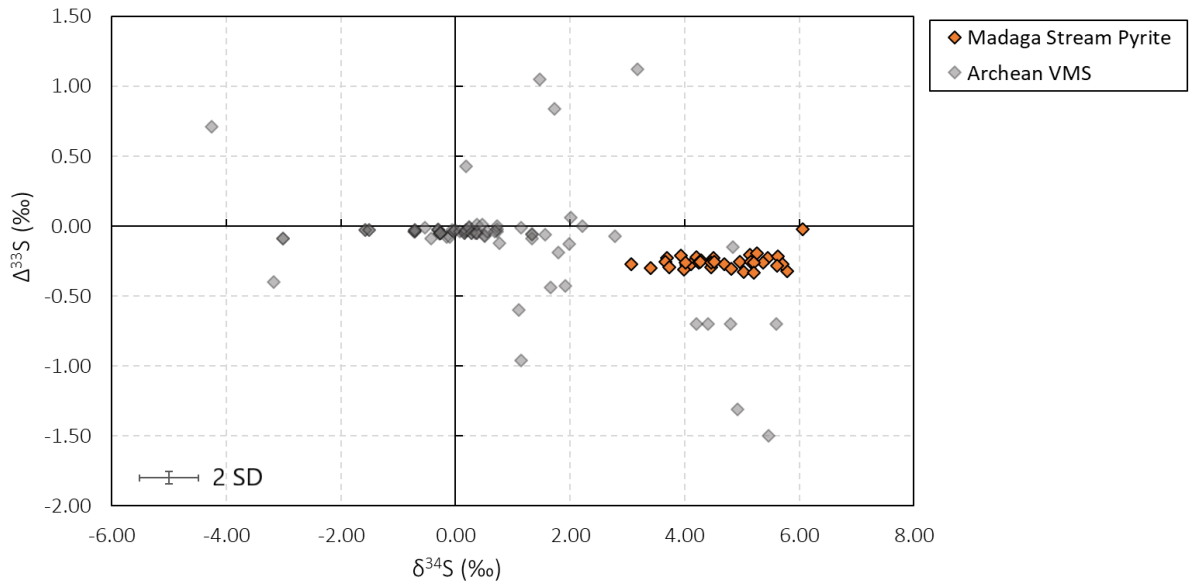

Figure 3.12. $\Delta^{33}S$ vs. $\delta^{34}S$ plot comparing the isotopic composition of pyrite from the Madaga Stream samples with the isotopic composition of sulfide minerals from Archean VMS deposits. Data from Jamieson et al. (2006, 2013), Bekker et al. (2009).

Isotopic signatures

As mentioned above, the isotopic signatures of pyrite grains from the Madaga Stream samples are similar to those observed for pyrite formed within Archean VMS deposits in a seafloor hydrothermal setting. The formation processes of sulfide minerals within these settings is well-known. First, the majority of dissolved sulfate in infiltrating seawater is removed via precipitation of anhydrite as the temperature of the infiltrating fluid increases during downwelling (Alt, 1995). The remaining sulfate then undergoes thermochemical sulfate reduction (TSR) through interaction with Fe^{2+}-bearing minerals in the wall rocks via equation 3.2 (Shanks et al., 1981; Shanks and Seyfried, 1987). Third, the product sulfide is mixed with sulfide leached from the volcanic host rock and any directly degassed magmatic sulfur (Woodruff and Shanks, 1988; Herzig et al., 1998). Finally, the sulfide is precipitated as sulfide minerals at or below the seafloor as the ascending hot fluids mix with cold seawater.

$$8Fe^{2+} + 10H^{+} + SO_4^{2-} \rightarrow 8Fe^{3+} + H_2S + 4H_2O \quad (3.2)$$

Determining whether the observed $\delta^{34}S$ values for these grains are consistent with the sulfur having undergone this sequence of processes is difficult, as the final $\delta^{34}S$ value will be dependent on a number of variables. These include the local concentration of seawater sulfate, the relative contributions of seawater sulfate, hydrothermal and/or magmatic sulfide and sulfide leached from the surrounding rocks and the initial $\delta^{34}S$ compositions of each of these components. Constraining each of these variables is beyond the scope of this study, however,

the similarities between the $\delta^{34}S$ values observed for these pyrite grains and from sulfide minerals from known Archean VMS deposits (Figure 3.12) provides evidence for the pyrite from the Madaga Stream samples having been formed through these processes.

Similarly, the observed $\Delta^{33}S$ values fall within the range previously observed for sulfide minerals from Archean VMS deposits (Figure 3.12). Jamieson et al. (2013) attributed these small negative $\Delta^{33}S$ values to reduction of seawater sulfate carrying negative $\Delta^{33}S$ signatures by iron-bearing hydrothermal fluids within hydrothermal chimneys and mounds. This would result in seafloor sulfide minerals with isotopic compositions between hydrothermal sulfide and seawater sulfate (Shanks and Seyfried, 1987); essentially, sulfur within the hydrothermal fluids would have diluted the negative $\Delta^{33}S$ signature of the seawater sulfate. Additionally, it could be expected that any sulfide leached from the volcanic wall rocks of the chimneys and mounds and any directly degassed magmatic sulfur which was incorporated into the pyrite would also dilute the negative seawater sulfate $\Delta^{33}S$ signature (Woodruff and Shanks, 1988; Herzig et al., 1998). This would result in the small negative $\Delta^{33}S$ signatures observed here and within sulfide minerals from other Archean VMS deposits.

The origin of the negative $\Delta^{36}S$ signatures observed within pyrite from the Madaga Stream samples is less clear and there is a lack of four sulfur isotope data from Archean VMS deposits to compare these signatures with, so it unknown whether these signatures are typical. It is highly unlikely that they were produced directly through MSR as sulfate reducing microbes are only active between temperatures of 0 – 110 °C and prefer temperatures of 20 – 40 °C (Postgate, 1984; Canfield, 2001b), which is much lower than expected for a seafloor hydrothermal environment. It may be possible, however, that the negative $\Delta^{36}S$ signatures are caused by dissolution and incorporation of biogenic sulfide produced through MSR from nearby sedimentary rocks (Marini et al., 2011). Unfortunately, this cannot be confirmed as the grains have been removed from their site of formation and so the pyrite from the surrounding sediments cannot be identified and analyzed. It may also be possible that the negative $\Delta^{36}S$ signatures were produced during TSR involving Fe^{2+} as the $\Delta^{36}S$ fractionation produced through this process is currently unknown.

As these grains formed within a VMS deposit in seafloor hydrothermal environment, the observed isotopic signatures are not representative of terrestrial sulfur reservoirs or fractionation processes occurring in terrestrial environments. Therefore, they are excluded in

all further discussion regarding determining the isotopic composition of terrestrial sulfur reservoirs and identifying the fractionation processes active within those reservoirs.

Isotopic signatures of diagenetic grains and grains of uncertain paragenesis

Both the diagenetic grains and grains of uncertain paragenesis within the Mageza Stream samples show similar isotopic signatures to the detrital grains within the same samples (Figure 3.7B, 3.8). This could be explained by these grains being formed through similar processes from a sulfur reservoir of similar isotopic composition or through reworking of detrital grains. Alternatively, it could mean that the paragenesis of the different morphologies have been interpreted incorrectly and that all grains are detrital, or that all grains are diagenetic.

In regards to the first option, that the grains formed from similar sulfur reservoirs, the isotopic signatures of the diagenetic grains and grains of uncertain paragenesis are similar to the isotopic signatures observed for diagenetic grains from other diamictites (Figure 3.13; Guy et al., 2012; Philippot et al., 2018). This argues that there was a consistent supply of crustal sulfur to Archean sedimentary basins/marine environments during deposition of glacial sediments. It also argues that after deposition, MSR was consistently an active process within these sediments. It is proposed that during deposition of glacial sediments the input of crustal sulfur by glaciers outweighed the atmospheric input of sulfur and encouraged the action of MSR, resulting in dominance of non-MIF sulfur signatures. In essence, during deposition of a diamictite, the input of crustal sulfur mimics the terrestrial sulfur reservoir and so similar isotopic compositions would be observed for pyrites formed within this environment and within terrestrial environments, such as fluvial sediments or the sedimentary environment in which the detrital grains from these samples originally formed. As mentioned above, it may also be possible that these grains simply represent reworked detrital grains, where sedimentary recycling had little to no effect on isotopic composition.

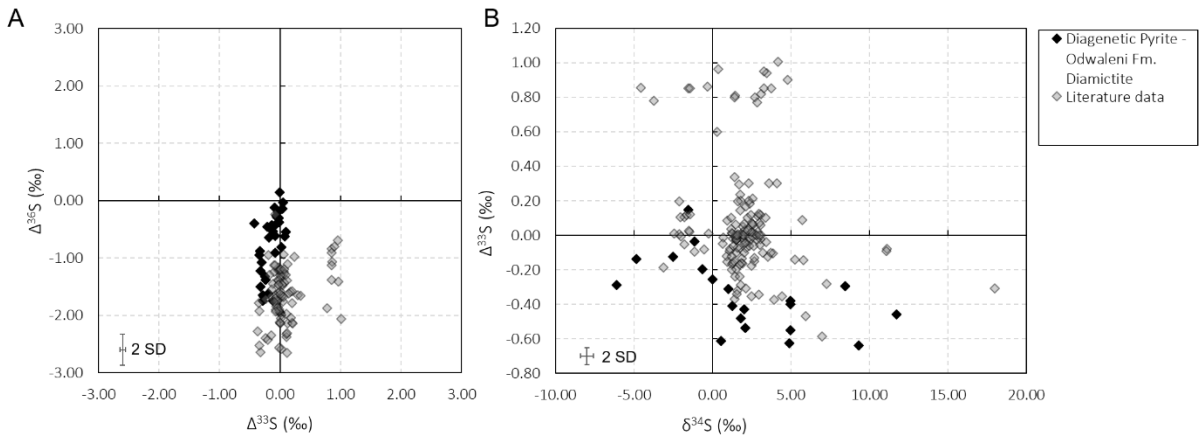

Figure 3.13. Comparison of the isotopic signatures of diagenetic pyrite and pyrite of uncertain paragenesis from the Odwaleni Formation diamictites and diagenetic pyrite from other Archean diamictites. A. $\Delta^{33}S$ vs. $\delta^{34}S$, B. $\Delta^{36}S$ vs. $\Delta^{33}S$. Data from Guy et al. (2012), Maynard et al. (2013), Philippot et al. (2018).

It is also acknowledged that the similarities may simply be due to errors made in determining the paragenesis of the different grain morphologies observed within the Mageza Stream samples. As previously noted, difficulties were encountered when attempting to determine paragenesis; certainly, this is why KW-SUB-1 and KW-SUB-2 grains are listed as having uncertain paragenesis.

Absence of positive $\Delta^{33}S$ signatures

Positive $\Delta^{33}S$ signatures consistent with preservation of the MIF elemental sulfur aerosol are absent from all of the grains analyzed within this study. Instead, what is observed are either $\Delta^{33}S$ values of ~0 ‰, consistent with MDF sulfur, or small negative $\Delta^{33}S$ values consistent with mixing between MDF sulfur and the MIF sulfate aerosol. Previously, Maynard et al. (2013) proposed that the prominence of negative $\Delta^{33}S$ signatures and absence of positive $\Delta^{33}S$ signatures within terrestrial rocks was due to the greater solubility of SO_4^{2-} compared to S_8. It was hypothesized that SO_4^{2-} would be transported into the crustal sediments via rainwater (meltwater could also contribute to this transportation), where S_8 would remain at the surface, where it would be vulnerable to erosion. However, certain issues arise when we consider the diagenetic grains from this study, which also fail to preserve positive $\Delta^{33}S$ signatures. If the S_8 aerosol was sitting at the surface, it would be expected that it would have been collected in the sediments entrained by a glacier as the glacier moved across that surface. Following this, it would be expected that, if solubility were the only barrier, the S_8 would be incorporated into diagenetic pyrite. However, that is not seen here, or in the diagenetic pyrite analyzed by Guy et al. (2012). This suggests that there may be some other barrier to the MIF elemental sulfur

aerosol being preserved in terrestrial environments and the pseudo-terrestrial environment created by deposition of the glacial sediments.

It is noted that a large amount of the diagenetic pyrite within the diamictites of the Turee Group that was analyzed by Philippot et al. (2018) does show positive $\Delta^{33}S$ values. The reason as to why positive $\Delta^{33}S$ signatures are preserved in diagenetic pyrite from this locality and not diamictites of the Kaapvaal Craton is unclear.

3.7 Conclusions

As shown, pyrite from the Mageza and Madaga Stream sampling sites preserve pyrite from different sources. Within the Mageza Stream sampling site, detrital and diagenetic pyrite species were identified, whilst the paragenesis of certain grain morphologies could not be determined. Detrital grains showed variable $\delta^{34}S$ values, consistently negative $\Delta^{36}S$ values and small negative to approximately zero $\Delta^{33}S$ values which were consistent with microbial sulfate reduction of a mixture of MIF sulfate and MDF crustal sulfate. None of the analyzed detrital grains preserved positive $\Delta^{33}S$ signatures consistent with preservation of the MIF elemental sulfur aerosol. This is conclusive with the earlier results of Maynard et al. (2013) and adds further weight to the suggestion that terrestrial environments preferentially preserve the MIF sulfate aerosol. Diagenetic grains and grains of uncertain paragenesis were observed to show similar isotopic signatures to the detrital grains. This was interpreted to represent a significant input of crustal sulfur during deposition of the diamictite which outweighed the atmospheric sulfur input and encouraged MSR.

All grains within the Madaga Stream samples were determined to be detrital due to trace element compositions inconsistent with a diagenetic origin. The elevated Co/Ni values, small negative $\Delta^{33}S$ values and restricted range of small $\delta^{34}S$ values were consistent with these grains having been sourced from a VMS deposit. As these grains formed in a seafloor hydrothermal setting, their isotopic composition does not provide relevant information regarding the isotopic composition of terrestrial sulfur reservoirs or the fractionation processes occurring within those reservoirs.

Due to the difficulties encountered in determining the paragenesis of diamictite-hosted pyrite grains and also the occurrence of detrital grains from a marine source (VMS deposit), it is suggested that diamictite-hosted pyrite may not be the most suitable tool for examining terrestrial sulfur reservoirs. There is large potential for mis-identifying paragenesis, which can lead to isotopic signatures being interpreted in the wrong context. Additionally, there is

potential that marine units now existing at the continental surface can be sampled by glaciers, which can also lead to interpretation of results in the wrong context.

Chapter 4: Sulfur isotope composition of paleosol-hosted pyrite

Abstract - A detailed morphological, trace element and multiple sulfur isotope study of sulfide minerals from four Archean paleosol profiles is presented. Two of these profiles, the Crown Lava paleosol from the Witwatersrand Supergroup, South Africa and the Cooper Lake paleosol from the Huronian Supergroup, Canada, preserved $\Delta^{33}S$ and $\Delta^{36}S$ values of approximately zero and small positive and negative $\delta^{34}S$ values. These isotopic compositions are consistent with unfractionated, igneous sulfur and suggest that the sulfur within these profiles has been inherited from the igneous parent materials. The remaining two profiles, the Dominion Reef paleosol and the Bird Lava paleosol, formed on the basement underlying and on lava within the Witwatersrand Supergroup, preserved similar $\Delta^{36}S$ and $\delta^{34}S$ values but showed small negative $\Delta^{33}S$ values. These signatures are conclusive with a mixture of unfractionated igneous sulfur and the atmospheric sulfate aerosol produced through photolysis of SO_2. Noticeably absent from any of the sulfide minerals analyzed are positive $\Delta^{33}S$ values, which shows that the photochemical sulfur aerosol was not preserved within paleosol environments.

4.1 Introduction

This chapter focusses on the sulfur isotope composition of sulfide minerals hosted within paleosols of the ~3000 – 2700 Ma Witwatersrand Supergroup and underlying basement, South Africa and the ~2400 – 2200 Ma Huronian Supergroup, Canada. A paleosol is defined to be a rock unit which has formed through in-situ weathering of a homogeneous substrate. This unit must display unidirectional changes in mineralogy, texture and chemistry that are consistent with soil forming processes and there must be identifiable soft-sediment deformation features along the contact between the paleosol and the overlying unit (Rye and Holland, 1998).

Paleosols were chosen for this study as they form through interactions between rocks and the atmosphere, hydrosphere and biosphere. As a result, they record unique information about the physical and chemical processes which occurred during these interactions and they act as excellent sources of information about past environments. Therefore, paleosols should be useful in examining the sulfur fractionation processes occurring in terrestrial environments during the Archean and the isotopic composition of terrestrial sulfur reservoirs. In particular, as paleosols form through extended exposure to the atmosphere, and the Archean sulfur cycle was dominated by atmospheric photolytic processes (Farquhar et al., 2000, 2001), these units provide an excellent opportunity to assess whether terrestrial environments preserve atmospheric mass-independently fractionated (MIF) sulfur and which fractionation processes were involved, or not involved, in preservation. The paleosols from the Witwatersrand and Huronian supergroups were specifically chosen as they are known paleosols which have previously undergone detailed study to determine that they formed through in-situ weathering (Grandstaff et al., 1986; Kimberley and Grandstaff, 1986; Palmer et al., 1989; Maynard, 1992; Sutton and Maynard, 1992; Holland and Rye, 1998; Maynard et al., 2013). The Huronian Supergroup paleosol is much younger than the other paleosols considered in this chapter, early Paleoproterozoic in comparison to Mesoarchean, and was chosen to represent a time period known to have higher magnitude MIF signatures (eg. Mojzsis et al., 2003; Ono et al., 2003, 2009; Kamber and Whitehouse, 2007; Kaufman et al., 2007; Patridge et al., 2008). It was expected that this would aid in identifying if MIF sulfur species were preserved in paleosols.

Studies of Archean paleosols have largely focussed on reconstructing atmospheric chemistry, in particular the concentrations of atmospheric oxygen at the time of formation (e.g. Holland

and Beukes, 1990; Murakami et al., 2001; Yamaguchi et al., 2007; Babechuk et al., 2019; Hao et al., 2019). Recently, however, a small number of studies have been completed on the sulfur isotope composition of Archean paleosol-hosted pyrite (Maynard et al., 2013, Nabhan et al., 2016, 2018), with these studies returning interesting results. A preliminary three-sulfur isotope (^{32}S, ^{33}S, ^{34}S) study showed that paleosol-hosted sulfide minerals recorded small negative $\Delta^{33}S$ signatures proposed to represent mixing between the MIF sulfate aerosol and unfractionated sulfur inherited from igneous parent rocks (Maynard et al., 2013). Additionally, both this study and studies completed by Nabhan et al. (2016, 2018) have demonstrated that paleosol-hosted sulfide minerals preserve negative $\delta^{34}S$ values consistent with microbial sulfate reduction (MSR) (Thode et al., 1951; Jones and Starkey, 1957; Harrison and Thode, 1958). This suggests that MSR was an active and possibly geochemically important process within terrestrial environments. However, none of the previous studies have employed the four-sulfur isotope (^{32}S, ^{33}S, ^{34}S, ^{36}S) analysis which is necessary for conclusive identification of MSR (Ono et al., 2006a; Johnston et al., 2007). Absent from these studies is any evidence for preservation of the MIF elemental sulfur reservoir which is frequently preserved in marine sediments (see Chapter 1). This implies that the isotopic composition of terrestrial sulfur reservoirs and the fractionation processes which occur in these environments may differ from that of marine environments.

This chapter presents a detailed study of the morphology, trace element composition and sulfur isotope signatures of sulfide minerals hosted by three Archean paleosols and one early Paleoproterozoic paleosol. Two of the profiles, the Crown Lava (~2910 Ma) and Cooper Lake (~2450 Ma) profiles, preserved isotopic signatures consistent with unfractionated igneous/magmatic sulfur, where the sulfur had most likely been inherited from the igneous parent materials. The Dominion Reef (>3100 Ma) and Bird Lava (~2900 – 2800 Ma) paleosols, preserved small negative $\Delta^{33}S$ values similar to those observed by Maynard et al. (2013), that were conclusive with a mixed igneous/magmatic and MIF sulfur source. The observation of small negative $\Delta^{33}S$ values and the complete absence of positive $\Delta^{33}S$ values provides further evidence that paleosol environments preferentially preserved the MIF sulfate aerosol and that the MIF elemental sulfur was not preserved in these environments. In contrast to previous studies, however, the isotopic signatures did not suggest that MSR was occurring in any of the analyzed profiles.

4.2 Geological context

South African paleosols

The Witwatersrand Supergroup is a Mesoarchean siliciclastic sequence located in the central Kaapvaal Craton. It unconformably overlies a greenstone basement and the volcano-sedimentary Dominion Group, dated at 3480 – 3030 Ma and 3090 – 3070 Ma, respectively (Armstrong et al., 1991; Robb et al., 1992; Poujel et al., 2003). A minimum age of ~2700 Ma is provided by felsic and mafic volcanics from the overlying Ventesdorp Supergroup, which yielded ages of 2709 ± 4 Ma and 2714 ± 8 Ma, respectively (U-Pb zircon; Armstrong et al., 1991).

Stratigraphically, the Witwatersrand Supergroup is divided into the lower West Rand Group and the upper Central Rand Group (Figure 4.1). The West Rand Group, which will be discussed further in Chapter 6, consists primarily of marine sedimentary rocks deposited in tidal to offshore marine environments, with minor conglomerate, diamictite and lava units (Eriksson et al., 1981; Tankard et al., 1982; Watchorn and O'Brien, 1991; Beukes, 1995). The Central Rand Group, which is discussed in more detail in Chapter 5, is predominantly composed of fluvial sedimentary rocks deposited in a braidplain environment (Catuneanu et al., 2001; Kositcin and Krapez, 2004; Schmitz et al., 2004; Frimmel et al., 2005a).

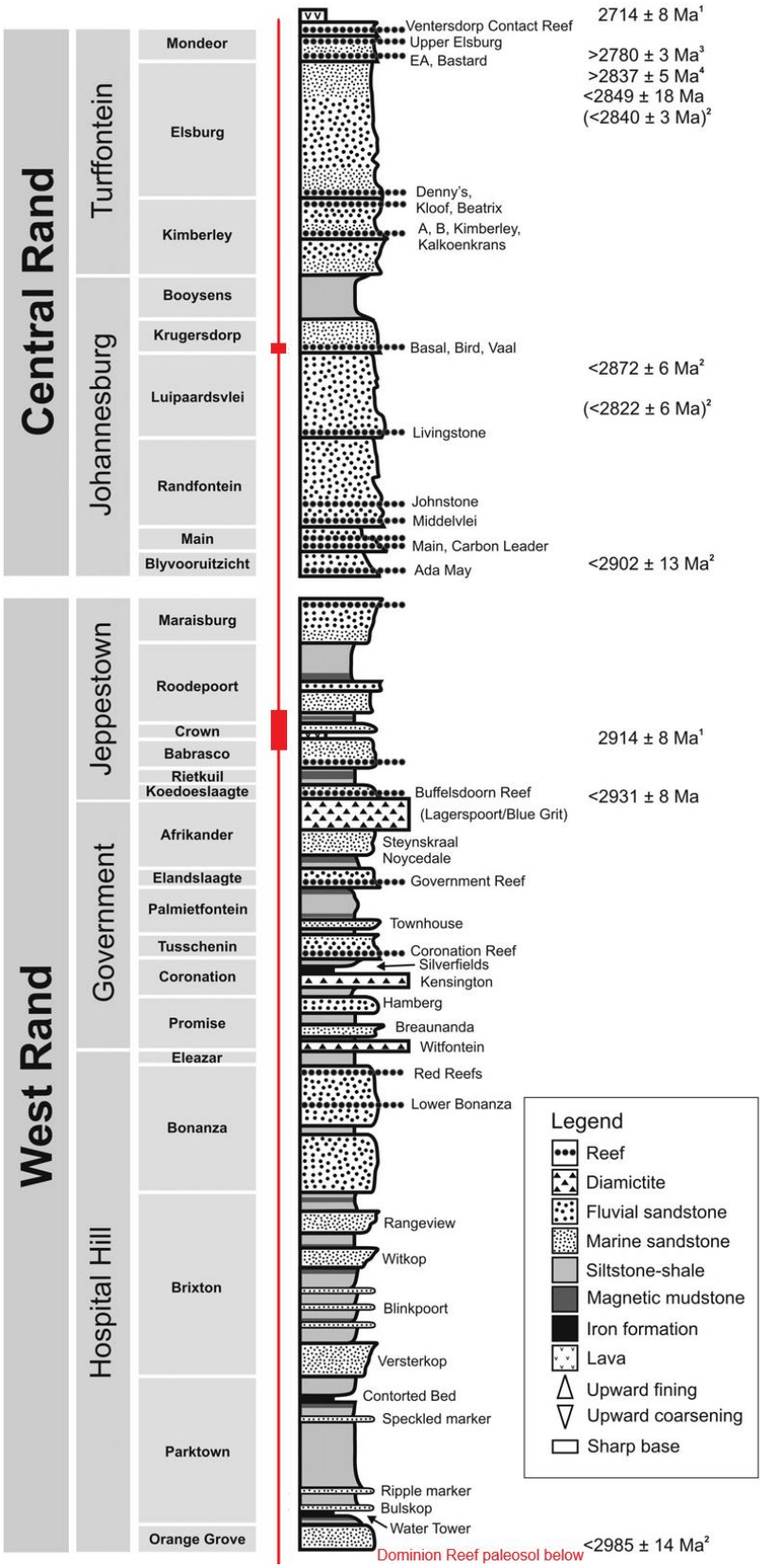

Figure 4.1. Stratigraphic column of the Witwatersrand Supergroup. Red boxes represent the stratigraphic locations of the sampled paleosols. Ages are SHRIMP U-Pb or Pb-Pb ages, where (1) zircon and xenotime (Armstrong et al., 1991), (2) zircon and xenotime (Kositcin and Krapez, 2004), (3) authogenic zenotime (Kositcin et al., 2003), and (4) zircon (Gutzmer et al., 1999). Modified from Guy et al. (2012).

Post-diagenesis, the Witwatersrand Supergroup experienced a number of regional metamorphic and hydrothermal events. These include pre-Ventesdorp compressive deformation and alteration (Rasmussen et al., 2007), lithospheric extension and high heat flow during the deposition of the Ventesdorp Supergroup (ca. 2700 Ma; Armstrong et al., 1991; Poujel et al., 1999; England et al., 2001), burial metamorphism due to the deposition of the Transvaal Supergroup (ca. 2370 Ma; Poujel et al., 1999; Frimmel and Minter, 2002; Meier et al., 2009); hydrothermal and tectono-thermal events prior to the intrusion of the Bushveld Complex (ca. 2200 – 2300 Ma and ca. 2140 Ma, respectively; Rasmussen et al., 2007; Schaefer et al., 2010), metamorphism related to the intrusion of the Bushveld Complex (ca. 2060 Ma; Gibson and Jones, 2002; Kositcin and Krapez, 2004; Rasmussen et al., 2007; Scoates and Friedman, 2008) and deformation related to the Vredefort impact event (ca. 2020 Ma; Kamo et al., 1996; Poujel et al., 1999). Despite this complex series of events, the Witwatersrand Supergroup has experienced only regional low-grade greenschist metamorphism, with a peak temperature of 250 – 350 °C and pressure of 100 – 300 kPa (Phillips, 1987; Frimmel et al., 1993). The fabric, texture and primary sedimentary structures are typically well-preserved.

The paleosols profiles sampled were the Dominion Reef paleosol, Crown Lava paleosol and Bird Lava paleosol (Figure 4.1).

Dominion Reef paleosol

The Dominion Reef paleosol formed on the granitic basement underlying the Dominion Group and the Witwatersrand Supergroup (Figure 4.1). Weathering has previously been suggested to have occurred between 2900 – 2800 Ma (Grandstaff et al., 1986; Holland and Rye, 1998) based on the date of an extrusive within the Dominion Group (2800 ± 60 Ma; Van Niekerk and Burger, 1969) and a granite underlying the Dominion Group (2900 ± 150 Ma; Nicolaysen et al., 1962). However, based on more recent ages provided for both the granitic basement (3480 – 3030 Ma) and the Dominion Group (3090 – 3070 Ma; Armstrong et al., 1991; Robb et al., 1992; Poujel et al., 2003), weathering is more likely to have occurred prior to 3090 Ma.

The unaltered parent material consists of a coarse-grained, hypidiomorphic, leucocratic granite composed predominantly of quartz, plagioclase, microcline and chlorite. Pyrite is present as an accessory mineral phase. Moving up profile, feldspars are progressively replaced by sericite and chlorite becomes more abundant. There is a corresponding

destruction of the crystalline texture and change in colour from light grey-green to green-yellow. A detailed mineralogical and textural description of the parent material and paleosol profile is given by Grandstaff et al. (1986).

Crown Lava paleosol

The Crown Lava paleosol formed on the basaltic Crown Lava, located in the Jeppestown Subgroup of the West Rand Group (Figure 4.1). The Crown Lava has been previously dated at 2914 ± 8 Ma (Armstrong, et al., 1991). Weathering has been proposed to have occurred between 2909-2910 Ma based on accumulation rates for the Witwatersrand Supergroup sandstones (J. B. Maynard, personal communication).

The unaltered parent material consists of a highly amygdaloidal flood basalt and mineralogy is dominated by fine-grained feldspar minerals. Moving up profile, there is a progressive destruction in texture, with the original aphanitic texture being replaced by a very fine, massive texture. Feldspar minerals are increasingly replaced by chlorite, with a corresponding change in colour from a dark grey-black to a grey-green colour. Amygdales are common in the lower half of the profile but become rarer moving upwards and are absent from the uppermost samples.

Bird Lava paleosol

The Bird Lava paleosol formed on the basaltic Bird Lava (also known as the Bird Amygdaloidal), located in the Johannesburg Subgroup of the Central Rand Group (Figure 4.1). Rye and Holland (1998) suggested weathering occurred between 2800 – 2700 Ma based on the ages of the surrounding units. However, more recent dating of detrital xenotime from the Luipaardsvlei Formation, which underlies the formation intruded by the Bird Lava (the Krugersdorp Formation, Figure 4.1) has returned an age of 2872 ± 6 Ma (Kositcin and Krapez, 2004). More recent dating also suggests that the overlying Elsburg Formation (Figure 4.1) was deposited prior to 2837 ± 5 Ma (Gutzmer et al., 1999). Therefore, weathering is older than originally proposed and occurred between ~2870 Ma and ~2840 Ma. Attempts to directly date the Bird Lava have been unsuccessful (Armstrong et al., 1991).

The unaltered parent material is an amygdaloidal basalt. Amygdales are infilled with quartz and occasionally contain fine grains of chalcopyrite. Moving up-profile, there is progressive destruction of texture and change in mineralogy; the feldspar minerals which dominate the parent material are first replaced, and then the resulting pseudomorphs are destroyed, with

fine-grained chlorite becoming the dominant mineral phase. Amygdales immediately become absent, whilst rutile is common in the lower and middle sections of the profile but disappears in the upper section. Siliceous and chloritic veinlets are also observed in the lower and middle sections. Corresponding to the change in mineralogy, the profile becomes progressively greener in colour moving upwards. A detailed mineralogical description can be found in Palmer et al. (1989).

Huronian Supergroup paleosol (Cooper Lake paleosol)

The Huronian Supergroup is an approximately 12 km-thick, early Paleoproterozoic volcano-sedimentary sequence deposited along the southern margin of the Superior Craton, Canada as a rift-to-drift sequence (Young et al., 2001; Young, 2015). Stratigraphically, from base to top, the Huronian Supergroup is divided into the Elliot Lake, Hough Lake, Quirke Lake and Cobalt Groups (Figure 4.2). The first three groups represent early rift sequence deposits whilst the Cobalt Group marks passive margin sedimentation. The upper three groups consist of broadly similar diamictite-mudstone-sandstone sequences interpreted to represent glacial-interglacial cycles (Hoffman, 1989; Bennet et al., 1991). The Elliot Lake Group is unique as it is the only sequence to contain volcanic rocks. It consists of the basal sandstones and conglomerates of the Livingstone Creek Formation, the volcanics of the Thessalon Formation and the upper conglomeratic Matinenda Formation (Figure 4.2; Bennett et al.,1991; Bennett, 2006).

Deposition of the Huronian Supergroup has been constrained to have occurred between ~2450 – 2200 Ma. A maximum age of 2452.5 ± 6.2 Ma is provided by zircons from the felsic volcanic rocks of the Copper Cliff Formation, within the Elliot Lake Group, near the base of the Supergroup (Krogh et al., 1984; Ketchum et al., 2013). A minimum age of 2219 Ma is provided by zircons from the oldest of the Nipissing gabbro sills, which intrude the entire succession (Corfu and Andrews, 1986).

The Huronian Supergroup has experience sub-greenschist to amphibolite facies metamorphism, with metamorphic grade generally increasing to the south. Zones of amphibolite facies are restricted and isolated, with the majority of the sequence having undergone sub-greenschist facies metamorphism (Card, 1978).

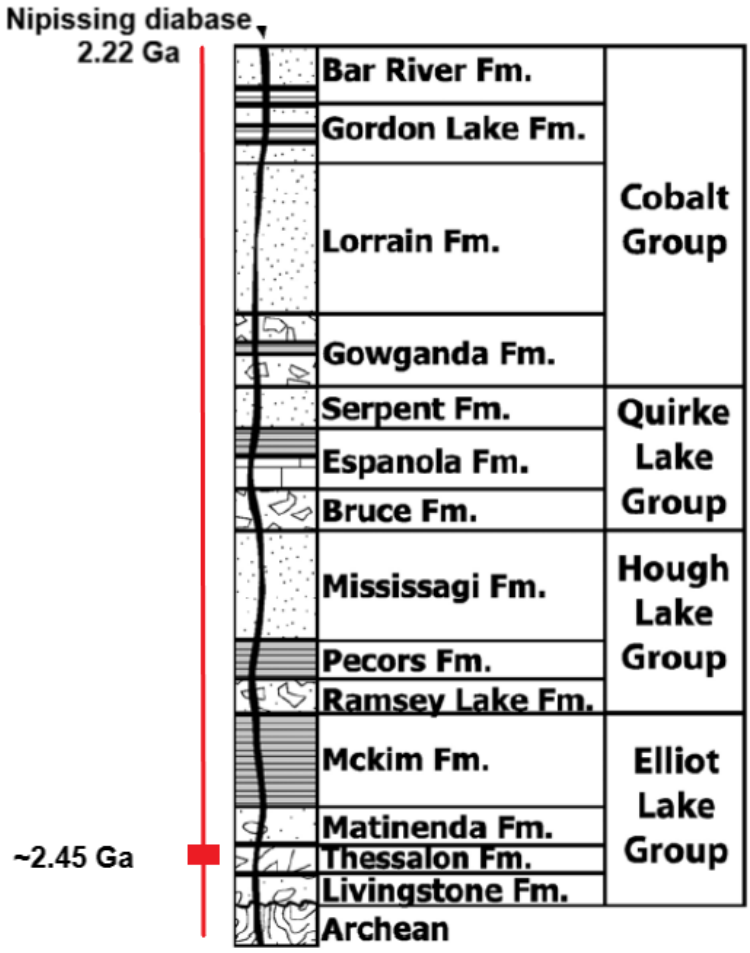

Figure 4.2. Stratigraphic column of the Huronian Supergroup. The red box represents the stratigraphic location of the sampled paleosol. Age of weathering is from Rye and Holland (1998) and age of the Nipissing Diabase is from Corfu and Andrews (1986). Modified from Papineau et al. (2007).

Cooper Lake paleosol

The Cooper Lake paleosol formed on a diabase dike intruding the Livingstone Creek Formation. The dike has been interpreted as part of the volcanic Thessalon Formation (Sutton and Maynard, 1992). The age of weathering has been proposed as ~2450 Ma (Rye and Holland, 1998) based on the age of related felsic volcanic rocks (Krogh et al., 1984; Ketchum et al., 2013) and the rapid sedimentation estimated for the lower rift-related sediments (Long, 2004).

The unaltered parent material is a diabase consisting predominantly of plagioclase, fine-grained chlorite, ilmenite and actinolite, with minor biotite (Sutton and Maynard, 1992). Moving up profile, plagioclase and fine-grained chlorite become less abundant and there is a corresponding increase in white mica (phengitic muscovite). Quartz rings, filled with a mixture of chlorite and white mica, are observed low in the profile and become progressively more deformed moving upwards (Sutton and Maynard, 1992; Babechuk et al., 2019). The

uppermost section of the profile consists of irregular quartz patches and fine-grained Ti-oxides in a matrix of white mica, where the original ophitic texture has been completely destroyed (Sutton and Maynard, 1992). A detailed mineralogical and textural description of the parent material and profile was provided by Sutton and Maynard (1992) and Babechuk et al. (2019).

4.3 Sampling information

Dominion Reef paleosol

Samples of the Dominion Reef paleosol were collected from the AngloGold drill core OGG1-1D, which was drilled approximately 25 km north of the town of Ottosdal in the central North West Province of South Africa. The approximate location of the drill hole is shown in Figure 4.3. Samples were taken of unaltered parent material (granitic basement), paleosol and the overlying Renosterspruit Formation. At the time of sampling, the core was housed at the Anglo-American Corporation core yard, Orkney, South Africa. The lithology, stratigraphic unit and depth of each samples is provided in Table 4.1.

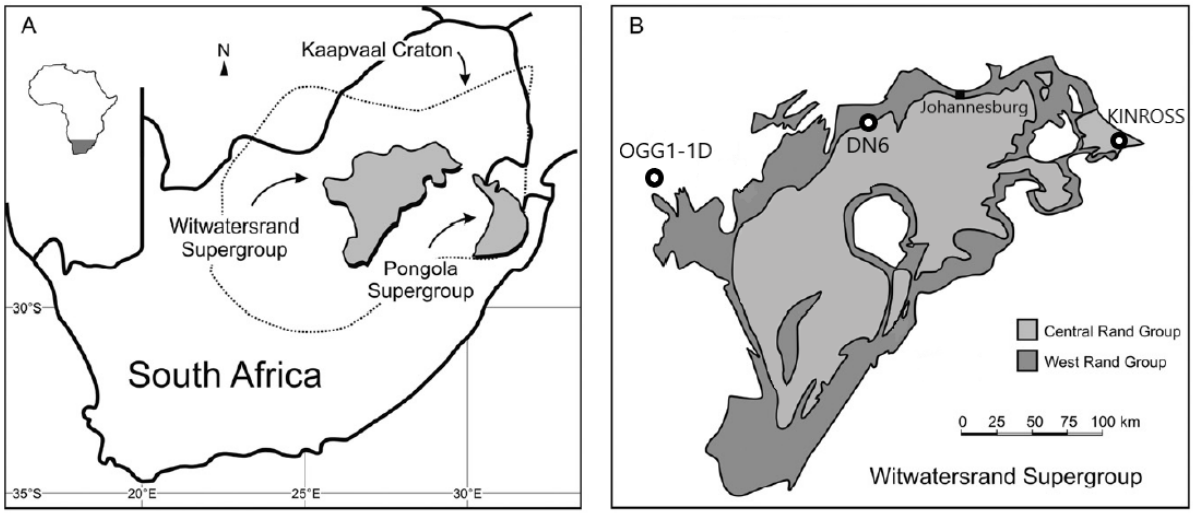

Figure 4.3. A. Geographic position of the Witwatersrand and Pongola supergroups on the Kaapvaal Craton. B. Geological map of the Witwatersrand Supergroup, showing the locations of the OGG1-1D and DN6 drill holes and Kinross mine. Modified from Guy et al. (2012).

Table 4.1. Sampling information for paleosol samples.

Sample Name	Lithology	Formation	Description	Depth (m)
		Dominion Reef paleosol		
OGG1-1D-17	Sandstone	Renosterspruit	-	289.31
OGG1-1D-18	Sandstone	Renosterspruit	-	289.37
OGG1-1D-19	Sandstone	Renosterspruit	-	289.38
OGG1-1D-16	Altered granite	Basement	-	290.09
OGG1-1D-8	Altered granite	Basement	-	290.12
OGG1-1D-9	Altered granite	Basement	-	290.15
OGG1-1D-11	Altered granite	Basement	-	290.68
OGG1-1D-13	Altered granite	Basement	-	291.61
OGG1-1D-15	Granite	Basement	-	291.78
		Crown Lava paleosol		
DN6-1	Quartzite	Roodeport	-	1153.8
DN6-2	Altered basalt	Crown Lava	-	1183.25
DN6-3	Altered basalt	Crown Lava	-	1183.30
DN6-4	Altered basalt	Crown Lava	-	1183.34
DN6-5	Altered basalt	Crown Lava	-	1183.39
DN6-6	Altered basalt	Crown Lava	-	1183.40
DN6-7	Altered basalt	Crown Lava	-	1188.30
DN6-8	Quartzite	Babrasco	-	1254.00
		Bird Lava Paleosol		
BAK-4D-2	Altered basalt	Bird Lava	5-15 cm below upper contact	~2500
BAK-4D-3	Altered basalt	Bird Lava	15-25 cm below upper contact	~2500
BAK-4D-4	Altered basalt	Bird Lava	25-35 cm below upper contact	~2500
BAK-4C	Altered basalt	Bird Lava	35 cm below upper contact	~2500
BAK-4B	Altered basalt	Bird Lava	80 cm below upper contact	~2500
		Cooper Lake paleosol		
CLD-49	Altered diabase	Thessalon	2.9 m below upper contact	-
CLD-50	Altered diabase	Thessalon	4 m below upper contact	-
CLD-53	Altered diabase	Thessalon	3.5 m below upper contact	-
TH4	Diabase	Thessalon	-	2276

Crown Lava paleosol

Samples of the Crown Lava paleosol were collected from the DN6 drill core, drilled in the vicinity of the town of Carletonville in the Gauteng Province of South Africa. The approximate location of the drill hole is shown in Figure 4.3. Samples were provided by J. B. Maynard and had been previously described in Maynard et al. (2013). The lithology, stratigraphic unit and depth of each samples is provided in Table 4.1.

Bird Lava paleosol

Samples of the Bird Lava paleosol were collected from the Kinross Mine (shaft #8) of the Evander Goldfields, located in the Mpumalanga province of South Africa. The location of the mine is shown in Figure 4.3. Samples were collected directly from the mine walls at a depth of ~2500 m. The lithology, stratigraphic unit and depth of each samples is provided in Table 4.1.

Cooper Lake paleosol

Samples of the Cooper Lake paleosol were collected from a small area of gravel road outcrops adjacent to Boundary Lake, in the Algoma District of northern Ontario, Canada. The outcrop exposure is located at 46º31’46” N, 83º 32’46” W, near the border between the Otter and Haughton Townships, north of the town of Thessalon. A sample of unweathered parent material was collected from drill core Imperial Oil 68.2 (DH68.2), drilled on the north shore of Cooper Lake. The approximate locations of the paleosol outcrops and drill hole are shown in Figure 4.4. Samples were provided by J. B. Maynard and have been described in Sutton and Maynard (1992). The lithology, stratigraphic unit and depth of each samples is provided in Table 4.1.

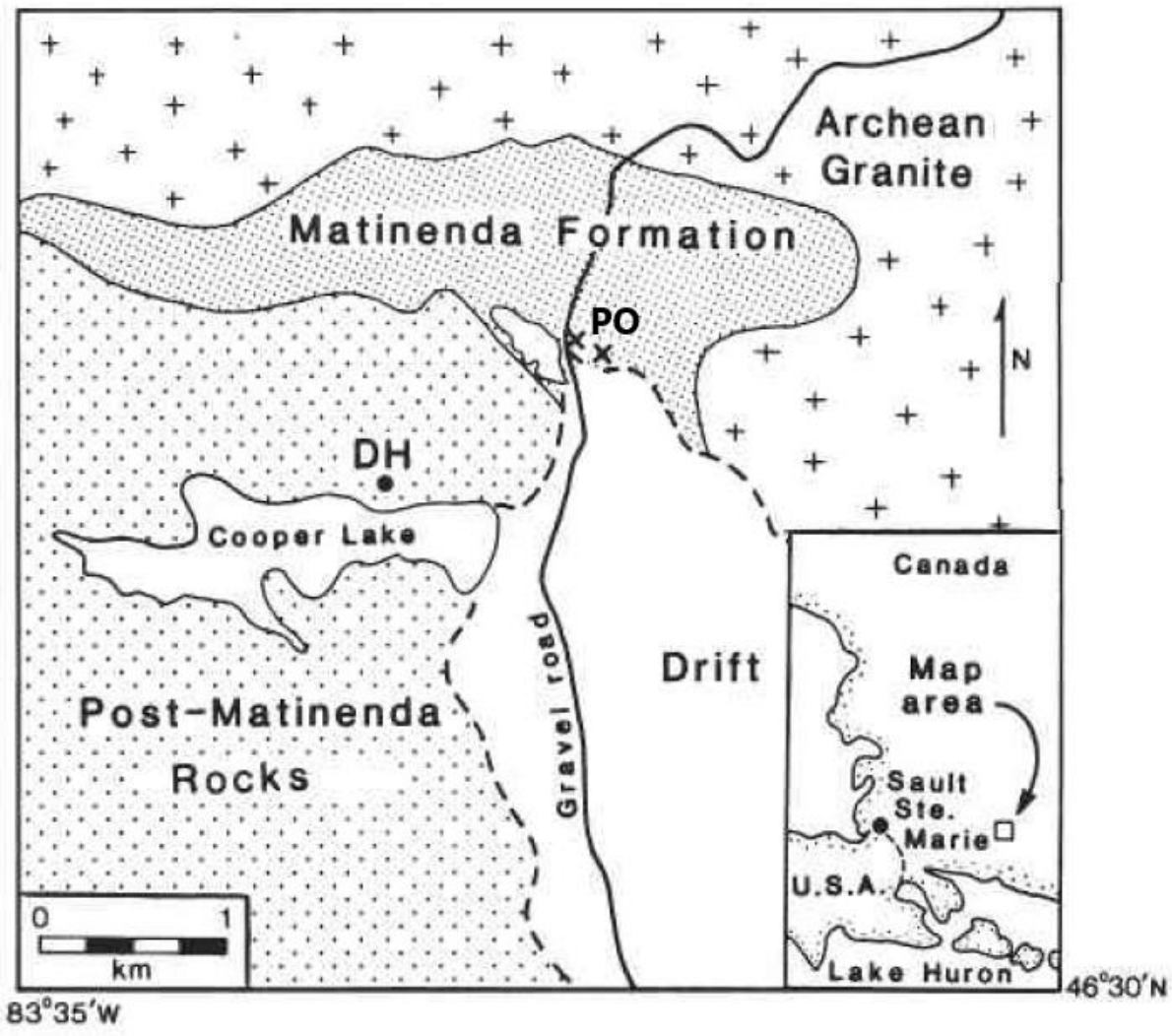

Figure 4.4. Map of the study area for the Cooper Lake paleosol. DH marks the location of Imperial Oil drill hole 68.2, from which the Thessalon volcanics sample was collected. PO marks the location of paleosol outcrops. Modified from Sutton and Maynard (1992).

4.4 Methods

Methods for sample characterisation and sulfur isotope analysis are provided in Chapter 2.

4.5 Results

Sample characterisation

Dominion Reef paleosol

Morphology and textural features

Pyrite was the dominant sulfide mineral, with lesser amounts of arsenopyrite, chalcopyrite, galena and sphalerite. The unaltered parent material was observed to contain only a limited number of sulfide minerals. Within the paleosol profile, sulfide mineral abundance was

variable; samples collected from low in the profile showed low to moderate amounts of sulfide minerals, whilst samples from the upper section of the profile contained moderate to high amounts of sulfide minerals. This is consistent with the observations of Maynard et al. (2013) of a zone of sulfur enrichment existing the upper sections of paleosols, a few centimetres below the upper contact with the overlying units.

Seven different morphologies of pyrite were observed and will be referred to as DR-EU-1, DR-SUB-1, DR-SUB-2, DR-AN-1, DR-AN-2, DR-AN-3 and DR-AN-4. Backscattered electron (BSE) images of these morphologies are provided in Figure 4.5.

DR-EU-1 grains were aggregates of euhedral, non-porous grains, ~600 µm in diameter. Inclusions of Fe-Ti oxides were observed adjacent to cracks and on the borders of the aggregates. These grains were observed only within the uppermost sample of the paleosol (OGG1-1D-16, at a depth of 290.90 m).

DR-SUB-1 grains were subhedral, porous grains, ranging in size from ~100 – 500 µm. Inclusions of galena were commonly observed, either as blebs or elongate, vein-like inclusions extending from pores or other imperfections within the grains. These grains were observed within the unaltered granite, the paleosol (only at a depth of 290.12 m) and within the overlying sandstone.

DR-SUB-2 grains were subhedral grains showing inclusion-rich, porous cores of intergrown pyrite and chalcopyrite, with a less inclusion-rich, less porous rim. Inclusions in the rim of the grain consisted of blebs and elongate, vein-like inclusions of arsenopyrite. These grains were ~500 µm in diameter. This grain type was observed only within the lowermost sample of the paleosol profile (sample OGG1-1D-13, at a depth of 291.61 m).

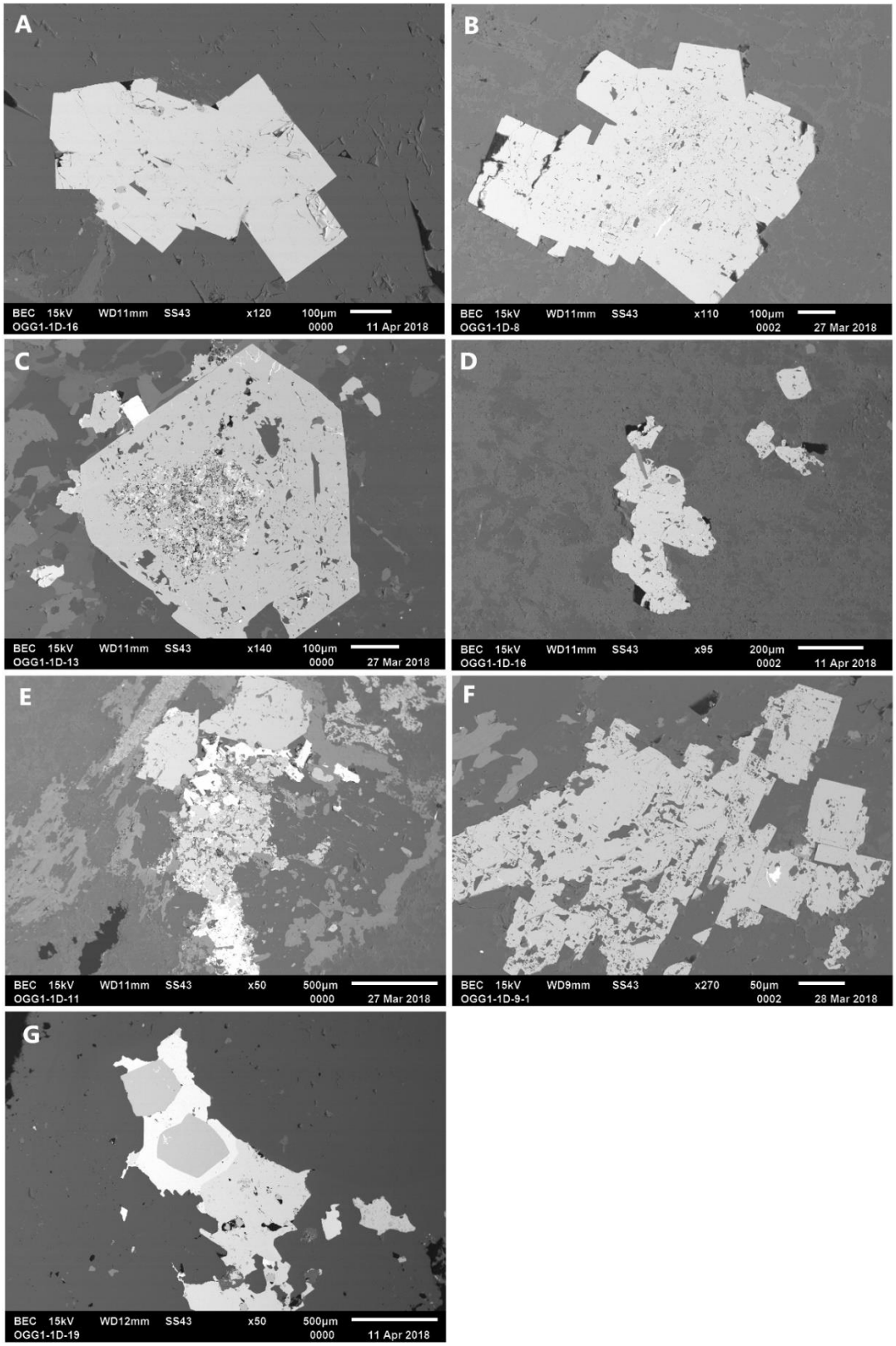

Figure 4.5. BSE photomicrographs of the different pyrite morphologies observed within Dominion Reef paleosol and overlying sandstone. A. DR-EU-1, B. DR-SUB-1, C. DR-SUB-2; observe intergrowth of pyrite and chalcopyrite (white) at core and vein-like inclusions of arsenopyrite (white) at core, D. DR-AN-1, E. DR-AN-2; observe intergrowths of arsenopyrite (white), F. DR-AN-3; observe bleb of galena within the pyrite grain, G. DR-AN-4; observe the pyrite grains, showing bleb-like inclusions of galena (white). The pyrite is encased in chalcopyrite (white), which forms an aggregate with sphalerite (light grey).

DR-AN-1 grains were irregularly-shaped anhedral, porous grains of varying sizes (~200 – 2000 μm). These grains contained randomly distributed blebs of other sulfide minerals, most commonly chalcopyrite, arsenopyrite and galena. These grains were observed within both the upper paleosol profile (samples OGG1-1D-16 and OGG1-1D-9 at depths of 290.09 - 290.12 m, respectively) and the overlying sandstone.

DR-AN-2 grains were aggregates of anhedral grains, ~500 μm in size and typically non-porous but with some large, irregularly-shaped pores present. These aggregates contained randomly-distributed, fine blebs of galena and arsenopyrite was sometimes observed to be intergrown with, or replacing, the pyrite. These grains were only observed within the paleosol profile (sample OGG1-1D-11, at a depth of 290.68 m).

DR-AN-3 grains were aggregates of anhedral, porous grains, ~400 μm in size, displaying crystallographically-aligned pores and relict grain boundaries. These aggregates were also observed to contain rare blebs of chalcopyrite and galena. These grains were only observed within the paleosol profile (sample OGG1-1D-9, at a depth of 290.15).

DR-AN-4 grains were anhedral, slightly rounded, inclusion-poor grains of pyrite within polymineralic aggregates consisting of chalcopyrite, sphalerite and galena. Pyrite grains within these aggregates were ~200 – 300 μm in diameter and contained rare blebs of galena. These grains were only observed within the overlying sandstone.

Trace element composition

A summary of the trace element composition of pyrite collected from the Dominion Reef paleosol, unaltered parent material and overlying sandstone is provided in Table 4.2. The full table of results and maps of analysis spots can be found in the Supplementary Information.

Pyrite from the three different lithological units showed overlapping ranges of all of the measured trace elements (Figure 4.6). Pyrite from the unaltered parent granite was observed to narrower ranges of trace element concentrations than pyrite from the other two units. However, this should be interpreted with caution, as trace element measurements could only be completed on one grain from the unaltered parent granite due to scarcity and size of grains.

Table 4.2. Summary of the trace element composition of pyrite grains from the Dominion Reef paleosol and underlying and overlying units.

Sample Name	Lithology	Mineral	Trace element	Min (ppm)	Max (ppm)	Median (ppm)	Mean (ppm)	StdDev (ppm)
OGG1-1D-8 (n = 13)	Altered granite	Pyrite	Co	0.390	118000	416	2330	3490
			Ni	2.06	4400	97.0	611	1200
			Cu	0.100	1610	34.0	378	588
			Zn	0.275	14.0	1.86	4.44	5.02
			As	69.9	25900	2380	3990	6880
			Co/Ni	0.017	10.6	3.20	4.08	3.30
OGG1-1D-9 (n = 14)	Altered granite	Pyrite	Co	1.21	1210	15.0	187	387
			Ni	1.71	567	8.35	119	175
			Cu	0.250	65.0	12.35	15.6	17.5
			Zn	0.215	30.6	3.80	6.00	8.18
			As	621	3080	1910	1760	869
			Co/Ni	0.075	9.85	1.17	2.38	2.98
OGG1-1D-11 (n = 7)	Altered granite	Pyrite	Co	1.54	396	40.9	101	143
			Ni	3.12	3330	25.5	556	1230
			Cu	1.12	660	32.4	150	245
			Zn	0.500	870	48.0	228	322
			As	1390	7130	1800	2510	2060
			Co/Ni	0.012	12.5	1.09	3.19	4.73
OGG1-1D-13 (n = 6)	Altered granite	Pyrite	Co	224	3230	441	958	1150
			Ni	55.2	432	66.3	143	149
			Cu	44.0	1880	125	462	720
			Zn	13.7	2160	81.5	450	845
			As	1110	13700	2310	4160	4790
			Co/Ni	0.745	18.2	6.87	8.91	7.01
OGG1-1D-15 (n = 3)	Granite	Pyrite	Co	277	665	487	476	194
			Ni	249	460	335	348	106
			Cu	17.7	39.8	20.2	25.9	12.1

Sample Name	Lithology	Mineral	Trace element	Min (ppm)	Max (ppm)	Median (ppm)	Mean (ppm)	StdDev (ppm)
			Zn	2.94	6.20	3.65	4.26	1.71
			As	1060	1570	1230	1290	262
			Co/Ni	2.67	6.31	3.15	4.04	1.97
OGG1-1D-16 (n = 12)	Altered granite	Pyrite	Co	1.67	2460	299	735	954
			Ni	15.9	1400	298	468	457
			Cu	0.300	13300	87.4	2520	4220
			Zn	13.7	2160	81.5	450	845
			As	1110	13700	2310	4155	4790
			Co/Ni	0.008	6.08	0.630	1.51	1.90
OGG1-1D-17 (n = 11)	Sandstone	Pyrite	Co	0.018	27.5	0.800	4.81	8.31
			Ni	0.870	875	95.0	181	255
			Cu	0.036	1.07	0.080	0.245	0.314
			Zn	0.175	1.60	0.355	0.475	0.417
			As	2.90	7180	2710	2884	2310
			Co/Ni	0.001	0.099	0.021	0.023	0.027
OGG1-1D-18 (n = 4)	Sandstone	Pyrite	Co	27.0	521	67.5	171	234
			Ni	7.80	34.5	15.8	18.5	11.9
			Cu	7.60	1060	114	324	500
			Zn	2.48	330	58.2	112	154
			As	67.4	1590	299	564	701
			Co/Ni	1.34	45.3	5.86	14.6	20.9
OGG1-1D-19 (n = 6)	Sandstone	Pyrite	Co	71.2	579	375	361	231
			Ni	21.9	748	358	362	312
			Cu	0.105	450	5.95	78.7	182
			Zn	0.220	240	41.2	74.1	95.8
			As	56.7	4800	2090	2260	2350
			Co/Ni	0.735	3.25	1.24	1.57	0.939

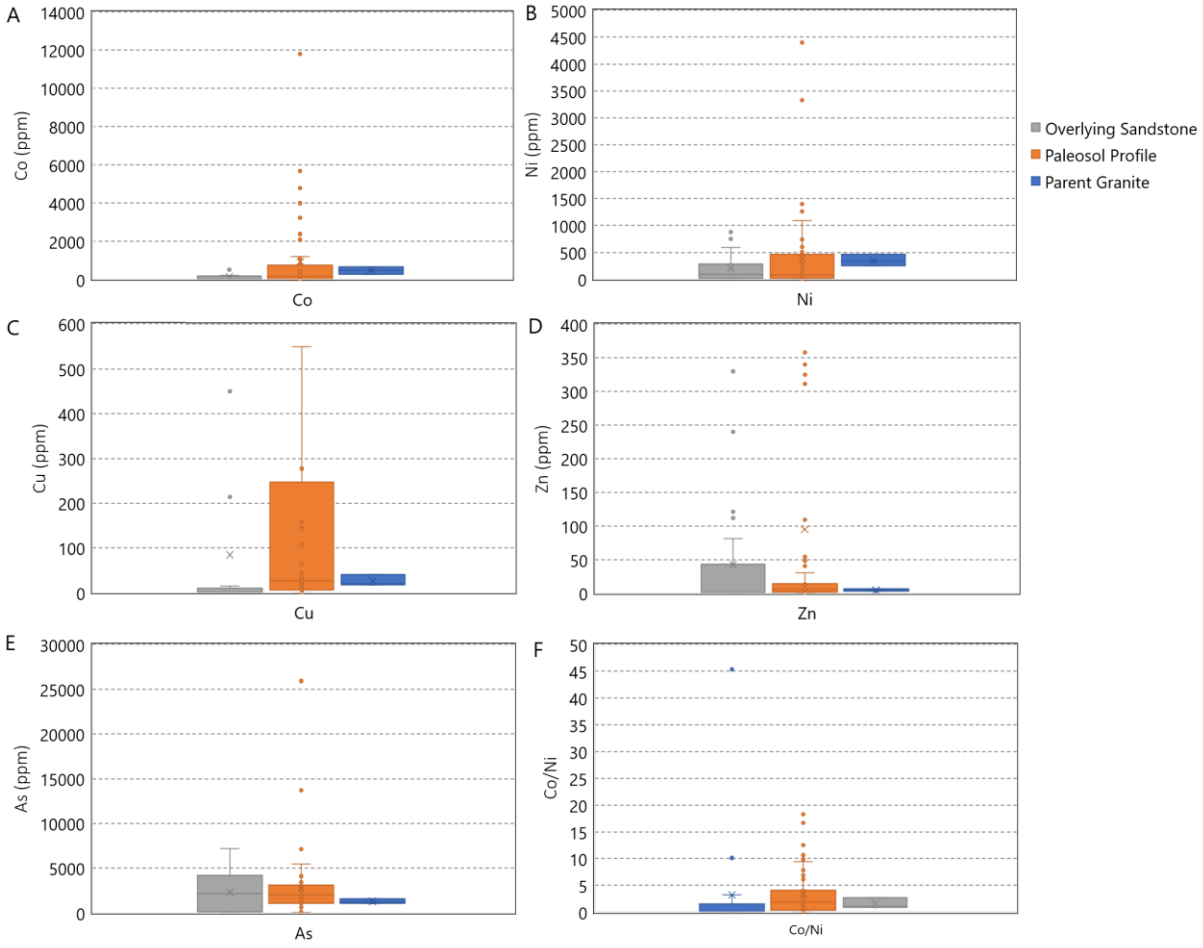

Figure 4.6. Box and whisker plots comparing the trace element concentrations and Co/Ni ratios of pyrite from the unaltered parent granite, the Dominion Reef paleosol profile and the overlying sandstone of the Renosterspruit Formation. A. Co concentrations, B. Ni concentrations, C. Cu concentrations, D. Zn concentrations, E. As concentrations, F. Co/Ni ratios.

Pyrite grains from the unaltered parent granite returned a range in Co concentrations of 277 – 665 ppm, with a median of 487 ppm (*M* = 476 ± 194 ppm, 1 *SD*, *n*=*3*). Ni concentrations showed a range of 249 – 460 ppm, median of 335 ppm (*M* = 348 ± 106 ppm, 1 *SD*, *n* =*3*). Cu concentrations ranged between 17.7 – 39.8 ppm, with a median of 20.2 ppm (*M* = 25.9 ± 12.1 ppm, 1 *SD*, *n* = *3*). Zn concentrations showed a range of 2.94 – 6.20 ppm, median of 3.65 ppm (*M* = 4.26 ± 1.71 ppm, 1 *SD*, *n* = *3*). As concentrations returned a range of 1060 – 1570 ppm, with a median of 1230 ppm (*M* = 1285 ± 262 ppm, 1 *SD*, *n* = *3*). Co/Ni values varied between 0.826 – 2.67, with a median of 1.06 (*M* = 1.52 ± 1.00, 1 *SD*, *n* = *3*). All measurements were made on DR-SUB-1 grains.

Grains from the paleosol profile returned a range in Co concentrations of 0.390 – 11800 ppm, with a median of 152 ppm (*M* = 927 ± 2000 ppm, 1 *SD*, *n* = *52*). Ni concentrations had a range of 1.71 – 4400 ppm, with a median of 83.0 ppm (*M* = 384 ± 786 ppm, 1 *SD*, *n* = *52*). Cu concentrations showed a range of 0.100 – 1060 ppm, with a median of 26.0 ppm (*M* = 755 ± 2230 ppm, 1 *SD*, *n* = 52). Zn concentrations ranged between 0.215 – 2160 ppm, with a median of 5.50 ppm (*M* = 94.8 ± 326 ppm, 1 *SD*, *n* = *52*). As concentrations had a range of 69.9 – 25900 ppm, with a median of 2020 ppm (*M* = 2790 ± 3930 ppm, 1 *SD*, *n* = *52*). Co/Ni values had a range of 0.008 – 18.2, with a median value of 1.83 (*M* = 3.47 ± 4.23, 1 *SD*, *n* = *52*). The different morphologies of pyrite grains measured within the paleosol profile typically displayed overlapping trace elements compositions, however, some morphologies could be distinguished from others on the basis of the concentrations of certain elements (Figure 4.7).

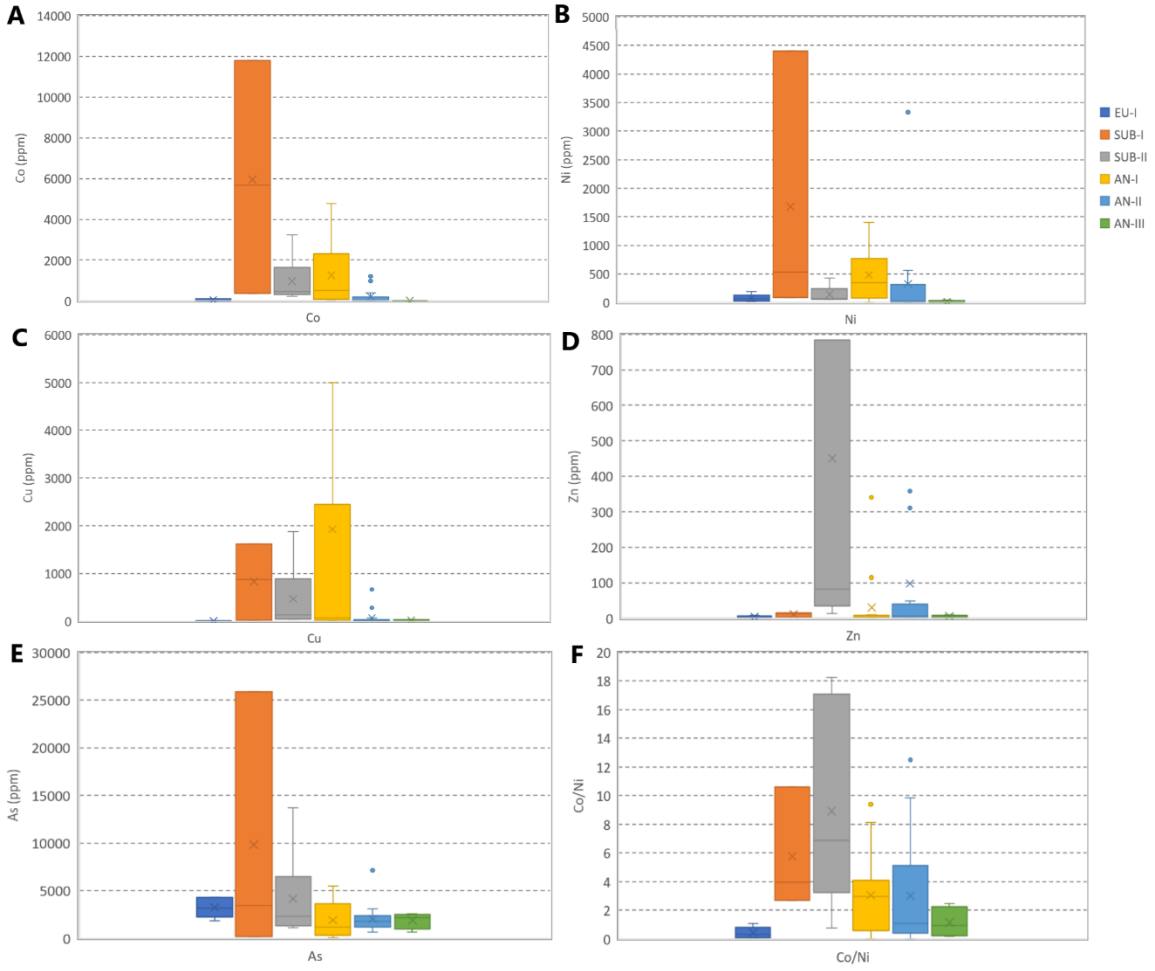

Figure 4.7. Box and whisker plots of the trace element compositions and Co/Ni ratios of the different grain morphologies observed in samples from the Dominion Reef paleosol profile. A. Co concentrations, B. Ni concentrations, C. Cu concentrations, D. Zn concentrations, E. As concentrations, F. Co/Ni ratios.

Pyrite from the overlying sandstone returned a range in Co concentrations of 0.018 – 579 ppm, with a median concentration of 27.0 ppm (*M* = 138 ± 216 ppm, 1 *SD*, *n = 21*). Ni concentrations showed a range of 0.870 – 875 ppm, with a median of 27.0 ppm (*M* = 202 ± 267 ppm, 1 *SD*, *n = 21*). Cu concentrations ranged between 0.036 – 1060 ppm, with a median of 0.480 ppm (*M* = 84.3 ± 247 ppm, 1 *SD*, *n = 21*). Zn concentrations showed a range of 0.175 – 330 ppm, with a median of 0.730 ppm (*M* = 42.8 ± 89.9 ppm, 1 *SD*). As concentrations ranged between 2.90 – 7180 ppm, with a median of 2140 ppm (*M* = 2260 ± 2220 ppm, 1 *SD*, *n = 21*). Co/Ni values showed a range of $8.61*10^{-4}$ – 45.3 ppm, with a median value of 1.06 (*M* = 1.52 ± 1.00, 1 *SD*, *n = 21*).

Within the sandstone samples, the three different pyrite morphologies (DR-SUB-1, DR-AN-1 and DR-AN-4) all showed distinct ranges of Co/Ni values by which they could be identified: DR-SUB-1 returned Co/Ni values of 10.1 – 45.3, DR-AN-1 grains returned Co/Ni values of $8.61*10^{-4}$ – 1.63 and DR-AN-4 grains returned Co/Ni values of 0.735 – 3.25 (Figure 4.8). Additionally, the different morphologies could also be distinguished on the basis of Co, Ni, Cu and Zn concentrations (Figure 4.8).

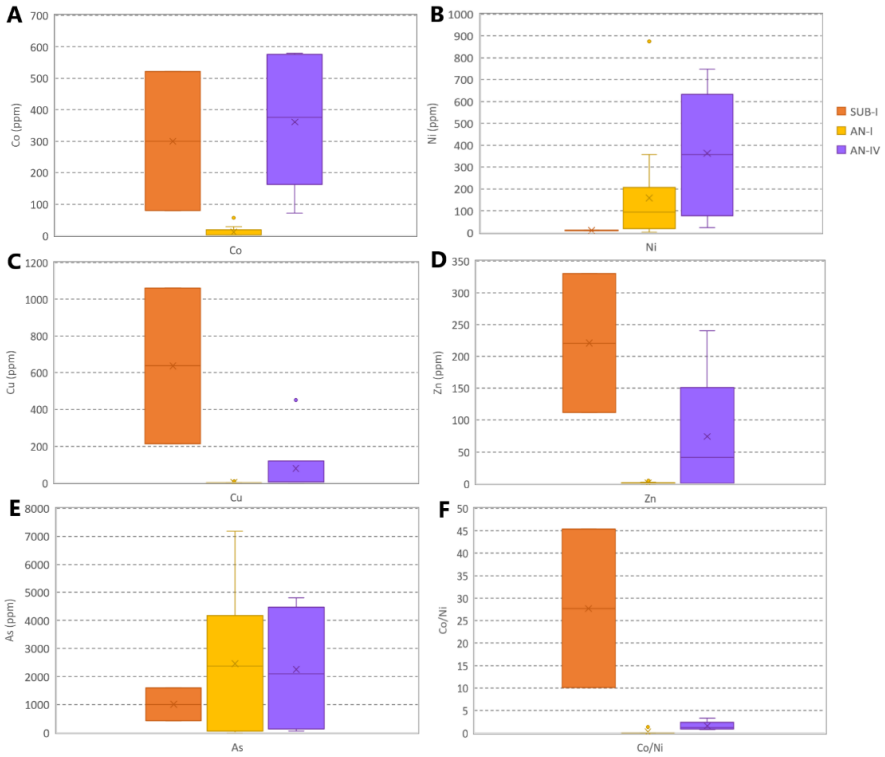

Figure 4.8. Box and whisker plots of the trace element compositions and Co/Ni ratios of the different pyrite morphologies observed in the sandstone overlying the Dominion Reef paleosol. A. Co concentrations, B. Ni concentrations, C. Cu concentrations, D. Zn concentrations, E. As concentrations, F. Co/Ni ratios.

Crown Lava paleosol

Morphology and textural features

Pyrrhotite was the dominant sulfide mineral observed within Crown Lava samples, with lesser pyrite and chalcopyrite. Paleosol samples were typically poor in sulfide minerals, with sulfide mineral abundance increasing slightly in the upper samples.

Two distinct morphologies of pyrrhotite and three distinct morphologies of pyrite were observed and will be referred to as CRNL-Po-1, CRNL-Po-2, CRNL-Py-1, CRNL-Py-2 and CRNL-Py-3. BSE images of these morphologies are provided in Figure 4.9.

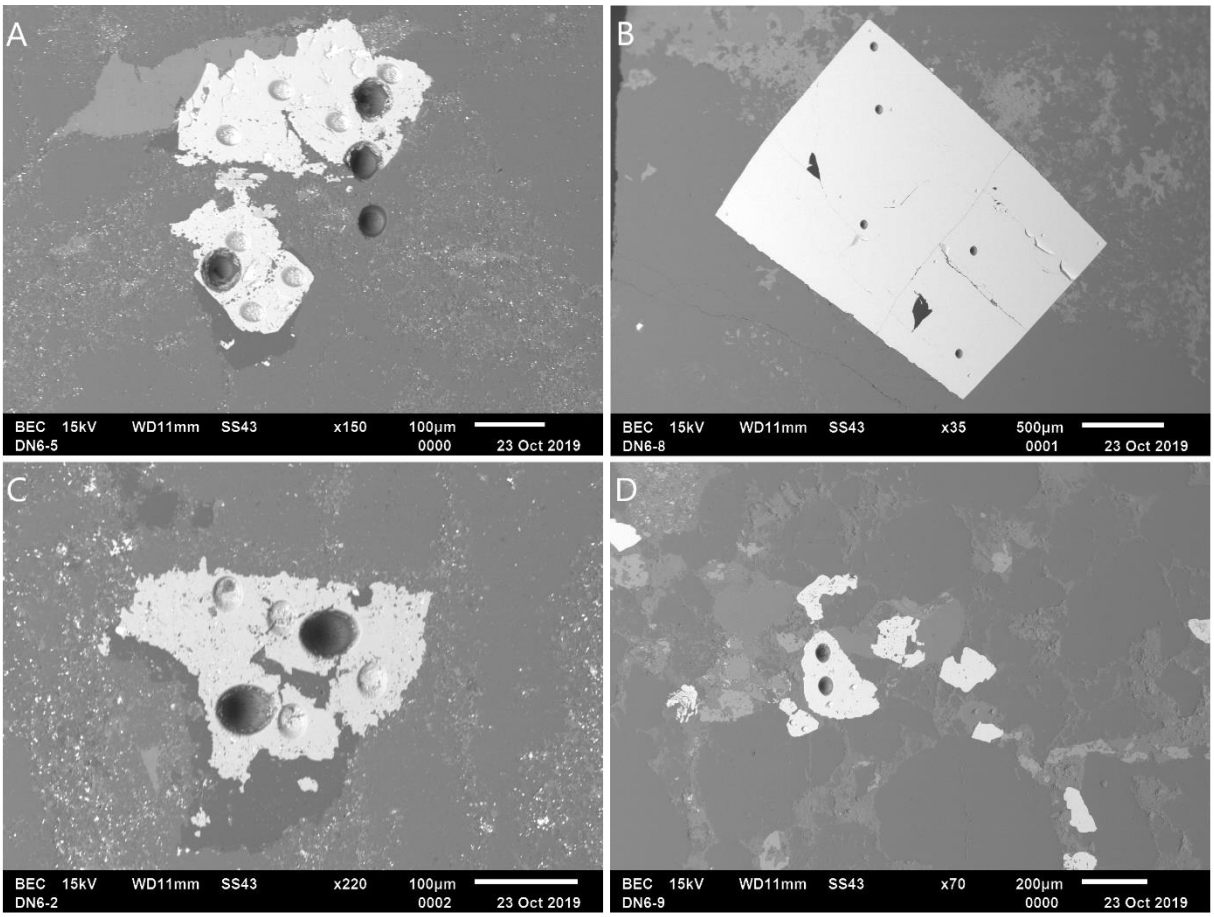

Figure 4.9. BSE photomicrographs of the different sulfide mineral morphologies observed within the Crown Lava paleosol and underlying and overlying units. A. CRNL-Po-1, B. CRNL-Py-1, C. CRNL-Py-2, CRNL-Py-3. Large spots are from LA-ICP-MS analysis, smaller spots are from SHRIMP analysis.

CRNL-Po-1 grains were anhedral, porous grains of pyrrhotite observed within the matrix of paleosol samples. These grains were ~500 – 1000 µm in size and contained blebs of chalcopyrite and pyrite.

CRNL-Po-2 grains were anhedral grains of pyrrhotite located within veinlets in the paleosol samples. These grains were ~300 – 500 µm in size contained blebs and elongate inclusions of chalcopyrite.

CRNL-Py-1 grains were euhedral, non-porous grains of pyrite found within paleosol samples and were ~1500 µm in size.

CRNL-Py-2 grains were irregularly-shaped, anhedral, porous grains of pyrite, ~200 – 500 µm in size, observed within paleosol samples.

CRNL-Py-3 grains were anhedral, typically rounded grains of pyrite observed within the underlying sandstones of the Babrasco Formation and overlying sandstones of the Roodepoort Formation. Grains within the Babrasco Formation were typically porous and those within the Roodepoort Formation were typically non-porous. Within both formations, grains were ~100 – 200 µm in size.

Trace element composition

A summary of the trace element composition of sulfide minerals from the Crown Lava paleosol and overlying and underlying units is provided in Table 4.3. The complete data set and maps of the analysis spots are provided in the Supplementary Information.

Pyrite from the three different lithological units typically showed overlapping ranges of trace element concentrations (Figure 4.10). However, pyrite from the underlying sandstone showed a wider range of Cu concentrations which extended to higher values than observed for pyrite from the paleosol profile and overlying sandstone (Figure 4.10). Similarly, pyrite from the paleosol profile showed a wider range of zinc concentrations and Co/Ni values, where both extended to higher values than observed for pyrite from the overlying and underlying sandstones (Figure 4.10).

Table 4.3. Summary of the trace element composition of sulfide minerals from the Crown Lava paleosol and overlying and underlying sandstones.

Sample Name	Lithology	Mineral	Trace element	Min (ppm)	Max (ppm)	Median (ppm)	Mean (ppm)	StdDev (ppm)
DN6-1 (n=2)	Quartzite	Pyrite	Co	267	990	629	629	511
			Ni	189	3180	1690	1690	2110
			Cu	3.73	420	212	212	294
			Zn	1.06	12.0	6.53	6.53	7.74
			As	860	1950	1400	1400	771
			Co/Ni	0.084	5.24	2.66	2.66	3.64
DN6-2 (n = 5)	Altered basalt	Pyrrhotite	Co	177	1400	394	660	524
			Ni	2930	6950	3250	4350	1770
			Cu	0.536	6.76	1.37	2.35	2.58
			Zn	0.00	469	0.00	93.9	210
			As	0.00	108	0.00	22.1	48.3
			Co/Ni	0.054	0.202	0.134	0.135	0.061
DN6-2 (n = 2)	Altered basalt	Pyrite	Co	281	2500	1390	1390	1570
			Ni	64.0	9730	4900	4900	6830
			Cu	36.6	321	179	179	201
			Zn	3.53	125	64.3	64.3	85.9
			As	47.7	136	91.9	91.9	62.4
			Co/Ni	0.26	4.39	2.32	2.32	2.92
DN6-3 (n = 3)	Altered basalt	Pyrrhotite	Co	209	415	300	308	103
			Ni	2720	3410	2970	3040	352
			Cu	0.911	7.90	5.62	4.81	3.56
			Zn	0.295	0.455	0.335	0.362	0.084
			As	0.00	710	0.00	237	410
			Co/Ni	0.077	0.122	0.101	0.100	0.022
DN6-4 (n = 4)	Altered basalt	Pyrrhotite	Co	163	566	339	352	172
			Ni	1450	3700	2930	2750	960
			Cu	0.844	28.12	2.13	8.31	13.22
			Zn	0.00	1.65	0.273	0.548	0.749
			As	3.32	408	9.41	108	201
			Co/Ni	0.052	0.392	0.112	0.167	0.155
DN6-5 (n = 1)	Altered basalt	Pyrrhotite	Co	29000	-	-	-	-
			Ni	518	-	-	-	-
			Cu	683	-	-	-	-
			Zn	11.9	-	-	-	-

Sample Name	Lithology	Mineral	Trace element	Min (ppm)	Max (ppm)	Median (ppm)	Mean (ppm)	StdDev (ppm)
			As	169	-	-	-	-
			Co/Ni	0.268	-	-	-	-
DN6-6 (n = 5)	Altered basalt	Pyrrhotite	Co	123	937	386	472	300
			Ni	3480	7900	3790	4710	1850
			Cu	1.70	4690	99.1	983	2070
			Zn	0.00	17.7	1.69	5.05	7.32
			As	1.07	88.4	70.0	52.8	35.1
			Co/Ni	0.035	0.119	0.105	0.095	0.034
DN6-7 (n= 5)	Altered basalt	Pyrite	Co	0.332	402	113	145	164
			Ni	0.920	4.30	2.71	2.66	1.48
			Cu	0.108	1.48	0.143	0.577	0.782
			Zn	0.094	7.79	3.94	3.94	5.44
			As	1000	2230	2070	1880	500
			Co/Ni	17.4	93.5	56.4	55.9	31.1
DN6-7 (n = 1)	Altered basalt	Pyrrhotite	Co	41.6	-	-	-	-
			Ni	1.89	-	-	-	-
			Cu	0.870	-	-	-	-
			Zn	0.00	-	-	-	-
			As	2330	-	-	-	-
			Co/Ni	22.6	-	-	-	-
DN6-8	Quartzite	Pyrite	Co	23.1	1300	571	616	644
			Ni	40.5	1210	310	468	518
			Cu	139	4570	590	1470	2080
			Zn	153	3860	605	1310	1720
			As	1.09	10.4	5.45	5.60	4.46
			Co/Ni	10.3	1130	507	539	556

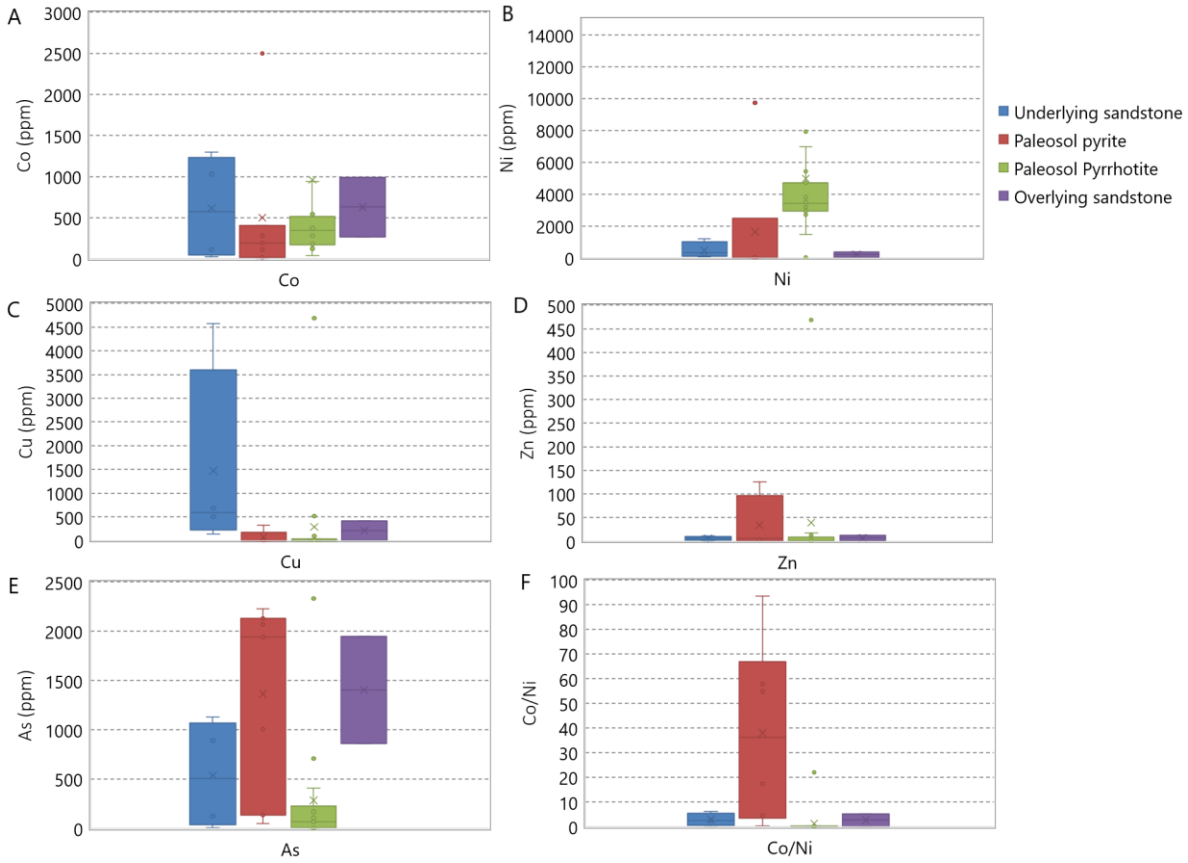

Figure 4.10. Box and whisker plots comparing the trace element concentrations and Co/Ni values of the pyrite and pyrrhotite from the underlying sandstones of the Babrasco Formation, the Crown Lava paleosol and overlying sandstones of the Roodepoort Formation. A. Co, B. Ni, C. Cu, D. Zn, E. As, F. Co/Ni values.

Pyrite from the underlying sandstone returned Co concentrations of 23.1 – 1300 ppm, with a median of 570.5 ppm (*M* = 616 ± 644 ppm, 1 *SD*, *n* = 4). Ni concentrations showed a range of 40.5 – 1210 ppm, with a median of 310 ppm (*M* = 468 ± 518 ppm, 1 *SD*, *n* = 4). Cu concentrations showed a range of 139 – 4570 ppm, with a median of 590 ppm (*M* = 1470 ± 2080 ppm, 1 *SD*, *n* = 4). Zn concentrations ranged between 1.09 – 10.4 ppm, with a median of 5.45 ppm (*M* = 5.60 ± 4.46 ppm, 1 *SD*, *n* = 4). As concentrations had a range of 10.3 – 1130 ppm, with a median of 507 ppm (*M* = 539 ± 556 ppm, 1 *SD*, *n* = 4). Co/Ni varied between 0.019 – 6.25, with a median value of 2.62 (*M* = 2.88 ± 2.56, 1 *SD*, *n* = 4).

Pyrrhotite from the paleosol profile returned Co concentrations of 41.6 – 7790 ppm, with a median of 386 ppm (*M* = 833 ± 1720 ppm, 1 *SD*, *n = 19*). Ni concentrations had a range of 1.89 – 29100 ppm, with a median of 3410 ppm (*M* = 4970 ± 6090 ppm, 1 *SD*, *n = 19*). Cu concentrations showed a range of 0.536 – 4690 ppm, with a median of 2.41 ppm (*M* = 289 ± 1070 ppm, 1 *SD*, *n = 19*). Zn concentrations had a range of 0.163 – 469 ppm, with a median value of 0.777 ppm (*M* = 39.2 ± 129 ppm, 1 *SD*, *n = 14*). As concentrations ranged from 1.07 – 2330 ppm, with a median of 70.4 ppm (*M* = 287 ± 621 ppm, 1 *SD*, *n = 14*). Matrix-hosted pyrrhotite (CRNL-Po-1) was observed to contain higher concentrations of Cu and As than vein-hosted pyrrhotite (CRNL-Po-2) (Figure 4.11).

Pyrite within the paleosol returned Co concentrations of 0.332 – 2500 ppm, with a median of 194 ppm (*M* = 501 ± 893 ppm, 1 *SD*, *n = 7*). Ni concentrations showed a range of 0.920 – 9730 ppm, with a median of 3.83 ppm (*M* = 1630 ± 3870 ppm, 1 *SD*, *n* = 6). Cu concentrations had a range of 0.108 – 321 ppm, with a median of 1.48 ppm (*M* = 71.9 ± 140 ppm, 1 *SD*, *n* = 5). Zn concentrations had a range of 0.094 – 125 ppm, with a median of 5.66 ppm (*M* = 34.1 ± 60.7 ppm, *n = 4*). As concentrations showed a range of 47.7 – 2230 ppm, with a median of 1940 ppm (*M* = 1370 ± 961 ppm, 1 *SD*, *n* = 7). Co/Ni values ranged between 0.257 – 93.5 ppm, with a median value of 36.1 ppm (*M* = 38.0 ± 36.7 ppm, 1 *SD*, *n = 6*). It was observed that CRNL-Py-1 showed lower concentrations of Co, Ni and Cu, higher concentrations of As and higher Co/Ni values than CRNL-Py-2 (Figure 4.11).

Two measurements made on pyrite from the overlying sandstone returned Co concentrations of 267 ppm and 990 ppm, Ni concentrations of 189 ppm and 3180 ppm, Cu concentrations of 3.73 ppm and 420 ppm, Zn concentrations of 1.06 ppm and 12.0 ppm and As concentrations of 860 ppm and 1950 ppm. Co/Ni values were 0.084 and 5.24.

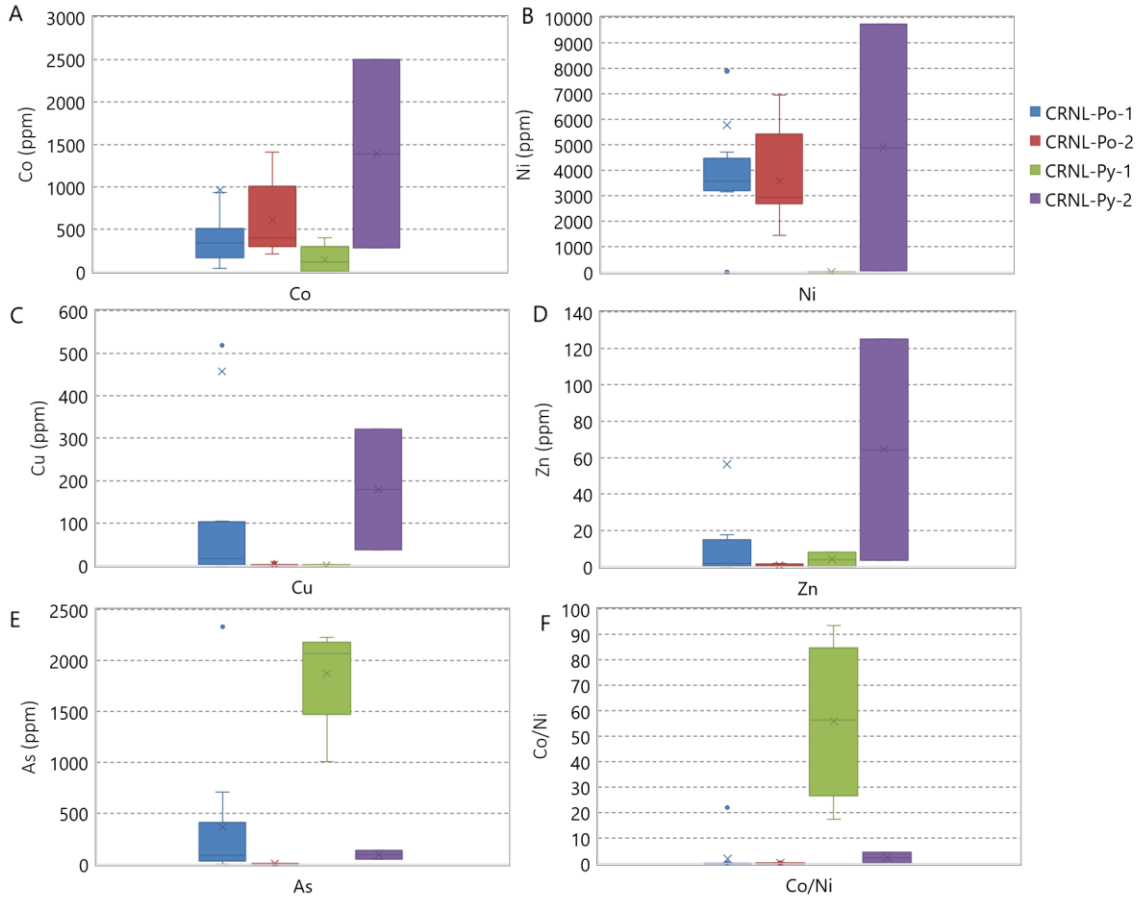

Figure 4.11. Box and whisker plots of the trace element composition and Co/Ni ratios of sulfide minerals from the Crown Lava paleosol. A. Co concentrations, B. Ni concentrations, C. Cu concentrations, D. Zn concentrations, E. As concentrations, F. Co/Ni values.

Bird Lava paleosol

Morphology and textural features

Pyrite was the dominant sulfide mineral observed within the Bird Lava paleosol, with chalcopyrite, arsenopyrite, Ni-Co-sulfides and Ni-sulfides being less abundant. Samples of unaltered parent material contained very few to no sulfide minerals. Sulfide mineral abundance through the paleosol profile was variable but typically low. The highest abundance was observed in the lowermost paleosol sample and in those samples collected from 15 – 35 cm below the upper contact (Table 4.1).

Five distinct morphologies of pyrite were observed and will be referred to as BL-AN-1, BL-AN-2, BL-AN-3, BL-AN-4 and BL-AN-5. BSE photomicrographs of these morphologies are provided in Figure 4.12.

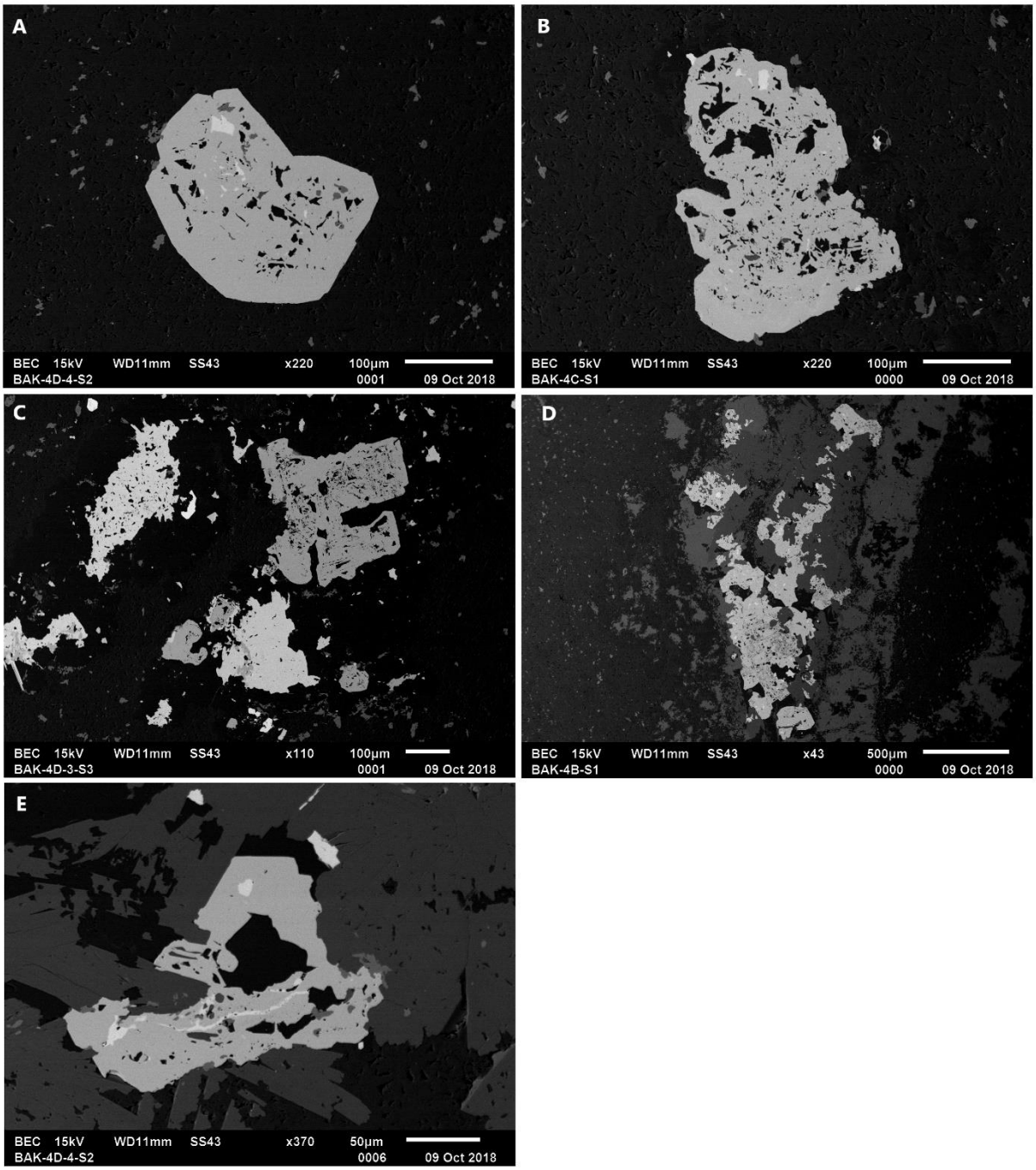

Figure 4.12. BSE photomicrographs of the different morphologies of pyrite observed within the Bird Lava paleosol. A. BL-AN-1; observe inclusions of Ni-sulfide and Ni-Co sulfide minerals (white), B. BL-AN-2; observe inclusions of Ti-oxide (white), C. BL-AN-3, D. BL-AN-4. E. BL-AN-5; observe inclusions of chalcopyrite and Ni-sulfide minerals (light grey).

BL-AN-1, BL-AN-2 and BL-AN-3 grains were found within the matrix of the paleosol samples. BL-AN-1 grains were anhedral, sometimes slightly rounded, porous and ~100 – 300 µm in diameter. These grains contained irregularly-shaped inclusions of Ni- and Ni-Co sulfides and chalcopyrite. BL-AN-2 grains were irregularly-shaped, anhedral, porous and

~100 – 200 µm in diameter. They contained irregularly-shaped inclusions of Ti-oxide. BL-AN-3 grains were ~200 µm in diameter, anhedral and had crystallographically-aligned pores.

BL-AN-4 and BL-AN-5 grains were found within veinlets within the paleosol samples. BL-AN-4 grains were anhedral, porous grains and were ~100 – 500 µm in diameter. Pores were occasionally observed to be crystallographically-aligned. Inclusions consisted of irregular, or vein-like inclusions of chalcopyrite and Ni- and Ni-Co sulfides. BL-AN-5 grains were anhedral, ~50-100 µm and displayed poorly-defined grain boundaries. These grains contained elongate, vein-like inclusions of chalcopyrite and Ni-sulfide and irregularly-shaped inclusions of matrix-material and the surrounding veinlet material.

Trace element composition

A summary of the trace element composition of pyrite from the Bird Lava paleosol is provided in Table 4.4. The complete data set and maps of analysis spots are provided in the Supplementary Information.

Pyrite within the bird lava paleosol showed a range in Co concentrations of 57.7 – 45900 ppm, with a median of 3800 ppm (M = 7200 ± 10100 ppm, 1 SD, n = 21). Ni concentrations had a range of 2260 – 124000 ppm, median of 6110 ppm (M = 13000 ± 26200 ppm, 1 SD, n = 3). Cu concentrations ranged between 20.1 – 37700 ppm, with a median of 850 ppm (M = 6270 ± 9990 ppm, 1 SD, n = 21). Zn concentrations showed a range of 1.11 – 148 ppm, with a median of 2.40 ppm (M = 27.3 ± 42.1 ppm, 1 SD, n = 21). As concentrations had a range of 10.1 – 13200 ppm, median of 1180 ppm (M = 1630 ± 2740 ppm, 1 SD, n = 21). Co/Ni values showed a range of 0.008 – 20.3, with a median value of 0.460 (M = 1.67 ± 4.35, 1 SD, n = 21).

Matrix hosted pyrite (BL-AN-1, BL-AN-2, BL-AN-3) and veinlet-hosted pyrite (BL-AN-4, BL-AN-5) were observed to show similar trace element compositions, except BL-AN-5 grains were observed to show elevated concentrations of Co, and Zn in comparison to both matrix-hosted and vein-hosted grains (Figure 4.13). When each morphology was considered separately, the trace element compositions typically overlapped, with the exception of the elevated concentrations of certain elements in BL-AN-5 grains previously mentioned.

Table 4.4. Summary of the trace element composition of pyrite grains from the Bird Lava paleosol.

Sample Name	Lithology	Mineral	Trace element	Min (ppm)	Max (ppm)	Median (ppm)	Mean (ppm)	StdDev (ppm)
BAK-4B	Altered basalt	Pyrite	Co	258	10400	309	3660	5840
			Ni	2910	5080	3920	3970	1090
			Cu	143	8600	920	3220	4670
			Zn	19.7	34.2	27.7	27.2	7.26
			As	10.1	26.8	24.4	20.4	9.03
			Co/Ni	0.051	3.57	0.079	1.23	2.03
BAK-4C	Altered basalt	Pyrite	Co	8900	45900	10500	21800	20900
			Ni	2260	10200	9510	7320	4400
			Cu	189	1480	210	626	739
			Zn	1.21	2.03	1.28	1.51	0.455
			As	1220	13200	1680	5380	6810
			Co/Ni	0.936	20.3	1.03	7.43	11.2
BAK-4D-2	Altered basalt	Pyrite	Co	2200	-	-	-	-
			Ni	14700	-	-	-	-
			Cu	14700	-	-	-	-
			Zn	32.8	-	-	-	-
			As	1590	-	-	-	-
			Co/Ni	0.150	-	-	-	-
BAK-4D-3	Altered basalt	Pyrite	Co	1470	11600	1510	5420	5390
			Ni	3710	124000	4520	30100	52600
			Cu	214	37700	395	11000	16500
			Zn	1.22	122	3.80	40.3	55.1
			As	1110	2200	1730	1690	425
			Co/Ni	0.09	0.782	0.335	0.389	0.249
BAK-4D-4	Altered basalt	Pyrite	Co	57.7	18200	3380	4790	5250
			Ni	4420	32000	6390	8960	8220
			Cu	20.1	21500	1730	6530	8400
			Zn	1.11	148	2.34	28.6	47.5
			As	19.4	1700	906	962	481
			Co/Ni	0.008	1.94	0.507	0.711	0.676

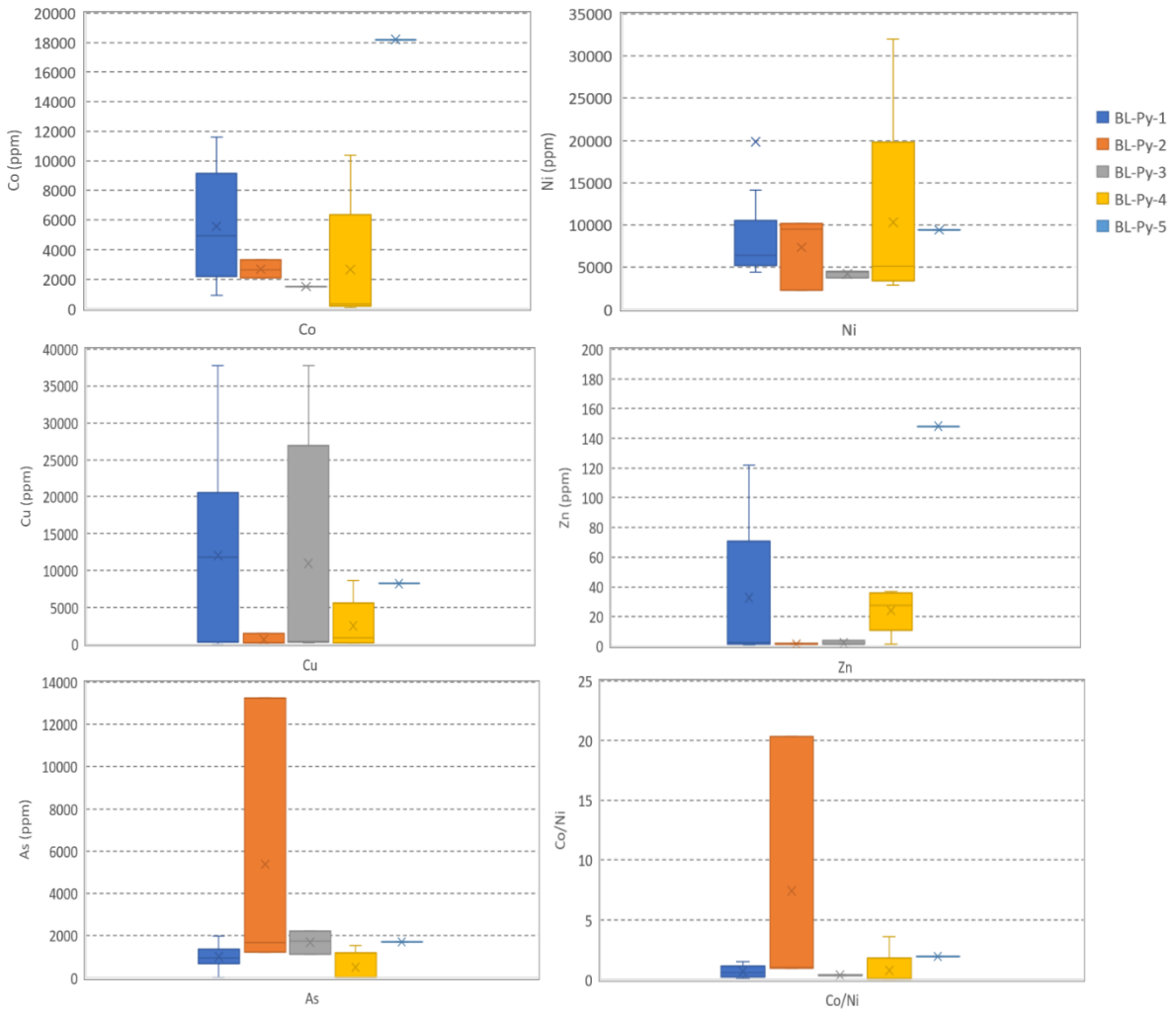

Figure 4.13. Box and whisker plots comparing the trace element composition and Co/Ni ratios of the different morphologies of pyrite grains observed within the Bird Lava paleosol. A. Co concentrations, B. Ni concentrations, C. Cu concentrations, D. Zn concentrations, E. As concentrations, F. Co/Ni ratios.

Cooper Lake paleosol

Morphology and textural features

Pyrite was the only sulfide mineral observed within the Cooper Lake paleosol and the unaltered parent diabase. The parent material was observed to be pyrite poor, with only two grains observed. Whilst still pyrite poor, the paleosol profile had higher abundance than the parent material.

Two morphologies of pyrite were observed within the paleosol profile, referred to as CPL-AN-1 and CPL-AN-2, and two morphologies were observed within the parent diabase: CPL-AN-3 and CPL-EU-1. BSE photomicrographs of these grains are provided in Figure 4.14.

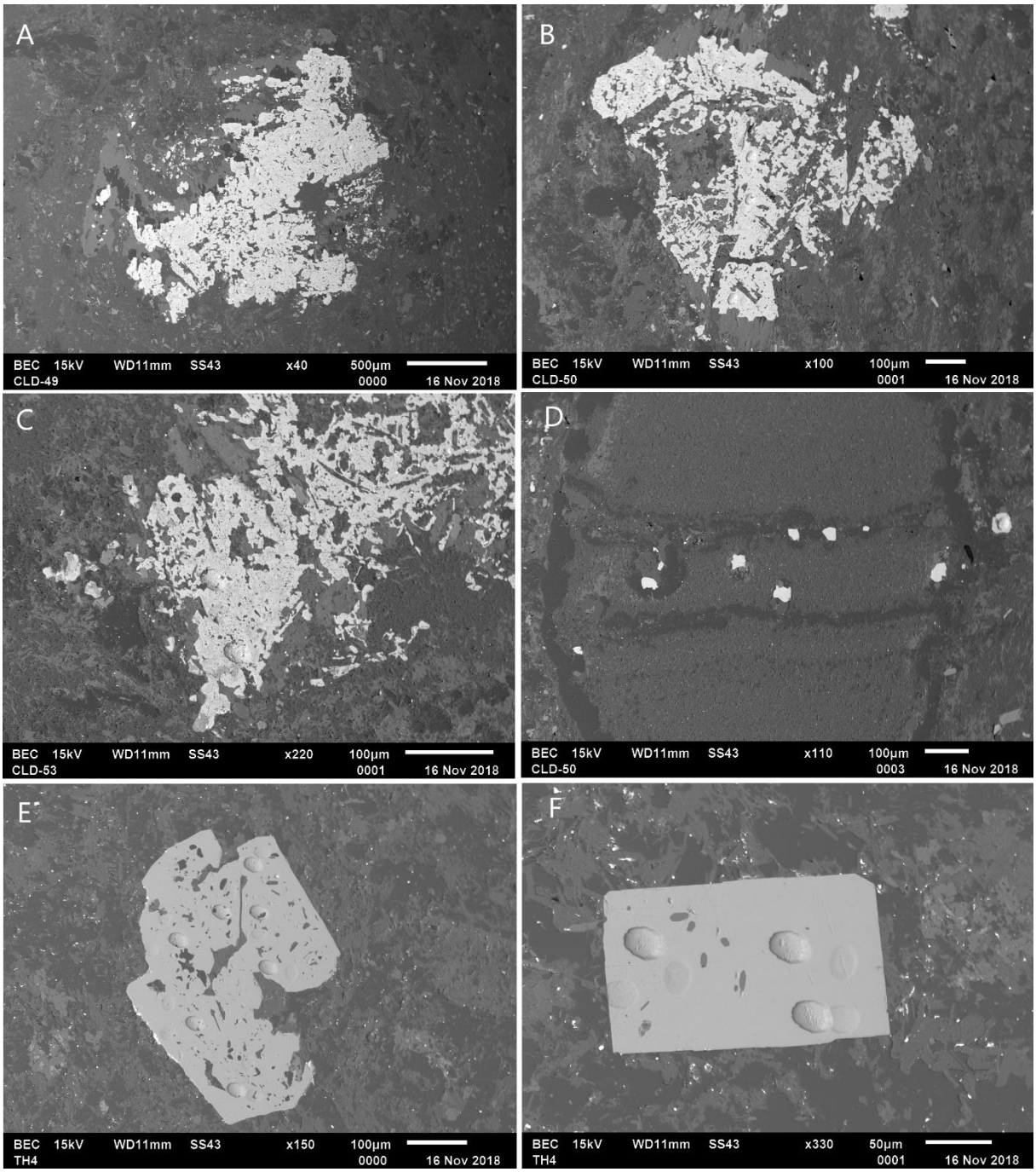

Figure 4.14. BSE photomicrographs of the different morphologies of pyrite grains observed within the Cooper Lake paleosol and parent material. A. CPL-EU-1, B. CPL-AN-1, C. CPL-AN-1, D. CPL-AN-2, E. CPL-AN-3, F. CPL-EU-1.

CPL-AN-1 grains were aggregates of anhedral, highly porous grains where the aggregates ranged in size from ~500 – 2000 µm. CPL-AN-2 grains were fine (~10 – 50 µm), irregularly-shaped, anhedral and inclusion-free. CPL-AN-3 grains were anhedral, ~500 µm in size and had large, irregularly-shaped and randomly-oriented pores. CPL-EU-1 grains were ~50 – 100 µm in size, euhedral and contained very few large pores, similar to those observed in CPL-AN-3.

Trace element composition

A summary of the trace element composition of pyrite from the Bird Lava paleosol is provided in Table 4.5. The complete data set and maps of analysis spots are provided in the Supplementary Information.

Within the parent diabase, the two pyrite morphologies (CPL-AN-3 and CPL-EU-1) returned distinct trace element compositions (Figure 4.15). However, only a small number of analyses could be completed due to fine grain size and scarcity of sulfide grains; the results should be interpreted with some caution. CPL-AN-3 grains returned Co concentrations of 1170 – 5190 ppm, median of 1230 ppm (M = 2530 ± 2300 ppm, 1 *SD*, n = 3), Ni concentrations of 940 – 1740 ppm, median of 1410 ppm (M = 1360 ± 402 ppm, 1 *SD*, n = 3), Cu concentrations of 1.69 – 2.75 ppm, median of 2.43 ppm (M = 2.29 ± 0.544. 1 *SD*, n = 3), Zn concentrations of 8.10 – 27.50 ppm, median of 9.20 ppm (M = 14.9 ± 10.9 ppm, *1* SD, n = 3) and As concentrations of 895 – 2050 ppm, median of 1760 ppm (M = 1570 ± 601 ppm, 1 *SD*, n = 3). Co/Ni values had a range of 0.672 – 5.52, median of 0.672 (M = 2.36 ± 2.74, 1 *SD*, n = 3). CPL-EU-1 grains showed Co concentrations of 35100 ppm and 36900 ppm, Ni concentrations of 57.8 and 58.6 ppm, Cu concentrations of 0.085 – 0.450 ppm, Zn concentrations of 0.720 – 1.03 ppm and As concentrations of 14200 ppm and 15100 ppm. Co/Ni values were 607 and 630.

Within the altered diabase, CPL-AN-2 grains were too fine to be analyzed and, therefore, all analyses were completed on CPL-AN-1 grains. These grains showed similar Co, Zn and As concentrations to CPL-AN-3 grains from the parent diabase but could be distinguished by lower Ni concentrations, higher Cu concentrations and higher Co/Ni values (Figure 4.15). No similarities were observed between CPL-AN-1 and CPL-EU-1 grains. Co concentrations had a range of 1210 – 13200 ppm, with a median of 4830 ppm (M = 5680 ± 2850 ppm, 1 *SD*, n = 24). Ni concentrations showed a range of 95.3 – 1050 ppm, median of 214 ppm (M = 271 ± 204 ppm, 1 *SD*, n = 24). Cu concentrations had a range of 89.3 – 30100 ppm, median of 444 ppm (M = 3120 ± 7760 ppm, 1 *SD*, n = 24). Zn concentrations showed a range of 3.26 – 46.4 ppm, with a median of 9.85 ppm (M = 12.8 ± 9.79 ppm, 1 *SD*, n = 24). As concentrations returned a range of 161 – 2240 ppm, median of 691 ppm (M = 780 ± 475 ppm, 1 *SD*, n = 24). Co/Ni values varied from 5.21 – 87.1, with a median value of 20.4 (M = 26.6 ± 18.7 ppm, n = 24).

Table 4.5. Summary of the trace element composition of pyrite grains from the Cooper Lake paleosol and unaltered parent material.

Sample Name	Lithology	Mineral	Trace element	Min (ppm)	Max (ppm)	Median (ppm)	Mean (ppm)	StdDev (ppm)
CLD-49 (n = 11)	Altered diabase	Pyrite	Co	3080	8300	5990	5670	1800
			Ni	95.3	307	195	184	62.2
			Cu	89.3	443	227	241	106
			Zn	3.26	16.3	8.00	8.39	4.11
			As	186	979	551	569	253
			Co/Ni	10.3	87.1	29.2	37.1	23.3
CLD-53 (n = 9)	Altered diabase	Pyrite	Co	1210	5480	4280	3850	1330
			Ni	132	300	217	219	61.2
			Cu	456	30100	1550	7700	11600
			Zn	5.40	46.4	13.0	16.4	12.7
			As	161	1200	760	722	318
			Co/Ni	5.21	24.7	18.3	18.2	5.68
CLD-50 (n = 4)	Altered diabase	Pyrite	Co	5240	13200	10400	9810	3760
			Ni	391	1050	529	625	304
			Cu	401	1370	627	756	448
			Zn	8.20	32.7	12.6	16.5	11.1
			As	721	2240	1500	1490	636
			Co/Ni	12.5	21.1	16.1	16.5	4.59
TH4	Diabase	Pyrite	Co	1170	36900	5190	15900	18400
			Ni	57.8	1740	940	841	769
			Cu	0.085	2.75	1.69	1.48	1.18
			Zn	0.720	27.5	8.10	9.31	10.9
			As	895	15100	2050	6800	7190
			Co/Ni	0.672	630	5.52	249	338

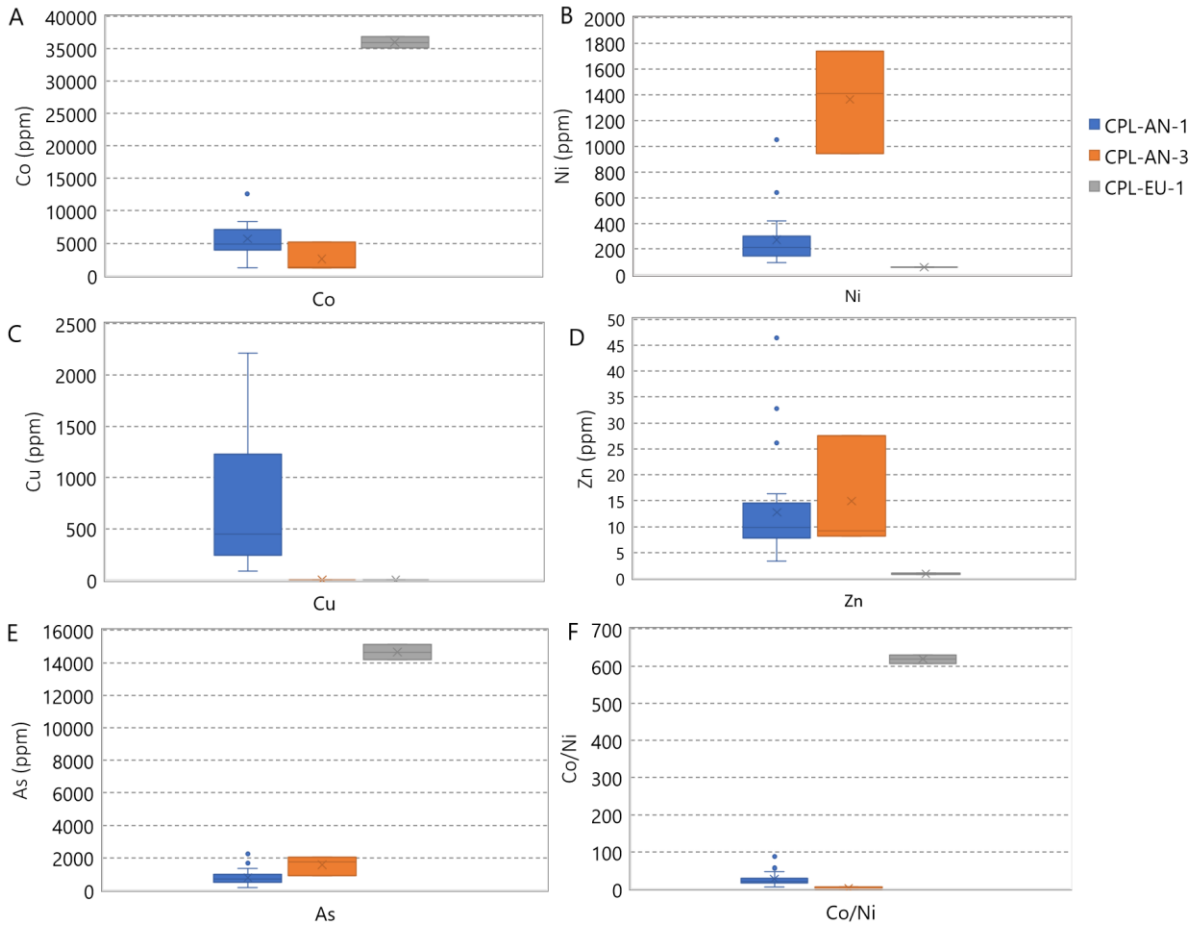

Figure 4.15. Box and whisker plots comparing the trace element compositions and Co/Ni ratios of the different morphologies of pyrite observed within the Cooper Lake paleosol and unaltered parent material. A. Co concentrations, B. Ni concentrations, C. Cu concentrations, D. Zn concentrations, E. As concentrations, F. Co/Ni ratios.

Sulfur isotope composition

A summary of the sulfur isotope results for sulfide minerals from each paleosol profile are presented in Table 4.6. The complete data set and maps of analysis spots are provided in the Supplementary Information.

Dominion Reef paleosol

Two measurements completed on pyrite from the unaltered parent granite returned $\delta^{34}S$ values of -1.33 ‰ and 1.75 ‰, $\Delta^{33}S$ values of -0.14 ‰ and -0.11 ‰ and $\Delta^{36}S$ values of -0.07 ‰ and 0.06 ‰ (Figure 4.16, 4.17).

Table 4.6. Summary of the sulfur isotope composition of pyrite from the Dominion Reef, Crown Lava, Bird Lava and Cooper Lake paleosols, unaltered parent materials and overlying and underlying units.

Sample Name	Lithology	Isotope ratio	Min (‰)	Max (‰)	Median (‰)	Mean (‰)	StdDev (‰)
			Dominion Reef Paleosol				
OGG1-1D-8 (n = 15)	Altered granite	$\delta^{34}S$	-4.80	1.14	-1.33	-0.50	1.90
		$\Delta^{33}S$	-0.20	-0.03	-0.12	-0.11	0.06
		$\Delta^{36}S$	-0.30	0.12	-0.09	-0.08	0.14
OGG1-1D-9 (n = 4)	Altered granite	$\delta^{34}S$	-0.60	0.84	-0.57	-0.22	0.71
		$\Delta^{33}S$	-0.20	-0.06	-0.09	-0.11	0.06
		$\Delta^{36}S$	-0.20	-0.06	-0.11	-0.12	0.06
OGG1-1D-11 (n = 11)	Altered granite	$\delta^{34}S$	1.19	6.00	2.81	3.13	1.87
		$\Delta^{33}S$	-0.01	0.18	0.12	0.09	0.08
		$\Delta^{36}S$	-0.59	-0.15	-0.35	-0.38	0.14
OGG1-1D-13 (n = 10)	Altered granite	$\delta^{34}S$	-7.48	1.40	-2.78	-2.55	2.64
		$\Delta^{33}S$	-0.15	0.02	-0.06	-0.07	0.06
		$\Delta^{36}S$	-0.31	0.25	-0.16	-0.12	0.15
OGG1-1D-15 (n = 2)	Granite	$\delta^{34}S$	-1.33	1.75	0.21	0.21	2.17
		$\Delta^{33}S$	-0.14	-0.11	-0.12	-0.12	0.02
		$\Delta^{36}S$	-0.07	0.06	0.00	0.00	0.10
OGG1-1D-16 (n = 14)	Altered granite	$\delta^{34}S$	-6.04	0.48	-0.53	-1.50	2.17
		$\Delta^{33}S$	-0.26	0.01	-0.13	-0.13	0.07
		$\Delta^{36}S$	-0.50	0.19	-0.13	-0.16	0.20
OGG1-1D-17 (n = 15)	Sandstone	$\delta^{34}S$	-2.67	1.02	-0.46	-0.44	0.99
		$\Delta^{33}S$	-0.25	-0.06	-0.12	-0.14	0.06
		$\Delta^{36}S$	-0.29	0.31	0.05	0.01	0.18
OGG1-1D-18 (n = 10)	Sandstone	$\delta^{34}S$	1.19	6.00	2.81	3.13	1.87
		$\Delta^{33}S$	-0.01	0.18	0.12	0.09	0.08

Sample Name	Lithology	Isotope ratio	Min (‰)	Max (‰)	Median (‰)	Mean (‰)	StdDev (‰)
OGG1-1D-18	Sandstone	$\Delta^{36}S$	-0.59	-0.15	-0.35	-0.38	0.14
OGG1-1D-19 (n = 9)	Sandstone	$\delta^{34}S$	-1.95	1.33	-0.45	-0.66	0.96
		$\Delta^{33}S$	-0.27	-0.14	-0.21	-0.20	0.05
		$\Delta^{36}S$	-0.83	0.12	-0.23	-0.31	0.34
			Crown Lava Paleosol				
DN6-1 (n = 11)	Quartzite	$\delta^{34}S$	1.67	15.73	2.63	5.72	5.15
		$\Delta^{33}S$	-0.15	0.09	-0.01	-0.01	0.07
		$\Delta^{36}S$	-0.46	0.32	-0.21	-0.14	0.22
DN6-2 pyrite (n = 5)	Altered basalt	$\delta^{34}S$	1.26	2.76	1.91	1.97	0.54
		$\Delta^{33}S$	-0.06	0.00	-0.02	-0.03	0.02
		$\Delta^{36}S$	-0.38	-0.02	-0.25	-0.24	0.14
DN6-2 pyrrhotite (11)	Altered basalt	$\delta^{34}S$	0.60	2.06	1.22	1.25	0.52
		$\Delta^{33}S$	-0.13	-0.02	-0.06	-0.08	0.04
		$\Delta^{36}S$	-0.85	-0.25	-0.51	-0.52	0.16
DN6-3 (n = 8)	Altered basalt	$\delta^{34}S$	0.24	2.06	1.12	1.23	0.56
		$\Delta^{33}S$	-0.14	-0.06	-0.11	-0.10	0.03
		$\Delta^{36}S$	-0.76	-0.25	-0.42	-0.45	0.16
DN6-4 (n = 18)	Altered basalt	$\delta^{34}S$	-0.03	4.06	1.97	2.03	0.78
		$\Delta^{33}S$	-0.14	0.00	-0.09	-0.09	0.04
		$\Delta^{36}S$	-0.67	0.08	-0.31	-0.30	0.21
DN6-5 (n = 7)	Altered basalt	$\delta^{34}S$	-0.35	1.88	0.83	0.84	0.69
		$\Delta^{33}S$	-0.14	-0.05	-0.07	-0.08	0.03
		$\Delta^{36}S$	-0.70	-0.31	-0.49	-0.52	0.14
DN6-6 (n = 9)	Altered basalt	$\delta^{34}S$	-0.61	1.55	0.99	0.69	0.90
		$\Delta^{33}S$	-0.12	0.05	-0.07	-0.05	0.06
		$\Delta^{36}S$	-0.99	-0.24	-0.49	-0.48	0.23
DN6-7 pyrite	Altered basalt	$\delta^{34}S$	1.95	2.84	2.20	2.31	0.31

Sample Name	Lithology	Isotope ratio	Min (‰)	Max (‰)	Median (‰)	Mean (‰)	StdDev (‰)
DN6-7 pyrite (n = 10)	Altered basalt	$\Delta^{33}S$	-0.27	-0.07	-0.17	-0.18	0.07
		$\Delta^{36}S$	-0.75	-0.13	-0.24	-0.31	0.18
DN6-7 pyrrhotite (n = 7)	Altered basalt	$\delta^{34}S$	1.84	6.87	4.24	4.25	1.47
		$\Delta^{33}S$	-0.13	0.00	-0.05	-0.05	0.04
		$\Delta^{36}S$	-0.65	-0.05	-0.32	-0.30	0.20
DN6-8 (n = 8)	Quartzite	$\delta^{34}S$	-4.71	5.87	2.61	1.58	3.95
		$\Delta^{33}S$	-0.26	-0.19	-0.23	-0.23	0.02
		$\Delta^{36}S$	-0.58	0.10	-0.18	-0.21	0.23
			Bird Lava Paleosol				
BAK-4D-2 (n = 2)	Altered basalt	$\delta^{34}S$	-3.33	-3.03	-	-	-
		$\Delta^{33}S$	-0.22	0.15	-	-	-
		$\Delta^{36}S$	-0.50	0.01	-	-	-
BAK-4D-3 (n = 9)	Altered basalt	$\delta^{34}S$	-7.91	-0.61	-1.77	-2.70	2.48
		$\Delta^{33}S$	-0.36	-0.21	-0.29	-0.29	0.05
		$\Delta^{36}S$	-0.31	0.22	-0.01	-0.02	0.19
BAK-4D-4 (n = 19)	Altered basalt	$\delta^{34}S$	-2.97	1.51	-0.80	-0.63	1.23
		$\Delta^{33}S$	-0.40	-0.22	-0.32	-0.32	0.05
		$\Delta^{36}S$	-0.44	0.26	-0.06	-0.07	0.19
BAK-4C (n = 4)	Altered basalt	$\delta^{34}S$	-1.06	1.91	0.16	0.29	1.40
		$\Delta^{33}S$	-0.35	-0.14	-0.22	-0.23	0.11
		$\Delta^{36}S$	-0.14	0.35	0.06	0.08	0.22
BAK-4B (n = 6)	Altered basalt	$\delta^{34}S$	-0.81	2.23	0.54	0.80	1.10
		$\Delta^{33}S$	-0.50	-0.28	-0.39	-0.39	0.07
		$\Delta^{36}S$	-0.39	0.03	-0.14	-0.16	0.14
			Cooper Lake Paleosol				
CLD-49 (n = 14)	Altered diabase	$\delta^{34}S$	-7.23	3.60	-1.15	-1.54	3.49
		$\Delta^{33}S$	-0.03	0.06	0.01	0.01	0.03
		$\Delta^{36}S$	-0.85	-0.03	-0.24	-0.30	0.27
CLD-53		$\delta^{34}S$	1.41	3.39	2.36	2.29	0.74

Sample Name	Lithology	Isotope ratio	Min (‰)	Max (‰)	Median (‰)	Mean (‰)	StdDev (‰)
CLD-53 (n = 10)	Altered diabase	$\Delta^{33}S$	0.03	0.14	0.11	0.10	0.03
		$\Delta^{36}S$	-0.53	0.51	0.08	-0.01	0.34
CLD-50 (n = 13)	Altered diabase	$\delta^{34}S$	-2.82	2.12	0.48	0.31	1.17
		$\Delta^{33}S$	-0.06	0.17	0.06	0.05	0.06
		$\Delta^{36}S$	-0.79	0.40	-0.24	-0.26	0.36
TH4 (n = 10)	Diabase	$\delta^{34}S$	-1.47	-0.33	-0.75	-0.80	0.33
		$\Delta^{33}S$	-0.03	0.06	0.01	0.01	0.03
		$\Delta^{36}S$	-1.13	0.21	-0.20	-0.30	0.40

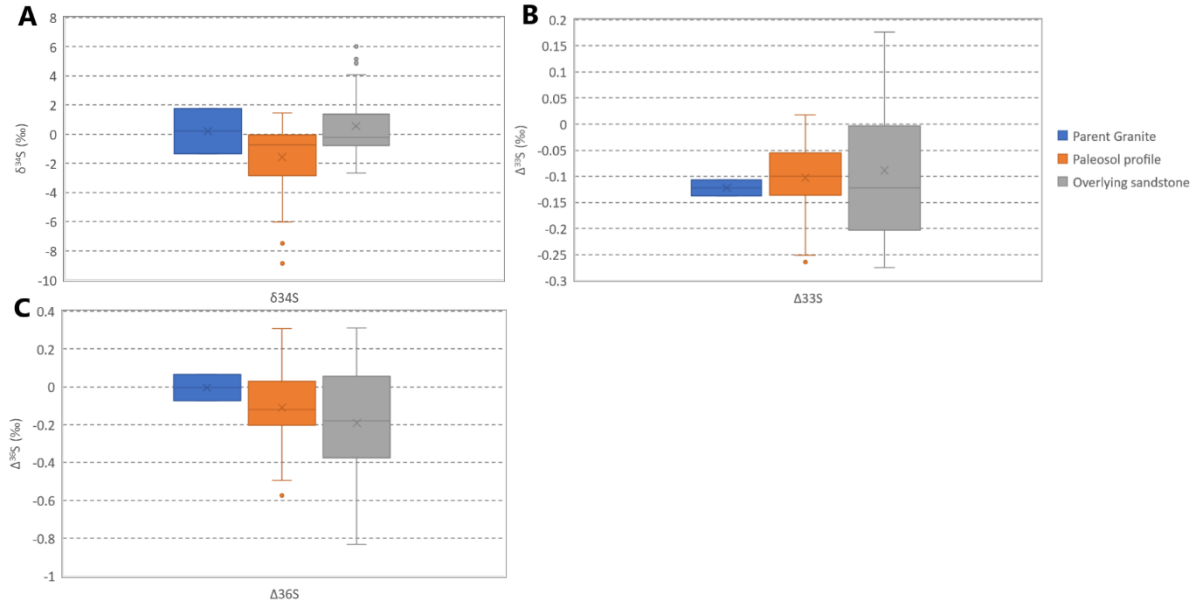

Figure 4.16. Box and whisker plots comparing the sulfur isotope compositions of pyrite grains from the Dominion Reef paleosol, unaltered parent material and overlying sandstone. A. $\delta^{34}S$, B. $\Delta^{33}S$, C. $\Delta^{36}S$.

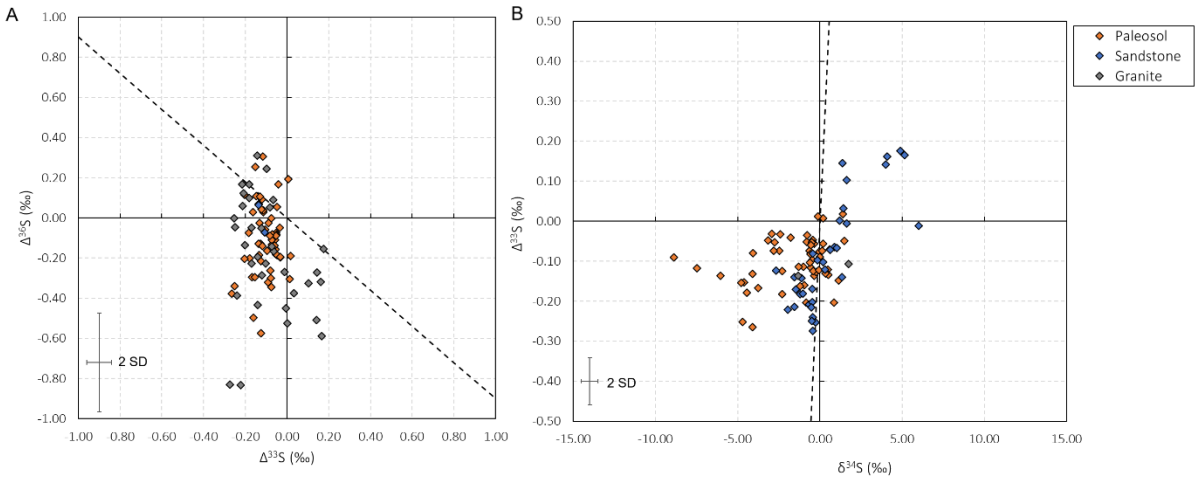

Figure 4.17. Isotopic composition of pyrite from the Dominion Reef paleosol, unaltered parent material and overlying unit. A. $\Delta^{36}S$ vs. $\Delta^{33}S$, B. $\Delta^{33}S$ vs. $\delta^{34}S$. The black dashed lines represent the ARA.

Fifty-four measurements completed on pyrite from the paleosol profile returned $\delta^{34}S$ values of -8.88 – 1.48 ‰ with a median of -0.721 ‰ (*M* = -1.58 ± 2.23 ‰, 1 *SD*). The $\Delta^{33}S$ values showed a range of -0.265 – 0.018 ‰, with a median of -0.100 ‰ (*M* = -0.103 ± 0.060 ‰, 1 *SD*) and the $\Delta^{36}S$ values returned a range of -0.574 – 0.305 ‰, with a median of -0.119 ‰ (*M* = -0.110 ± 0.178 ‰, 1 *SD*) (Figure 4.16, 4.17).

Thirty-four measurements completed on pyrite hosted the overlying sandstone showed a range in $\delta^{34}S$ of -2.67 – 6.00 ‰, with a median of -0.207 ‰ (*M* = 0.553 ± 2.11 ‰, 1 *SD*). The $\Delta^{33}S$ values had a range of -0.275 – 0.176 ‰ and a median of -0.122 ‰ (*M* = -0.089 ± 0.135 ‰, 1 *SD*). The $\Delta^{36}S$ values showed a range of -0.832 – 0.311 ‰, with a median -0.818 ‰ (*M* = -0.191 ± 0.282 ‰, 1 *SD*) (Figure 4.16, 4.17). The different morphologies showed similar isotopic compositions.

Crown Lava paleosol

Pyrite from the overlying sandstone showed a range in $\delta^{34}S$ values of 1.67 – 15.7 ‰, with a median of 2.63 ‰ (*M* = 5.72 ± 5.15 ‰, 1 *SD*, *n* = 11). The $\Delta^{33}S$ values showed a range of -0.154 – 0.095 ‰, with a median of -0.012 ‰ (*M* = -0.007 ± 0.073 ‰, 1 *SD*, *n* = 11) and the $\Delta^{36}S$ values returned a range of -0.459 – 0.317 ‰, with a median of -0.210 ‰ (*M* = -0.139 ± 0.221 ‰, 1 *SD*, *n* = 11) (Figure 4.18, 4.19).

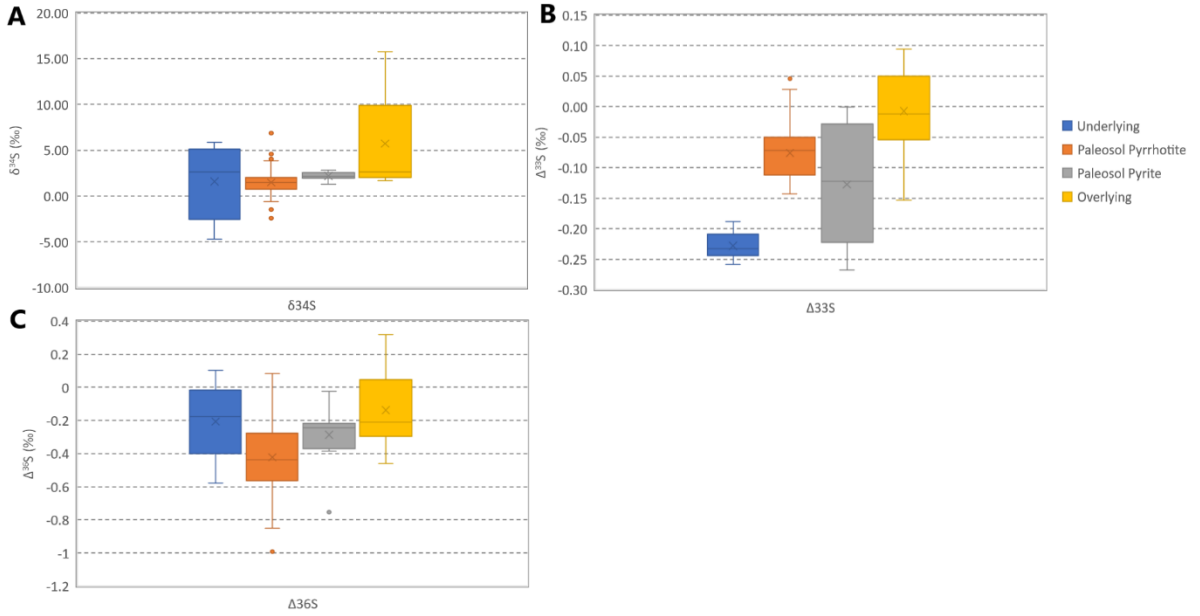

Figure 4.18. Box and whisker plots comparing the sulfur isotopic composition of sulfide minerals hosted by the Crown Lava and underlying and overlying units. A. $\delta^{34}S$, B. $\Delta^{33}S$, C. $\Delta^{36}S$.

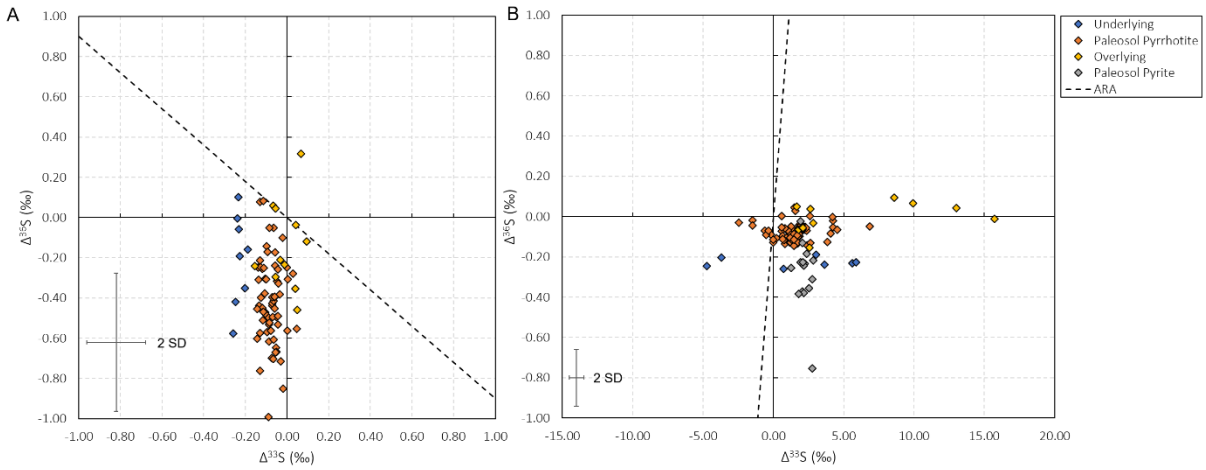

Figure 4.19. Isotopic composition of sulfide minerals from the Crown Lava paleosol and underlying and overlying units. A. $\Delta^{36}S$ vs. $\Delta^{33}S$, B. $\Delta^{33}S$ vs. $\delta^{34}S$. The black dashed lines represent the ARA.

Pyrrhotite from the paleosol profile showed a range of $\delta^{34}S$ values of -2.44 – 6.87 ‰, with a median of 1.48 ‰ (*M* = 1.51 ± 1.50 ‰, 1 *SD*, *n* = 64). The $\Delta^{33}S$ values had a range of -0.144 – 0.046 ‰, with a median of -0.074 ‰ (*M* = -0.077 ± 0.043 ‰, 1 *SD*, *n* = 64). The $\Delta^{36}S$ values had a range of -0.992 – 0.082 ‰, with a median of -0.438 ‰ (*M* = -0.420 ± 0.209 ‰, 1 *SD*, *n* = 64) (Figure 4.18, 4.19). Matrix-hosted pyrrhotite (CRNL-Po-1) and vein-hosted pyrrhotite (CRNL-Po-2) showed similar isotopic compositions.

Pyrite from the paleosol profile showed $\delta^{34}S$ values of 1.26 – 2.84 ‰, median of 2.15 ‰ (*M* = 2.20 ± 0.416 ‰, 1 *SD*, *n* = 15). The $\Delta^{33}S$ values showed a range of -0.268 – 0.000 ‰, with a

median of -0.123 ‰ (*M* = -0.128 ± 0.094 ‰, 1 *SD*, *n* = 15) and the $\Delta^{36}S$ values had a range of -0.753 - -0.023 ‰, with a median of -0.243 ‰ (*M* = -0.286 ± 0.162 ‰, 1 *SD*, *n* = 15) (Figure 4.18, 4.19). CRNL-Py-1 and CRNL-Py-2 showed similar $\delta^{34}S$ values but CRNL-Py-2 grains showed higher $\Delta^{33}S$ and lower $\Delta^{36}S$ values.

Pyrite from the underlying sandstone returned $\delta^{34}S$ values of -4.71 – 5.87 ‰, with a median value of 2.61 ‰ (*M* = 1.58 ± 3.95 ‰, 1 *SD*, *n* = 8). The $\Delta^{33}S$ values showed a range of -0.259 - -0.189 ‰, with a median of -0.232 ‰ (*M* = -0.228 ± 0.023 ‰, 1 *SD*, *n* = 8). The $\Delta^{36}S$ values had a range of -0.578 – 0.100 ‰, with a median of -0.176 ‰ (*M* = -0.208 ± 0.228 ‰, 1 *SD*, *n* = 8) (Figure 4.18, 4.19).

Bird Lava paleosol

Pyrite from the Bird Lava paleosol showed a range in $\delta^{34}S$ values of -7.91 – 2.23 ‰, with a median value of -0.804 ‰ (*M* = -0.915 ± 1.98 ‰, 1 *SD*, *n* = 40). The $\Delta^{33}S$ values had a range of -0.500 – 0.150 ‰, median of -0.311 ‰ (*M* = -0.300 ± 0.103 ‰, 1 *SD*, *n* = 40) and $\Delta^{36}S$ values had a range of -0.497 – 0.345 ‰, median of -0.058 ‰ (*M* = -0.064 ± 0.200 ‰, 1 *SD*, *n* = 40) (Figure 4.20). Matrix-hosted pyrite (BL-Py-1, BL-Py-2 and BL-Py-3) and veinlet-hosted pyrite (BL-Py-4, BL-Py-5) showed similar isotopic compositions and the different morphologies were also showed similar isotopic compositions.

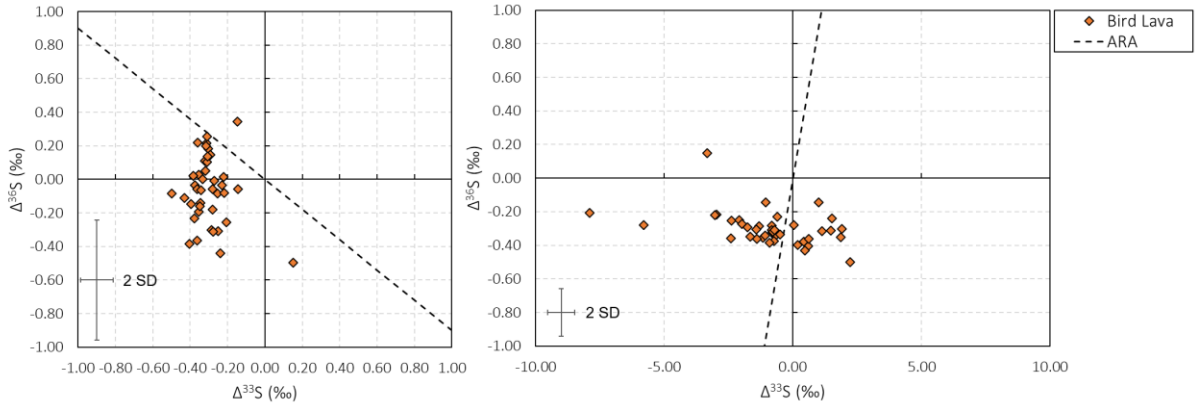

Figure 4.20. Isotopic composition of pyrite from the Bird Lava paleosol. A. $\Delta^{36}S$ vs. $\Delta^{33}S$, B. $\Delta^{33}S$ vs. $\delta^{34}S$.

Cooper Lake paleosol

Pyrite from the unaltered parent diabase displayed $\delta^{34}S$ values of -1.47 – 0.328 ‰, with a median value of -0.745 ‰ (*M* = -0.804 ± 0.331 ‰, 1 *SD*, *n* = 10), $\Delta^{33}S$ of -0.033 – 0.064 ‰, median of 0.012 ‰ (*M* = 0.006 ± 0.031 ‰, 1 *SD*, *n* = 10) and $\Delta^{36}S$ of -1.13 – 0.213 ‰, median of -0.202 ‰ (*M* = -0.300 ± 0.400 ‰, 1 *SD*, *n* = 10) (Figure 4.21, 4.22). CPL-AN-3 and CPL-EU-1 grains were observed to show similar isotopic compositions.

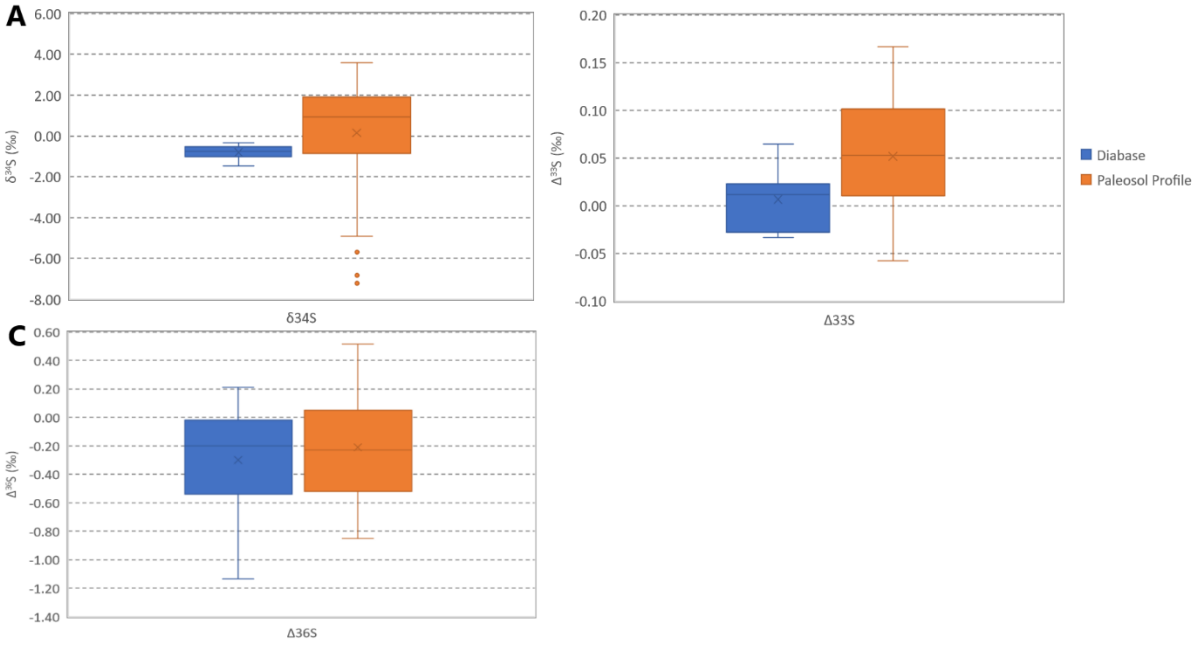

Figure 4.21. Box and whisker plots of the isotopic composition of pyrite from the Cooper Lake paleosol and unaltered parent material. A. $\delta^{34}S$, B. $\Delta^{33}S$, C. $\Delta^{36}S$.

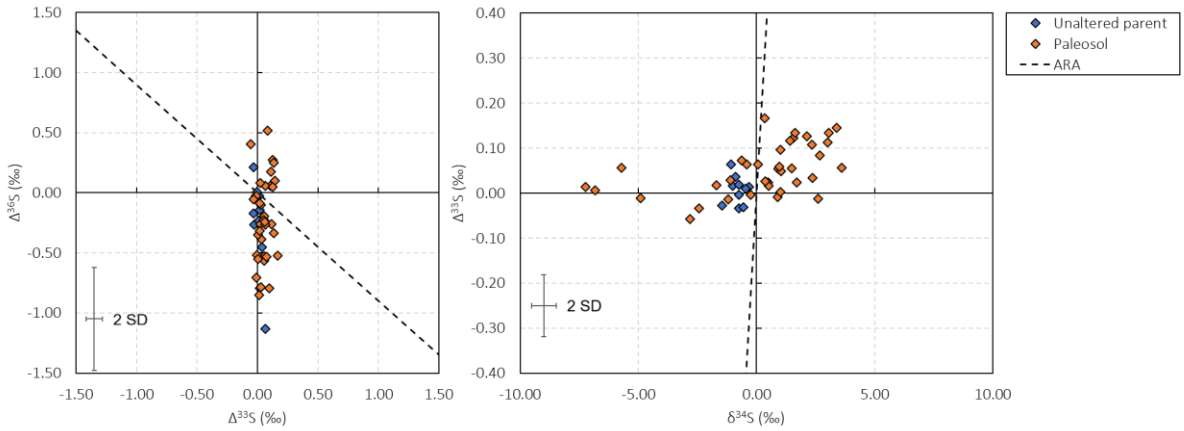

Figure 4.22. Isotopic composition of pyrite from the Cooper Lake paleosol and unaltered parent material. A. $\Delta^{36}S$ vs. $\Delta^{33}S$, B. $\Delta^{33}S$ vs. $\delta^{34}S$.

Pyrite from the paleosol profile showed similar isotopic compositions to pyrite from the parent material, however, it was observed that paleosol samples showed a wider range in $\delta^{34}S$. Pyrite grains from the paleosol profile showed $\delta^{34}S$ values of -7.23 – 3.60 ‰, median of 0.929 ‰ (M = 0.146 ± 2.72 ‰, 1 *SD*, n = 37), $\Delta^{33}S$ of -0.058 – 0.166 ‰, median of 0.053 ‰ (M = 0.052 ± 0.055 ‰, 1 *SD*, n = 37) and $\Delta^{36}S$ of -0.850 – 0.515 ‰, median of -0.228 ‰ (M = -0.211 ± 0.337 ‰, 1 *SD*, n = 37) (Figure 4.19, 4.20). CPL-AN-1 and CPL-AN-2 grains showed similar isotopic compositions (Supplementary Information).

4.6 Discussion

Sulfide paragenesis

Determining the paragenesis of paleosol-hosted sulfide minerals proved to be difficult, largely because the morphology and trace element composition of paleosol-hosted pyrite grains has not been studied before. In particular, it is uncertain what the trace element composition of diagenetic pyrite which formed inside a paleosol would be (and if and how it would have formed). Due to this, the author is reluctant to use the criteria set out from studies of diagenetic pyrite within shales and sandstones (Guy et al., 2010; Gregory et al., 2015a) to either confirm or reject that sulfide grains are diagenetic.

Additionally, there is only a limited amount of trace element data available from pyrite hosted within igneous rocks and the composition of this pyrite has been observed to be variable and controlled, at least in part, by the composition of the host rock (Hawley and Nichol, 1961; Loftus-Hills and Solomon, 1967; Price, 1972). Therefore, it is also difficult to determine whether or not the sulfide minerals within the paleosol profile represent primary igneous sulfides inherited from the respective parent materials. One course of action was to compare the trace element composition of sulfides within the parent material to that of pyrite within the paleosol profile, which would show whether or not paleosol-hosted sulfide minerals had been directly inherited from the parent materials. However, the parent materials were observed to be either sulfide mineral-poor, or completely devoid of sulfide minerals, which made this approach difficult. Therefore, the discussion of paragenesis below should be regarded as tentative.

Dominion Reef paleosol

Unaltered parent material

Pyrite grains within the unaltered parent material are proposed to be magmatic in origin. This is largely due to their location within unaltered granite, which suggests that they represent disseminated primary sulfides. There is only limited trace element data available from pyrite hosted by granites, which makes it difficult to confirm a magmatic origin. However, the low concentrations of Co and Ni, and variable but low Co/Ni values are somewhat similar to values previously obtained from granite-hosted pyrite (Figure 4.6; Loftus-Hills and Solomon, 1967).

Paleosol profile

For many of the grains within the Dominion Reef paleosol profile, paragenesis could not be conclusively determined. However, some suggestions about the timing of sulfide formation are proposed.

CR-EU-1 grains are proposed to be epigenetic in origin due to their large size and euhedral shape, both of which are frequently observed in epigenetic grains (e.g. Saager, 1970; McClay and Ellis, 1983; Craig et al., 1998; Guy et al., 2010). Epigenetic grains of similar morphology have previously been observed within the Witwatersrand Supergroup (e.g. Feather and Koen, 1975; Hirdes and Saager, 1983; Guy et al., 2010, 2014). Additionally, these grains show low concentrations of Co and Ni, which is common in epigenetic pyrite (Utter, 1978; Meyer et al., 1990; Guy et al., 2010; Koglin et al., 2010). However, this should be interpreted with caution as low concentrations of Co and Ni are also observed within granite-hosted pyrite (Loftus-Hills and Solomon, 1967). Yet, the trace element composition of these grains differs from that of grains within the unaltered parent material, suggesting that they do not represent inherited primary igneous sulfides.

DR-AN-3 grains are also proposed to be epigenetic in origin, due to the high abundance, large size and presence of crystallographically-aligned pores, all of which are conclusive with rapid growth and an epigenetic origin (Ramdohr, 1958; Saager, 1970; McClay and Ellis, 1983; Craig et al., 1998). Epigenetic grains with these features have previously been observed within the Witwatersrand Supergroup (e.g. Saager, 1970; Guy et al., 2014). These grains also show low concentrations of Co and Ni, similar to CR-EU-1 grains and have trace element compositions that are distinct from that of pyrite within the unaltered parent material.

For the rest of the morphologies, paragenesis is less clear. DR-SUB-1, DR-SUB-2, DR-AN-1 and DR-AN-2 grains may also be epigenetic due to the variability in Co and Ni concentrations and variation of Co/Ni values within single samples and even within single grains (Bralia et al., 1979). Apart from this, the morphology of these grains is inconclusive in regards to paragenesis, especially for DR-SUB-1 and DR-AN-1 grains. The presence of a distinct rim and core texture in DR-SUB-2 grains could suggest an epigenetic overgrowth but there is a lack of corresponding zonation in the isotopic and trace element composition which argues against this. Similarly, whilst the intergrowth of arsenopyrite and pyrite within DR-AN-2 grains may also suggest an epigenetic origin, it is also possible that the arsenopyrite is

replacing pre-existing pyrite. Additionally, for these grains, the trace element concentrations overlap that of the pyrite within the unaltered parent material.

Overlying sandstone

DR-AN-4 grains are interpreted to be epigenetic in origin. The co-existence of pyrite with chalcopyrite, galena and sphalerite is common in hydrothermal deposits/environments, where these minerals commonly replace the earlier formed pyrite (Saager, 1970; Edwards, 1947). Within the DR-AN-4 aggregates, this relationship can be seen as the pyrite grains maintain distinct grain boundaries (Figure 4.5G), suggesting they formed earlier than the surrounding sulfides. Additionally, the morphology of the galena inclusions within the pyrite are similar to replacement textures referred to as sub-graphic intergrowths (Edwards, 1947) which suggests that the pyrite is being replaced by galena. The relatively low Co and Ni concentrations and the observed Co/Ni values are similar to those previously obtained from epigenetic pyrite within sedimentary rocks of the Witwatersrand Supergroup (Guy et al., 2010).

Both DR-SUB-1 and DR-AN-1 grains are also interpreted to be epigenetic in origin. The morphology of these two grain types is indistinct in regards to paragenesis but the low concentrations of Co and Ni are conclusive with an epigenetic origin (Ramdohr, 1958; Saager, 1970; McClay and Ellis, 1983; Craig et al., 1998) and are similar to concentrations previously observed within epigenetic grains from the Witwatersrand Supergroup (Guy et al., 2010). DR-SUB-1 grains also show elevated Co/Ni values that are higher than previously observed for diagenetic grains within various sedimentary environments (Guy et al., 2010; Gregory et al., 2015a).

Crown Lava paleosol

Underlying quartzite

CRNL-Py-3 grains within the underlying quartzite of the Babrasco Formation were determined to be detrital in origin. These grains display rounded edges consistent with mechanical transport and are found in association with rounded grains of other heavy minerals, such as Ti-oxides, that are frequently found in detrital or placer deposits. Additionally, the inter-grain heterogeneity in trace element concentrations and $\delta^{34}S$ values is consistent with a detrital origin and likely reflects variation in the source rocks (Meyer et al., 1990; Barton and Hallbauer, 1996; England et al., 2002). The provenance of detrital grains is discussed in a later section.

Paleosol profile

Pyrite within the paleosol profile was determined to be epigenetic in origin. CRNL-Py-1 grains were determined to be epigenetic due to the large grain size and euhedral shape (Saager, 1970; McClay and Ellis, 1983; Craig et al., 1998; Guy et al., 2010). Additionally, these grains have low Co, Ni concentrations that are consistent with an epigenetic origin (Ramdohr, 1958; Saager, 1970; McClay and Ellis, 1983; Craig et al., 1998) and similar to concentrations previously observed within epigenetic grains from the Witwatersrand Supergroup (Guy et al., 2010). However, the homogeneity of the isotopic signatures in these grains (see Supplementary Information) suggests that the grains have been mobilized and recrystallized during metamorphism (Seal et al., 2006) rather than representing true hydrothermal pyrite. Such grains have previously been observed within the Witwatersrand Supergroup and referred to as 'psuedo-hydrothermal' (Saager, 1970). The origin of CRNL-Py-2 grains is less distinct, however, they are also proposed to be epigenetic due to the high intra-grain variability in Co and Ni concentrations and Co/Ni values (Bralia et al., 1979). These grains also show homogeneity in their isotopic signatures that suggests that they could be pseudo-hydrothermal.

Pyrrhotite grains within the paleosol profile are determined to represent primary igneous sulfides inherited from the parent material. Inclusions of chalcopyrite and pyrite, such as that observed within CRNL-Po-1 and CRNL-Po-2 grains are frequently observed within pyrrhotite of magmatic origin (Arnold, 1967). Additionally, the Co and Ni concentrations and Co/Ni values are similar to those previously observed for magmatic accessory pyrrhotite (Cambel and Jarkovsky, 1969). Whilst CRNL-Po-2 grains are observed within veinlets, necessitating an epigenetic origin, the similarities in the isotopic signatures between CRNL-Po-2 and CRNL-Po-1 grains implies that have been remobilized from within the paleosol profile without significant input of outside sulfur.

Overlying sandstone

Pyrite within sandstone of the overlying Roodepoort Formation is determined to be detrital in origin. Similar to the grains within the overlying Babrasco Formation, these grains are rounded and found in close association with rounded grains of other heavy minerals that are common in detrital/placer deposits. They also show similar inter-grain heterogeneity in trace element concentrations and $\delta^{34}S$ values that is consistent with a detrital origin and grains being collected from multiple sources (Meyer et al., 1990; Barton and Hallbauer, 1996; England et al., 2002).

Bird Lava paleosol

For many of the pyrite grains within the Bird Lava paleosol, paragenesis could not be conclusively determined. In regards to the matrix-hosted grains, it is suggested that BL-AN-3 grains are epigenetic origin due to the presence of crystallographically-aligned pores (Saager, 1970). BL-AN-2 grains may also be epigenetic in origin due to the variation in Co/Ni levels at a sample and even a grain level (Bralia et al., 1979). The paragenesis of BL-AN-1 grains is uncertain.

As both BL-AN-4 and BL-AN-5 grains are found within veinlets, it can be concluded that they are epigenetic in origin. The high variability in Co and Ni concentrations in BL-AN-4 grains provides further support for an epigenetic origin (Bralia et al., 1979). However, similar to the veinlet-hosted pyrrhotite in the Crown Lava paleosol profile, the similarities in the isotopic compositions of veinlet- and matrix-hosted grains suggests that the veinlet-hosted grains represent remobilized sulfur from within the profile.

Cooper Lake paleosol

Unaltered parent material

CPL-AN-3 and CPL-EU-1 grains are both found within unaltered diabase and therefore they likely represent primary igneous sulfides. Whilst the Co and Ni concentrations within these grains are dissimilar to those previously observed for pyrite in basic igneous rocks (low Ni, high or low Co; Hawley and Nichol, 1961), this does not necessarily eliminate this explanation, as the amount of available data is limited and was subsequently interpreted to represent mixing of multiple sulfur sources (Price, 1972). The morphology of these grains does not provide significant information in regards to paragenesis.

Paleosol Profile

The paragenesis of pyrite grains within the paleosol profile is uncertain. The morphology of CPL-Py-1 grains is unlike that of epigenetic grains, which are more typically euhedral and either non-porous or show crystallographically-aligned pores or are found within veins (e.g. Saager, 1970; Craig et al., 1998; Guy et al., 2010). However, Co/Ni values were observed to be high and showed high intragrain variability (Supplementary Information), arguing against a diagenetic origin (Price, 1973; Bralia et al., 1979). These grains also differ in both morphology and trace element composition from grains within the unaltered parent material, suggesting that may not represent primary igneous sulfides inherited directly from the parent material.

No trace element measurements were able to be completed on CPL-Py-2 grains due to the small grain size and the size of the analysis spot used for LA-ICP-MS analysis. The fine, anhedral, inclusion-free grains are similar in appearance to fine diagenetic grains previously observed by Guy et al. (2010), suggesting that CPL-Py-2 grains may also be diagenetic in origin.

Introduction of sulfur through hydrothermal activity

It needs to be considered whether the sulfur within these profiles is representative of the paleosol environment or if it was introduced via hydrothermal fluids. This is particularly important due to the difficulties encountered in determining the paragenesis of the sulfide grains analyzed within this study. Here, two possibilities are considered: (1) that the profiles were formed through hydrothermal activity and are not actually paleosols; (2) that sulfur was introduced into the profiles through later hydrothermal activity.

Formation of the profiles through hydrothermal activity

The first possibility that needs to be considered is that the analyzed paleosol profiles do not in fact represent weathering but were formed through hydrothermal activity. In this scenario, all of the pyrite observed within these profiles would be epigenetic in origin. This situation is considered unlikely based on a wealth of previous research.

With the exception of the Crown Lava paleosol, Rye and Holland (1998) compiled the results of previous studies and determined that all of the analyzed profiles sufficiently fulfilled the criteria for being identified as a paleosol: the unit formed on a homogenous parent material and was preserved in place; the unit exhibits unidirectional changes in mineralogy, texture and chemical composition consistent with soil forming processes; there are identifiable soft-sediment deformation features along the contract between the unit and the overlying material. Maynard et al. (2013) later determined that the Crown Lava paleosol also sufficiently fulfilled these criteria. Additionally, Sutton et al. (1990) analyzed the bulk chemistry of a number of Witwatersrand profiles and found that alteration was asymmetric and extended unidirectionally from stratigraphic and structural features. Hydrothermal alteration associated with faulting and preferential flow of fluids along conglomerate layers was found to have played only a minimal role, if any, in producing the paleosol profiles. In terms of the Cooper Lake paleosol, detailed chemical, mineralogical and textural studies have shown that the alteration within this profile is also consistent with weathering and inconsistent with hydrothermal activity (Bennet, 1990; Sutton and Maynard, 1992; Utsunomiya et al., 2003;

Babechuk et al., 2019). Based on this evidence, the paleosols are considered to be true paleosol profiles representative of weathering.

Introduction of sulfur through later hydrothermal activity

The second possibility is that sulfur was introduced into the profiles through later hydrothermal activity. Under this situation, a large portion, if not all, of the observed sulfide minerals would be epigenetic in origin.

As discussed in the introduction, the Witwatersrand Supergroup has experienced multiple hydrothermal events involving large-scale fluid flow (e.g. Armstrong et al., 1991; Kamo et al., 1996; Poujel et al., 1999; England et al., 2001; Frimmel and Minter, 2002; Rasmussen et al., 2007; Meier et al., 2009; Schaefer et al., 2010). Similarly, the Huronian Supergroup has also experienced multiple post-depositional events (e.g. Card, 1978; Mossman et al., 1993; Young et al., 2001). These events are particularly important when studying paleosols, as paleosols can act as preferential pathways for fluid flow where they act as zones of weakness (due to the original alteration caused by weathering) between more competent units.

The paleosol profiles analyzed within this study either lack mineralogical evidence of pervasive fluid-flow post-weathering or show mineralogical evidence for later potassium metasomatism, which was not recorded to have introduced sulfur into the profiles (Grandstaff et al., 1986; Sutton et al., 1990). The exception to this is the Cooper Lake paleosol, where barite has been added to the profile post-weathering (Sutton and Maynard, 2002; Babechuk et al., 2019). However, in this case, the barite is isolated and is only observed infilling fractures; it was interpreted to be relatively late in comparison to the rest of the profile, including the observed sulfide minerals (Sutton and Maynard, 2002). Whilst samples from both the Crown Lava and Bird Lava paleosols show evidence of hydrothermal activity, in the form of veinlets, the sulfur isotope data does not suggest that hydrothermal fluids introduced sulfur into the profiles. Additionally, whilst many of the grains are suggested to be epigenetic in origin, it is more likely that they represent mobilization and recrystallization of sulfur from within the profiles, similar to the pseudo-hydrothermal grains described by Saager (1970), as there is little to no evidence for hydrothermal activity in the majority of samples. Based on the lack of evidence for pervasive hydrothermal activity which introduced sulfur into these profiles, it is considered unlikely that the sulfur in these profiles was introduced through hydrothermal fluids.

Interpreting isotopic signatures

As it has been established that the sulfur within these profiles is unlikely to have been introduced through later hydrothermal activity, the isotopic signatures can be interpreted in respect to the paleosol environments.

Crown Lava and Cooper Lake paleosols

The isotopic signatures within samples from the Crown Lava and Cooper Lake paleosol profile are consistent with igneous/magmatic sulfur. These samples typically returned narrow ranges of $\delta^{34}S$ values, where the ranges were centred around zero, and near-zero to zero $\Delta^{33}S$ and $\Delta^{36}S$ values (for the Crown Lava samples, $\Delta^{36}S$ values fall within error of zero), with these isotopic compositions being typical of igneous sulfur (Macnamara et al., 1951; Thode et al., 1961; de Hoog et al., 2001). The sulfur isotope composition of pyrite from the Cooper Lake paleosol and the unaltered parent material were also observed to be similar, which would be expected if the sulfur within this profile had been inherited from the parent material. Differences in morphology and trace element composition, however, imply that some form of recycling has occurred during weathering and that primary igneous grains were not simply preserved in place. This may also account for the greater range in isotopic signatures observed for grains from the paleosol profile. In contrast, the morphology and trace element composition of pyrrhotite within the Crown Lava paleosol is similar to that previously observed for magmatic accessory pyrrhotite (Arnold, 1967; Cambel and Jarkovsky, 1969), implying that recycling was minimal within this profile.

Dominion Reef and Bird Lava paleosols

Sulfide minerals within Dominion Reef and Bird Lava paleosol profiles preserved similar $\delta^{34}S$ and $\Delta^{36}S$ values to those within the Crown Lava and Cooper Lake profiles. However, they preserve small negative $\Delta^{33}S$ values, in the order of ~-0.50 - -0.15 ‰ that are inconsistent with an igneous sulfur signature and suggest incorporation of sulfur sourced from the MIF sulfate aerosol (Farquhar et al., 2001). Two options are explored: (1) that the signatures represent the muted $\Delta^{33}S$ and $\Delta^{36}S$ signatures observed throughout the Mesoarchean, and (2) that they represent mixing between igneous and MIF sulfur.

The first option is that the signatures are purely atmospheric and that the muted values are due to the Mesoarchean age of the samples. Muted $\Delta^{33}S$ and $\Delta^{36}S$ values are consistently observed in sulfur minerals of Mesoarchean age. These minerals show a range of ~4 ‰ in $\Delta^{33}S$ and ~6 ‰ in $\Delta^{36}S$, in comparison to ranges of ~14 ‰ across the Eo-, Paleo- and Neoarchean eras

(Figure 4.23). However, the restricted ranges in $\Delta^{33}S$ and $\Delta^{36}S$ values observed for Mesoarchean samples are still much wider than the ranges observed for samples from the Dominion Reef and Bird Lava paleosols, which returned ranges of ~0.65 ‰ and ~1.35 ‰ for $\Delta^{33}S$ and $\Delta^{36}S$, respectively (Figure 4.23). Additionally, previous analysis of sulfide minerals from the units surrounding these paleosol profiles have returned higher magnitude $\Delta^{33}S$ and $\Delta^{36}S$ values, showing that these extremely muted signatures are not a feature of this specific locality (Figure 4.24; Guy et al., 2012). Therefore, whilst the muted Mesoarchean signatures may have contributed to the small signatures observed here, this option cannot fully explain what is observed.

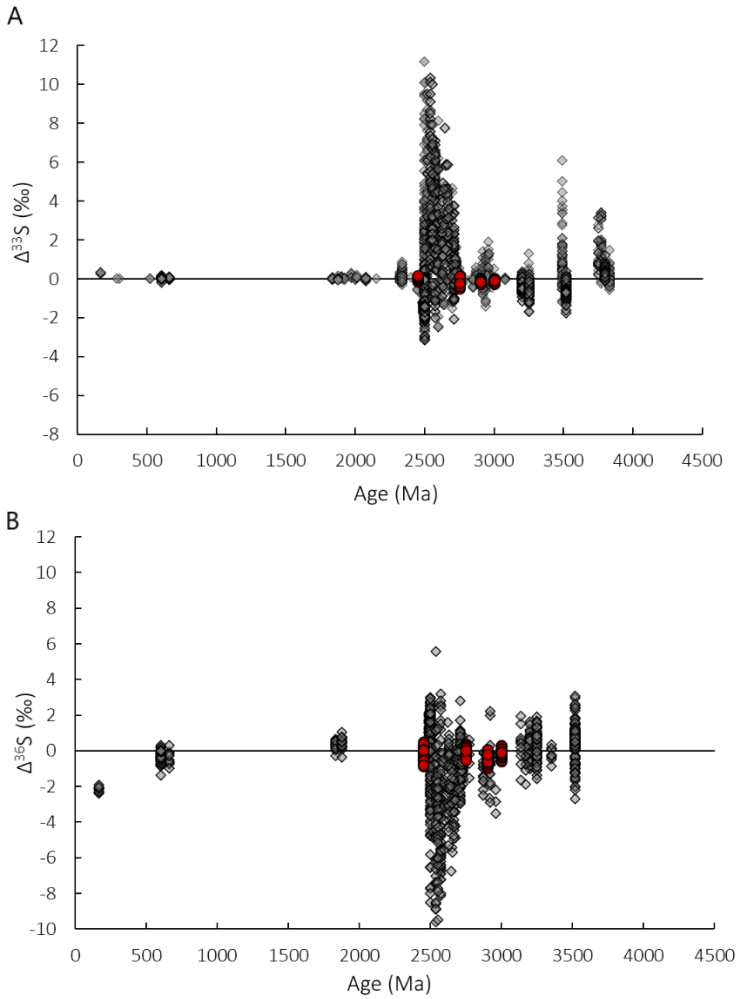

Figure 4.23. A. Plot of $\Delta^{33}S$ vs. age, B. Plot of $\Delta^{36}S$ vs. age. Filled red circles represent data collected from paleosol-hosted sulfide minerals from this study. Filled grey circles represent literature data. Data from Mojzsis et al. (2003), Ono et al. (2003, 2006a, 2009), Bekker et al. (2004); Johnston et al. (2005a, 2006), Papineau et al. (2005, 2007), Whitehouse et al. (2005), Cates and Mojzsis (2006), Ohmoto et al. (2006), Kamber and Whitehouse (2007), Domagal-Goldman et al. (2008), Patridge et al. (2008), Cates (2009); Hofmann et al., 2009, Thomazo et al. (2009), Guy et al. (2012), Zerkle et al. (2012), Kurzweil et al. (2013), Maynard et al. (2013), Zhelezinskaia et al. (2014), Izon et al. (2015), Crockford et al. (2016), Muller et al. (2016, 2017), Roerdink et al. (2016), Sansjofre et al. (2016), Mishima et al. (2017).

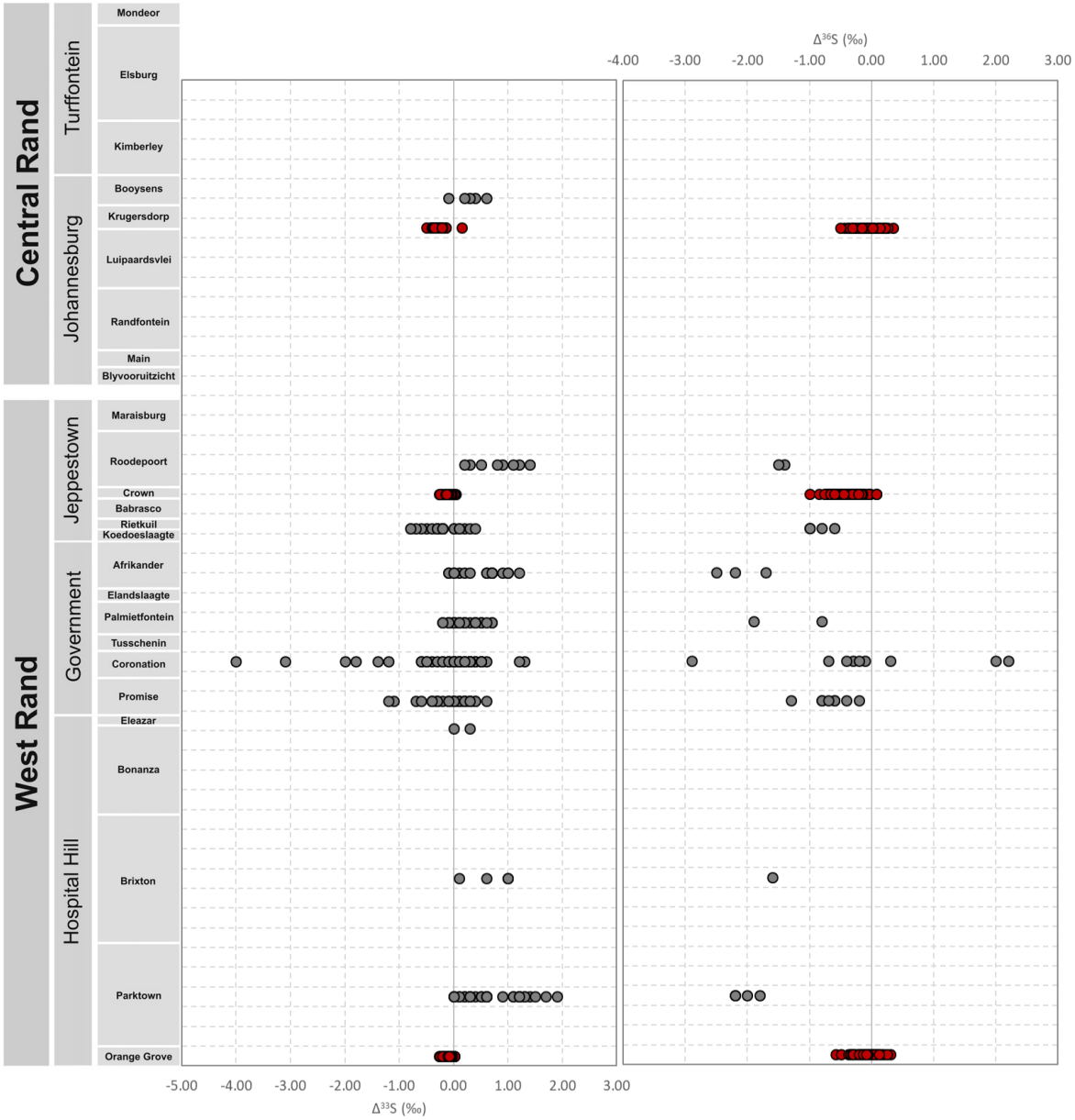

Figure 4.24. Plot of $\Delta^{33}S$ and $\Delta^{36}S$ values vs. stratigraphy for the Witwatersrand Supergroup. Filled red circles represent data collected from paleosol-hosted sulfide minerals from this study. Filled grey circles represent literature data from units within the Witwatersrand Supergroup. Data from Guy et al. (2012).

The second option is that the signatures represent mixing between atmospherically-derived MIF sulfate and igneous sulfur inherited from the parent material. This has previously been proposed by Maynard et al. (2013), who observed similar small negative $\Delta^{33}S$ values in paleosol-hosted sulfide minerals. Under this hypothesis, MIF sulfate, carrying a negative $\Delta^{33}S$ signature and positive $\Delta^{36}S$ signature, is introduced during weathering, and mixes with igneous sulfur with $\Delta^{33}S$ and $\Delta^{36}S$ values of approximately zero, which dilutes the atmospheric MIF signatures. In addition to the observed negative $\Delta^{33}S$ values, evidence for an atmospheric sulfur input during weathering is provided by the presence of a 2 – 3 m-thick

zone of sulfur enrichment identified within a number of paleosol profiles by Maynard et al. (2013), with this enrichment zone existing within a few centimetres of the upper paleosol surface. The presence of this enrichment zone at similar depths in multiple profiles of different ages and from different localities suggests that sulfur is consistently introduced into Archean profiles through the same process, proposed to occur during weathering. Introduction of atmospheric sulfur is further supported by the greater abundance of sulfide minerals within the paleosol profiles in comparison to within unaltered parent materials. Additionally, when the isotopic composition of pyrite within the Dominion Reef paleosol is compared to that of pyrite within the parent material, it is observed that the paleosol-hosted pyrite shows greater ranges in $\delta^{34}S$, $\Delta^{33}S$ and $\Delta^{36}S$, which encompass the range observed in the parent material (Figure 4.16). This is what would be expected if atmospherically-derived sulfur had been mixed with sulfur from the parent material. Evidence for inheritance of igneous sulfur within the paleosol profiles is provided by the isotopic composition of sulfides within the Crown Lava and Cooper Lake paleosols, which preserve igneous sulfur signatures. On the basis of the evidence given above, this is the preferred explanation for the isotopic signatures observed within the Dominion Reef and Bird Lava paleosol.

Methods of fixing sulfate within the profiles

As mentioned above, the negative $\Delta^{33}S$ signatures of sulfides within the Dominion Reef and Bird Lava paleosols suggest that the atmospheric sulfur preserved in the paleosol profiles was dominantly derived from the sulfate aerosol. This preferential preservation has previously been attributed to the greater solubility of the sulfate aerosol, where sulfate would be carried by rainwater into the profile whilst elemental sulfur would accumulate at the surface and be vulnerable to erosion (Maynard et al., 2013). However, questions are raised as to how this sulfate was transformed to sulfide and fixed within the profiles. Here we consider the options of MSR and thermochemical sulfate reduction (TSR).

Previously, it has been suggested that the sulfate was fixed through MSR, followed by reaction of the sulfide with iron to form pyrite (Maynard et al., 2013). However, this is not supported by the results of this study. When plotted in $\Delta^{36}S$-$\Delta^{33}S$ space, samples do not show the characteristic array of $\Delta^{36}S/\Delta^{33}S$ = ~-6.9 that is produced by MSR (Ono et al., 2006a, Johnston et al., 2007) and the $\Delta^{36}S$ values for the Bird Lava paleosol samples fall within error of zero (Figure 4.18). Additionally, the observed $\delta^{34}S$ values are a mixture of low magnitude positive and negative values, which are unlike the large, variable and typically negative $\delta^{34}S$ values produced through MSR (Thode et al., 1951; Goldhaber and Kaplan, 1975; Canfield

and Teske, 1996; Johnson et al., 2007). Therefore, MSR was unlikely to have been the method by which sulfate was fixed in these profiles and this emphasizes the importance of analyzing all four stable isotopes of sulfur when trying to recognize the action of MSR.

Whilst MSR is unlikely to have been the method which fixed sulfate within these profiles, Nabhan et al. (2016, 2018) previously observed that pyrite within a paleosol profile in the Baberton Greenstone Belt showed large negative $\delta^{34}S$ values consistent with MSR. It is suggested that this profile was more sulfate rich than the profiles analyzed within this study, which may have made it a more favourable environment for sulfate-reducing microbes. Nabhan et al. (2016) recorded observations of silicified gypsum nodules, suggesting high concentrations of sulfate were present. However, it is further suggested that pyrite grains from this profile undergo four sulfur isotope analysis to confirm that the isotopic signatures are fully consistent with MSR.

The other option is through abiotic sulfur reduction, specifically TSR. TSR in the presence of hydrocarbons has been shown to occur at temperatures as low as 80 – 100 °C (Ohmoto and Goldhaber, 1997; Machel, 2001) and therefore could possibly have occurred within the profiles. The isotopic signatures produced by this process, however, are variable, making it difficult to identify in the rock record. Whilst it consistently produces positive $\Delta^{33}S$, it may produce positive or negative $\Delta^{36}S$ and $\delta^{34}S$ values (Watanabe et al., 2009). Therefore, TSR can be neither confirmed nor rejected as the method by which sulfate was fixed within the profile. In order to confirm or eliminate this method, the isotopic signatures produced through this process need to be better constrained.

Differences in isotopic signatures across the analyzed profiles

The lack of preservation of an atmospheric sulfur signature in the Crown Lava and Cooper Lake paleosol profiles is attributed to the depths the analyzed samples were collected from, rather than any differences between these profiles and the Dominion Reef and Bird Lava paleosol profiles. As previously mentioned, these samples were from the same sets previously analyzed by Maynard et al. (2013). However, the samples from this study were collected from depths outside the recognized sulfur enrichment zones that are believed to contain the atmospherically-derived sulfur (Table A1, Figure A.1, Appendix). Therefore, there may only have been sulfur inherited from the parent material present within these samples. This may also explain the differences between the $\Delta^{33}S$ values from these profiles presented in this

study and those presented by Maynard et al. (2013), who analyzed sulfide minerals from within the enrichment zones.

Overlying and underlying sedimentary rocks

Sandstone overlying the Dominion Reef paleosol

Due to the similarities between the isotopic signatures observed within profile and the overlying sandstone, it is probable that the sulfur has been inherited from the paleosol. Samples were collected close to the upper paleosol surface (Table 4.1) and incorporation of material from paleosols into the immediately overlying units is common (Holland and Zbinden, 1988; Rye and Holland, 1998).

Units under- and overlying the Crown Lava paleosol

The provenance of detrital grains within the underlying quartzite of the underlying Babrasco Formation is unclear. These grains have fine, randomly-distributed pores and show similar textures to diagenetic grains previously observed within the Witwatersrand Supergroup (e.g. Guy et al., 2010) and other Archean sedimentary sequences (e.g. Gregory et al., 2015b). The small non-zero positive and negative $\delta^{34}S$ values and $\Delta^{33}S$ and $\Delta^{36}S$ values of approximately zero could represent either a crustal MDF source (Guy et al., 2014) or a magmatic or hydrothermal source (Hofmann et al., 2009). However, these grains show low concentrations of Co, Ni and As, which is typical of hydrothermal pyrite (Utter, 1978; Meyer et al., 1990; Guy et al., 2010; Koglin et al., 2010) and has also been observed within certain types of igneous grains (Loftus-Hills and Solomon, 1968). This contradicts the seemingly diagenetic texture of these grains. Therefore, the source of these grains remains unclear.

Non-porous grains from the sandstones of the overlying Roodepoort Formation are proposed to represent an igneous/magmatic or hydrothermal source. The grains are consistently non-porous, however, some grains showed euhedral overgrowths with crystallographically-aligned pores that were interpreted to represent later epigenetic overgrowths. Due to high spatial resolution of the SHRIMP-SI analysis method, these overgrowths were able to be avoided during sulfur isotope analysis. The overgrowths themselves were not able to analyzed as they were too fine for the analysis spot size used for four sulfur isotope analysis. The morphology of non-porous grains forming the cores are inconclusive in regards to origin, as detrital grains with this texture have been shown to represent numerous sources (e.g. Hofmann et al., 2009; Large et al., 2013). However, the variable $\delta^{34}S$ values and $\Delta^{33}S$ and $\Delta^{36}S$ values of approximately zero were observed to be similar to the composition of re-worked

hydrothermal and magmatic grains previously observed by Hofmann et al. (2009). There are only two trace element measurements from these grains and the author is somewhat reluctant to interpret them as, due to the larger spot size used during LA-ICP-MS analysis, they could represent mixtures of multiple pyrite generations. Therefore, based on the isotopic composition, these grains are proposed to represent reworked igneous or hydrothermal grains.

Redox conditions during paleosol formation

As previously mentioned, past studies of Archean paleosols have largely focused on determining the redox conditions during paleosol formation (e.g. Holland and Zbinden, 1988; Holland and Beukes, 1990; Murakami et al., 2001; Yamaguchi et al., 2007; Babechuk et al., 2019). Here, the presence of small MIF signatures within the Dominion Reef and Bird Lava paleosols is conclusive with anoxic conditions during weathering (Pavlov and Kasting, 2002). This is in agreement with a large amount of evidence that the Witwatersrand Supergroup, or at least parts of it, was deposited under anoxic conditions, including the preservation of MIF signatures in diagenetic pyrite (e.g. Guy et al., 2012) and the presence of placer deposits of pyrite and uraninite (e.g. Krupp et al., 1994; England et al., 2002; Frimmel et al., 2005b; Depiné et al., 2013).

The results of this study do not provide any information regarding the redox conditions during the formation of the Crown Lava and Cooper Lake paleosols. However, sulfur isotope studies of the units surrounding these profiles shows that MIF sulfur aerosols were being deposited before and after paleosol formation (Papineau et al., 2007; Guy et al., 2012; Cui et al., 2018) and therefore conditions were likely also anoxic during paleosol formation. In regards to the Cooper Lake paleosol, further support for anoxic conditions is supplied by major, trace and ultra-trace element and Fe isotope data which showed mobility of Fe and retention of elements mobile under oxidizing conditions (Babechuk et al., 2019).

4.7 Conclusions

As shown, pyrite hosted by paleosol profiles preserves igneous/magmatic sulfur inherited from the parent material or a combination of inherited igneous sulfur and sulfur sourced from the MIF sulfate aerosol. Whether or not there is preservation of a MIF sulfate signature appears to be related to the location of the pyrite within the profile, with sulfur bearing the MIF signature likely being present only within a sulfur enrichment zone located in the upper section of the paleosol profiles. The results presented here are in agreement with the results of Maynard et al. (2013) from analyses of paleosol-hosted pyrite and the absence of pyrite

bearing positive $\Delta^{33}S$ signatures provides further evidence that paleosols preferentially preserve the MIF sulfate aerosols over the MIF elemental sulfur aerosol. Unlike results from Maynard et al. (2013) and Nabhan et al. (2016, 2018), however, there is no evidence for MSR, suggesting that the MIF sulfate was transformed to sulfide and fixated within the paleosol profiles through some other mechanism.

Chapter 5: Isotopic composition of pyrite hosted by fluvial sedimentary rocks

Abstract - A detailed morphological, trace element and multiple sulfur isotope study of pyrite from fluvial sedimentary rocks of the ~2900 – 2780 Ma Central Rand Group of the Witwatersrand Supergroup is presented. Detrital pyrite shows isotopic and trace element compositions consistent with grains being sourced from magmatic, hydrothermal and sedimentary environments. Diagenetic pyrite preserves small negative to zero $\Delta^{33}S$ values and small positive $\delta^{34}S$ values that are conclusive with a mixture of mass-dependent sulfur and the atmospheric sulfate aerosol produced through photolysis of SO_2. Negative $\Delta^{36}S$ values may suggest the action of microbial sulfate reducers. Two species of epigenetic pyrite are identified, the first of which shows similar signatures to detrital and diagenetic pyrite and represents remobilisation of sulfur from within the Central Rand Group. The second species preserves highly unusual isotopic signatures, where both $\Delta^{33}S$ and $\Delta^{36}S$ are negative, with significant, large fractionations present in $\Delta^{36}S$. This is suggested to possibly represent microbial sulfate reduction of photochemical sulfate or photoexcitation of volcanic sulfur species. Conspicuously absent from any of the pyrite analyzed are positive $\Delta^{33}S$ values, and an isotopic composition on the atmospheric $\Delta^{36}S/\Delta^{33}S$ array. This shows that the photochemical elemental sulfur aerosol was not preserved in this fluvial environment or within the surrounding environments from which detrital pyrite was sourced from.

5.1 Introduction

This chapter focusses on the sulfur isotope composition of pyrite hosted within sediments of the fluvial-dominated Central Rand Group. These sediments were chosen to examine the sulfur isotope composition of terrestrial environments as they contain both detrital and diagenetic pyrite. This allows for examination of the sulfur isotope composition of the continental surface through analysis of the detrital pyrite and also determination of the sulfur isotope composition of fluvial environments and the fractionation processes occurring in those environments, through analysis of the diagenetic pyrite. The sediments of the Central Rand Group were chosen specifically as the stratigraphy and sedimentology is well-defined. Additionally, they directly overlie the marine-dominated West Rand Group, which will allow for a direct comparison between the sulfur isotopic composition of fluvial and marine sediments in later chapters.

There is a reasonable amount of isotopic data available from fluvial-sediment hosted sulfide minerals. However, the majority of these studies have focussed on detrital pyrite hosted within the Quartz Pebble Conglomerates (QPCs) of the Central Rand Group (Hoefs et al., 1968; England et al., 2002; Hofmann et al., 2009; Large et al., 2013; Guy et al., 2014), the overlying Ventersdorp Contact Reef (VCR; Zhao et al., 1998; Hofmann et al., 2009) and reefs and conglomerates of the neighbouring Pongola Supergroup (Hofmann et al., 2009). The isotopic composition of diagenetic pyrite in fluvial sediments and pyrite within non-conglomeratic fluvial sediments remains largely undefined, with only one study currently available that considers diagenetic pyrite within non-conglomeratic fluvial sediments (Guy et al., 2012). Additionally, there is a scarcity of four sulfur isotope data, with many studies analysing only ^{32}S and ^{34}S (e.g. Hoefs et al., 1968; Zhao et al., 1998; England et al., 2002; Large et al., 2013), only one study analysing ^{32}S, ^{33}S and ^{34}S (Hofmann et al., 2009) and only two studies analysing all four isotopes (Guy et al., 2012, 2014). Even within those studies which have analyzed the four isotopes, the amount of ^{36}S data is limited and $\Delta^{36}S$ values are largely undiscussed.

From these studies, multiple sulfur sources have been identified for detrital and diagenetic pyrite. Within their study of detrital pyrite hosted by the QPC's, Guy et al. (2014) identified three sources of sulfur: (1) Mass-Independently Fractionated (MIF) photochemical sulfur and sulfate, that falls on the Archean Reference Array (ARA) of $\Delta^{33}S = 0.9*\delta^{34}S$ (Ono et al., 2003), (2) a mixture of MIF sulfate and Mass-Dependently Fractionated (MDF) marine

sulfate, with small negative $\Delta^{33}S$ and small positive $\delta^{34}S$ values, and (3) MDF crustal sulfate with $\Delta^{33}S$ values of approximately zero and small positive $\delta^{34}S$ values. Of these, the MDF crustal sulfur was the most abundant. Hofmann et al. (2009) identified similar MIF and MDF crustal sources, however separated Guy et al. (2014)'s MDF crustal sulfate into a magmatic/high temperature metamorphism related hydrothermal reservoir and a sedimentary non-MIF reservoir. Diagenetic pyrite within fluvial sediments of the upper West Rand Group showed broadly similar isotopic signatures, with small negative $\Delta^{33}S$ values and small positive $\delta^{34}S$ values that were interpreted to represent mixing between MIF photochemical and MDF crustal and marine sulfur reservoirs (Guy et al., 2012). Deviation from the $\Delta^{36}S/\Delta^{33}S$ ARA in $\Delta^{36}S$ was suggested to be evidence of Microbial Sulfate Reduction (MSR). Therefore, it seems that sulfide minerals within fluvial sediments preserve sulfur dominantly sourced from crustal and marine MDF sources, with minor input from MIF sources and possible input of sulfur produced through MSR. The emergence of a dominant MDF crustal source has been suggested to be linked to either oxidative weathering of sulfide minerals and/or the advent of modern plate tectonic processes and oxidized volcanic gasses (Guy et al., 2010, 2014).

This chapter presents a detailed study of the morphology, trace element composition and sulfur isotope signatures of sulfide minerals hosted by fluvial sedimentary rocks of the Central Rand Group. Detrital, diagenetic and epigenetic pyrite species were identified. Detrital pyrite was determined to preserve sulfur from hydrothermal and/or magmatic sources and a mixed MIF and MDF source. Diagenetic pyrite showed similar signatures to those observed by Guy et al. (2012) that were conclusive with a mixed MIF and MDF crustal source and possible action of microbial sulfate reducers. Two species of epigenetic pyrite were identified, the first of which showed similar isotopic signatures to detrital and diagenetic grains, suggesting that hydrothermal activity had remobilized pyrite from within the Central Rand Group. The second species showed unusual negative $\Delta^{33}S$ and negative $\Delta^{36}S$ signatures, with large fractionations in $\Delta^{36}S$. This is proposed to represent possible MSR of MIF sulfate or photoexcitation of volcanic sulfur species. The isotopic signatures of both detrital and diagenetic grains provide further evidence for an active crustal sulfur flux during deposition of the Central Rand Group. However, the preservation of detrital pyrite and low concentrations of the redox sensitive elements Se and Mo argue against oxidative weathering of sulfide minerals as a source of this flux. The complete absence of positive $\Delta^{33}S$ signatures

provides further evidence that MIF elemental sulfur was not being preserved in terrestrial environments.

5.2 Geological context

The Central Rand Group is the upper group of the Witwatersrand Supergroup, South Africa. A broad description of the geology of the Witwatersrand Supergroup was provided in Chapter 4.

The Central Rand Group is divided stratigraphically, from bottom to top, into the Johannesburg and Turffontein Subgroups (Figure 5.1). A maximum age of deposition is provided by detrital zircons, which returned an age of 2902 ± 13 Ma (Kositcin and Krapez, 2004). A minimum age of 2780 ± 3 Ma is given by authigenic xenotime (Kosticin et al., 2003), however, based on stratigraphic correlations between the Mozaan Group of the Pongola Supergroup and the Witwatersrand Supergroup, it is possible that sedimentation ended at ~2840 Ma (Gutzmer et al., 1999). It is overlain by the auriferous Ventesdorp Contact Reef (VCR), with an erosional contact. It is underlain by the predominantly marine sediments of the West Rand Group, where the contact is gradational and diachronous, with a southeast younging direction (Tankard et al., 1982).

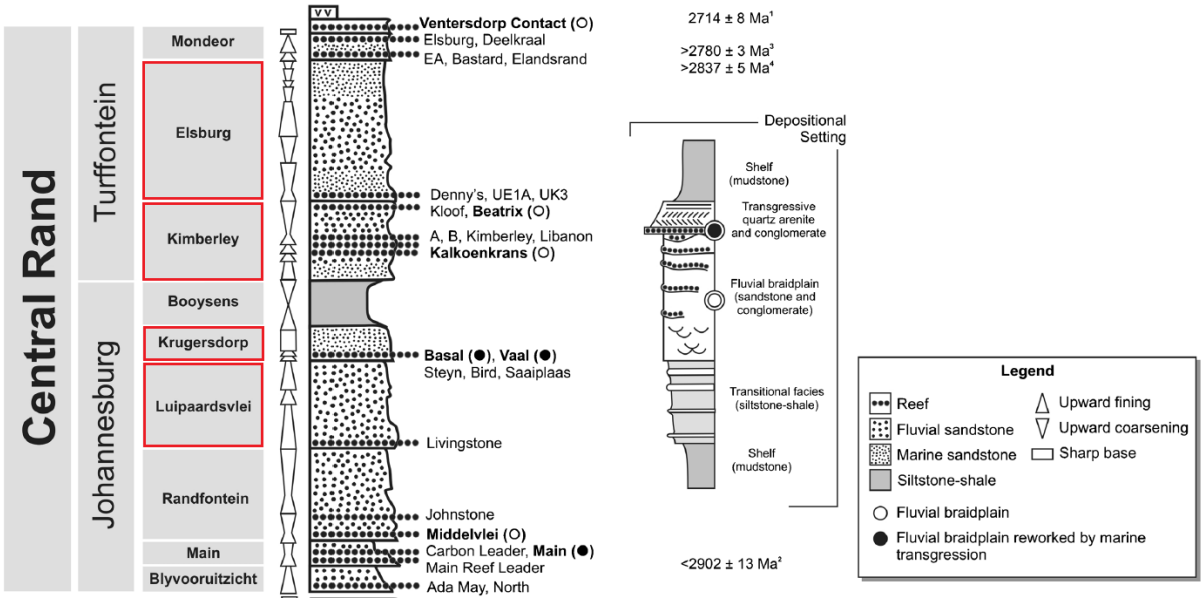

Figure 5.1. Simplified stratigraphic column of the Central Rand Group. Sampled formations are outlined in red. Ages are SHRIMP U-Pb or Pb-Pb after Frimmel et al. (2005a), where (1) zircon (Armstrong et al., 1991), (2) zircon and xenotime (Kositcin and Krapez, 2004), (3) authigenic xenotime (Kositcin et al., 2003) and (4) zircon (Gutzmer et al., 1999). From Guy et al. (2014).

The Central Rand Group consists of arenaceous and rudaceous rocks, with lesser argillaceous and volcanic units. It is dominated by fluvial braidplain sedimentary rocks deposited in a restricted retroarc foreland basin setting (Catuneanu, 2001; Kositcin and Krapez, 2004; Schmitz et al., 2004; Frimmel et al., 2005a). Laterally continuous mudstones and transgressive shallow marine arenites mark marine incursions, with tidal reworking recorded at the intersections of fluvial and shallow marine units (Els, 1998; Kositcin and Krapez, 2004). Also present are a number of prominent gold-bearing conglomerates, which are overlain by transgressive shallow marine quartz arenites (Guy et al., 2014).

5.3 Sampling information

Samples within this study were collected from the Anglogold drill core MMB6. The core was drilled in the locality of Viljoenskroon township, in the Free State province of South Africa, at 27º0'44.58" S, 26º43'16.19" E. The approximate location is shown in Figure 5.2.

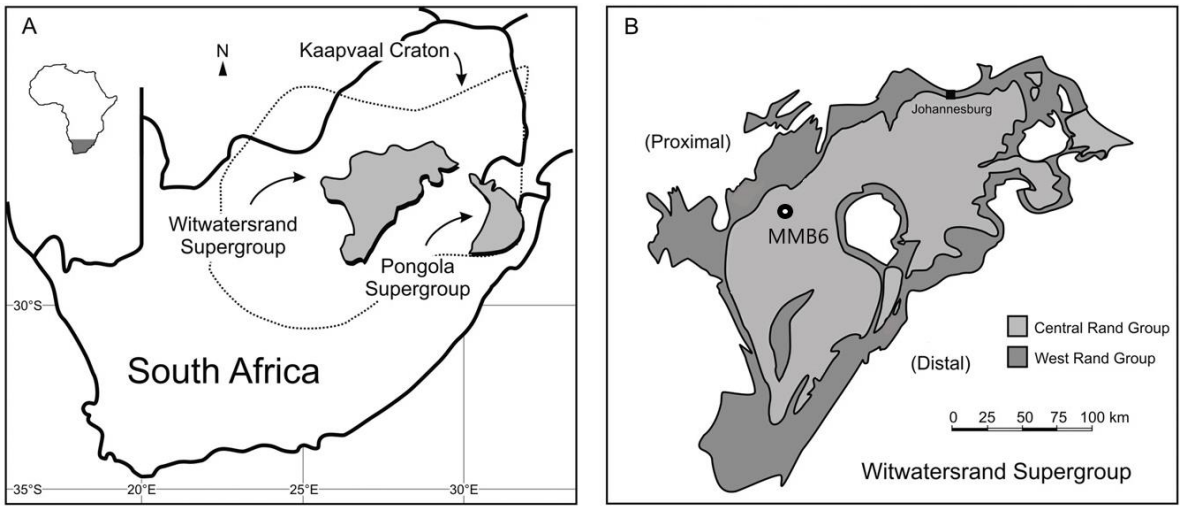

Figure 5.2. A. Geographic position of the Witwatersrand and Pongola supergroups on the Kaapvaal Craton. B. Geological map of the Witwatersrand Supergroup, showing the location of the MMB6 drill core. Modified from Guy et al. (2012).

Samples were collected from the Luipaardsvlei and Krugersdorp formations of the Johannesburg Subgroup and the Kimberley and Elsburg formations of the Turffontein Subgroup (Figure 5.1). Within the MMB6 drill core, the Luipaardsvlei Formation consisted of a granular sandstone with rare, thin beds of pebble conglomerate and a domain of massive pyrite, where pyrite infills pore spaces and encloses the surrounding grains. The Krugersdorp Formation consisted of clast-supported conglomerate in pebbly grit and light grey, quartzitic, very coarse sandstone. The Kimberley Formation was a grey, medium-grained, mature

sandstone and the Elsburg Formation was a grey, very coarse, mature sandstone. The lithology, stratigraphic unit and depth of each sample is provided in Table 5.1.

Table 5.1. Sampling information for Central Rand Group samples.

Sample Name	Formation	Lithology	Depth (m)
MMB6-6	Elsburg	Sandstone	3035.57
MMB6-7	Elsburg	Sandstone	3035.58
MMB6-4	Kimberley	Sandstone	3163.97
MMB6-5	Kimberley	Sandstone	3163.98
MMB6-11	Kimberley	Sandstone	3164.01
MMB6-2	Krugersdorp	Sandstone	3294.12
MMB6-1	Krugersdorp	Conglomerate	3304.91
MMB6-9	Krugersdorp	Conglomerate	3304.94
MMB6-12	Luipaardsvlei	Sandstone	3351.23
MMB6-3	Luipaardsvlei	Sandstone	3351.27

5.4 Methods

Sample characterisation and SHRIMP-SI sulfur isotope analysis

Methods for sample characterisation and SHRIMP-SI sulfur isotope analysis are provided in Chapter 2.

Bulk sulfur isotope analysis

Bulk sulfur isotope analysis of certain grains was undertaken to confirm unusual isotopic compositions. Analysis took place at the Equipe Géochimie des isotopes stables, within the Institut de Physique du Globe de Paris. Approximately 1 – 3 g of powdered sample was transferred to a 50 mL boiling flask attached to a distillation apparatus similar to that described by Forrest and Newman (1977). Reduced sulfur was converted to H_2S using a sub-boiling Cr^{2+}-HCl mixture (Canfield et al., 1986), then transferred to a containing silver nitrate trap (0.2 M) using high purity nitrogen and bubbled. The precipitated silver sulfide (Ag_2S) was rinsed and dried, before being wrapped in aluminium foil and loaded into a nickel bomb for fluorination with excess F_2 (10-100-fold) overnight at 250 °C. Product SF_6 was purified using cryogenic and gas chromatography techniques under protocol similar to that used by most laboratories (Labidi et al., 2012). The purified SF_6 was then quantified and analyzed

using a dual inlet ThermoFinnigan MAT 253 where *m/z* = 127^+, 128^+, 129^+ and 131^+ ion beams were monitored. The $\delta^{34}S$, $\Delta^{33}S$ and $\Delta^{36}S$ values are presented in the standard delta notation against V-CDT. Analytical reproducibility was typically ≤0.2 ‰, 0.02 ‰ and 0.2 ‰ for $\delta^{34}S$, $\Delta^{33}S$ and $\Delta^{36}S$ respectively.

5.5 Results

Sample characterisation

Morphology and textural features

Pyrite was the only sulfide mineral observed within samples from the Central Rand Group. Sulfide abundance was variable. Within the Luipaardsvlei Formation, there was a domain of massive pyrite where abundance was extremely high but pyrite was scarce outside this domain. Similarly, in both the Kimberley and Elsburg formations, pyrite-rich layers were observed in otherwise pyrite-poor rock. Abundance was moderate and consistent throughout the Krugersdorp Formation.

Eight distinct morphologies were observed within the samples from the Central Rand Group and will be referred to as CR-EU-1, CR-EU-2, CR-EU-3, CR-AN-1, CR-AN-2, CR-AN-3, CR-AN-4 and CR-AN-5. Backscattered electron (BSE) images of these morphologies are provided in Figure 5.3.

CR-EU-1 were aggregates of euhedral, porous grains, commonly showing crystallographically-aligned pores and ranging in size from ~200 – 700 µm in diameter. They occurred within conglomerates of the Krugersdorp Formation and were observed to overprint the surrounding clasts.

CR-EU-2 were non-porous, euhedral grains, observed both as isolated grains and as aggregates. The individual grains ranged in size from ~100 – 800 µm. They occurred within the Kimberley Formation and were observed to overprint the surrounding sandstone. Grains were occasionally observed to be growing off CR-AN-4 grains and etching with NaOCl revealed the presence of anhedral cores (likely also CR-AN-4 grains) within some grains and aggregates (Figure 5.4).

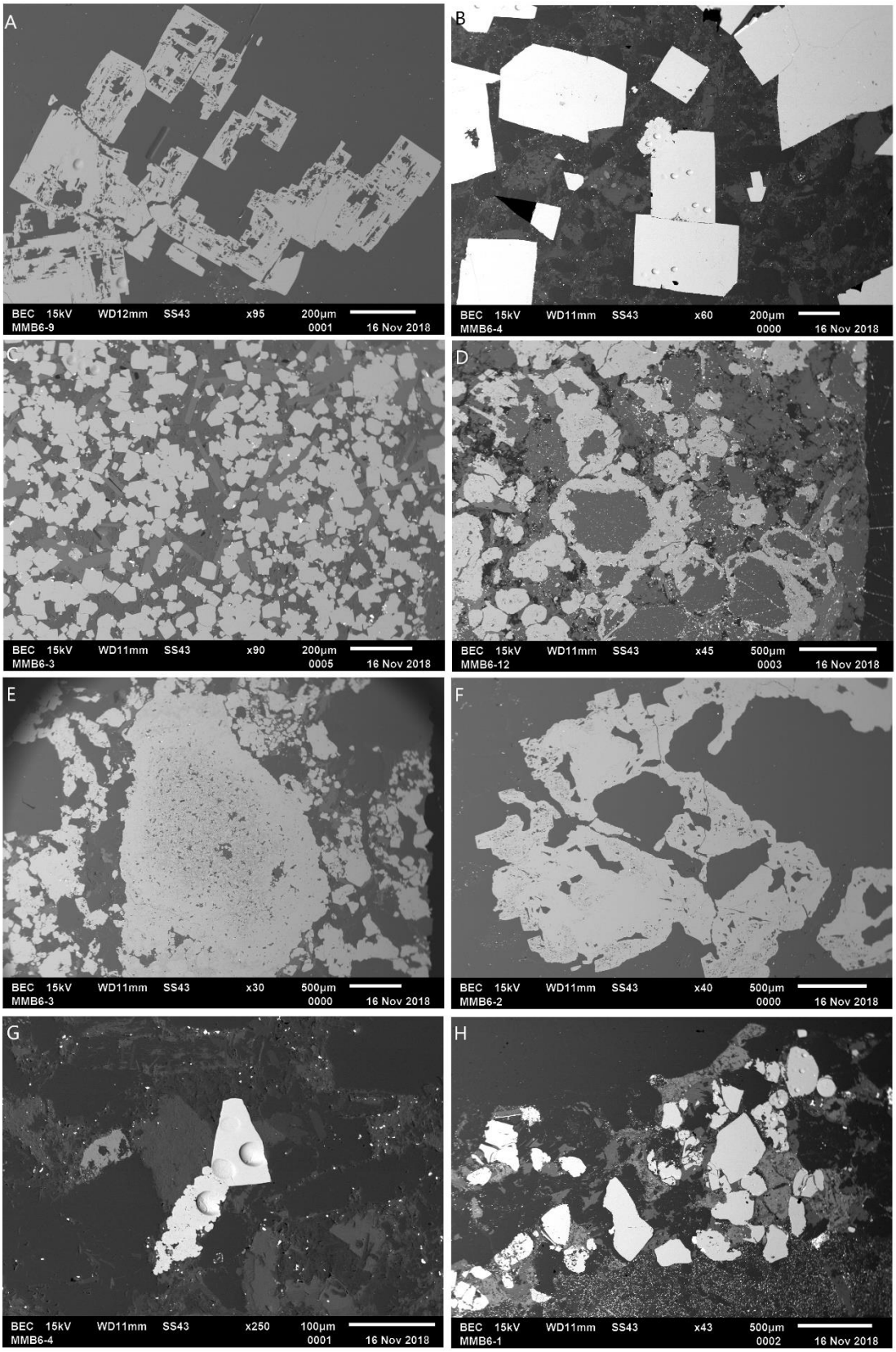

Figure 5.3. BSE photomicrographs of the different morphologies of pyrite grains observed within sedimentary rocks of the Central Rand Formation. (A). CR-EU-1, (B). CR-EU-2, (C) CR-EU-3, (D) CR-AN-1, (E) CR-AN-2, (F) CR-AN-3, (G) CR-AN-4, (H) CR-AN-5.

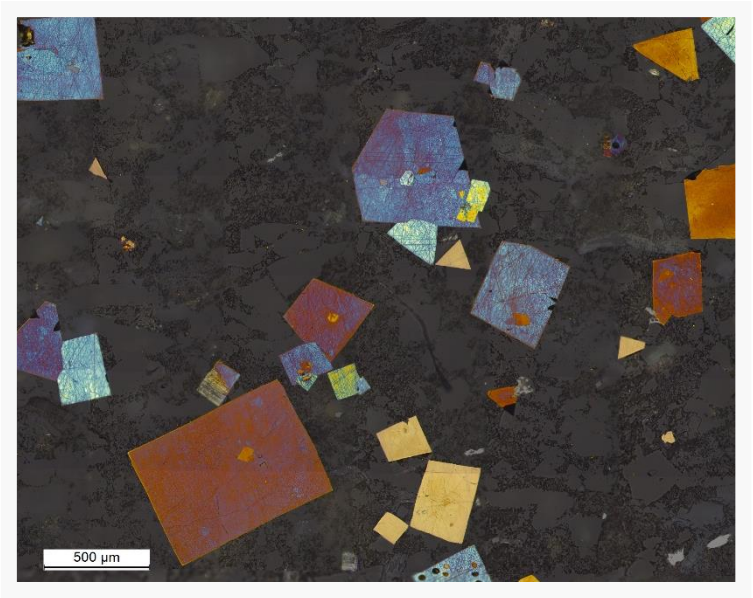

Figure 5.4. Photomicrograph of CR-EU-2 grains after etching with NaOCl. Note the presence of anhedral cores within some grains and aggregates.

CR-EU-3 were fine, euhedral to subhedral, non-porous grains observed within the Luipaardsveli Formation. They were ~20 – 200 µm in size and occurred both as isolated grains and as aggregates.

CR-AN-1 refers to massive pyrite, variably porous and non-porous, which infilled spaces between grains and overprinted the edges of grains in the sandstone of the Luipaardsvlei Formation. This pyrite was sometimes observed to be intergrown with Ti-oxide.

CR-AN-2 was a nodule composed of closely-packed variably porous, anhedral grains (Figure 5.5), ~3000 µm in diameter and also observed within the Luipaardsvlei Formation. Individual grains within the nodule range in size between ~50 – 200 µm in diameter.

CR-AN-3 were irregularly-shaped anhedral aggregates, with variable porosity, commonly showing distinct porous and non-porous zones. Within porous zones, pores were frequently crystallographically-aligned. These aggregates were > 1000 µm in diameter and were observed within the Krugersdorp Formation.

CR-AN-4 were irregularly-shaped anhedral grains, with low porosity and were ~100 – 200 µm in diameter. They were typically found in close association with CR-EU-2 grains within the Kimberley Formation but were substantially rarer.

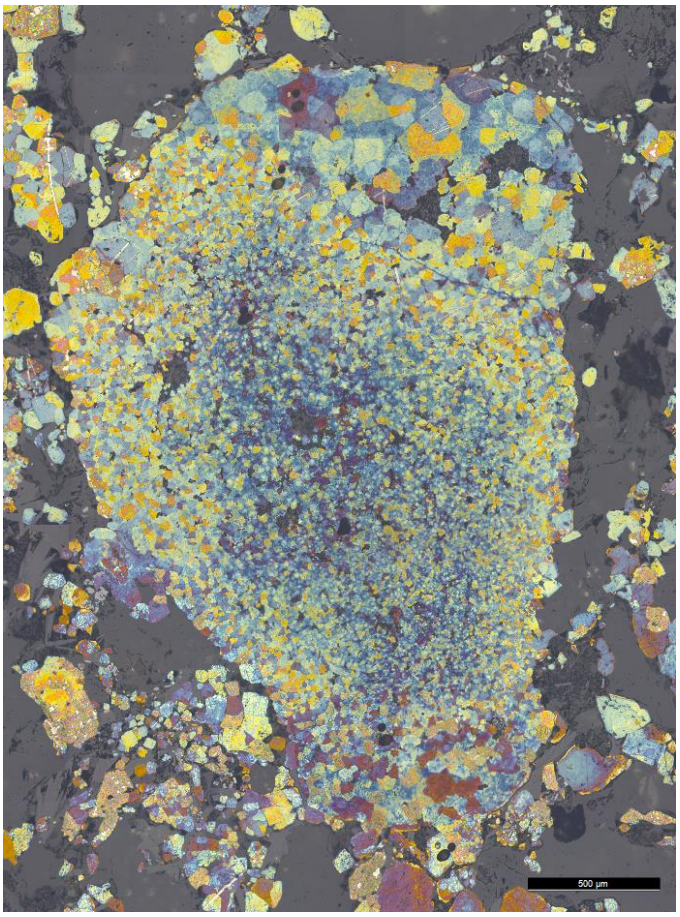

Figure 5.5. Photomicrograph of CR-AN-2 nodule after etching with NaOCl.

CR-AN-5 were rounded grains with variable porosity, found between clasts in conglomerates of the Krugersdorp Formation and forming bands within sandstones of the Elsburg Formation. Grains were ~200 – 500 µm in diameter. In both formations, these grains are found in association with rounded grains of Ti-oxide and, in the Krugersdorp Formation, rounded zircon grains.

Trace element composition

A summary of the trace element composition of pyrite from each sample is provided in Table 5.2. The complete data set and maps of analysis spots are provided in the Supplementary Information.

Table 5.2. Summary of the trace element composition of pyrite grains from the Central Rand Group.

Sample Name	Element	Min (ppm)	Max (ppm)	Median (ppm)	Mean (ppm)	StDev (ppm)
MMB6-3	Co	21.5	557	81.0	169	183
(n = 9)	Ni	92.0	1600	220	587	644
	Cu	12.0	63.1	28.3	32.2	18.0
	Zn	0.890	65.0	3.10	10.8	20.6
	As	47.0	6660	1520	2240	2390
	Se	2.47	33.2	7.50	13.3	10.6
	Mo	BDL	BDL	-	-	-
	Co/Ni	0.065	0.730	0.368	0.388	0.201
MMB6-12	Co	0.116	795	19.6	99.5	245
(n = 10)	Ni	27.2	4780	915	1250	1300
	Cu	7.60	57.7	13.1	21.5	16.5
	Zn	0.490	7.40	1.24	2.19	2.29
	As	91.8	3870	1110	1390	1030
	Se	2.16	19.0	5.59	7.05	4.90
	Mo	BDL	0.042	-	-	-
	Co/Ni	0.003	0.166	0.022	0.040	0.054
MMB6-1	Co	2.71	1210	245	441	503
(n = 8)	Ni	16.2	890	60.1	152	299
	Cu	0.075	180	39.4	60.9	71.7
	Zn	0.240	0.550	0.330	0.346	0.091
	As	14.3	22100	3940	7120	8440
	Se	3.56	169	14.05	38.0	55.8
	Mo	BDL	BDL	-	-	-
	Co/Ni	0.167	18.1	0.838	4.87	6.83
MMB6-2	Co	2.46	106	20.0	38.5	44.3
(n = 5)	Ni	6.60	605	117	239	276
	Cu	2.85	8.40	5.30	5.71	2.13
	Zn	BDL	0.980	0.455	0.510	0.288
	As	634	1860	1450	1290	477
	Se	1.10	11.5	4.70	5.36	3.85
	Mo	BDL	0.001	-	-	-
	Co/Ni	0.099	0.579	0.231	0.278	0.185
MMB6-9	Co	1.47	3300	63.0	1120	1890
(n = 3)	Ni	5.40	1850	480	778	958
	Cu	BDL	5.80	3.99	3.99	2.57
	Zn	0.420	1.90	1.08	1.13	0.741
	As	4.10	3670	26.8	1230	2110
	Se	2.39	188	21.1	70.5	102

Sample Name	Element	Min (ppm)	Max (ppm)	Median (ppm)	Mean (ppm)	StDev (ppm)
	Mo	BDL	BDL	-	-	-
	Co/Ni	0.131	1.78	0.272	0.729	0.916
MMB6-4	Co	0.168	350	23.0	74.7	112
(n =15)	Ni	692	2930	1750	1840	672
	Cu	0.220	451	1.72	41.7	117
	Zn	0.360	9.60	1.36	2.62	3.03
	As	474	2340	1510	1400	660
	Se	0.530	1.20	0.740	0.771	0.197
	Mo	BDL	24.2	-	-	-
	Co/Ni	$1.26*10^{-4}$	0.434	0.012	0.058	0.119
MMB6-5	Co	41.0	1010	175	295	316
(n = 8)	Ni	1240	3220	1950	2170	684
	Cu	1.23	110	12.3	32.8	44.1
	Zn	BDL	28.9	3.08	9.28	11.6
	As	1070	3240	1930	2020	847
	Se	40.2	80.7	61.4	58.4	14.8
	Mo	BDL	0.111	-	-	-
	Co/Ni	0.021	0.544	0.093	0.141	0.168
MMB6-11	Co	231	1990	665	793	463
(n = 14)	Ni	250	4570	2250	2130	1510
	Cu	0.360	830	2.09	172	312
	Zn	1.28	10.5	5.34	5.57	4.29
	As	157	3760	1850	1870	1260
	Se	5.08	98.2	59.8	51.9	30.6
	Mo	BDL	7.50	-	-	-
	Co/Ni	0.072	3.23	0.323	0.859	0.952
MMB6-6	Co	166	1740	1060	1030	592
(n = 8)	Ni	52.3	777	434	405	256
	Cu	0.350	86.0	59.0	51.1	41.5
	Zn	0.690	11.9	7.70	7.00	4.79
	As	3.00	1440	134	319	484
	Se	10.6	122	25.7	37.7	36.8
	Mo	BDL	1.38	1.06	0.816	0.718
	Co/Ni	2.09	4.30	2.53	2.86	0.802

Luipaardsvlei Formation

Pyrite returned Co concentrations of 0.116 – 795 ppm, with a median of 46.3 ppm and a mean of 132 ± 215 ppm (1 *SD*, *n* = 19). Ni concentrations showed a range of 27.2 – 4780 ppm, with a median of 812 ppm and mean of 935 ± 1070 ppm (1 *SD*, *n* = 19). Cu concentrations had a range of 7.60 – 63.1 ppm, median of 24.4 ppm, mean of 26.6 ± 17.6 ppm (1 *SD*, *n* = 19). Zn concentrations ranged between 0.310 – 65.0 ppm, median of 1.78 ppm, mean of 6.09 ± 14.6 ppm (1 *SD*, *n* = 19) and As concentrations showed a range of 47.0 – 6660 ppm, with a median of 1110 ppm and a mean of 1920 ± 2070 ppm (1 *SD*, *n* = 19). Se concentrations had a range of 2.16 – 33.2 ppm, median of 6.41 ppm, mean of 10.0 ± 8.52 ppm (1 *SD*, *n* = 19). Mo concentrations ranged from below the limit of detection to 0.042 ppm. Co/Ni values had a range of 0.003 – 0.730, a median of 0.108 and a mean of 0.205 ± 0.227 (1 *SD*, *n* = 19).

CR-AN-1 and CR-AN-2 grains could be distinguished on the basis of Ni concentrations and Co/Ni values but otherwise showed similar trace element compositions (Figure 5.6). CR-AN-1 grains showed higher Ni concentrations, with a range of 27.2 – 4780 ppm, median of 970 ppm and mean of 1210 ± 1120 ppm (1 *SD*, *n* =14) and lower Co/Ni values, with a range of 0.003 – 0.548, median of 0.0244 and mean of 0.116 ± 0.163 (1 *SD*, *n* = 0.164). In comparison, CR-AN-2 returned Ni concentrations of 92.0 – 220 ppm, median of 108 ppm and mean of 132 ± 59.1 ppm (1 *SD*, *n* = 4) and Co/Ni values of 0.192 – 0.503, median of 0.422 and mean of 0.385 ± 0.141 (1 *SD*, *n* = 4). Only one measurement was completed on a CR-EU-3 grain and so it could not be determined if this morphology showed a distinct trace element composition.

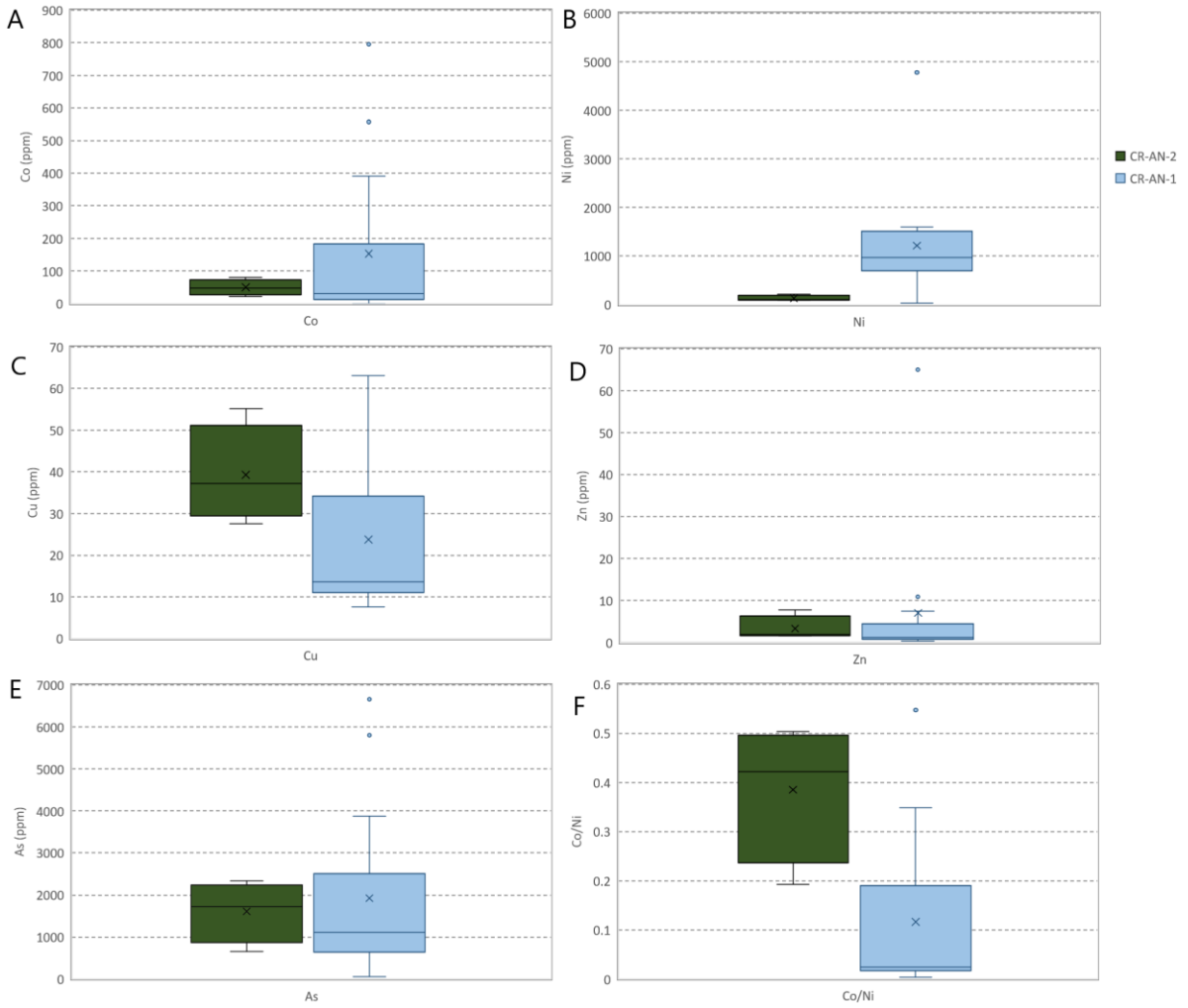

Figure 5.6. Box and whisker plots comparing the trace element composition and Co/Ni ratios of pyrite morphologies observed within the Luipaardsvlei Formation. A. Co concentrations, B. Ni concentrations, C. Cu concentrations, D. Zn concentrations, E. As concentrations, F. Co/Ni values.

Krugersdorp Formation

Pyrite from the Krugersdorp Formation returned Co concentrations of 1.47 – 3300 ppm, with a median of 41.1 ppm and mean of 443 ± 860 ppm (1 *SD*, *n* = 16). Ni concentrations had a range of 5.40 – 1850 ppm, median of 70.8 ppm and mean of 297 ± 493 ppm. Cu concentrations showed a range of 0.070 – 180 ppm, median of 5.10 ppm and mean of 32.7 ± 57.0 ppm (1 *SD*, *n* = 16). Zn concentrations returned a range of 0.240 – 1.90 ppm, with a median of 0.352 and a mean of 0.545 ± 0.436 ppm (1 *SD*, *n* = 16). As concentrations ranged between 4.10 – 22100 ppm, with a median of 1220 ppm and mean of 4190 ± 6561 ppm (1 *SD*, *n* = 16). Se concentrations showed a range of 1.10 – 188 ppm, median of 7.20 ppm and mean of 33.9 ± 58.3 ppm (1 *SD*, *n* = 16). Mo concentrations ranged from below the limit of detection to 0.065 ppm. Co/Ni values had a range of 0.099 – 18.1, median of 0.307 and mean of 2.66 ± 5.21 (1 *SD*, *n* = 16).

CR-AN-3 and CR-AN-5 grains showed distinct ranges of both Cu and As concentrations (Figure 5.7). CR-AN-3 grains showed higher Cu concentrations, with a range of 2.85 – 180 ppm, median of 7.75 ppm and mean of 51.5 ± 66.0 ppm (1 *SD*, *n* = 10) and higher As concentrations, with a range of 634 – 22100 ppm, median of 1680 ppm and mean of 6330 ± 7550 ppm (1 *SD*, *n* = 10). In contrast, CR-AN-5 grains showed Cu concentrations of 0.070 – 2.17 ppm, with a median of 0.140 ppm and mean of 0.524 ± 0.921 ppm (1 *SD*, *n* = 5) and As concentrations of 4.10 – 29.9 ppm, with a median of 26.4 ppm and mean of 20.3 ± 10.8 ppm (1 *SD*, *n* = 5). Inter-grain heterogeneity was high across the three CR-AN-5 grains measured (see Supplementary Information). Only one measurement was completed on CR-EU-1 grains, therefore it could not be determined if this morphology showed a distinct trace element composition.

Kimberley Formation

Within samples from the Kimberley Formation, pyrite returned Co concentrations of 0.168 – 1990 ppm, with a median of 231 ppm and mean of 394 ± 457 ppm (1 *SD*, *n* = 37). Ni concentrations showed a range of 250 – 4570 ppm, with a median of 1940 ppm and mean of 2020 ± 1050 ppm (1 *SD*, *n* = 37). Cu concentrations had a range of 0.115 – 830 ppm, median of 1.72 and mean of 77.9 ± 199 ppm (1 *SD*, *n* = 37). Zn concentrations returned a range of 0.205 – 28.9 ppm, with a median of 0.650 ppm and mean of 3.15 ± 5.43 ppm (1 *SD*, *n* = 37). As concentrations showed a range of 157 – 3760 ppm, median of 1670 ppm and mean of 1710 ± 976 ppm (1 *SD*, *n* = 37). Se concentrations showed a range of 5.08 – 98.2 ppm, median of 53.6 ppm and mean of 50.5 ± 23.0 ppm (1 *SD*, *n* = 37). Mo concentrations ranged from below the limit of detection to 24.2 ppm. Co/Ni values ranged between $1.26*10^{-4}$ and 3.23, with a median value of 0.116 and mean of 0.379 ± 0.695.

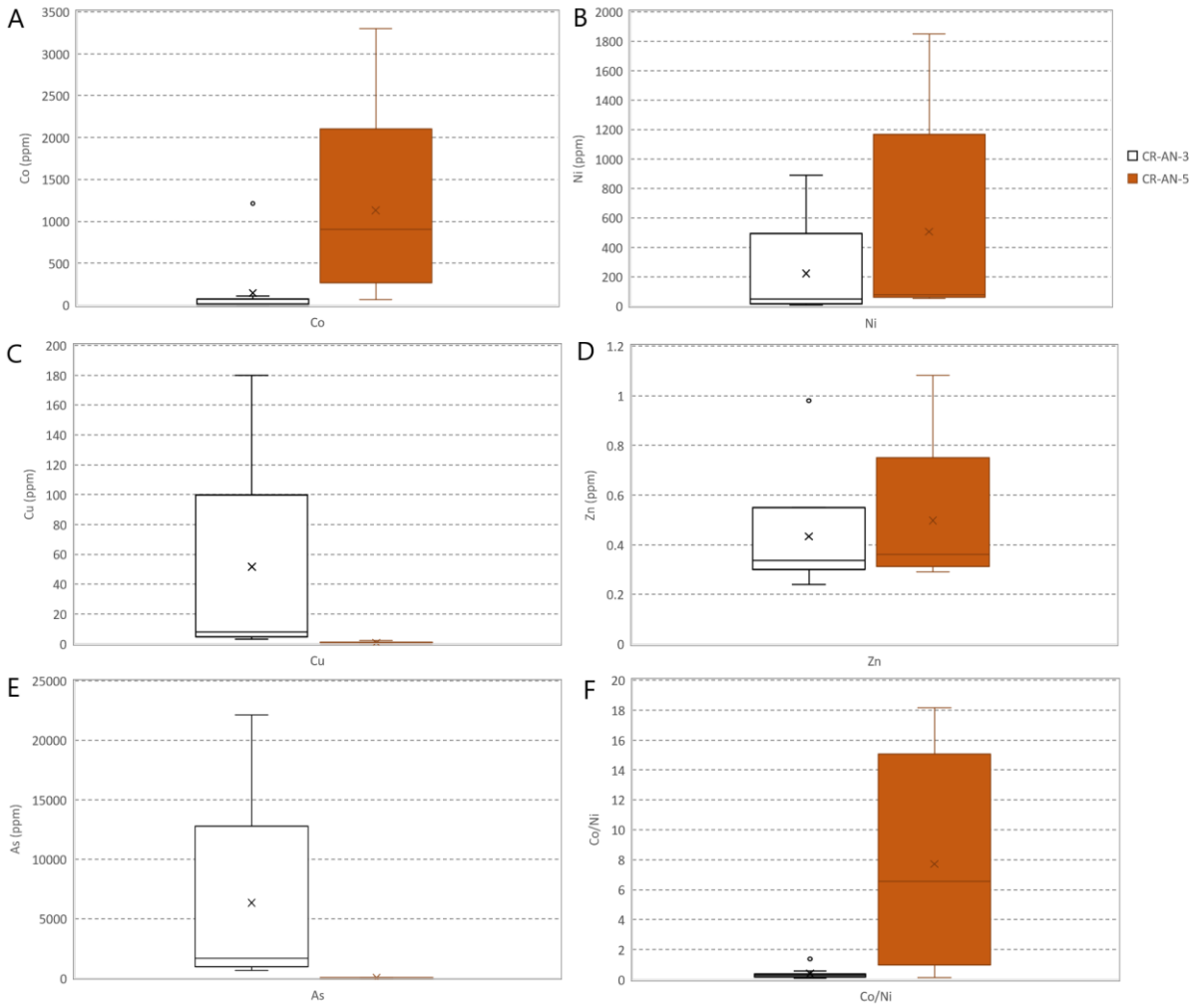

Figure 5.7. Box and whisker plots comparing the trace element compositions and Co/Ni ratios of pyrite morphologies observed within the Krugersdorp Formation. A. Co concentrations, B. Ni concentrations, C. Cu concentrations, D. Zn concentrations, E. As concentrations, F. Co/Ni ratios.

CR-EU-2 and CR-AN-4 could be distinguished based on Ni, Cu, Zn and As concentrations and Co/Ni values (Figure 5.8). CR-EU-2 grains showed higher Ni concentrations, with a range of 617 – 4570 ppm, median of 2010 ppm and mean of 2210 ± 944 ppm (1 *SD*, *n* = 33) , and higher As concentrations, with a range of 474 – 3760 ppm, median of 1800 ppm and mean of 1880 ± 896 ppm (1 *SD*, *n* = 33). Concentrations of Cu and Zn and Co/Ni values were lower in CR-EU-2 grains. Cu concentrations showed a range of 0.115 – 110 ppm, median of 1.29 ppm and mean of 11.9 ± 28.0 ppm (1 *SD*, *n* = 33) and Zn concentrations showed a range of 0.205 – 28.9 ppm, median of 0.560 ppm and mean of 2.45 ± 5.37 ppm (1 *SD*, *n* = 33). Co/Ni values showed a range of $1.26*10^{-4}$ – 3.23, with a median of 0.072 ppm and mean of 0.267 ± 0.627. In contrast, CR-AN-4 grains showed Ni concentrations of 250 – 692 ppm, median of 383 ppm and mean of 427 ± 203 ppm, Cu concentrations of 451 – 830 ppm, median of 605 ppm and mean of 623 ± 157 ppm (1 *SD*, *n* = 4), Zn concentrations of 6.98 –

10.5 ppm, median of 8.90 ppm and mean of 8.82 ± 1.48 ppm and As concentrations of 157 – 578 ppm, median of 315 ppm and mean of 340 ± 191 ppm (1 *SD*, *n* = 4). Co/Ni values showed a range of 0.434 – 1.64, with a median of 1.57 and mean of 1.30 ± 0.580.

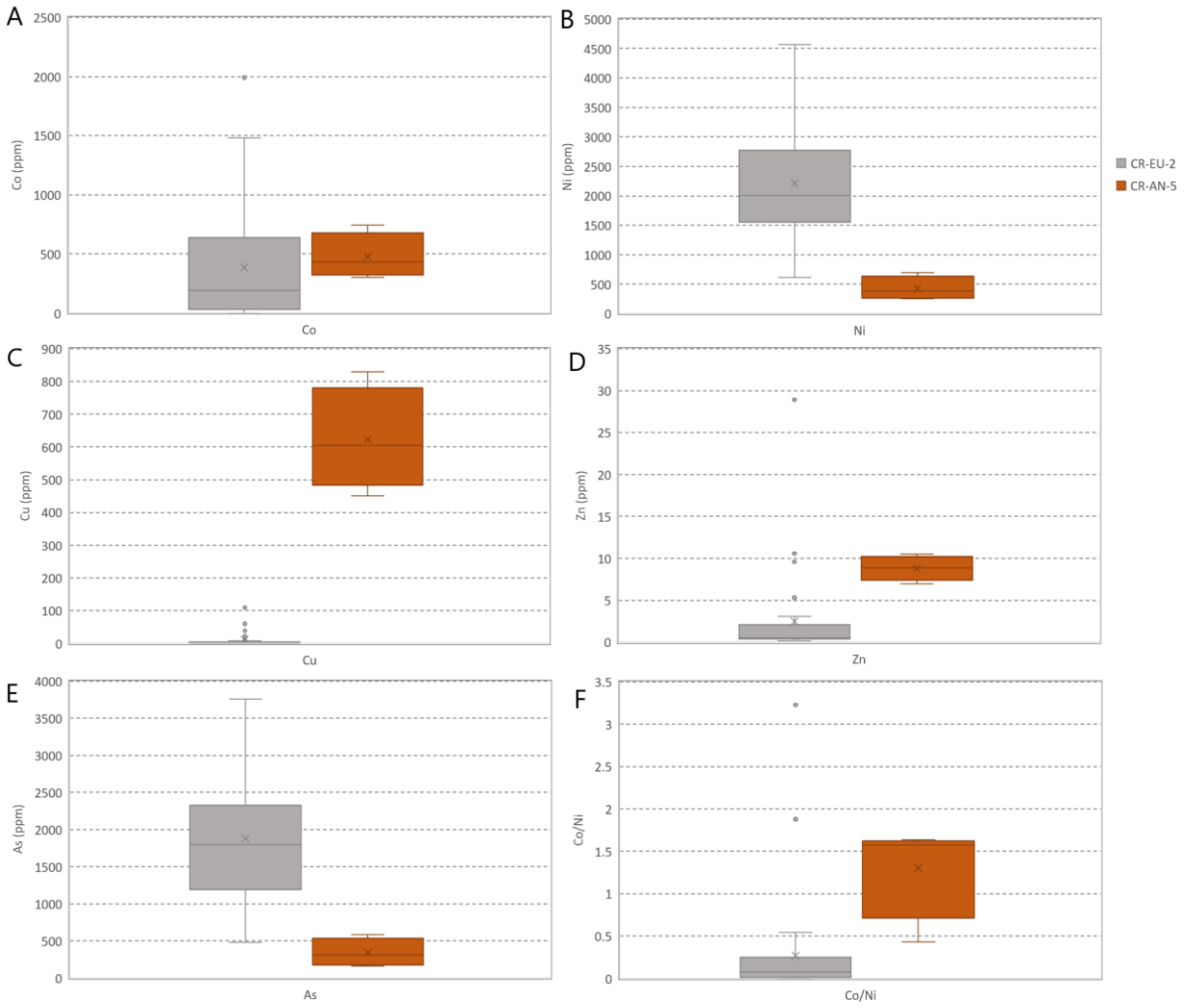

Figure 5.8. Box and whisker plots comparing the trace element composition and Co/Ni ratios of pyrite morphologies observed within the Kimberley Formation.

Elsburg Formation

Within the Elsburg Formation, CR-AN-5 grains showed Co concentrations of 166 – 1740 ppm, with a median of 1060 ppm and mean of 1030 ± 592 ppm (1 *SD*, *n* = 8). Ni concentrations showed a range of 52.3 – 777 ppm, median of 434 ppm and mean of 405 ± 256 ppm (1 *SD*, *n* = 8). Cu concentrations had a range of 0.350 – 86.0 ppm, median of 59.0 ppm and mean of 51.1 ± 41.5 ppm (1 *SD*, *n* = 8). Zn concentrations showed a range of 0.690 – 11.9 ppm, median of 7.70 ppm and mean of 7.00 ± 4.79 ppm (1 *SD*, *n* = 8). As concentrations showed a range of 3.00 – 1440 ppm, with a median of 134 ppm and mean of 319 ± 484 ppm (1 *SD*, *n* = 8). Se concentrations had a range of 10.6 – 122 ppm, median of 25.7 ppm and

mean of 37.7 ± 36.8 ppm (1 *SD*, *n* = 8). Mo concentrations ranged from below the limit of detection to 1.38 ppm. Co/Ni values had a range of 2.09 – 4.30, with a median value of 2.53 and mean of 2.86 ± 0.802 (1 *SD*, *n* = 8). Individual grains showed distinct trace element compositions (Supplementary Information).

Sulfur isotope composition

A summary of the sulfur isotope composition of pyrite from each sample is provided in Table 5.3. The complete data set and maps of analysis spots are provided in the Supplementary Information.

Luipaardsvlei Formation

Sulfur isotope compositions were similar across all three morphologies (Figure 5.9). The $\delta^{34}S$ values showed a range of 2.54 – 9.65 ‰, with a median of 4.33 ‰ and mean of 4.58 ± 1.24 ‰ (1 *SD*, *n* = 31). The $\Delta^{33}S$ values showed a range of -0.40 – 0.10 ‰, median of -0.17 ‰ and mean of -0.14 ± 0.12 ‰ (1 *SD*, *n* = 31) and $\Delta^{36}S$ values showed a range of -0.97 – 0.27 ‰, median of -0.46 ‰ and mean of -0.43 ± 0.34 ‰ (1 *SD*, *n* = 31).

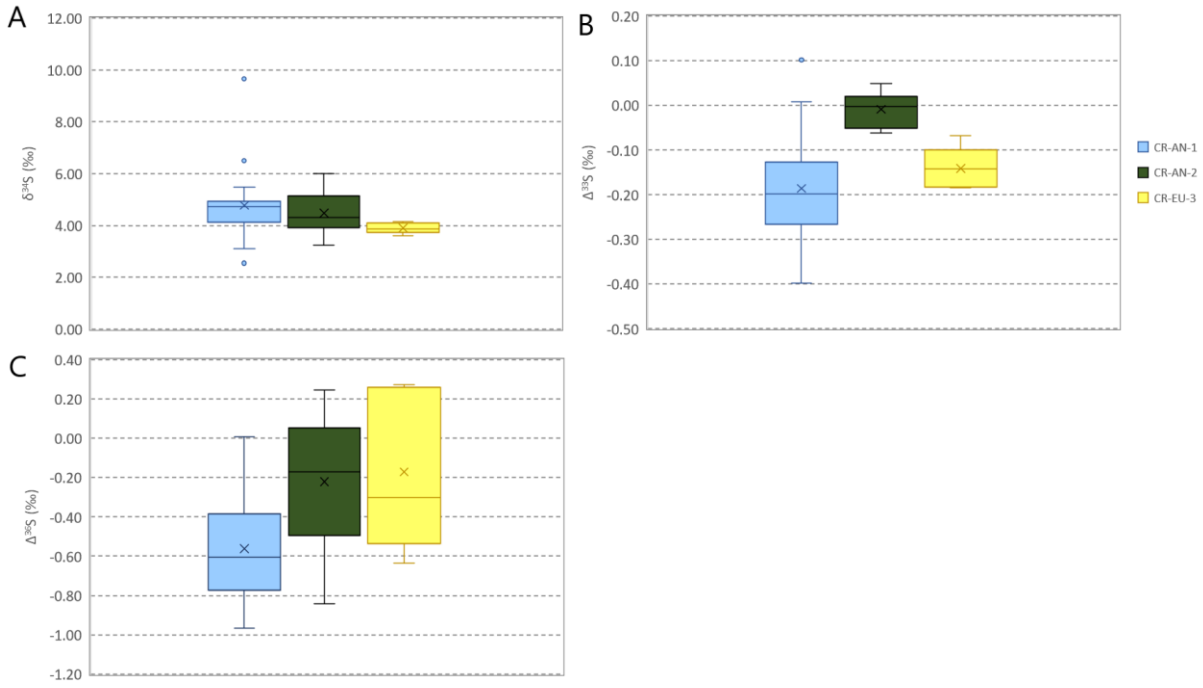

Figure 5.9. Box and whisker plots comparing the isotopic composition of the different pyrite morphologies observed within the Luipaardsvlei Formation. A. $\delta^{34}S$, B. $\Delta^{33}S$, C. $\Delta^{36}S$.

Table 5.3. Summary of the sulfur isotope composition of pyrite from the Central Rand Group.

Sample name	Isotope ratio	Min (‰)	Max (‰)	Median (‰)	Mean (‰)	StdDev (‰)
			SHRIMP-SI Analysis			
MMB6-3	$\delta^{34}S$	2.54	5.99	4.01	4.03	0.793
(n = 16)	$\Delta^{33}S$	-0.184	0.102	-0.055	-0.060	0.087
	$\Delta^{36}S$	-0.843	0.272	-0.342	-0.273	0.358
MMB6-12	$\delta^{34}S$	4.10	9.65	4.84	5.16	1.38
(n = 15)	$\Delta^{33}S$	-0.398	-0.124	-0.233	-0.236	0.073
	$\Delta^{36}S$	-0.965	-0.167	-0.647	-0.606	0.233
MMB6-1	$\delta^{34}S$	-1.48	5.79	2.65	1.63	2.58
(n = 10)	$\Delta^{33}S$	-0.061	0.039	0.009	0.001	0.033
	$\Delta^{36}S$	-0.613	0.341	-0.087	-0.087	0.282
MMB6-2	$\delta^{34}S$	2.60	7.16	3.70	4.17	1.41
(n = 15)	$\Delta^{33}S$	-0.281	0.057	-0.126	-0.121	0.090
	$\Delta^{36}S$	-0.831	-0.096	-0.420	-0.479	0.255
MMB6-9	$\delta^{34}S$	2.89	4.99	3.58	3.85	0.863
(n = 10)	$\Delta^{33}S$	-0.161	0.034	-0.052	-0.052	0.055
	$\Delta^{36}S$	-0.622	-0.083	-0.275	-0.277	0.166
MMB6-4	$\delta^{34}S$	-15.9	5.35	4.82	3.96	4.23
(n = 24)	$\Delta^{33}S$	-0.877	-0.094	-0.659	-0.653	0.141
	$\Delta^{36}S$	-2.39	-0.126	-1.93	-1.85	0.403
MMB6-5	$\delta^{34}S$	-3.68	21.9	4.89	4.86	3.50
(n = 35)	$\Delta^{33}S$	-0.970	-0.005	-0.650	-0.622	0.215
	$\Delta^{36}S$	-2.41	-0.355	-2.01	-1.84	0.533
MMB6-11	$\delta^{34}S$	0.416	5.33	4.24	3.30	1.74
(n = 24)	$\Delta^{33}S$	-0.879	0.045	-0.732	-0.525	0.364
	$\Delta^{36}S$	-2.56	0.017	-2.08	-1.54	0.924
MMB6-6	$\delta^{34}S$	-3.21	3.66	-0.739	-0.247	2.76
(n = 10)	$\Delta^{33}S$	-0.722	-0.028	-0.162	-0.253	0.246
	$\Delta^{36}S$	-0.980	0.616	-0.225	-0.184	0.488
			Bulk Analysis			
MMB6-4	$\delta^{34}S$	4.78	4.94	4.79	4.84	0.090
(n = 3)	$\Delta^{33}S$	-0.692	-0.686	-0.691	-0.690	0.003
	$\Delta^{36}S$	-2.06	-1.89	-1.99	-1.98	0.085
MMB6-5	$\delta^{34}S$	4.55	4.92	4.63	4.70	0.195
(n = 3)	$\Delta^{33}S$	-0.722	-0.692	-0.707	-0.707	0.015
	$\Delta^{36}S$	-2.08	-1.92	-2.07	-2.02	0.090
MMB6-11	$\delta^{34}S$	4.50	4.90	4.55	4.65	0.218
(n = 3)	$\Delta^{33}S$	-0.758	-0.729	-0.731	-0.739	0.016
	$\Delta^{36}S$	-2.01	-1.82	-1.86	-1.90	0.100

Krugersdorp Formation

As within the Luipaardsvlei Formation, sulfur isotope compositions were similar across the observed morphologies (Figure 5.10). However, CR-AN-5 grains were observed to show a wider range in $\delta^{34}S$ values than the other two morphologies (Figure 5.10A). The $\delta^{34}S$ values showed a range of -1.48 – 7.16 ‰, with a median of 3.39 ‰ and mean of 3.35 ± 2.01 ‰ (1 *SD*, *n* = 35). The $\Delta^{33}S$ values showed a range of -0.28 – 0.06 ‰, median of -0.06 and mean of -0.07 ± 0.08 ‰ (1 *SD*, *n* = 35) and $\Delta^{36}S$ values returned a range of -0.83 – 0.34 ‰, with a median of -0.30 ‰ and mean of -0.31 ± 0.29 ‰ (1 *SD*, *n* = 35).

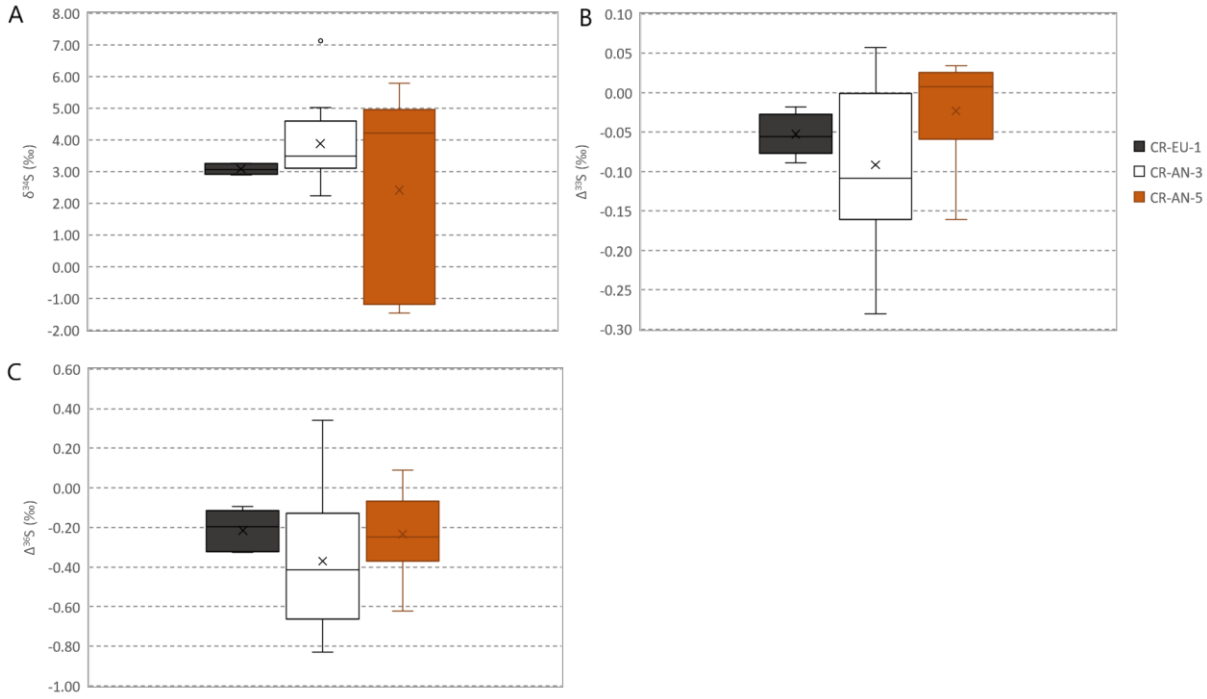

Figure 5.10. Box and whisker plots comparing the isotopic composition of the different pyrite morphologies observed within the Krugersdorp Formation. A. $\delta^{34}S$, B. $\Delta^{33}S$, C. $\Delta^{36}S$.

Kimberley Formation

Within the Kimberley Formation, CR-EU-2 and CR-AN-4 grains showed distinctly different isotopic compositions (Figure 5.11). CR-EU-2 grains showed $\delta^{34}S$ values of 3.71 – 6.20 ‰, with a median of 4.82 ‰ and a mean of 4.77 ± 0.39 ‰ (1 *SD*, *n* = 70). The $\Delta^{33}S$ values showed a range of -0.97 - -0.55 ‰, mean of -0.71 ± 0.09 ‰ (1 *SD*, *n* = 70) and $\Delta^{36}S$ values returned a range of -2.56 - -1.02 ‰, with a median of -2.02 ‰ and a mean of 0.202 ± 0.245 ‰ (1 *SD*, *n* = 70). In comparison, CR-AN-4 grains showed $\delta^{34}S$ values with a range of -15.86 – 21.85 ‰, median of 0.93 ‰ and mean of 0.78 ± 7.89 ‰ (1 *SD*, *n* = 13). The $\Delta^{33}S$ values showed a range of -0.12 – 0.05 ‰, with a median of -0.06 ‰ and mean of -0.05 ±

0.05 ‰ (1 *SD*, *n* = 13) and $\Delta^{36}S$ values returned a range of -0.70 – 0.02 ‰, with a median of -0.36 ‰ and mean of -0.37 ± 0.23 ‰.

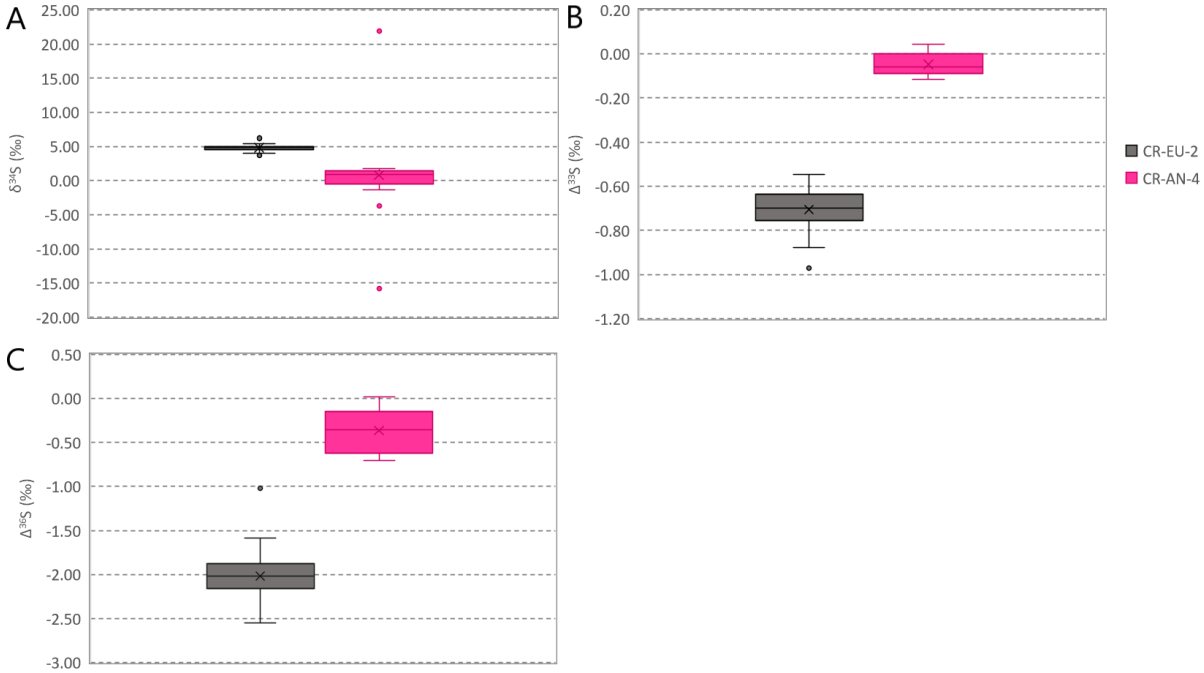

Figure 5.11. Box and whisker plots comparing the isotopic composition of the different pyrite morphologies observed within the Kimberley Formation. A. $\delta^{34}S$, B. $\Delta^{33}S$, C. $\Delta^{36}S$.

Elsburg Formation

CR-AN-5 grains within the Elsburg Formation showed $\delta^{34}S$ values of -3.21 – 3.66 ‰, with a median of -0.74 ‰ and mean of -0.25 ± 2.76 ‰ (1 *SD*, *n* = 10). Individual grains showed distinct ranges of $\delta^{34}S$ values (Table 5.4). The $\Delta^{33}S$ values showed a range of -0.72 - -0.03 ‰, with a median of -0.16 ‰ and mean of -0.25 ± 0.25 ‰ (1 *SD*, *n* = 10) and the $\Delta^{36}S$ values showed a range of -0.98 – 0.62 ‰, median of -0.23 ‰ and mean of -0.18 ± 0.49 ‰ (1 *SD*, *n* = 10).

5.6 Discussion

Pyrite paragenesis

Trace element measurements and morphological and textural observations identified detrital, diagenetic and epigenetic pyrite species.

Table 5.4. $\delta^{34}S$ values of CR-AN-5 grains from the Elsburg Formation.

Sample	Grain Number	Analysis spot number	$\delta^{34}S$ (‰)
MMB6-6	1	1.1	0.88
MMB6-6	1	1.2	2.46
MMB6-6	2	2.1	-2.20
MMB6-6	2	2.2	-1.97
MMB6-6	2	2.3	0.49
MMB6-6	3	3.1	-3.21
MMB6-6	3	3.2	-3.02
MMB6-6	3	3.3	-3.00
MMB6-6	4	4.1	3.66
MMB6-6	4	4.2	3.43

Detrital grains

CR-AN-5 grains from the Elsburg and Krugersdorp formations were determined to be detrital in origin. These grains display the rounded edges that are typical of grains that have undergone mechanical transport. Both the non-porous and porous grains are similar in appearance to detrital pyrite previously observed within the Central Rand Group. Non-porous grains are comparable to 'compact rounded grains' described by Saager (1970), 'compact pyrite' described by England et al. (2002) and 'DET-1' pyrite described by Guy et al. (2010, 2014). Porous grains are analogous in texture to 'porous rounded pyrite' from Saager (1970), 'well-rounded porous pyrite' from England et al. (2002) and 'reworked syngenetic and diagenetic pyrite' from Guy et al. (2014). Additionally, CR-AN-5 grains form bands or lag deposits where they are associated with rounded grains of heavy minerals, including titanium oxides and zircon. This morphology and concentration of heavy minerals is typical of detrital mineral, or placer, deposits. The inter-grain heterogeneity in trace element concentrations and $\delta^{34}S$ values observed for CR-AN-5 grains is also conclusive with a detrital origin and likely reflects variation in the source rocks (Meyer et al., 1990; Barton and Hallbauer, 1996; England et al., 2002). The provenance of detrital grains is discussed in a later section.

Diagenetic grains

CR-EU-3, CR-AN-1, CR-AN-2 and CR-AN-4 grains were determined to be diagenetic in origin. Small euhedral pyrite grains such as CR-EU-3 are believed to precipitate directly from solution during diagenesis (Taylor and Macquaker, 2000). Similar grains have been

previously been observed within the Witwatersrand Supergroup and interpreted to be diagenetic in origin (Guy et al., 2010, 2014).

CR-AN-1 grains were identified to be cement concretions, which infilled pore spaces and overprinted the edges of surrounding grains and clasts during diagenesis (Carstens, 1986; Salles-Martinez, 1996). The limited number of point contacts between the grains of the sandstone suggests that the cement concretions formed relatively early during diagenesis (Salles-Martinez, 1996). Whilst there are no direct analogues of the trace element composition of diagenetic pyrite grains within fluvial sandstones, the trace element compositions of CR-AN-1 grains are comparable to diagenetic grains from other sedimentary environments (Price, 1972; Gregory et al., 2015a) and to diagenetic pyrite cements previously observed within the Witwatersrand Supergroup (Guy et al., 2010). Similarly, Co/Ni, Cu/Ni, Zn/Ni and As/Ni values typically fall within the range of values observed for diagenetic pyrite (Price, 1972; Gregory et al., 2015a). As these grains are from a different sedimentary environment than those analyzed in Gregory et al. (2015), which focused on grains from black shales, their trace element composition has also been compared to the trace element composition of diagenetic cements within the Witwatersrand Supergroup to confirm their paragenesis. It was observed that the Co/Ni, Co/As and Ni/As relationships are similar to those previously observed for pyrite of this morphology within the Witwatersrand Supergroup (Guy et al., 2010). This provides further evidence for a diagenetic origin.

CR-AN-2 was interpreted to represent a displacive nodule which formed during diagenesis (Salles-Martinez, 1996). Displacive nodules have previously been observed within the Witwatersrand Supergroup, both in situ within the West Rand Group (Guy et al., 2010) and as detrital grains/fragments within quartz pebble conglomerates of the Central Rand Group (England et al., 2002; Guy et al., 2014). Whilst the texture of the nodule observed here differs from that of many of the nodules previously observed (England et al., 2002, Figure 6A-D; Guy et al., 2014, Figure 3j-m;) a texture consisting of numerous closely-packed, anhedral crystals, such as seen in CR-AN-2, is common in diagenetic pyrite nodules (Gregory et al., 2019). Trace element concentrations were within the ranges previously observed for diagenetic pyrite (Price, 1972; Gregory et al., 2015a) and Co/Ni, Cu/Ni and Zn/Ni values also fell within ranges for diagenetic pyrite. As/Ni values were observed to fall outside the set range ($0.10 < As/Ni < 10$; Gregory et al., 2015a), however, as mentioned above, these values were defined from pyrite from a different sedimentary environment and therefore this does not necessarily exclude a diagenetic origin. The Co/As and Ni/As relationships for this nodule

were observed to be similar to those from diagenetic grains within the Witwatersrand Supergroup (Guy et al., 2010), suggesting that a diagenetic origin is still the most likely conclusion. The scarcity of matrix inclusions (Figure 5.3) and low levels of variation and lack of zonation in both trace element concentrations and $\delta^{34}S$ values suggest that the nodule formed early during diagenesis when sediment porosity was high and pore waters were still connected to the overlying water column (Gregory et al., 2019).

CR-AN-4 grains were determined to be diagenetic on the basis of their conformity with the surrounding matrix and trace element composition. As with the morphologies discussed above, trace element concentrations and Co/Ni, Cu/Ni, Zn/Ni and As/Ni values fell within the ranges for diagenetic pyrite (Price et al., 1972; Gregory et al., 2015a).

Epigenetic grains

Both CR-AN-3 and CR-EU-1 grains were identified as epigenetic due to large crystal size (>500 µm), high abundance and the presence of crystallographically-aligned pores (Figure 5.3). All of these features are found in epigenetic pyrite grains (Ramdohr, 1958; Saager, 1970; McClay and Ellis, 1983; Craig et al., 1998; Guy et al., 2010) and epigenetic grains and overgrowths showing similar features have previously been observed within the Witwatersrand Supergroup (e.g. Saager et al., 1970; Guy et al., 2010, 2014). Additionally, these aggregates were observed to overprint the clasts and grains of the surrounding rocks, suggesting late formation. The As/Ni values for both morphologies were elevated and typically outside of the range for diagenetic pyrite (Gregory et al., 2015a). The Co/As and Ni/As values for these grains were also observed to be outside of the field of values previously observed for diagenetic pyrite from the Witwatersrand Supergroup (Guy et al., 2010), providing further evidence for an epigenetic origin. Whilst the low Co/Ni values are similar to those observed for diagenetic pyrite (Price, 1972; Guy et al., 2014; Gregory et al., 2015a), analyses of epigenetic pyrite have also returned low Co/Ni values similar to those observed for these morphologies (Price et al., 1972; Guy et al., 2010). This highlights the importance of using a combination of morphological observations and trace element analyses to determine paragenesis. In many of the CR-AN-3 grains from sample MMB6-2, it appears that the porous zones represent epigenetic overgrowths, however, there is no significant difference in the trace element and isotopic compositions of the porous and non-porous zones.

CR-EU-2 grains were similarly identified as epigenetic due to the large crystal size, abundance and the observation that they overprinted the surrounding morphology (Figure

5.3B, G). The observation of anhedral cores and offshoots (Figure 5.3B, G) also provided evidence for late formation, with the euhedral overgrowths showing different trace element and isotopic compositions. Where the euhedral grains had grown around an anhedral core, the overgrowths were typically >100 µm in thickness (Figure 5.4), which is thicker than expected for diagenetic overgrowths (~10 µm; Guy et al., 2014). Similar epigenetic grains, aggregates and overgrowths have been previously observed within the Witwatersrand Supergroup (e.g. Feather and Koen, 1975; Hirdes and Saager, 1983; Guy et al., 2010) and show similar Co, Ni and As concentrations and Co/Ni, Co/As and As/Ni relationships to CR-EU-2 grains (Guy et al., 2010).

Provenance of detrital grains

Previously, detrital pyrite grains within the Central Rand Group have been linked to numerous source terrains. These include, but are not limited to, sedimentary successions (Dimroth, 1979; Hallbauer, 1986; Hofmann et al., 2009; Large et al., 2013; Guy et al., 2014), granite-greenstone basement and igneous sources (Utter, 1978; Hirdes and Saager, 1983; Hofmann et al., 2009; Koglin et al., 2010; Guy et al., 2014), volcanogenic massive sulfide deposits (Hofmann et al., 2009) and metamorphic/hydrothermal terrains (Meyer et al., 1990; Hofmann et al., 2009; Guy et al., 2014). On the basis of textural, isotopic and trace element evidence, it is proposed that the detrital grains within the Krugersdorp and Elsburg formations have been collected from hydrothermal, hydrothermal or magmatic, and sedimentary source rocks.

Non-porous grains from both the Krugersdorp and Elsburg formations are interpreted to represent an igneous or hydrothermal source. The non-porous texture is inconclusive in regards to origin, as grains with this texture have been shown to represent numerous sources (e.g. Hofmann et al., 2009; Large et al., 2013). Similarly, the isotopic composition is inconclusive, where the small positive and negative $\delta^{34}S$ values (~-2 to + 6 ‰) and $\Delta^{33}S$ and $\Delta^{36}S$ values of approximately zero (Figure 5.12) could represent either a crustal MDF source (Guy et al., 2014) or a magmatic or hydrothermal source (Hofmann et al., 2009). However, these grains show low concentrations of Co, Ni and As, which is typical of hydrothermal pyrite (Utter, 1978; Meyer et al., 1990; Guy et al., 2010; Koglin et al., 2010) and eliminates diagenetic pyrite carrying an MDF crustal sulfur signature as an option. The source cannot be further narrowed as the trace element composition of magmatic/igneous pyrite is largely undefined, with the behaviour of Co and Ni believed to reflect that in the source rocks (Price, 1972).

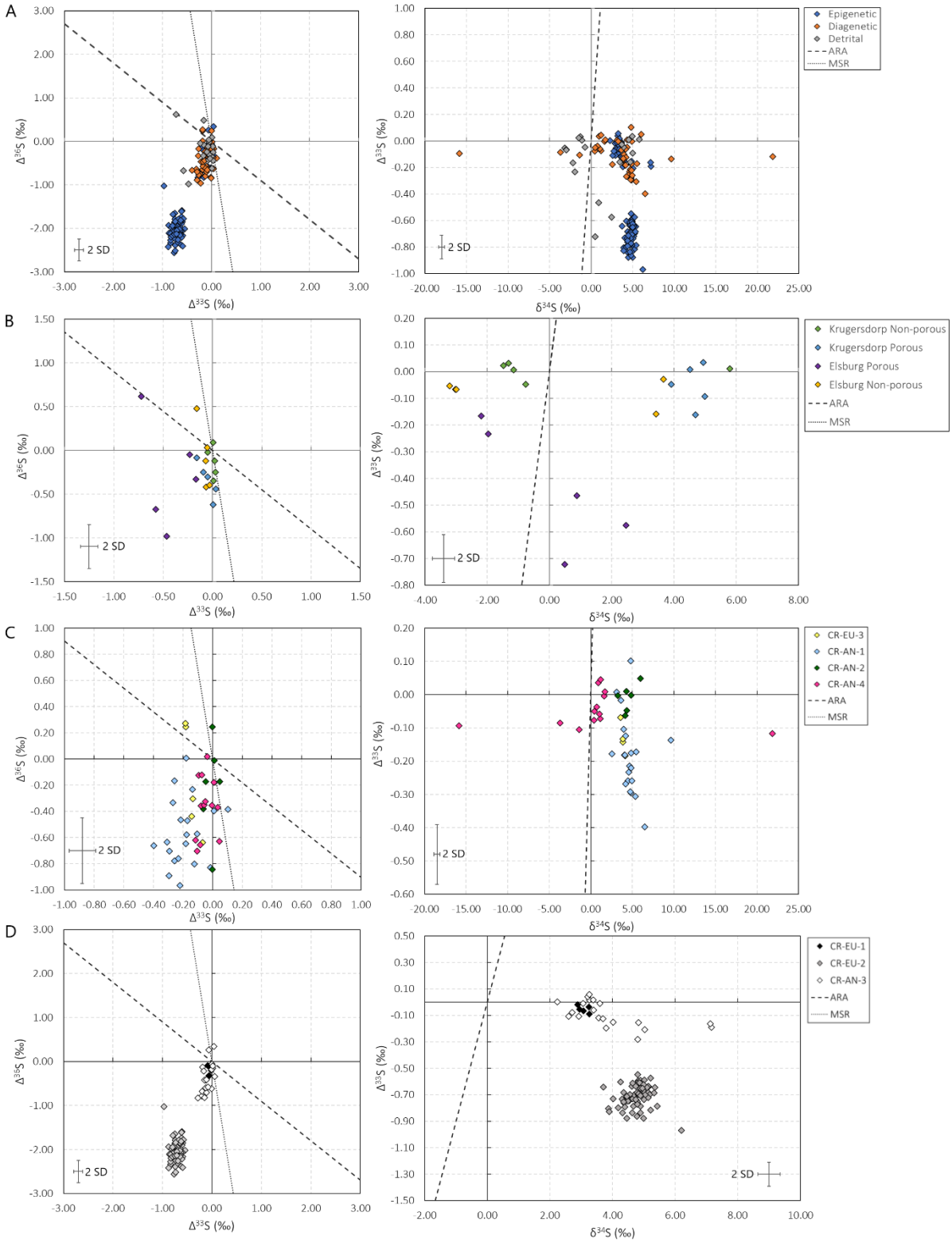

Figure 5.12. Sulfur isotope plots for data collected from pyrite grains from the Central Rand Group. A. Data separated by paragenesis, B. Data from detrital grains, separated by formation and texture, C. Data for diagenetic grains separated by morphology, D. Data from epigenetic grains separated by morphology.

Porous grains within the Krugersdorp Formation are suggested to be reworked epigenetic grains, i.e. they were collected from a hydrothermal source. These grains show a similar texture to epigenetic CR-EU-1 and CR-AN-3 grains, where they have large, irregularly-shaped pores (Figure 5.13). This is in contrast to many of the porous detrital grains observed within the QPCs, which show radial, banded, dendritic and other textures consistent with a diagenetic origin (Saager et al., 1970; England et al., 2002; Large et al., 2013; Guy et al., 2014). Additionally, the grains show a restricted range in positive $\delta^{34}S$ values and $\Delta^{33}S$ and $\Delta^{36}S$ values of approximately zero (Figure 5.12), that are consistent with a hydrothermal or igneous origin. This isotopic composition is observed to be similar to that of epigenetic grains (CR-EU-1, CR-AN-4) observed within this study, re-worked epigenetic grains observed by Guy et al. (2014) and grains interpreted to have been collected from a magmatic or hydrothermal source by Hofmann et al. (2009) (Figure 5.14). A hydrothermal source is favoured due to the similarities in texture between these grains and observed epigenetic grains. Trace element data is unavailable from these grains due to their high porosity.

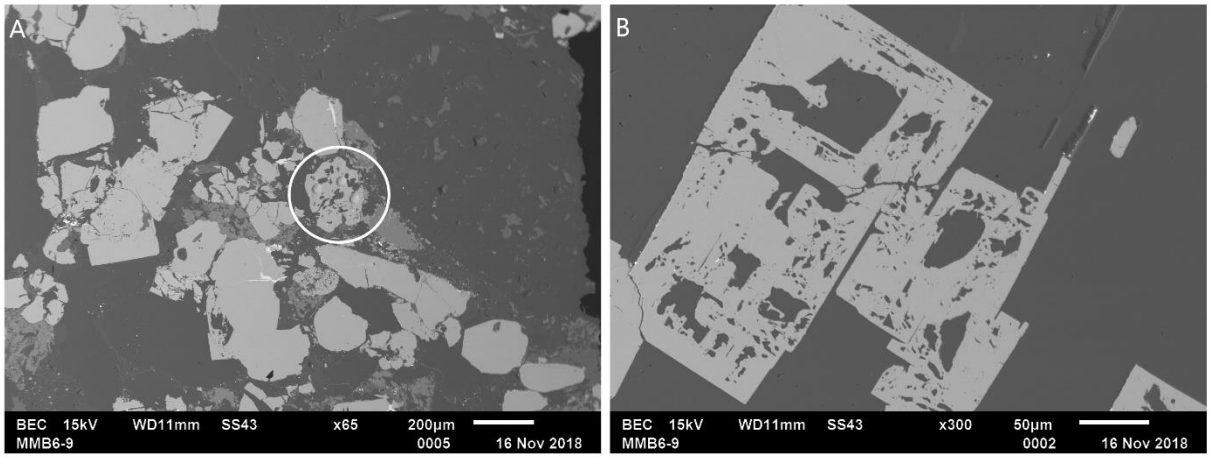

Figure 5.13. Comparison of the texture of A. Porous detrital grains within the Krugersdorp Formation (grain of interest shown in white) and B. CR-EU-1 epigenetic grains. Note similarity in pore shapes and distribution.

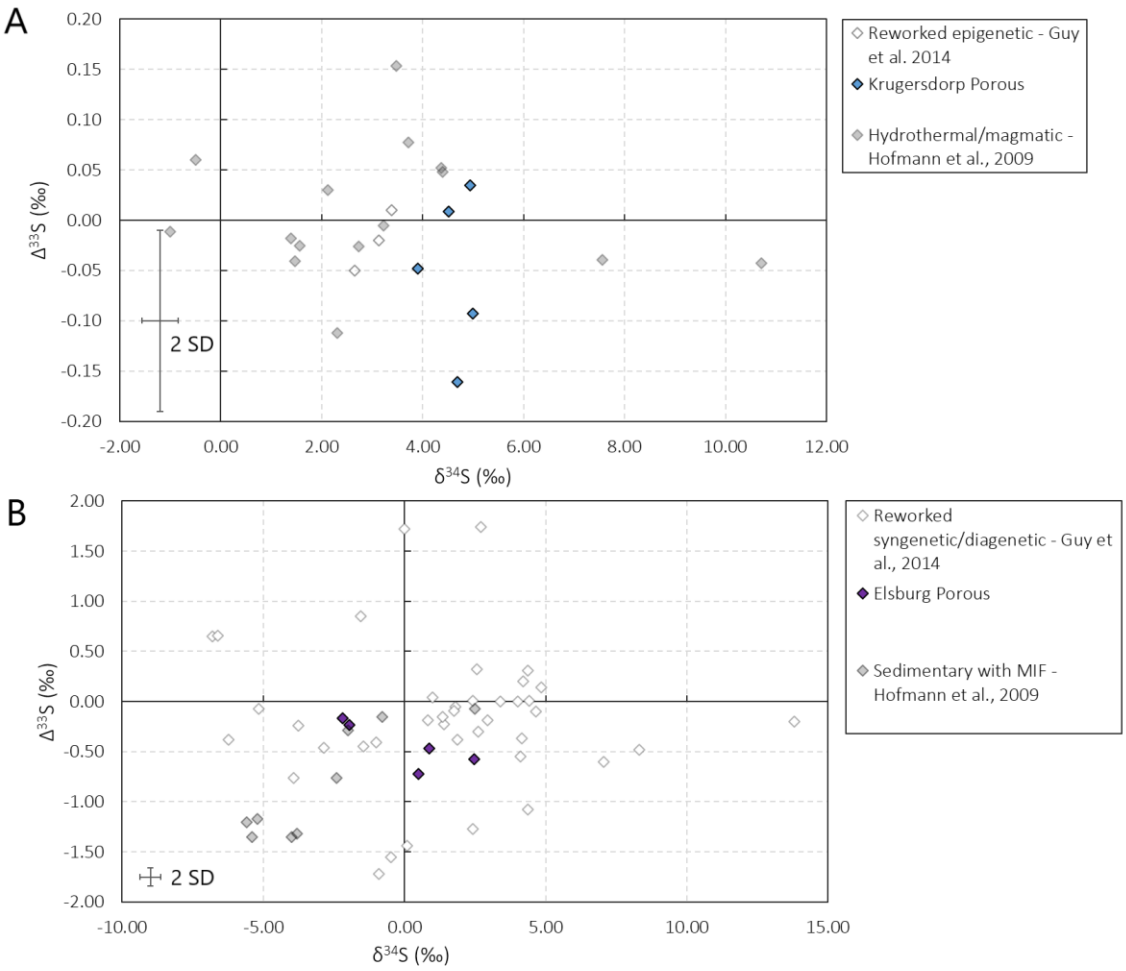

Figure 5.14. A. Comparison of isotopic composition of porous detrital grains from the Krugersdorp Formation and re-worked epigenetic grains (Guy et al., 2014) and re-worked magmatic/hydrothermal grains (Hofmann et al., 2009) previously observed within reefs and conglomerates of the Kaapvaal Craton. B. Comparison of isotopic composition of porous detrital grains from the Elsburg Formation and re-worked syngenetic/diagenetic grains (Guy et al., 2014) and reworked sedimentary grains (Hofmann et al., 2009) previously observed within reefs and conglomerates of the Kaapvaal Craton.

Porous grains from the Elsburg Formation are interpreted to be re-worked diagenetic grains originating from a sedimentary source. These grains show fine, randomly-distributed pores and show a similar texture to that of diagenetic grains observed both within the Witwatersrand Supergroup (e.g. Guy et al., 2010) and elsewhere (e.g. Gregory et al., 2015a, b). The small positive and negative $\delta^{34}S$ values are inconclusive in regards to provenance, but the small, resolvable negative $\Delta^{33}S$ values and non-zero $\Delta^{36}S$ values (Figure 5.12) suggest incorporation of atmospheric MIF sulfur (Farquhar et al., 2000, 2001) and thus a likely diagenetic origin. In $\Delta^{33}S$-$\delta^{34}S$ space, these grains show similar isotopic composition to 're-worked syngenetic/diagenetic grains' observed by Guy et al. (2014) and 'sedimentary' grains observed by Hofmann et al. (2009) from the QPC's (Figure 5.14). Observed concentrations of

Co, Ni and As and Co/Ni values are similar to those previously obtained from diagenetic pyrite from the Witwatersrand Supergroup (Guy et al., 2010; Large et al., 2013).

Isotopic signatures of diagenetic grains

CR-AN-1 grains

CR-AN-1 grains from the Luipaardsvlei Formation could be distinguished from other diagenetic grains due to small but resolvable negative $\Delta^{33}S$ values, where all other diagenetic species showed $\Delta^{33}S$ values of approximately zero (Figure 5.12C). The observed negative $\Delta^{33}S$ values suggest incorporation of sulfur sourced from the MIF sulfate aerosol (Farquhar et al., 2001). However, there is substantial deviation from the Archean Reference Array (ARA) in $\Delta^{36}S$ (Figure 5.12C) that suggests that these signatures were not produced solely through atmospheric photolysis reactions. Instead, it is possible that the signatures represent either mixing between MIF and MDF sulfur pools, a combination of atmospheric and other fractionation processes or a different process all together. These options are discussed below.

The first option is that the signatures represent mixing between MIF and MDF sulfur. When compared to literature data, the isotopic signatures in CR-AN-1 grains are similar to those previously observed by Guy et al. (2012, 2014) in fluvial sediments of the West and Central Rand Groups (Figure 5.15). These signatures were explained to represent mixing between atmospheric MIF sulfate, crustal MDF sulfate, where crustal sulfur carries $\Delta^{33}S$ values of approximately zero and $\delta^{34}S$ of ~0 - +10 ‰ (Chaussidon et al., 1989; Ohmoto and Goldhaber, 1997; Guy et al., 2012) and marine MDF sulfate, with $\delta^{34}S$ of ~5 – 15 ‰ (Lambert et al., 1978; Canfield and Raiswell, 1999; Ono et al., 2003) and $\Delta^{33}S$ of approximately zero (Guy et al., 2014). Under this hypothesis, the MIF sulfate would contribute negative $\Delta^{33}S$ values, whilst the MDF sulfur would dilute the $\Delta^{33}S$ values and provide positive $\delta^{34}S$ values, resulting in the small negative $\Delta^{33}S$ values and small positive $\delta^{34}S$ values observed in CR-AN-1 grains (Figure 5.12C).

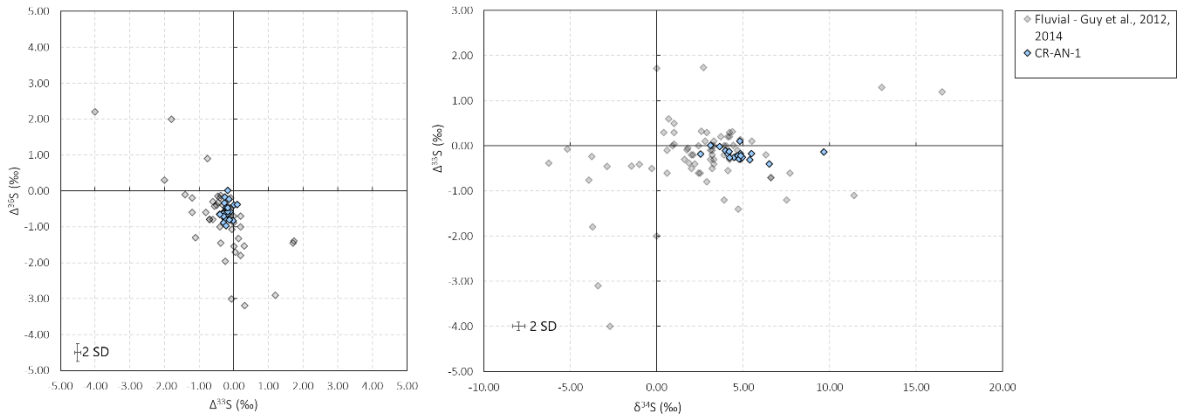

Figure 5.15. Comparison of the isotopic signatures of CR-AN-1 grains and reworked syngenetic/diagenetic grains from the QPCs within the Central Rand Group (Guy et al., 2014) and diagenetic grains from fluvial sedimentary rocks of the upper West Rand Group.

This explanation is largely agreeable, however does not explain the small, but resolvable, negative $\Delta^{36}S$ values observed both within the grains from this study and from Guy et al. (2012, 2014). It may be possible that adding a sulfur component produced through MSR would explain these negative $\Delta^{36}S$ values, as this process discriminates against the heavy isotopes, typically producing negative $\Delta^{36}S$ values (Ono et al., 2006a; Johnston et al., 2007). MSR may have involved the MIF sulfate aerosol (e.g. Shen et al., 2009; Zhelezinskaia et al., 2014; Mishima et al., 2017) or it may have involved MDF sulfate, with the product sulfur being mixed with both the MIF sulfate and crustal sulfur. The positive $\delta^{34}S$ values of the other two sulfur sources may have masked the negative $\delta^{34}S$ values typically produced through MSR (Thode et al., 1951; Jones and Starkey, 1957; Harrison and Thode, 1958), resulting in the small positive values observed here. Evidence for MSR within fluvial sediments of the Witwatersrand Supergroup has previously been recorded by Guy et al. (2012), in the form of variable $\delta^{34}S$ values and covariation of sulfur and organic carbon contents. Therefore, it would not be beyond reason that sulfur would be contributed from this source.

The second option is that the isotopic signatures record MSR of the MIF sulfate aerosol. This has previously been observed in numerous Archean sedimentary successions, where this process caused deviation from the ARA in $\Delta^{36}S$ and $\Delta^{33}S$, where $\Delta^{33}S$ and $\Delta^{36}S$ values are forced downwards off the ARA, along a slope of $\Delta^{36}S/\Delta^{33}S$ = ~-6.9, the characteristic slope produced by MSR (Ono et al., 2006a; Johnston et al., 2007; Ueno et al., 2008; Shen et al., 2009; Zhelezinskaia et al., 2014; Mishima et al., 2017). Similar to previous studies, CR-AN-1 grains show a steep $\Delta^{36}S/\Delta^{33}S$ trend which extends downwards from a negative $\Delta^{33}S$ value, suggesting that these signatures could have been produced through MSR. However, the

relatively restricted range of small positive $\delta^{34}S$ values observed for the CR-AN-1 grains is atypical of MSR, which typically produced large and variable fractionations in $\delta^{34}S$ (Thode et al., 1951; Jones and Starkey, 1957; Harrison and Thode, 1958). Additionally, for MSR, fractionation in $\Delta^{36}S$ scales with fractionation in $\delta^{34}S$ (Johnston et al., 2007). Experimentally, it has been shown that $\Delta^{36}S$ fractionations of ~1 ‰ (such as the fractionations seen in CR-AN-1 grains), require a $^{34}\alpha$ value of between ~0.965 – 0.985 ‰ (Johnston et al., 2007), where α is the fractionation factor between two reservoirs, as given by Equation 5.1:

$$^{3x}\alpha = \frac{^{3x}R_A}{^{3x}R_B} \quad (5.1)$$

Where A and B represent the two sulfur pools of interest.

When these $^{34}\alpha$ values of ~0.965 – 0.985 are inserted into Equation 5.2, it shows that negative $\delta^{34}S$ fractionations of ~15 – 35 ‰ correspond with $\Delta^{36}S$ fractionations of ~1 ‰.

$$\delta^{34}S = 1000 \times (^{34}\alpha - 1) \quad (5.2)$$

The $\delta^{34}S$ value of Archean non-marine surface waters is currently undefined but could be expected to be similar to the $\delta^{34}S$ value of Archean seawater as MIF sulfate would have been the major source of sulfate for both pools (due to the dominance of atmospheric photolysis reactions during the Archean). For CR-AN-1 grains, even if the maximum estimate of $\delta^{34}S$ = ~16 ‰ for Archean seawater sulfate (Lambert et al., 1987; Canfield and Raiswell, 1999; Ono et al., 2003) is used to estimate the $\delta^{34}S$ values of the surface water, the $\delta^{34}S$ fractionations required to produce the observed $\Delta^{36}S$ values could not have produced the $\delta^{34}S$ values observed for these grains. Therefore, it does not seem likely that the observed signatures were produced through MSR of MIF sulfate.

As mentioned in Chapter 3, two other processes are known to produce small negative $\Delta^{33}S$ values: photolysis of carbonyl sulfide (OCS) and biomass burning. As previously described, photolysis reactions involving OCS and UV radiation of wavelengths 200 – 260 nm results in dissociation of OCS to carbon monoxide and elemental sulfur (Sidhu et al., 1966; Rudolph and Inn, 1981). This process causes small, typically negative fractionations in $\Delta^{33}S$ and $\Delta^{36}S$ of ~-0.20 - +0.05 ‰ for $\Delta^{33}S$ and ~-1.40 – 0.20 ‰ for $\Delta^{36}S$ (Lin et al., 2011). The fractionations in $\delta^{34}S$ are also negative, and within the range of ~2 – 7 ‰ (Lin et al., 2011). Whilst the fractionations in $\Delta^{33}S$ and $\Delta^{36}S$ produced through this process are similar to the isotopic composition of the CR-AN-1 grains, it is unknown whether the observed $\delta^{34}S$ values could be

produced through this process because the $\delta^{34}S$ composition of Archean atmospheric OCS is unknown. The $\delta^{34}S$ value of modern atmospheric OCS has been estimated at ~11 ‰ (Newman et al., 1991) and if this estimate is used the observed $\delta^{34}S$ values could have been produced through this process. However, modern atmospheric OCS is sourced from a number of sources that would not have been active during the Archean, such as wetlands, biomass burning and anthropogenic activities (Watts, 2000; Montzka et al., 2007; Schmidt et al, 2013), and omission of these sources may impact the $\delta^{34}S$ value of atmospheric OCS. Additionally, whilst OCS has been proposed to be an abundant atmospheric sulfur species prior to the Pongola glaciations (Ueno et al., 2009), it is unknown what role it played in the atmosphere after these events. Questions are also raised as to why the elemental sulfur produced through this process would be preserved in terrestrial environments when the elemental sulfur produced through SO_2 photolysis was not (positive $\Delta^{33}S$ signatures were not observed in fluvial sediments, diamictites or paleosols). Extra research regarding OCS photolysis, such as defining the $\delta^{34}S$ value of Archean OCS, further constraining the sulfur isotope fractionations produced by OCS (currently there is only one study available) and investigating the role and availability of OCS in the Archean atmosphere, is required before this option can be considered further. However, it seems unlikely that OCS is the source of the observed signatures.

Also as previously described, primary sulfate produced during biomass burning has been observed to carry $\Delta^{33}S$ values of ~0.03 - -0.23 ‰ and $\Delta^{36}S$ values of ~-0.54 - -2.06 ‰ (Shaheen et al., 2014). However, as in Chapter 3, this option is not considered to be viable for producing these samples as biomass burning is unlikely to have occurred during the Archean. This is due to the limited amount of biomass and low atmospheric oxygen concentrations, which likely would have prevented combustion.

Regardless of the origin of these signatures, the similarity between the isotopic signatures of these grains and re-worked diagenetic grains within the QPCs (Figure 5.15) provides support for suggestions that pyrite within the QPCs was sourced from sediments of the Central Rand Group (Dimroth, 1979; Hallbauer, 1986; Large et al., 2013; Guy et al., 2014).

CR-EU-3 and CR-AN-2 grains

Both CR-EU-3 grains and CR-AN-2 grains show similar restricted ranges of $\delta^{34}S$ to CR-AN-1 grains but have $\Delta^{33}S$ of ~0 ‰. The observed $\Delta^{36}S$ values are also ~0 ‰, with the exception of two outliers of ~-0.80 ‰ and ~-0.60 ‰ (Figure 5.12C). These isotopic signatures are conclusive with MDF sulfur, sourced from either a juvenile volcanic source or a mixed crustal

source such as the one described by Guy et al. (2012). Either of these sources could have produced the small positive $\delta^{34}S$ values observed for these grains (Macnamara et al., 1951; Thode et al., 1961; Sakai et al., 1984; Chaussidon et al., 1989; Torssander et al., 1989; Guy et al., 2012).

Previously, Guy et al. (2014) suggested that similar isotopic compositions observed within detrital pyrite of the QPCs may represent MSR occurring in a sulfate-limited environment. As mentioned above, some data points collected from these grains do show negative $\Delta^{36}S$ values that could suggest action of MSR (Ono et al., 2006a; Johnston et al., 2007). However, the majority of $\Delta^{36}S$ values fall within error of zero. As the amount of data collected from these morphologies is limited, further analysis would be required to assess whether the grains show the characteristic relationship of $\Delta^{36}S/\Delta^{33}S$ = ~-6.9 produced by MSR (Ono et al., 2006a; Johnston et al., 2007). At present, the explanation of a continentally-derived MDF sulfur source is preferred.

CR-AN-4 grains

Similar to CR-EU-3 and CR-AN-2 grains, CR-AN-4 grains show $\Delta^{33}S$ values of approximately zero. In contrast to those morphologies, and also CR-AN-1 grains, CR-AN-4 grains show variable $\delta^{34}S$ values, with both large positive and large negative values ($\delta^{34}S$ = -15.9 - +21.85 ‰; Figure 5.12C). Inter-grain variation is also observed to be high (Supplementary Information). Immediately, continentally-sourced MDF sulfur can be eliminated as a potential sulfur source, as the observed range in $\delta^{34}S$ exceeds that proposed for crustal sulfur ($\delta^{34}S$ = ~0 – 10 ‰; Guy et al., 2012) and that known for volcanic sulfur (Macnamara et al., 1951; Thode et al., 1961; Sakai et al., 1984; Chaussidon et al., 1989; Torssander et al., 1989). Atmospherically-derived MIF sulfur is also unlikely to be the cause as data does not lie on the ARA in $\Delta^{36}S$-$\Delta^{33}S$ space nor in $\Delta^{33}S$-$\delta^{34}S$ space (Figure 5.12C). The variable $\delta^{34}S$ values and negative $\Delta^{36}S$ values instead suggest that the sulfur was sourced from MSR. The data do appear to show a steep trend in $\Delta^{36}S$-$\Delta^{33}S$ space (Figure 5.12C), however, further data would need to be collected to confirm whether the data lie on the MSR trend of $\Delta^{36}S/\Delta^{33}S$ = ~-6.9 (Ono et al., 2006a; Farquhar et al., 2007).

Isotopic signatures of epigenetic grains

CR-EU-1 and CR-AN-3 grains

The isotopic signatures of both CR-EU-1 and CR-AN-3 grains are very similar to the signatures observed for diagenetic and detrital grains in this study (Figure 5.12). The overlap

between the isotopic compositions suggests that the epigenetic pyrite represents sulfur that has been re-mobilized from within sediments of the Central Rand Group. It is unlikely that the sulfur was sourced from the underlying sediments of the West Rand Group as they are dominated by diagenetic pyrite carrying positive $\Delta^{33}S$ signatures (Farquhar et al., 2007; Guy et al., 2012).

CR-EU-2 grains

The isotopic signatures of CR-EU-2 grains are significantly different from other epigenetic grains and from the diagenetic and detrital grains. The negative $\Delta^{33}S$ and $\Delta^{36}S$ values are of greater magnitude than observed for other morphologies (Figure 5.12; $\Delta^{33}S$ = ~-0.8 ‰, $\Delta^{36}S$ = ~-2 ‰). Therefore, unlike the other epigenetic grains, the sulfur in these grains could not have been remobilized from within the Central Rand Group. The isotopic signatures themselves, are highly unusual, and deviate significantly from the ARA in $\Delta^{36}S$-$\Delta^{33}S$ and $\delta^{34}S$-$\Delta^{33}S$ space (Figure 5.12D). Similar to the diagenetic CR-AN-1 grains, these signatures cannot be explained solely through photolysis of SO_2. Here, two possibilities are considered: (1) that the signatures represent MSR of MIF sulfate, and (2) that the signatures represent photoexcitation of volcanic sulfur species.

As mentioned above, MSR of MIF sulfate produces deviations from the ARA in $\Delta^{36}S$ (Shen et al., 2009; Zhelezinskaia et al., 2014; Mishima et al., 2017). Here, CR-EU-2 grains show deviation from the ARA of ~2 – 3 ‰ (Figure 5.12D). Currently, MSR is the only known fractionation process which can cause such significant negative fractionations in $\Delta^{36}S$, and so seems a likely explanation for the observed signatures. MSR of MIF sulfate is also supported by the observed negative $\Delta^{33}S$ values. However, the observed $\delta^{34}S$ values ($\delta^{34}S$ = ~+5 ‰) do not support MSR. As explained for CR-AN-1 grains, fractionations in $\Delta^{36}S$ scale with fractionation in $\delta^{34}S$ (Johnston et al., 2007) and the magnitude of $\Delta^{36}S$ fractionations observed for CR-EU-2 grains would require very large fractionations in $\delta^{34}S$ that are not observed. It is noted however, that the uniformity in the isotopic compositions of CR-EU-2 grains suggests that the isotopic compositions were homogenized when the sulfur was transported in the hydrothermal fluids (Supplementary Information). This would have masked the extent of fractionation in $\delta^{34}S$, making it difficult to determine if the signatures were consistent with MSR. Certainly, the identification and analysis of diagenetic grains showing similar signatures would be beneficial. However, with the present data, this explanation cannot be either conclusively confirmed or eliminated.

The second option is that these signatures have been produced through photoexcitation of SO_2, an explanation which has been previously suggested for similar isotopic signatures (Bouyon et al., 2018). Laboratory experiments conducted by Whitehall and Ono (2012) showed that elemental sulfur produced through photoexcitation of SO_2 into the 250 – 330 nm absorption band carries positive $\Delta^{33}S$ and $\Delta^{36}S$ signatures, in the order of ~13.4 – 16.5 ‰ for $\Delta^{33}S$ and +8.7 – +11.1 ‰ for $\Delta^{36}S$. As necessitated by mass balance, the residual SO_2 carries negative $\Delta^{33}S$ and $\Delta^{36}S$ signatures, showing ranges of -3.91 - -0.53 ‰ and -3.1 – -0.3 ‰, respectively (Whitehall and Ono, 2012). It is this signature in the residual SO_2 that would have been preserved in CR-EU-2 grains. The observed $\Delta^{33}S$ and $\Delta^{36}S$ signatures fall within the ranges produced through the laboratory experiments and so this may be a viable explanation. However, questions do arise as to how these signatures came to be preserved in the rock record, with modelling suggesting that preservation of the isotopic signatures produced through photoexcitation in the 250 – 330 nm band is difficult and only possible under certain atmospheric conditions (Whitehall and Ono, 2012). Indeed, it needs to be asked what would have prevented the residual SO_2 being involved in further atmospheric reactions, such as the photolysis reactions which are believed to dominate the Archean atmosphere (Farquhar et al., 2001). As with the previous explanation, further investigation is needed before this possibility can be confirmed or eliminated. This further research would need to include additional investigation into the isotopic signatures produced through photoexcitation of SO_2, the stability of the products in the Archean atmosphere and how the products could be preserved within sedimentary environments.

Continental sulfur flux and the composition of terrestrial sulfur

Previously, abundance of diagenetic and detrital pyrite in proximal fluvial sedimentary rocks (Guy et al., 2010) and the presence of reworked sedimentary pyrite grains in reefs and conglomerates of the Kaapvaal and Zimbabwe Cratons (Saager et al., 1986; Hofmann et al., 2009; Rantzch et al., 2011; Guy et al., 2014) have been offered as evidence for the development of an active continental sulfur flux during deposition of the Central Rand Group (Guy et al., 2014). The muted or zero $\Delta^{33}S$ and $\Delta^{36}S$ signatures observed in many of the grains analyzed in this study provide further evidence for input of MDF sulfur into the Witwatersrand Basin.

However, evidence from this study argues against previous suggestions that this sulfur flux was due to oxidative weathering of sulfide minerals (Guy et al., 2010, 2014). Detrital pyrite was observed within both the Elsburg and Krugersdorp formations, with the preservation of

detrital pyrite requiring low oxygen conditions inconclusive with oxidative weathering (Reimer and Mossman, 1990; Rasmussen and Buick, 1999). Additionally, concentrations of the redox sensitive elements Se and Mo are both low within diagenetic pyrite from this study (Table 5.2); Mo concentrations are consistently below detection limits, whilst the majority of Se concentrations fall within or below typical Archean background levels (~10 ppm; Large et al., 2014). Both Se and Mo are mobile under oxidative conditions. Therefore, if oxidative weathering was occurring, it would be expected that there would be an increase in the amount of these elements supplied to fluvial environments and that diagenetic pyrite would preserve elevated concentrations (Large et al., 2014). However, this is not observed. Therefore, the increased sulfur flux must be due to some other mechanism/s.

Composition of fluvial sulfur

As mentioned above, the isotopic signatures of pyrite analyzed within this study provide evidence for a significant MDF crustal sulfur flux into fluvial environments. The small negative $\Delta^{33}S$ values observed in some diagenetic and detrital grains also provide evidence of input of the MIF sulfate aerosol (Farquhar et al., 2000, 2001). However, there is a complete absence of pyrite carrying positive $\Delta^{33}S$ signatures conclusive with input of the MIF elemental sulfur aerosol. It is unlikely that one aerosol was being deposited and not the other, and therefore there must be some barrier present to the elemental sulfur aerosol being preserved in both the continental environments that the crustal sulfur was sourced from and within the fluvial environments themselves. Previously, it has been suggested that terrestrial environments preserve the MIF sulfate aerosol preferentially as its greater solubility allows it to soak into the continental surface where the MIF elemental sulfur aerosol is eroded (Maynard et al., 2013). However, the composition of diagenetic pyrite within this study argues against this, as it is expected that a large portion of the eroded MIF elemental sulfur would be introduced into rivers, where it could be incorporated into diagenetic pyrite. It seems more likely that for some reason, the mechanism by which MIF elemental sulfur is preserved in the rock record is not active within these environments. This will be discussed in detail within Chapter 7.

5.7 Conclusions

As shown, pyrite hosted by fluvial sediments preserves a combination of MDF crustal and marine sulfur and the MIF sulfate aerosol. Additionally, action of microbial sulfate reducers within fluvial sediments is suggested by negative $\Delta^{36}S$ values. The isotopic data presented here, provides further evidence for the suggestions of Guy et al. (2010, 2014) that there was a

significant continental sulfur flux during deposition of the Central Rand Group. However, preservation of detrital pyrite and low concentrations of Se and Mo within diagenetic pyrite argue against this flux being caused by oxidative weathering of sulfide minerals. Additionally, the complete absence of pyrite bearing positive $\Delta^{33}S$ signatures shows that the MIF elemental sulfur aerosol was preserved in neither the crustal environments that sulfur was sourced from, nor the fluvial environments in which diagenetic pyrite formed.

Chapter 6: Isotopic composition of pyrite hosted by marine clastic sedimentary rocks

Abstract - A detailed morphological, trace element and multiple sulfur isotope study of sulfide minerals from the ~2900 Ma Roodepoort Formation of the Witwatersrand Supergroup is presented. Diagenetic pyrite from the lower section of the formation shows steep $\Delta^{36}S/\Delta^{33}S$ trends consistent with microbial sulfate reduction. Elevated concentrations of the redox sensitive trace element Se, which are up to an order of magnitude higher than the baseline Archean levels, show that microbial sulfate reduction occurred during a period of oxygenation. Diagenetic pyrite from the upper section of the formation show a $\Delta^{36}S/\Delta^{33}S$ trend that is steeper than the mass independent fractionation array ($\Delta^{36}S/\Delta^{33}S$ = -0.90) and shallower than the microbial sulfate reduction array ($\Delta^{36}S/\Delta^{33}S$ = -6.90). This is argued to represent an interplay of photolytic and microbial fractionations that occurred during a return to anoxic conditions. Further four sulfur isotope analysis of Mesoarchean sulfide minerals collected from outside the Kaapvaal Craton would be beneficial in determining whether this interplay was a localized effect. Conspicuously absent from any of the pyrite analyzed is negative $\Delta^{33}S$ signatures, which shows that the photochemical sulfate aerosol was not preserved in this shallow marine environment.

6.1 Introduction

The previous chapters have focussed on examining sulfide minerals hosted by various types of terrestrial sedimentary rocks. In this chapter, however, the focus is the isotopic composition of sulfide minerals hosted by shallow marine sedimentary rocks of the ~2900 Ma Roodepoort Formation. This was undertaken in order to provide a comparison between the isotopic composition of marine and terrestrial environments and identify if different fractionation processes were dominant in the different environments (this will be discussed further in Chapter 7). The Roodepoort Formation, specifically, was chosen as its position within the West Rand Group of the Witwatersrand Supergroup allows for a more direct comparison with the data presented in previous chapters. As the majority of data presented so far has also been collected from sedimentary rocks of the Kaapvaal Craton, any differences between the isotopic compositions of those samples and the samples from this chapter are unlikely to be due to variations in local environmental conditions.

As previously described, the current Archean sulfur isotope record is predominantly composed of data collected from marine sedimentary rocks. Typically, what is preserved in the marine rocks are MIF signatures, with non-zero $\Delta^{33}S$ and $\Delta^{36}S$ and $\Delta^{36}S/\Delta^{33}S$ of ~-0.90. Steeper $\Delta^{36}S/\Delta^{33}S$ slopes of ~-1.5 have been observed within the Meso- and Neoarchean but are interpreted to represent changes in atmospheric chemistry which affected the photolysis source reactions rather than the action of a different fractionation process (Farquhar et al., 2007; Zerkle et al., 2012; Izon et al., 2015; Mishima et al., 2017). Far less common are isotopic signatures indicative of microbial sulfate reduction (MSR), which are observed at ~3450 – 3200 Ma, ~2900 Ma and ~2650 – 2500 Ma (Kamber and Whitehouse, 2007; Kaufman et al., 2007; Ueno et al., 2008; Shen et al., 2009; Wacey et al., 2010; Guy et al., 2012; Zhelezinskaia et al., 2014; Mishima et al., 2017; Eickmann et al., 2018). Where four-isotope data is available, these signatures show negative $\Delta^{33}S$ and deviations from the MIF array in $\Delta^{36}S$ (Ueno et al., 2008; Shen et al., 2009; Zhelezinskaia et al., 2014; Mishima et al., 2017). On this basis, it was expected that the shallow marine sedimentary rocks of the Roodepoort Formation would preserve a MIF signature, probably with a steepened $\Delta^{36}S/\Delta^{33}S$ array such as that previously observed in Mesoarchean South African sedimentary rocks (Farquhar et al., 2007).

This chapter presents a detailed study of the morphology, trace element composition and sulfur isotope signatures of sulfide minerals hosted by shallow marine sedimentary rocks of

the Mesoarchean Roodepoort Formation. Sulfur isotope signatures show that diagenetic pyrite within the lower section of the Roodepoort Formation preserve evidence of MSR. Elevated Se concentrations congruent with increased oxidative weathering demonstrate that this MSR occurred during a period of oxygenation. Signatures in the upper section represent interplay between microbial and atmospheric MIF processes, suggesting a return to anoxic conditions. This provides further evidence that MSR was an important fractionation process during periods of the Archean and suggests that steepening of the $\Delta^{36}S/\Delta^{33}S$ array during the Mesoarchean may represent microbial activity. The complete absence of negative $\Delta^{33}S$ signatures suggests that the MIF sulfate aerosol was not being preserved in this shallow marine environment.

6.2 Geological context

The Roodepoort Formation occurs within the Jeppestown Subgroup of the West Rand Group of the Witwatersrand Supergroup, South Africa. A broad description of the geology of the Witwatersrand Supergroup was provided within Chapter 4.

The West Rand Group occupies a roughly oval area of approximately 42 000 km^2 and has an average thickness of 4650 m (Tankard et al., 1982). It is stratigraphically divided, from bottom to top, into the Hospital Hill, Government and Jeppestown Subgroups (Figure 6.1). The Hospital Hill Subgroup predominantly consists of sandstone (quartz arenite), with interspersed layers of siltstone-shale, mudstone and banded iron formation (BIF). Both the Government and Jeppestown Subgroups are dominated by feldspathic sandstone and wackestone, intercalated with siltstone-shale and magnetic mudstone (Guy et al., 2010). The West Rand Group is interpreted to have been deposited in an offshore marine setting (Eriksson et al., 1981), with fluvial braidplain facies present in the proximal parts of the basin (Beukes, 1995). Marine and shelf depofacies dominate the lower parts of the sequence, with fluvial, braidplain and distal marine shelf depofacies defining the middle and upper parts of the sequence (Eriksson et al., 1981; Tankard et al., 1982; Watchorn and O'Brien, 1991; Beukes, 1995). A maximum age of sedimentation is provided by detrital zircons, which returned an age of 2985 ± 14 Ma (Kositcin and Krapez, 2004). A minimum age is provided by the age of lavas in the Crown Formation, which returned an age of 2914 ± 8 Ma (Armstrong et al., 1991).

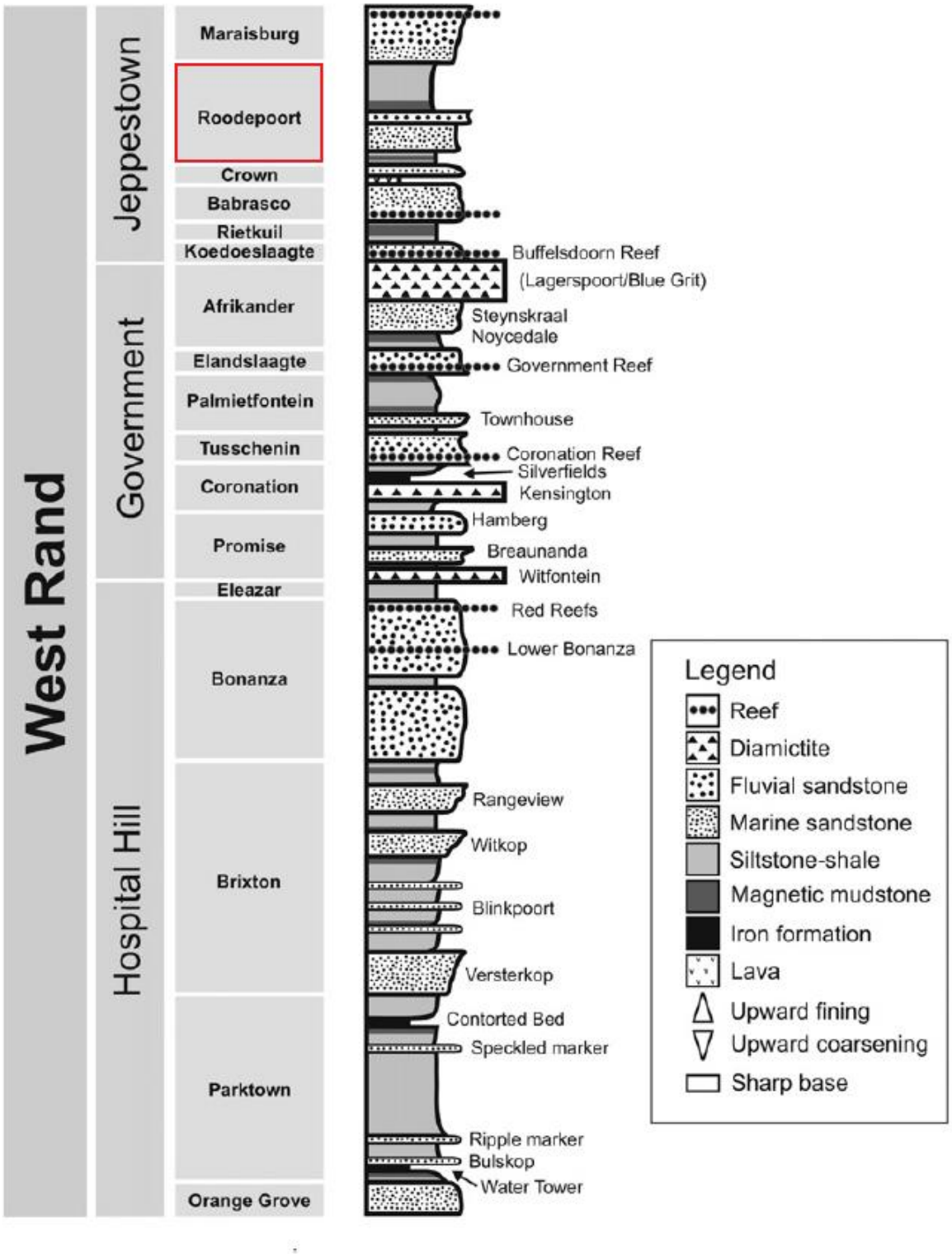

Figure 6.1. Stratigraphic column of the West Rand Group of the Witwatersrand Supergroup. The location of the Roodepoort Formation is outlined in red. Modified from Guy et al. (2012).

6.3 Sampling information

Samples analyzed within this study were collected from the Anglo American drillcore AM1 which intersects distal strata of the Government and Jeppestown Subgroups. The location of

the drill site is given in Figure 6.2. Within this core, the Roodepoort Formation consists of sandstone and shale, deposited in a marine shelf environment (Guy et al., 2012). The lithology and depth of each sample is provided in Table 6.1.

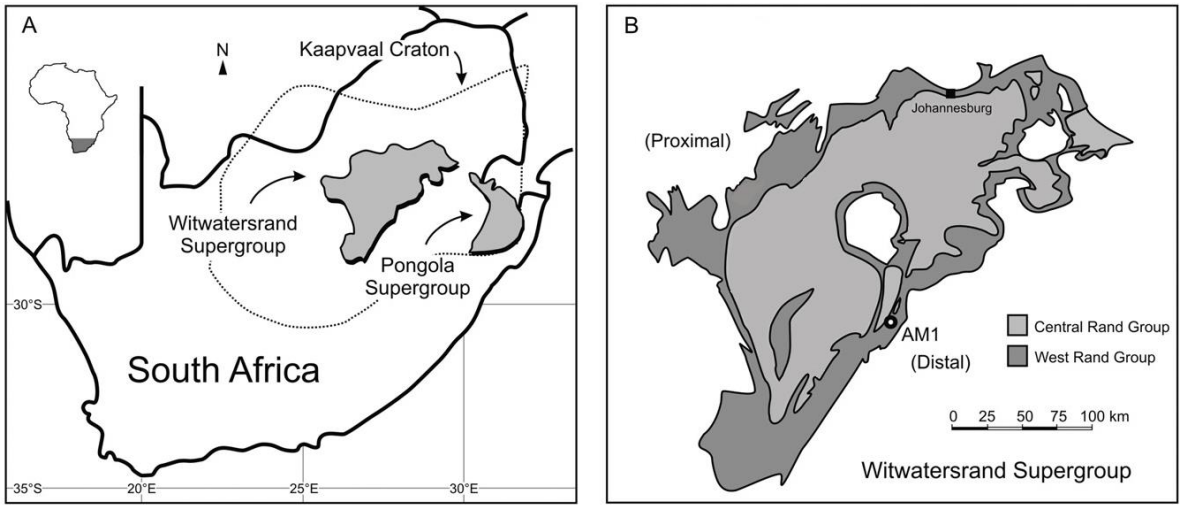

Figure 6.2. A. Geographic position of the Witwatersrand and Pongola supergroups on the Kaapvaal Craton. B. Geological map of the Witwatersrand Supergroup, showing the approximate location of the AM1 drill hole.

Table 6.1. Sampling information for samples collected from the Roodepoort Formation.

Sample Name	Sampling Depth (m)	Lithology
AM1-1	1010.63	Shale
AM1-2	1015.04	Shale
AM1-3	1019.68	Shale
AM1-4	1020.63	Shale
AM1-5	1037.23	Shale
AM1-6	1037.63	Shale
AM1-7	1039.34	Sandstone
AM1-8	1043.18	Sandstone

6.4 Methods

Methods for sample characterisation and sulfur isotope analysis are provided in Chapter 2.

6.5 Results

Sample characterisation

Morphology and textural features

Pyrite was the dominant sulfide mineral observed within the Roodepoort Formation. Pyrrhotite was also observed, but was considerably rarer and was not analyzed during this study. Sulfide mineral abundance was variable and was not observed to correlate with depth. Samples AM1-1 and AM1-6 were observed to have the highest abundance, followed by AM1-2, AM1-3, AM1-5 and AM1-7. Samples AM1-4 and AM1-8 showed the lowest abundance.

Eight main morphologies of pyrite were observed within the Roodepoort Formation. These morphologies, described below, will be referred to as R-EU-1, R-SUB-1, R-AN-1, R-AN-2, R-AN-3, R-AN-4, R-AN-5 and R-AN-6. Backscattered electron (BSE) images of these morphologies are provided in Figure 6.3.

R-EU-1 grains are euhedral and moderately porous, showing both very fine and large, more irregularly-shaped pores. They are present both as aggregates and individual grains and are ~100 – 200 µm in diameter. R-SUB-1 grains are subhedral and porous, with variable pore sizes. Rare, fine inclusions of chalcopyrite are also observed and are randomly-distributed within the grains. Grains are ~200 – 400 µm in diameter.

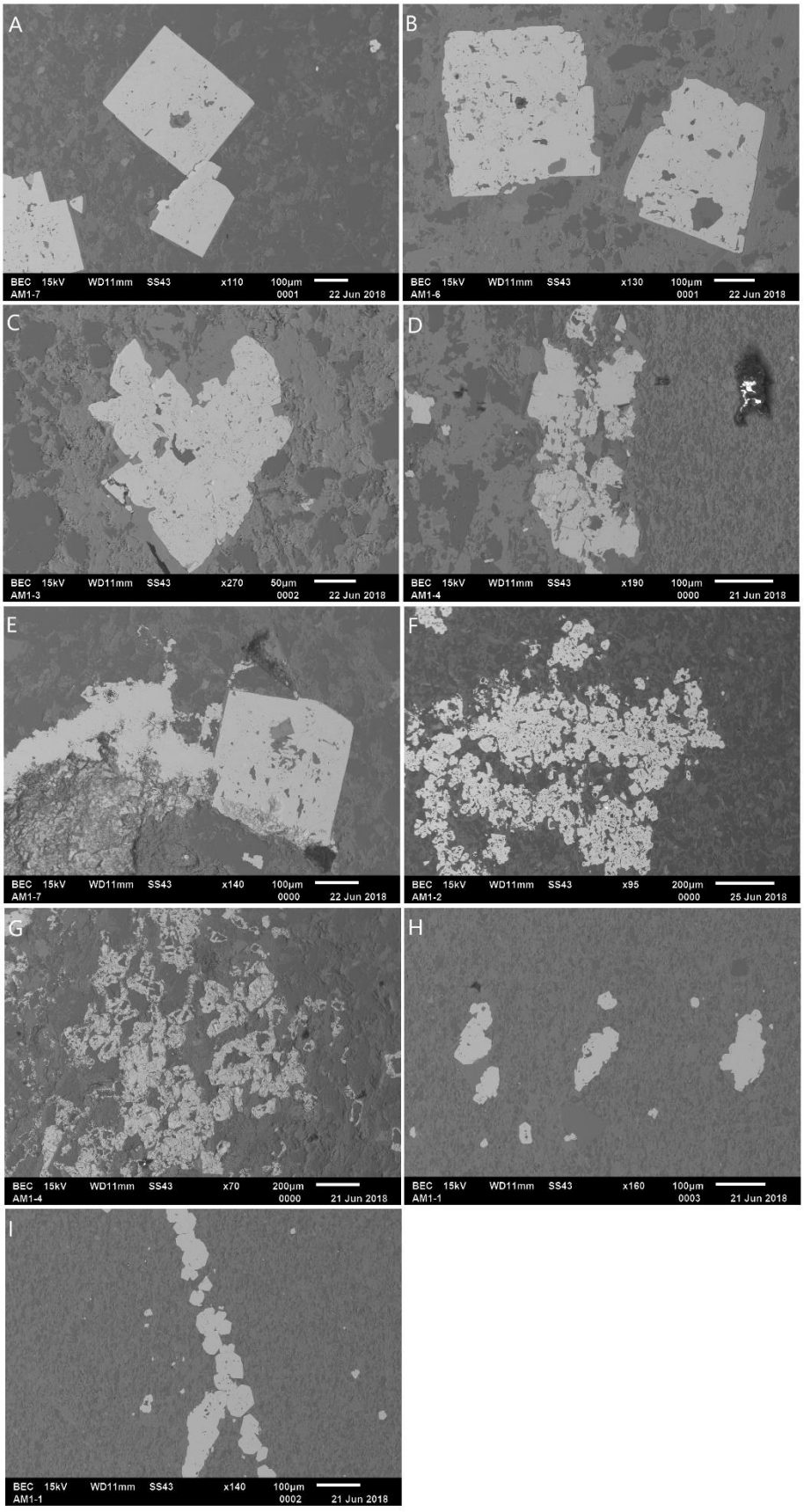

Figure 6.3. BSE photomicrographs of the different morphologies of pyrite grains observed within the Roodepoort Formation. A. R-EU-1, B. R-SUB-1, C. R-AN-1, D. R-AN-2, E. R-AN-3, F. R-AN-4, dendritic aggregate G. R-AN-4, skeletal dendrite, H. R-AN-5, I. R-AN-6.

R-AN-1 grains are irregularly-shaped anhedral, porous grains. They are occasionally observed to contain rounded inclusions of Fe-Ti- and Fe-Cr-oxides. Grains range in size from ~200 – 500 µm in diameter. R-AN-2 grains are irregularly-shaped anhedral grains with variable porosity. They conform to laminae within the samples and contain fine blebs of chalcopyrite. Grains range in size from ~50 – 200 µm in diameter. R-AN-3 grains are irregular to elongate anhedral, non-porous, inclusion-free grains. These grains are commonly found in close association with R-EU-1 and R-SUB-1 grains, where they appear to grow from euhedral and subhedral grains. Fine disseminated grains of pyrite are commonly observed around the grain borders. R-AN-4 are dendritic pyrite growths, of which two types are observed. The first are irregular dendritic aggregates and are observed within samples AM1-1 and AM1-2. These aggregates are highly porous, showing fine, randomly-distributed pores and also contain rare blebs and elongate vein-like inclusions of chalcopyrite. They range in size from ~500 - > 1000 µm in diameter. The second type are fine, skeletal dendritic growths and are observed within sample AM1-8. They are less porous than the other dendritic pyrite and do not contain inclusions of other sulfide minerals. They are similar in size to the other dendritic aggregates. R-AN-5 grains are fine, irregularly-shaped, disseminated anhedral grains. They are typically non-porous but some grains do show very limited numbers of pores. Grains are ~50 – 100 µm in diameter. R-AN-6 show similar morphology, texture and size to R-AN-5 grains but are aggregated, forming a distinct band which crosscuts the sample.

Trace element composition

A summary of the trace element composition of pyrite from each sample is provided in Table 6.2. The complete data set and maps of analyses spots are provided in the Supplementary Information.

Pyrite grains from the Roodepoort Formation returned Co concentrations of 9.30 – 4280 ppm, median of 546 ppm (*M* = 783 ± 870 ppm, 1 *SD*, *n* = 98), Ni concentrations of 9.70 – 3830 ppm, median of 386 ppm (*M* = 625 ± 657 ppm, 1 SD, *n* = 98), Cu concentrations of 2.02 – 4260 ppm, median of 24.3 ppm (*M* = 245 ± 766 ppm, 1 *SD*, *n* = 98), Zn concentrations of 0.205 – 5100 ppm, median of 9.30 ppm (*M* = 79.9 ± 518 ppm, 1 *SD*, *n* = 98), As concentrations of 19.3 – 8850 ppm, median of 2140 ppm (*M* = 2270 ± 1790 ppm, 1 *SD*, *n* = 98) and Se concentrations of 3.60 – 169 ppm, median of 43.9 ppm (*M* = 43.9 ± 53.6 ppm, 1 *SD*, *n* = 98). Co/Ni values had a range of 0.057 – 11.0, with a median value of 1.23 (*M* = 1.87 ± 2.05 ppm, 1 *SD*, *n* = 98).

Table 6.2. Summary of the trace element composition of pyrite from the Roodepoort Formation.

Sample Name	Lithology	Trace element	Min (ppm)	Max (ppm)	Median (ppm)	Mean (ppm)	StdDev (ppm)
AM1-1 (n = 15)	Shale	Co	136	1760	815	740	495
		Ni	135	2400	311	602	609
		Cu	2.02	399	4.60	32.2	102
		Zn	2.06	29.7	11.6	13.0	10.4
		As	19.3	1200	384	441	364
		Co/Ni	0.057	4.70	1.78	2.08	1.56
AM1-2 (n = 8)	Shale	Co	578	3320	2475	2210	977
		Ni	462	2330	980	1060	587
		Cu	9.00	48.0	14.6	20.2	13.1
		Zn	10.6	219	23.3	54.2	72.9
		As	446	6230	910	1730	1907
		Co/Ni	0.926	3.97	2.29	2.22	0.938
AM1-3 (n = 7)	Shale	Co	110	3780	1160	1390	1150
		Ni	274	3830	774	1280	1300
		Cu	8.30	470	65.0	112	162
		Zn	8.99	126	14.0	31.4	42.2
		As	2400	6550	4620	4480	1360
		Co/Ni	0.069	4.88	2.72	2.29	1.89
AM1-4 (n = 5)	Shale	Co	103	645	178	322	253
		Ni	30.8	670	116	279	303
		Cu	20.6	5260	28.6	1590	2340
		Zn	2.56	47.2	10.6	15.7	18.3
		As	776	3250	1770	1930	905
		Co/Ni	0.330	4.69	3.34	2.58	1.85
AM1-5 (n = 21)	Shale	Co	32.4	1520	547	560	455
		Ni	36.3	1270	287	394	322
		Cu	3.70	1230	67.0	159	289
		Zn	29.8	0.630	6.56	9.57	8.49
		As	466	4420	2230	2310	845
		Co/Ni	0.372	3.52	1.22	1.56	1.06
AM1-6 (n = 20)	Shale	Co	10.3	1670	413	539	498
		Ni	9.70	1660	358	516	506
		Cu	3.30	4160	33.9	503	1040
		Zn	1.21	5100	8.30	313	1140
		As	1230	3530	2455	2330	690
		Co/Ni	0.175	6.43	1.36	1.56	1.46

Sample Name	Lithology	Trace element	Min (ppm)	Max (ppm)	Median (ppm)	Mean (ppm)	StdDev (ppm)
AM1-7 (n = 17)	Sandstone	Co	9.30	640	68.6	196	200
		Ni	22.9	2340	422	711	715
		Cu	11.1	135	64.7	70.7	71.5
		Zn	5.50	162	18.7	27.6	38.3
		As	126	8850	3370	3670	2670
		Co/Ni	0.117	0.572	0.237	0.262	0.135
AM1-8 (n = 5)	Sandstone	Co	690	4280	1700	2140	1510
		Ni	73.0	1770	286	537	760
		Cu	3.30	14.8	5.44	7.20	5.00
		Zn	5.80	9.80	8.50	8.32	1.67
		As	386	1610	520	773	549
		Co/Ni	1.62	11.0	9.45	7.49	4.09

The different morphologies typically showed overlapping ranges in trace element concentrations, with a small number of exceptions (Figure 6.4). R-AN-3 grains were observed to show consistently higher Zn concentrations and lower Se concentrations than other morphologies. Additionally, R-AN-3 and R-EU-1 grains were observed to show lower and more restricted ranges of Co/Ni values, although only a small number of measurements were completed on each of these morphologies, so this may have contributed to the lower variation. Based on As concentrations, the morphologies could be divided into two groups; R-EU-1, R-SUB-1, R-AN-1 and R-AN-2 grains showed similar concentrations and R-AN-3, R-AN-4, R-AN-5 and R-AN-6 showed similar concentrations that were consistently lower than those observed for the previous group.

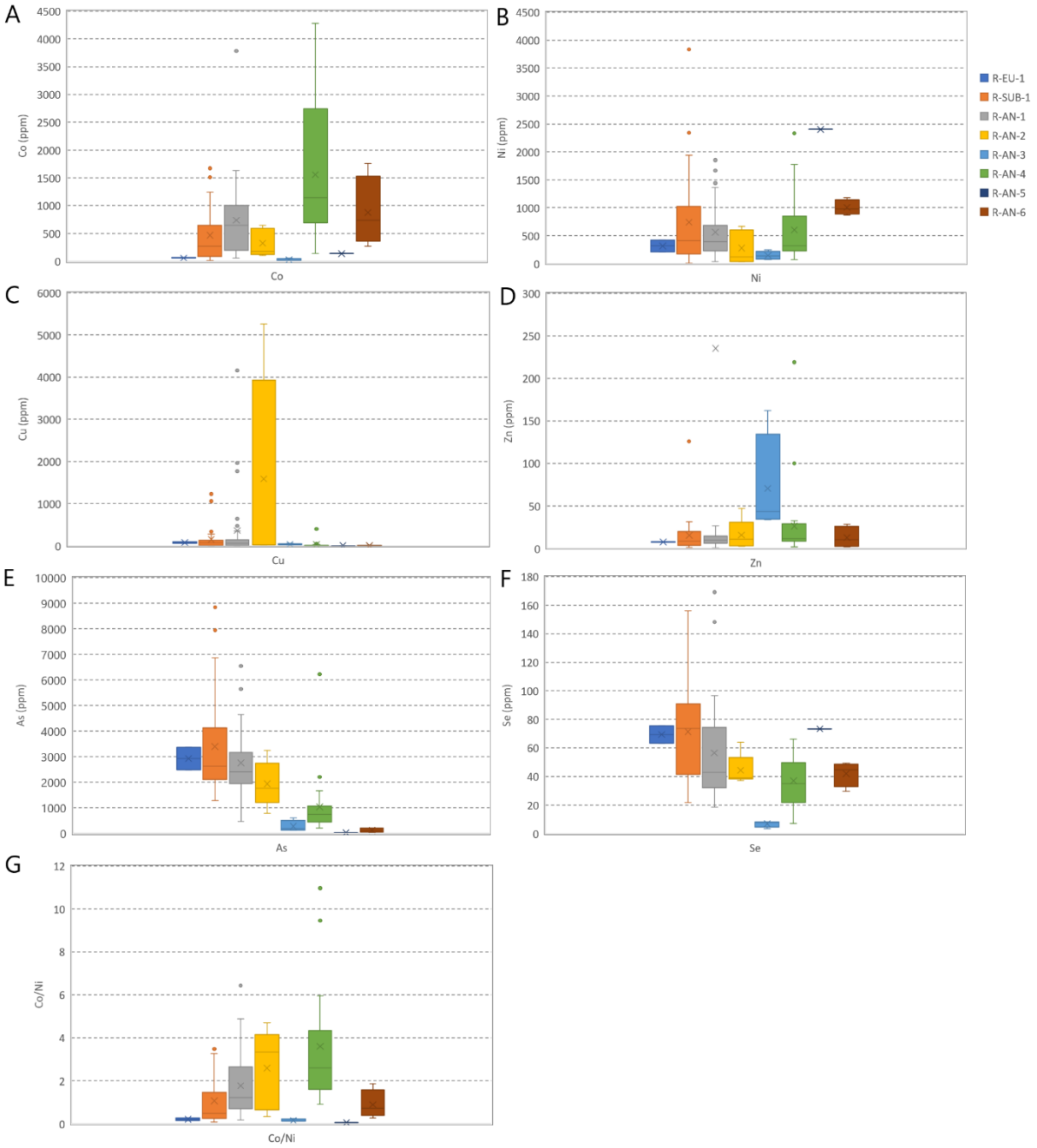

Figure 6.4. Box and whisker plots comparing the trace element composition and Co/Ni ratios of the different pyrite morphologies observed within the Roodepoort Formation. A. Co concentrations, B. Ni concentrations, C. Cu concentrations, D. Zn concentrations, E. As concentrations, F. Se concentrations, G. Co/Ni ratios.

Sulfur isotope composition

A summary of the sulfur isotope composition of pyrite from each sample is provided in Table 6.3. The complete data set and maps of analysis spots are provided in the Supplementary Information.

Table 6.3. Summary of the isotopic composition of pyrite grains from the Roodepoort Formation.

Sample Name	Lithology	Isotope ratio	Min (‰)	Max (‰)	Median (‰)	Mean (‰)	StdDev (‰)
AM1-1 (n = 31)	Shale	$\delta^{34}S$	1.37	7.58	2.82	2.93	1.13
		$\Delta^{33}S$	0.188	0.402	0.276	0.271	0.046
		$\Delta^{36}S$	-1.32	-0.458	-0.913	-0.898	0.208
AM1-2 (n = 16)	Shale	$\delta^{34}S$	3.02	7.74	4.77	4.96	1.30
		$\Delta^{33}S$	0.113	0.325	0.244	0.241	0.046
		$\Delta^{36}S$	-0.920	-0.251	-0.667	0.186	-0.618
AM1-3 (n = 17)	Shale	$\delta^{34}S$	0.539	4.30	1.27	1.59	0.919
		$\Delta^{33}S$	0.542	0.803	0.710	0.696	0.078
		$\Delta^{36}S$	-1.95	-1.26	-1.64	-1.64	0.180
AM1-4 (n = 18)	Shale	$\delta^{34}S$	-1.17	3.45	0.097	0.272	1.06
		$\Delta^{33}S$	0.382	0.579	0.487	0.490	0.060
		$\Delta^{36}S$	-2.04	-1.37	-1.63	-1.62	0.177
AM1-5 (n = 29)	Shale	$\delta^{34}S$	1.40	8.53	2.84	2.96	1.31
		$\Delta^{33}S$	-0.118	0.150	0.038	0.039	0.058
		$\Delta^{36}S$	-0.918	0.019	-0.455	-0.462	0.198
AM1-6 (n = 17)	Shale	$\delta^{34}S$	2.23	5.13	3.15	3.17	0.751
		$\Delta^{33}S$	-0.085	0.145	0.004	0.018	0.057
		$\Delta^{36}S$	-0.826	-0.005	-0.500	-0.477	0.197
AM1-7 (n = 30)	Sandstone	$\delta^{34}S$	-15.75	3.76	2.06	-2.87	7.40
		$\Delta^{33}S$	-0.083	0.506	0.026	0.094	0.170
		$\Delta^{36}S$	-2.05	-0.068	-0.473	-0.796	0.571
AM1-8 (n = 13)	Sandstone	$\delta^{34}S$	3.50	8.14	4.50	4.93	1.35
		$\Delta^{33}S$	-0.182	0.100	-0.096	-0.081	0.080
		$\Delta^{36}S$	-0.493	-0.075	-0.231	-0.232	0.130

Pyrite grains from the Roodepoort Formation could be divided into three groups on the basis of their isotopic signatures. Samples AM1-1, AM1-2, AM1-3 and AM1-4, referred to as Group 1, returned $\delta^{34}S$ values of -1.17 – 7.74 ‰, (median = 2.50 ‰, M = 2.46 ± 1.93 ‰, 1 *SD*, n = 82), $\Delta^{33}S$ values of 0.113 – 0.803 ‰, (median of 0.300 ‰, M = 0.401 ± 0.186 ‰, 1 *SD*, n = 82) and $\Delta^{36}S$ values of -2.04 - -0.251 ‰, (median of -1.08 ‰, M = -1.16 ± 0.465 ‰, n = 82). When plotted in $\Delta^{36}S$-$\Delta^{33}S$ space, $\Delta^{36}S$ is observed to correlate with $\Delta^{33}S$: $\Delta^{36}S = -1.99*\Delta^{36}S - 0.36$ (R = -0.80).

Samples AM1-5, AM1-6, AM1-8 and R-EU-1 and R-SUB-1 grains from AM1-7, referred to as Group 2, showed $\delta^{34}S$ values of 1.40 – 8.53 ‰ (median of 3.00 ‰, *M* = 3.28 ± 1.31 ‰, 1 *SD*, *n* = 77), $\Delta^{33}S$ values of -0.182 – 0.150 ‰ (median of 0.004 ‰, *M* = -0.001 ± 0.073 ‰, 1 *SD*, *n* = 77) and $\Delta^{36}S$ values of -0.918 – 0.019 ‰ (median of -0.406 ‰, *M* = -0.406 ± 0.205 ‰, 1 *SD*, *n* = 77).

With the exception of R-AN-3 grains, the different morphologies did not display distinct isotopic compositions (Figure 6.5). Instead, depth seems to have a larger control. Group 1 samples were collected from the upper section of the Roodepoort Formation at depths between 1010.63 – 1020.63 m. Both Group 2 and Group 3 samples were collected from the lower section of the Roodepoort Formation, at depths of 1037.23 – 1043.18 m.

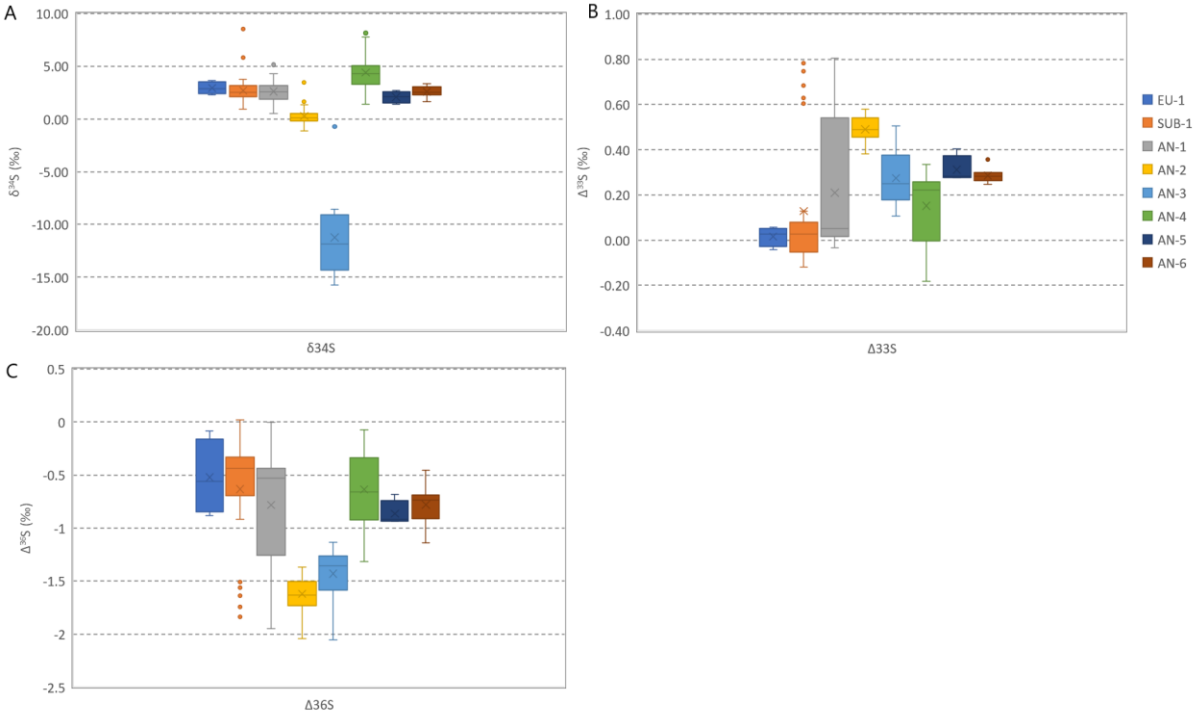

Figure 6.5. Box and whisker plots comparing the isotopic compositions of the different pyrite morphologies observed within the Roodepoort Formation. A. $\delta^{34}S$, B. $\Delta^{33}S$, C. $\Delta^{36}S$.

6.6 Discussion

Determining sulfide paragenesis

Trace element measurements and morphological and textural observations identified diagenetic species but the paragenesis of two pyrite morphologies remain uncertain.

Diagenetic grains

R-SUB-1, R-AN-1, R-AN-2, R-AN-4, R-AN-5 and R-AN-6 grains were determined to be diagenetic in origin. R-SUB-1 grains show similar morphology and texture to diagenetic, subhedral, porous grains previously observed within the Witwatersrand Supergroup, including within the Roodepoort Formation (Guy et al., 2010, Figure 6.J). Additionally, Co, Ni and As concentrations and Co/Ni, Co/As and Ni/As values all fell within the ranges previously observed for diagenetic pyrite from the Witwatersrand Supergroup. The majority of grains also showed Co/Ni, Cu/Ni and Zn/Ni values within the ranges observed for diagenetic pyrite from other localities (Price, 1972; Gregory et al., 2015a). Whilst As/Ni values were higher than previously observed for diagenetic grains ($0.10 < As/Ni < 10$; Gregory et al., 2015a), as mentioned above, Co/As and Ni/As values were similar to previously observed for diagenetic grains from this locality. Therefore, a diagenetic origin is still feasible.

R-AN-1 grains were less distinct in regards to morphology and texture, however, the irregular shape, relatively small grain size (~50 – 200 µm) and random distribution of pores (Figure 6.3C) is largely inconsistent with an epigenetic origin. Epigenetic grains tend to be larger (>500 µm), euhedral and either non-porous or showing crystallographically-aligned pores (e.g. Saager, 1970; McClay and Ellis, 1983; Craig et al., 1998; Guy et al., 2010). R-AN-1 grains also lack the rounding that is typical of detrital grains. Therefore, the morphology is most consistent with a diagenetic origin. Additionally, the trace element concentrations and Co/Ni, Co/As and Ni/As relationships are similar to those previously observed for diagenetic pyrite from the Witwatersrand Supergroup (Guy et al., 2010), and Co/Ni, Cu/Ni and Zn/Ni values fall within the ranges observed for diagenetic grains from other localities (Price, 1972; Gregory et al., 2015a).

R-AN-2 grains conform to laminae within the samples. This is commonly observed for grains which form during diagenesis and indicates that ions were preferentially transported along layers permeable to pore waters (Carstens, 1985). As with the R-SUB-1 and R-AN-1 grains, the Co/Ni, Co/As and Ni/As values fell within the ranges previously observed for diagenetic pyrite from the Witwatersrand Supergroup (Guy et al., 2010). Co, Ni and As concentrations also fell within ranges observed for diagenetic pyrite from this locality.

Dendritic pyrite, such as R-AN-4 grains, forms during diagenesis via direct precipitation from porewaters (Carstens, 1985), where growth is controlled by diffusion (MacLachlan and

Carlson, 1952). Similar dendritic aggregates and skeletal dendrites to those seen in this study have previously been observed within the Witwatersrand Supergroup (Guy et al., 2010). Whilst dendritic pyrite can also be produced through hydrothermal activity, this occurs only at high degrees of supersaturation, such as within submarine hydrothermal chimneys where the fluids are stagnant (Murowchick and Barnes, 1987). Pyrite crystals growing from fluids flowing in veins are unlikely to have diffusion-controlled growth and so dendritic morphologies are uncommon in hydrothermal veins (Endo, 1975). Therefore, it is unlikely that the observed dendritic grains are epigenetic in origin. Additionally, the trace element compositions of R-AN-4 grains are consistent with a diagenetic origin, with Co, Ni and As concentrations falling within ranges previously observed for diagenetic pyrite in this locality (Guy et al., 2010) and elsewhere (Price, 1972; Gregory et al., 2015a). Co/Ni, Co/As and Ni/As relationships also fall within ranges previously observed for diagenetic pyrite from this locality (Guy et al., 2010) and Cu/Ni, Zn/Ni and As/Ni values fall within the defined ranges for diagenetic pyrite (Gregory et al., 2015a).

The origin of R-AN-5 grains was more difficult to determine, however, they are proposed to be diagenetic in origin. The morphology is quite indistinct, however, similar to R-AN-1 grains, they lack any of the morphological and textural features that are characteristic of epigenetic or detrital grains. Additionally, the fine, disseminated, anhedral to subhedral grains observed here (Figure 6.3G) are similar in morphology and texture to diagenetic grains observed by Gregory et al. (2015b) within shales of the Western Australian Hamersley and Fortescue Groups (Gregory et al., 2015b supplementary information, Figure A1.7, A1.48). Only one trace element measurement was obtained from this grain type, so it should be interpreted with caution, however the Co and Ni concentrations and Co/Ni value were within the ranges previously observed for diagenetic pyrite from this locality and elsewhere (Price, 1972; Guy et al., 2010; Gregory et al., 2015a).

R-AN-6 grains are similar in morphology to R-AN-5 grains but form a distinct band within the sample. Whilst this band could be interpreted to be a veinlet, this is unlikely as the matrix between sections of this sulfide band is intact; there is no vein material which has cross cut the matrix (Figure 6.3H). Additionally, the band of sulfides does not have a consistent width and grains do not appear to be constrained within any boundaries (Figure 6.3H); it would be expected that if this was a vein, that the grains would be confined within and conform to the boundaries of the vein (e.g. Guy et al., 2010, Figure 7K). Additionally, the measured trace

element compositions are consistent with a diagenetic origin. The Co/Ni, Co/As and Ni/As relationships are similar to those previously observed for diagenetic pyrite from the Witwatersrand Supergroup (Guy et al., 2010) and Co/Ni, Cu/Ni, Zn/Ni and As/Ni values fall within the defined ranges for diagenetic pyrite (Gregory et al., 2015a). Co and Ni concentrations also fall within ranges previously observed for diagenetic pyrite (Guy et al., 2010; Gregory et al., 2015a).

Grains with uncertain paragenesis

The paragenesis of both R-EU-1 and R-AN-3 grains is uncertain. For R-EU-1 grains, morphology does not provide any definitive information regarding paragenesis; euhedral grains can be either diagenetic (e.g. Taylor and Macquaker, 2000; Guy et al., 2010; Chapter 5, this study) or epigenetic (e.g. Saager, 1970; Craig et al., 1998; Guy et al., 2010; Chapter 5, this study). R-EU-1 grains are smaller than typical for epigenetic euhedral grains and similar in size to diagenetic euhedral grains previously observed within the Witwatersrand Supergroup (Guy et al., 2010). However, concentrations of Co and Ni within these grains are low (Figure 6.4A, B) and similar to concentrations previously observed within epigenetic grains (Utter, 1978; Meyer et al., 1990; Guy et al., 2010; Koglin et al., 2010). Only two trace element measurements were obtained from these grains, however, so the trace element results given above should be interpreted with some caution. The isotopic signatures of these grains and R-SUB-1 grains within the same samples are similar and, as R-SUB-1 grains have been determined to be diagenetic, this may also provide evidence for a diagenetic origin, or perhaps a pseudo-hydrothermal origin, as described by Saager (1970). Further investigation would be required in order to determine the paragenesis.

Similarly, the morphology, trace element composition and isotopic signatures of R-AN-3 grains are inconclusive in regards to paragenesis. The morphology of these grains is dissimilar to both diagenetic and epigenetic grains previously observed within the Witwatersrand Supergroup (e.g. Saager, 1970; England et al., 2002; Guy et al., 2010. 2012, 2014). They do, however, appear to be conformable with the matrix and don't overprint the surrounding minerals. Concentrations of Co, Ni and As are low, which is typical of hydrothermal pyrite (Utter, 1978; Meyer et al., 1990; Guy et al., 2010; Koglin et al., 2010). However, these grains are uniformly depleted in all of the measured trace elements (Supplementary Information), which may be representative of late diagenetic pyrite which formed when pore waters were no longer connected to the overlying water column. In these circumstances, later formed pyrite can have muted trace element concentrations (Gregory et al., 2015a). The variation in the

isotopic signatures observed for these grains is also more consistent with a diagenetic origin. It would be expected if the sulfur had originally been deposited elsewhere and then transported via fluid to the current location that the signatures would have been homogenized, at least to some degree, during transport. Additionally, there is no evidence for hydrothermal activity within the surrounding matrix. Therefore, there is evidence for a diagenetic origin but further investigation would be needed to confirm this.

Isotopic signatures

Group 2 grains

Group 2 grains showed small positive $\delta^{34}S$ and $\Delta^{33}S$ values and small negative $\Delta^{36}S$ values. Here we explore two possible explanations; (1) that these signatures represent MSR, or (2) that they represent mass-dependently fractionated (MDF) crustal sulfur.

The first option is that the signatures represent MSR. This is supported by the consistently negative $\Delta^{36}S$ values (Figure 6.6), which shows that the grains are depleted in ^{36}S. This is a characteristic feature of MSR, which discriminates against the heavy isotopes (Ono et al., 2006a; Johnston et al., 2007). Additionally, when plotted in $\Delta^{36}S$-$\Delta^{33}S$ space, a large portion of the data plot on or around the MSR array of $\Delta^{36}S/\Delta^{33}S$ = ~-6.9 (Figure 6.6; Ono et al., 2006a; Johnston et al., 2007). For MSR, fractionation in $\Delta^{33}S$ and $\Delta^{36}S$ scales with fractionation in $\delta^{34}S$ (Johnston et al., 2007). Data from Group 2 grains also shows broad trends between $\delta^{34}S$ and $\Delta^{33}S$ and $\delta^{34}S$ and $\Delta^{36}S$ where $\delta^{34}S$ decreases with increasing $\Delta^{33}S$ and decreasing $\Delta^{36}S$ (Figure 6.7), which is what is expected for MSR (Johnston et al., 2007).

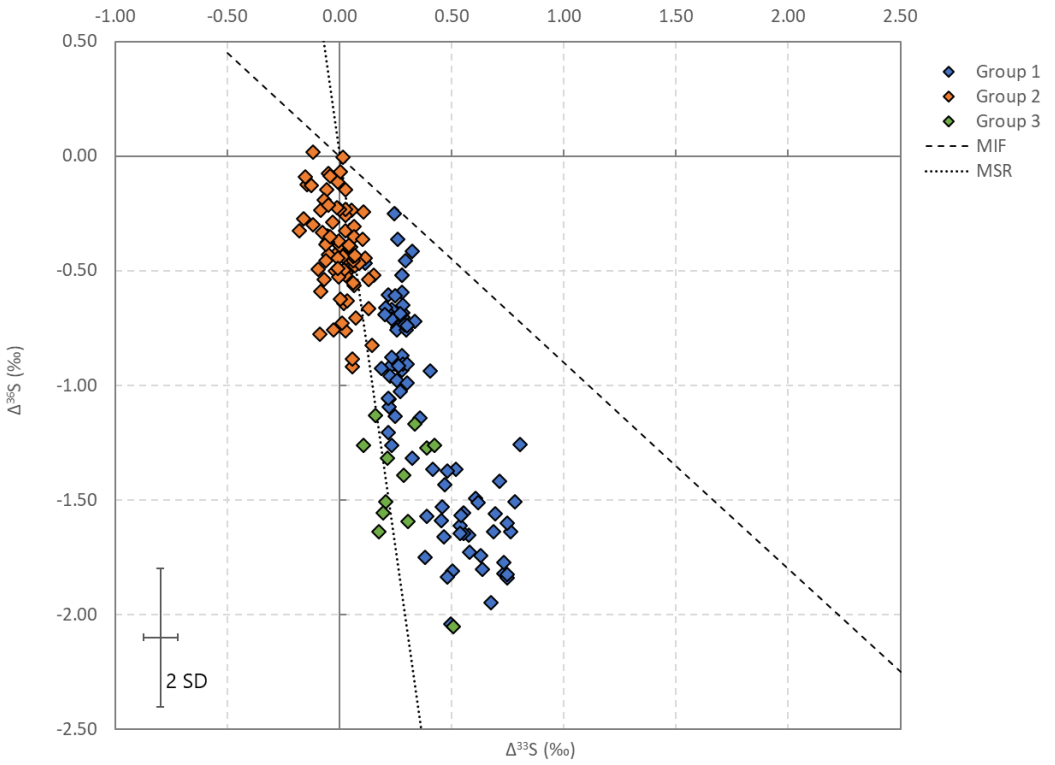

Figure 6.6. $\Delta^{36}S$ vs. $\Delta^{33}S$ plot for data collected from pyrite grains from the Roodepoort Formation. Data is separated by group.

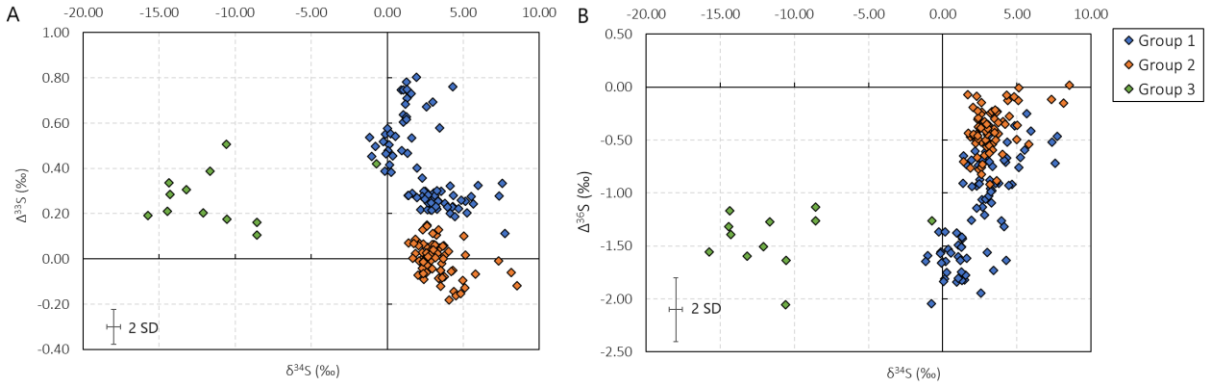

Figure 6.7. Isotope plots for data collected from pyrite grains from the Roodepoort Formation. A. $\Delta^{33}S$ vs. $\delta^{34}S$, B. $\Delta^{36}S$ vs. $\delta^{34}S$.

The fractionation in $\delta^{34}S$ for these samples is restricted (Figure 6.7) but within limits previously observed for MSR during the Archean (Sim et al., 2019). Group 2 grains show a range in $\delta^{34}S$ of ~1.5 – 8.5 ‰. Using an estimate of $\delta^{34}S$ = +3 - +16 ‰ for Archean seawater sulfate (Lambert et al., 1987; Canfield and Raiswell, 1999; Ono et al., 2003), this means that the maximum fractionation that could be preserved in the Group 2 grains is ~14.5 ‰ (based on the highest estimate for Archean seawater sulfate and the lowest values observed for Group 2 pyrite: 1.5 ‰ – 16 ‰ = -14.5 ‰). Therefore, the fractionations for Group 2 grains are lower than the majority of fractionations observed for modern environments, where

fractionations of less than ~20 ‰ are rare (Sim et al., 2019). However, for samples older than ~2500 Ma, while some show large fractionations in $\delta^{34}S$ (e.g. Aoyama and Ueno, 2017), fractionations in $\delta^{34}S$ during MSR are typically low and rarely exceed 20 ‰ (Sim et al., 2019). These small fractionations have been varyingly attributed to represent Rayleigh effects due to sulfate limitation (Gomes and Hurtgen, 2015), low oceanic sulfate concentrations (Habicht et al., 2002; Fike et al., 2009; Crowe et al., 2014) and greater availability of electron donors (Sim et al., 2019). Regardless of the cause, the restricted fractionations in $\delta^{34}S$ for Group 2 grains are consistent with previous data obtained for MSR during the Archean.

Another test for identifying MSR is to look at the $^{33}\lambda$ and $^{36}\lambda$ values and $^{36}\lambda/^{33}\lambda$ ratio (e.g. Johnston et al., 2007, 2008). The $^{33}\lambda$ and $^{36}\lambda$ values describe exponents for fractionation within a system and are defined as:

$$^{33}\lambda = \frac{\ln\left(1+\frac{\delta^{33}S_{H2S}}{1000}\right)-\ln\left(1+\frac{\delta^{33}S_{SO4}}{1000}\right)}{\ln\left(1+\frac{\delta^{34}S_{H2S}}{1000}\right)-\ln\left(1+\frac{\delta^{34}S_{SO4}}{1000}\right)} \quad (6.1)$$

$$^{36}\lambda = \frac{\ln\left(1+\frac{\delta^{36}S_{H2S}}{1000}\right)-\ln\left(1+\frac{\delta^{36}S_{SO4}}{1000}\right)}{\ln\left(1+\frac{\delta^{34}S_{H2S}}{1000}\right)-\ln\left(1+\frac{\delta^{34}S_{SO4}}{1000}\right)} \quad (6.2)$$

These equations describe the observed relationship between a sulfide-sulfate pair of samples (Mook, 2001; Farquhar et al., 2003; Johnston et al., 2005b) but can be modified to describe a suite of sulfide samples, as was done for this study (Equation A1, A2, Appendix). Values fluctuate around the reference exponents of 0.515 for ^{33}S-^{32}S and 1.90 for ^{36}S-^{32}S for a variety of mass-dependent processes. As the λ values are calculated independent of the magnitude of $\delta^{34}S$ fractionation, they allow for the character of different fractionation mechanisms to be directly compared. The $^{36}\lambda/^{33}\lambda$ ratio, defined by equation 6.3, allows for the covariation of ^{33}S and ^{36}S to be directly assessed, without involving ^{34}S.

$$\frac{^{33}\lambda}{^{36}\lambda} = \frac{\ln\left(1+\frac{\delta^{36}S_{H2S}}{1000}\right)-\ln\left(1+\frac{\delta^{36}S_{SO4}}{1000}\right)}{\ln\left(1+\frac{\delta^{33}S_{H2S}}{1000}\right)-\ln\left(1+\frac{\delta^{33}S_{SO4}}{1000}\right)} \quad (6.3)$$

In this case, the calculated $^{33}\lambda$, $^{36}\lambda$ values and $^{36}\lambda/^{33}\lambda$ ratio are inconclusive in regards to the origin of the isotopic signatures of Group 2 grains. The calculated $^{33}\lambda$ value of 0.515 (0.5146) could be conclusive with either MSR, which produces $^{33}\lambda < 0.515$ (Johnston et al., 2007), or MSD, which produces $^{33}\lambda \geq 0.515$ (Johnston et al., 2007, 2008). The $^{36}\lambda$ value of 1.838 may

also suggest MSD, which has been observed to produce $^{36}\lambda < 1.90$ but the previously observed values are higher than what is observed here (Johnston et al., 2007). Similarly, the $^{36}\lambda/^{33}\lambda$ ratio of 3.571 is much lower than the values previously observed for MSD and for MSR (Johnston et al., 2007, 2008). The observed isotopic signatures provide evidence against MSD, however, as this process produces fractionations of -0.1 - +0.5 ‰ in $\Delta^{36}S$ (Johnston et al., 2005b, 2007; Shen et al., 2009), this could not explain the consistently negative $\Delta^{36}S$ values of the Group 2 grains. The use of λ values to identify the action of different sulfur metabolisms is still developing and perhaps with the development of a larger database the λ values calculated here may be able to be better interpreted. In the time being, the isotopic signatures are largely conclusive with MSR and so this is the preferred interpretation.

The second option to be considered is that the signatures represent MDF crustal sulfur that had been introduced into the Witwatersrand Basin from the surrounding area. Previously, the isotopic composition of crustal sulfur from this locality has been estimated at $\Delta^{33}S = \sim 0$ ‰ and $\delta^{34}S = \sim 0$ - +10 ‰ (Chaussidon et al., 1989; Ohmoto and Goldhaber, 1997; Guy et al., 2012), which is similar to the signatures observed for Group 2 grains. However, whilst the Group 2 grains showed small $\Delta^{33}S$ values, those values are still resolvable and are not 0 ‰. The consistently negative $\Delta^{36}S$ values are also inconsistent with a MDF crustal sulfur source. Additionally, whilst there has been evidence of crustal sulfur previously observed within the Witwatersrand Supergroup (Guy et al., 2012, 2014), this has consistently been within fluvial clastic rocks, not marine clastic rocks, such as those analyzed within this chapter. On this basis, introduction of MDF crustal sulfur is unlikely to have been the source of the isotopic signatures of Group 2 grains.

Group 3 grains

Group 3 isotopic signatures are also consistent with MSR. When plotted in $\Delta^{36}S$-$\Delta^{33}S$ space, these data plot on or close to the recognized MSR array of $\Delta^{36}S/\Delta^{33}S = -6.9$ (Ono et al., 2006a) (Figure 6.6). The calculated $^{33}\lambda$ value of 0.494 and $^{36}\lambda$ value of 2.00 are also consistent with MSR, which produces $^{33}\lambda < 0.515$ and $^{36}\lambda > 1.90$ (Johnston et al., 2007). Furthermore, these values, and also the $^{36}\lambda/^{33}\lambda$ ratio of 4.06, are all similar to values calculated from suites of natural samples which have experienced MSR (e.g. Crockford et al., 2016; Sansjofre et al., 2016, Supplementary Information).

The observed $\delta^{34}S$ values also support action of MSR. The negative $\delta^{34}S$ values indicate that the sulfides are enriched in ^{32}S; this is agreeable with MSR, which concentrates ^{32}S in the product sulfide (Thode et al., 1951; Jones and Starkey, 1957; Harrison and Thode, 1958). Group 3 grains show a range in $\delta^{34}S$ values of ~-8 - -16 ‰ (excluding one outlying value of $\delta^{34}S$ of -0.71 ‰). Using the estimated range in $\delta^{34}S$ of +3 - +16 ‰ for Archean seawater sulfate (Lambert et al., 1987; Canfield and Raiswell, 1999; Ono et al., 2003), Group 3 grains preserve fractionations between 11 – 32 ‰ (minimum possible fraction based on the lowest estimate for Archean seawater and highest value for Group 3 grains: -8 ‰ – 3 ‰ = -11 ‰ and maximum fractionation based on the highest estimate for Archean seawater and lowest value for Group 3 grains: -16 ‰ – 16 ‰ = -32 ‰). This is consistent with fractionations observed in both culture studies and samples from post-Archean natural environments (e.g. Canfield and Teske, 1996; Canfield, 2001a; Ono et al., 2006a; Johnston et al., 2007).

The reason why Group 3 grains show larger $\delta^{34}S$ fractionations that are more similar to those observed in modern environments, whilst Group 2 grains show restricted $\delta^{34}S$ fractionations is uncertain. It is unlikely that the Group 3 grains represent transport of sulfur from much younger rocks, as the observed variation in the isotopic signatures is unlikely to have survived transport in hydrothermal fluids. Instead, it seems that MSR likely occurred in situ, and as this occurs in pore waters, it likely occurred during diagenesis. It could be suggested that Group 3 grains represent earlier fractionation in a sulfate limited environment, where Rayleigh fractionation effects resulted in repressed fractionations in the later formed Group 2 grains. However, there is no correlation between depth and $\delta^{34}S$ (Figure A2, Appendix), as would be expected in a closed system where Rayleigh effects were occurring (Seal, 2006). Additionally, if Group 3 grains had been formed earlier in a closed system, it would be expected that they would be enriched in trace elements relative to Group 2 grains (Gregory et al., 2015a), where here the opposite of that is true. Conversely, if Group 3 grains were to have formed later than Group 2 grains, an influx of sulfate post-formation of Group 2 grains, causing local sulfate enrichment, may explain the greater $\delta^{34}S$ fractionations in Group 3 grains but how this would occur without also replenishing the trace element supply is unknown. Alternatively, it may be possible that different species of sulfate reducing microbes have been active, where these different species fractionate $\delta^{34}S$ to different extents.

Group 1 grains

Group 1 isotopic signatures plot between the MSR and MIF lines in $\Delta^{36}S$-$\Delta^{33}S$ space and, when plotted as a group, show a trend of $\Delta^{36}S/\Delta^{33}S$ = ~-2 (Figure 6.8A). Similar $\Delta^{36}S/\Delta^{33}S$ trends have been observed during both the Mesoarchean (Farquhar et al., 2007; Mishima et al., 2017) and the Neoarchean (Zerkle et al., 2012; Izon et al., 2015). Of particular note is that similar trends to those observed within study were previously observed within Mesoarchean sediments from South Africa (Farquhar et al., 2007). Here we explore three possible explanations for this slope: (1) a change in atmospheric chemistry which steepened the MIF $\Delta^{36}S/\Delta^{33}S$ array, (2) secondary microbial fraction of MIF sulfur, and (3) mixing between MIF sulfur and sulfide produced through MSR.

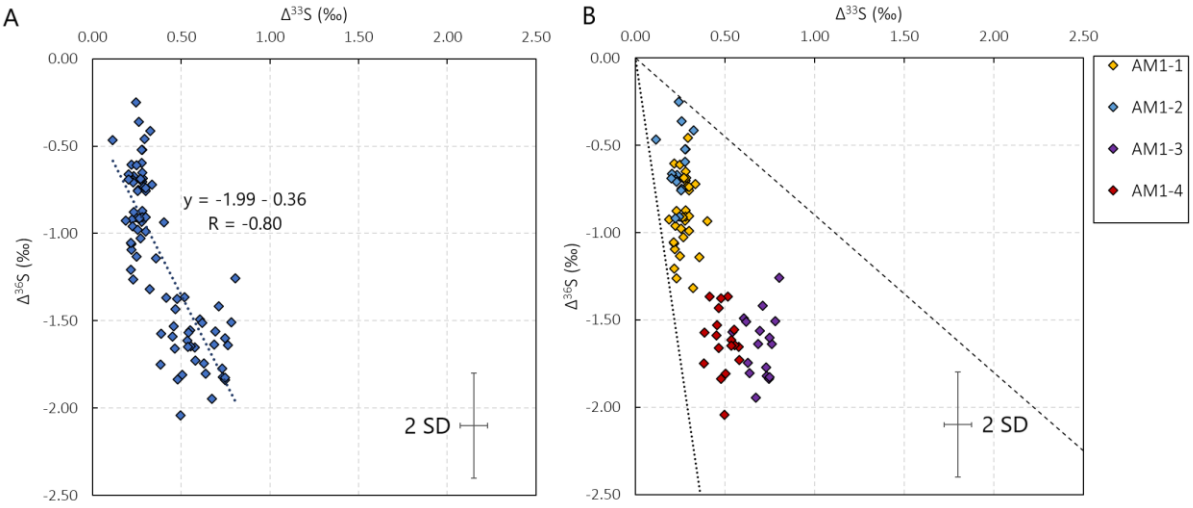

Figure 6.8. A. Plot of $\Delta^{36}S$ vs. $\Delta^{33}S$ for data from Group 1 grains, showing trend of $\Delta^{36}S/\Delta^{33}S$ = ~-2. B. Plot of $\Delta^{36}S$ vs. $\Delta^{33}S$ for data from Group 1 grains, with data separated by sample.

First to be explored is the hypothesis that the $\Delta^{36}S/\Delta^{33}S$ trend was caused by a change in atmospheric chemistry which altered the MIF $\Delta^{36}S/\Delta^{33}S$ array. This is the explanation which has previously been used to explain $\Delta^{36}S/\Delta^{33}S$ trends steeper than ~-0.90 in samples from the same locality as in this study (Farquhar et al., 2007). The $\Delta^{36}S/\Delta^{33}S$ array produced by photolysis of SO_2 is wavelength dependent, i.e. the $\Delta^{36}S/\Delta^{33}S$ slope changes depending on the wavelength of UV light involved in the photolysis reactions (Farquhar et al., 2001). Therefore, it has been proposed that a change in atmospheric chemistry that would alter the transparency of the atmosphere, and therefore the wavelengths of UV light penetrating the atmosphere, could be responsible for steepening the MIF $\Delta^{36}S/\Delta^{33}S$ array (Farquhar et al., 2007). Due to the correlation between steepened $\Delta^{36}S/\Delta^{33}S$ arrays and high magnitude negative $\delta^{13}C_{org}$ values observed within Neoarchean sedimentary rocks, it has been proposed

that the steepened slopes are caused by an atmospheric organic haze formed due to an enhanced biogenic methane flux (Zerkle et al., 2012; Izon et al., 2015). However, when Group 1 isotopic signatures are plotted by sample in $\Delta^{36}S$-$\Delta^{33}S$ space, instead of collectively as a group, it is revealed that data do not form a continuous array of slope ~-2 (Figure 6.8B). Instead, each sample forms an individual steep array, where there is substantial deviation from the MIF array in $\Delta^{36}S$, similar to what has previously been observed for MSR of MIF sulfate (Shen et al., 2009; Zhelezinskaia et al., 2014; Mishima et al., 2017). This is dissimilar to the continuous linear arrays produced by photolysis experiments (Farquhar et al., 2001, Figure 4). Therefore, it is unlikely that these signatures can be attributed to a change in atmospheric chemistry.

The second option is that the signatures represent microbial fractionation of MIF elemental sulfur. In previous studies, negative $\Delta^{33}S$ values associated with negative $\delta^{34}S$ values have been interpreted to represent microbial reduction of the MIF sulfate aerosol (e.g. Shen et al., 2009; Wacey et al., 2010; Zhelezinskaia et al., 2014; Mishima et al., 2017). Positive $\Delta^{33}S$ values associated with negative $\delta^{34}S$ values have been interpreted to signify microbial disproportionation of the MIF elemental sulfur reservoir (e.g. Philippot et al., 2007; Bontognali et al., 2012; Wacey et al., 2010). However, what is seen in this data set is positive $\Delta^{33}S$ values and predominantly *positive* $\delta^{34}S$.

These signatures may have been produced through a combination of MSD and MSR, as previously suggested by Wacey et al. (2010). MSD of elemental sulfur to sulfate produces positive fractionations in $\delta^{34}S$ that are typically between 16 – 20 ‰ (Canfield et al., 1998; Canfield, 2001b). If the reactant sulfur were to have been the elemental sulfur aerosol, the product would be sulfate with positive $\Delta^{33}S$ and positive $\delta^{34}S$, as MSD produces negligible fractionations in $\Delta^{33}S$ (Johnston et al., 2005b, 2007; Shen et al., 2009). Using the known relationship of $\Delta^{33}S = 0.9*\delta^{34}S$ for MIF sulfur (Ono et al., 2003), the original $\delta^{34}S$ value of the MIF sulfur would be between ~0 – 1 ‰ ($\Delta^{33}S$ values for Group 1 grains are between 0.11 – 0.80 ‰). Therefore, the $\delta^{34}S$ of the product sulfate would likely be between ~16 – 21 ‰. If MSD was followed by MSR, the increase in $\delta^{34}S$ caused by MSD would mask the decrease in $\delta^{34}S$ caused by MSR. Using the estimated values of +16 - +21 ‰ for the sulfate, the degree of fractionation in $\delta^{34}S$ preserved in Group 1 grains would be between -22 ‰ and -8 ‰ (based on maximum and minimum $\delta^{34}S$ values observed in Group 1 sulfides: -1.17 ‰ – 21 ‰ = -22.17 ‰ and 7.74 ‰ – 16 ‰ = -8.26 ‰). This is within the range of fractionations observed

for MSR during the Archean (Sim et al., 2019). As the fractionations in $\Delta^{33}S$ and $\Delta^{36}S$ produced by MSD are low, the final $\Delta^{33}S$ and $\Delta^{36}S$ values would be similar as to what would be produced by MSR alone; small increases in $\Delta^{33}S$ and larger decreases $\Delta^{36}S$. This is what is seen in the Group 1 data. This combination of processes is difficult to empirically prove but it is known that certain microbes can act as both sulfur disproportionators and sulfate reducers (e.g. *Desulfobulbus proponicus;* Canfield et al., 1998), so it is not unreasonable that both metabolisms would be active within the same environment at approximately the same time.

The third option is that the isotopic signatures observed within Group 1 grains represent mixing between MIF sulfur and sulfur produced through MSR. In this case, the steep $\Delta^{36}S/\Delta^{33}S$ arrays formed by the samples in Group 1 represent mixing lines extending between the MIF array and MSR array.

The isotopic signatures of Group 2 and Group 3 grains have already shown that MSR was occurring within the sediments of the Roodepoort Formation. Various evidence points to this occurring during a period of oxygenation (e.g. Crowe et al., 2013; Large et al., 2014; Planavsky et al., 2014; elevated Se concentrations observed during this study). The upper section of the Roodepoort Formation, however, preserves evidence of the MIF elemental sulfur aerosol, which requires a return to anoxic conditions that allowed for the restart of the photolysis reactions which produce MIF isotopic signatures (Pavlov and Kasting, 2002). Whilst immediate evidence for a return to anoxic conditions is lacking, evidence is provided higher in the Witwatersrand Supergroup, where placer deposits of pyrite and uraninite are common (Krupp et al., 1994; England et al., 2002; Frimmel et al., 2005b; Depiné et al., 2013). Se concentrations are elevated in Group 1 grains but this could possibly be explained by a lag between the decrease in atmospheric oxygen and the complete incorporation of Se already present within the water column into minerals. Mixing between the atmospherically-derived sulfur and the sulfide being produced through MSR in the sediments would then be responsible for the observed isotopic signatures.

It is unclear however, whether the observed $\delta^{34}S$ values could be explained through this mixing scenario. Therefore, some form of secondary microbial fractionation of MIF sulfur is the preferred explanation.

The signatures observed within Group 1 grains highlight the importance of analysing all four stable isotopes of sulfur when attempting to identify MIF sulfur. If only ^{32}S, ^{33}S and ^{34}S had

been analyzed, the deviation in $\Delta^{36}S$ from the MIF array would not have been able to be observed. As a result, the observed $\Delta^{33}S$ signatures would have been mistakenly interpreted to represent a purely atmospheric signature.

MSR during the Archean

The isotopic signatures of pyrite collected from the Roodepoort Formation confirm the action of MSR at ~2900 Ma. Initial evidence was provided by Guy et al. (2012), who observed covariation between sulfur and organic carbon contents and variation in $\delta^{34}S$ in sedimentary rocks of the Government and Jeppestown Subgroups, and Eickmann et al. (2018) who observed high magnitude negative $\delta^{34}S$ values in sulfides from dolomites of the Nsuze Group of the Pongola Supergroup. This confirms that during certain periods of the Archean, MSR was a geochemically important process within the sulfur cycle. But why is MSR only intermittently important, having been active between 3450 – 3200 Ma, ~2650 – 2500 Ma and now at ~2900 Ma?

As previously mentioned, there is a growing body of evidence for a period of oxygenation during the Mesoarchean (e.g. Crowe et al., 2013; Large et al., 2014; Planavsky et al., 2014; Ossa Ossa et al., 2016, 2019; Gosh and Baidya, 2017; Wang et al., 2018). This, combined with the elevated Se concentrations observed during this study, suggests that the MSR observed here occurred during a period when atmospheric oxygen was higher than baseline Archean levels ($<10^{-5}$*present atmospheric levels; Pavlov and Kasting, 2002). Similarly, observations of MSR between ~2650 – 2500 Ma occur in tandem with evidence for pulses of oxygenation (e.g. Anbar et al., 2007; Wille et al., 2007; Stueken et al., 2015; Koehler et al., 2018). This suggests that there is a link between action of MSR and increased atmospheric oxygen. It is possible that increased oceanic sulfate concentrations due to oxidative weathering of sulfide minerals is responsible. Higher sulfate concentrations would both make the environment more conducive to development of colonies of sulfate-reducing microbes and allow for larger and more recognisable isotopic fractionations (Habicht et al., 2002). However, this could not explain why MSR was occurring at ~3450 Ma, where there is no evidence for oxygenation.

Isotopic composition of seawater sulfate

Previously, where MSR has been observed within the Archean, the sulfides have shown negative $\Delta^{33}S$ (Ueno et al., 2008; Shen et al., 2009; Zhelezinskaia et al., 2014; Mishima et al.,

2017; Eickmann et al., 2018). However, Group 2 and 3 grains show low magnitude positive $\Delta^{33}S$ and the MSR array extends from approximately the origin in $\Delta^{36}S$-$\Delta^{33}S$ space (Figure 6.6). This suggests that the reactant sulfate had $\Delta^{33}S$ of ~ 0 ‰. This is at odds with estimates of the isotopic composition of Archean seawater sulfate, where $\Delta^{33}S$ is estimated to be ~-2 ‰ (Ono et al., 2003; Zhelezinskaia et al., 2014). It is suggested that this discrepancy is due to a predominantly riverine rather than atmospheric input of sulfate during the deposition of the Roodepoort Formation. Elevated Se concentrations observed during this study and previously observed by Large et al. (2014) suggest increased oxidative weathering caused by a rise in atmospheric oxygen concentrations within the locality of the Witwatersrand Basin. Further evidence for oxygenation during the Mesoarchean is provided by a number of different geochemical proxies, including Cr, Mo and U isotopes (Crowe et al., 2013; Planavsky et al., 2014; Wang et al., 2018) and Mn, Fe and REE systematics (Ossa Ossa et al., 2016, 2019; Ghosh and Baidya, 2017). Under conditions where oxidative weathering was occurring, a large amount of sulfate entering the Witwatersrand Basin would have been sourced from weathering of terrestrial sulfide minerals. As oxidative weathering of sulfide minerals does not cause isotopic fractionation, the isotopic composition of sulfate produced through weathering can be estimated from the composition of terrestrial sulfides from this area. Previously, it has been suggested that crustal sulfur in this locality would have $\Delta^{33}S$ = ~0 ‰ (Guy et al., 2012), which is consistent with what is needed to produce the signatures observed in Group 2 and 3 grains. The $\Delta^{33}S$ value of crustal sulfur from this locality can also be estimated by averaging data from previous studies of detrital pyrite (Hofmann et al., 2009) and from the previous chapters of this thesis which focused on terrestrial sulfide minerals. Using this method provides an estimate of $\Delta^{33}S$ = -0.04 ‰, which is also consistent with the isotopic signatures observed in Group 2 and 3 grains.

Steepening of the Mesoarchean MIF $\Delta^{36}S/\Delta^{33}S$ array

The data within this study show that steepening of the $\Delta^{36}S/\Delta^{33}S$ array observed in the Mesoarchean Roodepoort Formation was most likely caused by microbial fractionation of MIF sulfur. However, further research is required before it can be determined if this was a local or global phenomenon. At present, there is a paucity of four sulfur isotope data collected from Mesoarchean samples and data from this study, Farquhar et al. (2007) and Guy et al. (2012) were all collected from the same locality (the Kaapvaal Craton). Whilst Farquhar et al. (2007) attributed the steepened $\Delta^{36}S/\Delta^{33}S$ to changes in atmospheric chemistry, data within that study which was collected from the Moodies Group of the Pongola Supergroup and the

Government and Jeppestown Subgroups of the Witwatersrand Supergroup lie on steep trends in $\Delta^{36}S$-$\Delta^{33}S$ space that may indicate microbial action. It is suggested that re-examination of those samples may reveal similar signatures to what was observed within this study.

Outside of the Kaapvaal Craton, a steepened $\Delta^{36}S/\Delta^{33}S$ trend has also been observed within sedimentary rocks of the Mesoarchean Dharwar Supergroup, India (Mishima et al., 2017). This steepened trend was observed to occur in association with evidence of microbial activity. This suggests steepening of the Mesoarchean $\Delta^{36}S/\Delta^{33}S$ array due to microbial action may have been a global phenomenon but further evidence is required before this can be conclusively determined.

Attenuated $\Delta^{33}S$ and $\Delta^{36}S$ signatures during the Mesoarchean

As described in Chapter 1, $\Delta^{33}S$ and $\Delta^{36}S$ signatures are muted. Mesoarchean samples show a range in ~4 ‰ in $\Delta^{33}S$ and ~6 ‰ for $\Delta^{36}S$ in comparison to ranges of ~14 ‰ for both $\Delta^{33}S$ and $\Delta^{36}S$ across the Eo-, Paleo- and Neoarchean eras (Farquhar and Wing, 2005). This has attenuation has been attributed to various causes, including but not limited to, a transient increase in atmospheric oxygen (Ono et al., 2006b), other changes in atmospheric chemistry (Thomazo et al., 2009; Domagal-Goldman et al., 2008; Farquhar et al., 2007), changes in the oxidation state of volcanic sulfur volatiles (Halevy et al., 2010) and dilution of the atmospheric signal by crustal mass-dependent sulfur (Guy et al., 2012). A definitive cause has not yet been determined.

Ono et al. (2006b)'s proposal of a transient increase in atmospheric oxygen was disputed by Farquhar et al. (2007) who observed $\Delta^{36}S/\Delta^{33}S$ trends within Mesoarchean samples that, whilst steeper than the typical MIF array, were argued to still represent photolysis reactions occurring under anoxic conditions. Whist this author's interpretation of these steepened trends differs from that of Farquhar et al. (2007), it still requires an input of MIF sulfur and anoxic conditions. Yet, what was also observed were samples which showed a purely microbial signature and a complete absence of a MIF sulfur input. It was also determined that these purely microbial signatures occurred in tandem with an increase in atmospheric oxygen. Therefore, at least at this locality, there was a time where an increase in atmospheric oxygen prevented the action of the photolysis reactions, conclusive with the hypothesis of Ono et al. (2006b). Oxidative weathering during this period of increased atmospheric oxygen could also have mobilized MDF sulfur, which would have then diluted the MIF sulfur deposited during

the remainder of the Mesoarchean, contributing to the muted $\Delta^{33}S$ and $\Delta^{36}S$ values. Therefore, it is suggested that the muted signatures are due to a combination of those hypotheses proposed by Ono et al. (2006b) and Guy et al. (2012).

6.7 Conclusions

As shown, MSR was active during the Mesoarchean. This adds to a growing body of evidence that MSR was a geochemically important process within the Archean sulfur cycle at certain times within the Paleo-, Meso- and Neoarchean. Elevated concentrations of the redox sensitive trace element Se show that this MSR occurred in tandem with increased atmospheric oxygen. A steepened $\Delta^{36}S/\Delta^{33}S$ MIF array observed within the upper section of the Roodepoort Formation is argued to have been caused by microbial fractionation of the MIF elemental sulfur reservoir. This microbial action includes possible action by both sulfur disproportionating and sulfate reducing microbes. It is suggested that further detailed four isotope studies are undertaken of Mesoarchean sulfide minerals from different localities in order to determine whether this steepening due to microbial action is a localized or global phenomenon.

Also of importance is that sulfides from this study preserve small positive $\Delta^{33}S$ values, which is evidence for the preservation of the MIF elemental sulfur aerosol. There is a complete absence of pyrite bearing negative $\Delta^{33}S$ signatures consistent with preservation of sulfur sourced from the MIF sulfate aerosol. This is in direct contrast to the data presented in the previous three chapters, where terrestrial sulfide minerals consistently preserved the MIF sulfate aerosol and there was no evidence for preservation of the MIF elemental sulfur aerosol. This will be discussed in Chapter 7.

Chapter 7: Synthesis and concluding remarks

7.1 Introduction

Despite the large amount of multiple sulfur isotope data collected from Archean sulfide minerals, little research has been done to investigate the isotopic composition of terrestrial sulfur reservoirs. As a consequence, the current understanding of the Archean sulfur cycle is incomplete. Additionally, the limited amount of well constrained four sulfur isotope data collected from Mesoarchean samples has hindered interpretations of unusual trends observed in sulfur isotope data from this era.

This thesis expands the current set of multiple sulfur isotope data collected from terrestrial sedimentary rocks, adding to the data previously collected from fluvial clastic sedimentary rocks by Hofmann et al. (2009) and Guy et al. (2012, 2014) and from paleosols and glacial diamictites by Maynard et al. (2013). This extends the work previously completed by Maynard et al. (2013) attempting to determine the isotopic composition of terrestrial sulfur reservoirs. Also presented was new data collected from marine clastic sedimentary rocks, which will be contrasted with the terrestrial data in the following discussion in order to determine if terrestrial and marine sulfur reservoirs showed differing isotopic compositions.

As both the terrestrial and marine samples analyzed within this study were Mesoarchean in age, this thesis simultaneously expands the current set of well-constrained four sulfur isotope data available from Mesoarchean samples. The collected data provides new insights into the causes of both the attenuated $\Delta^{33}S$ and $\Delta^{36}S$ signatures and steepened MIF $\Delta^{36}S/\Delta^{33}S$ array observed during this era.

7.2 Summary of results

The work presented in Chapter 3 investigated the isotopic composition of diamictite-hosted pyrite. Difficulties were experienced in determining the paragenesis of these grains, however, diagenetic grains and two species of detrital grains were able to be identified. The first species of detrital grains showed trace element compositions and isotopic signatures consistent with the grains having been collected from a sedimentary source. The variable $\delta^{34}S$ values, small negative or approximately zero $\Delta^{33}S$ values and negative $\Delta^{36}S$ values obtained from these grains were consistent with microbial sulfate reduction (MSR) of a mixture of the

atmospheric mass-independently fractionated (MIF) sulfate aerosol and mass-dependently fractionated (MDF) crustal sulfur. In contrast, the second species of detrital grains showed trace element compositions and isotopic signatures consistent with the pyrite having been sourced from a volcanogenic massive sulfide (VMS) deposit. Diagenetic grains showed similar isotopic compositions to the first species of detrital grains. This was interpreted to represent an increased flux of crustal sulfur during deposition of glacial sediments, which outweighed the atmospheric sulfur flux. The isotopic compositions of the first species of detrital grains and the diagenetic grains suggested that terrestrial sulfide minerals preserved a mixture of atmospheric MIF sulfate and MDF sulfur but did not preserve sulfur sourced from the MIF elemental sulfur aerosol.

Chapter 4 examined the isotopic composition of paleosol-hosted sulfide minerals. Pyrite from two of the four analyzed paleosol profiles showed small negative $\Delta^{33}S$ values that were interpreted to represent a mixture of MIF sulfate and magmatic sulfur from the igneous parent materials. How this mixing occurred and how the MIF sulfate was fixated within the paleosol profiles is uncertain but the small positive and negative $\delta^{34}S$ and $\Delta^{36}S$ values observed for these samples are inconsistent with MSR. The two remaining paleosols preserved similar small positive and negative $\delta^{34}S$ and $\Delta^{36}S$ values but showed $\Delta^{33}S$ values of approximately 0 ‰. Sulfides from these samples were interpreted to be composed solely of magmatic sulfur inherited from the parent material. The lack of MIF sulfate observed within sulfides from these profiles is proposed to be due to the samples being collected from outside a known zone of sulfur enrichment which is consistently observed within the upper few centimetres of Archean paleosols and conceivably consists of atmospherically-derived sulfur species. The isotopic signatures of sulfides from these paleosols added to the evidence from Chapter 3 that terrestrial sulfide minerals preserved MIF sulfate and MDF sulfur but did not preserve MIF elemental sulfur.

Chapter 5 presented a study of the isotopic composition of pyrite hosted by fluvial clastic sedimentary rocks. Detrital pyrite showed isotopic and trace element compositions consistent with the grains being sourced from magmatic, hydrothermal and sedimentary environments. Grains from magmatic and hydrothermal environments showed small $\delta^{34}S$ values and $\Delta^{33}S$ and $\Delta^{36}S$ values of approximately zero whilst the grains from sedimentary environments showed similar isotopic signatures to detrital grains of sedimentary origin analyzed within Chapter 3. Two populations of diagenetic pyrite were identified, where the first population showed small positive $\delta^{34}S$ values and small negative to approximately zero $\Delta^{33}S$ values that

are consistent with a mixture of MIF sulfate and MDF crustal sulfur. These grains also showed consistently negative $\Delta^{36}S$ values that may be indicative of MSR. The other population of diagenetic grains showed similar small positive $\delta^{34}S$ values but had $\Delta^{33}S$ and $\Delta^{36}S$ values of approximately 0 ‰. This was interpreted to represent MDF sulfur, sourced from either a juvenile volcanic source or a mixed crustal source. As for both Chapter 3 and Chapter 4, these results showed that terrestrial sulfide minerals preserved MIF sulfate and MDF sulfur species but did not preserve MIF elemental sulfur.

Finally, in contrast to the previous three chapters, Chapter 6 presented sulfur isotope data collected from pyrite hosted by marine rocks, specifically marine clastic sedimentary rocks. Two populations of data were observed. The first population, corresponding to samples collected from greater depths, showed variable $\delta^{34}S$ values, small positive to approximately zero $\Delta^{33}S$ values and negative $\Delta^{36}S$ values, where data displayed steep negative $\Delta^{33}S/\Delta^{36}S$ trends. These signatures were interpreted to represent MSR of MDF sulfate. These signatures, coupled with the observed elevated concentrations of the redox sensitive elements selenium and molybdenum, provide new evidence for a period of oxygenation during the Mesoarchean. The second population, consisting of the shallower samples, showed positive $\Delta^{33}S$ values and negative $\Delta^{36}S$ values but deviated from the Archean Reference Array (ARA) in $\Delta^{36}S$. This was interpreted to represent microbial fractionation of MIF elemental sulfur, involving both MSR and microbial sulfur disproportionation. In stark contrast to the results of the previous chapters, positive $\Delta^{33}S$ values consistent with preservation of MIF elemental sulfur are observed, where negative $\Delta^{33}S$ values consistent with preservation of MIF sulfate are absent.

7.3 Synthesis and discussion

Isotopic composition of terrestrial sulfur reservoirs

As summarized above, detrital and diagenetic pyrite species from diamictites, paleosols and fluvial clastic sediments either preserve $\Delta^{33}S$ and $\Delta^{36}S$ signatures of approximately 0 ‰, consistent with MDF sulfur, or small negative $\Delta^{33}S$ signatures consistent with a mixture of MIF sulfate and MDF sulfur (Figure 7.1). This is consistent with previous data collected from pyrite hosted by fluvial clastic sediments (Hofmann et al., 2009; Guy et al., 2012, 2014), paleosols and diamictites (Maynard et al., 2013). Together, the data from this thesis and from previous studies provides a convincing argument that Archean terrestrial sulfur reservoirs consisted of MIF sulfate and MDF sulfur (Figure 7.2). Compiling this data, the average isotopic composition of Archean terrestrial sulfur reservoirs can be estimated as follows: $\delta^{34}S$

= 1.41 ± 3.89 ‰ (1 *SD*, *n* = 300), $\Delta^{33}S$ = -0.18 ± 0.43 ‰ (1 *SD*, *n* = 300), $\Delta^{36}S$ = -0.40 ± 0.67 (1 *SD*, *n* = 232). This confirms the previous hypothesis of Maynard et al. (2013) that Archean terrestrial sediments contained a sulfur reservoir which was partly comprised of MIF sulfate.

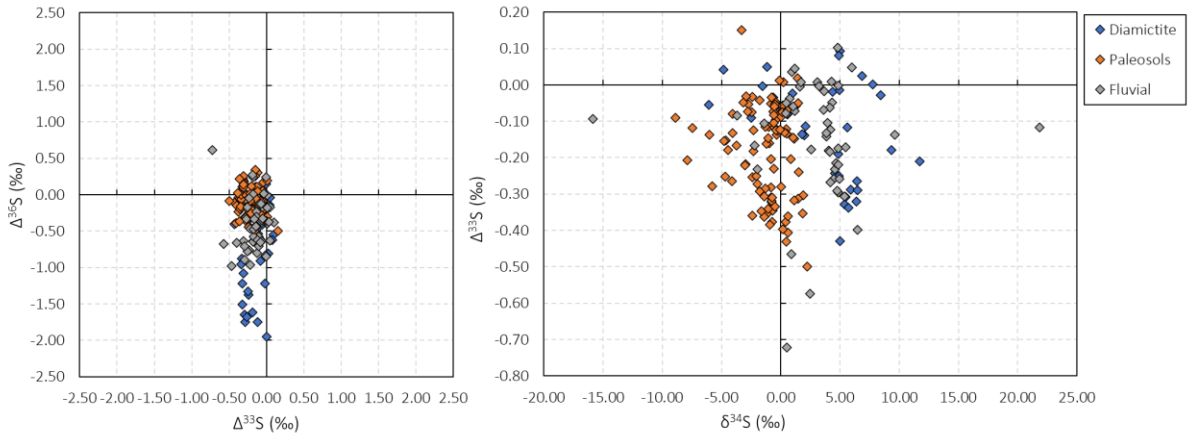

Figure 7.1. Compiled isotopic signatures of diamictite-, paleosol-, and fluvial clastic sediment-hosted sulfide minerals. A. $\Delta^{36}S$ vs. $\Delta^{33}S$, B. $\Delta^{33}S$ vs. $\delta^{34}S$. Excluded from these plots are detrital grains from the diamictite samples that were determined to be from a VMS deposit, grains from the Cooper Lake and Crown Lava samples, detrital grains from the fluvial samples determined to be sourced from igneous and hydrothermal source rocks and epigenetic grains from the fluvial samples.

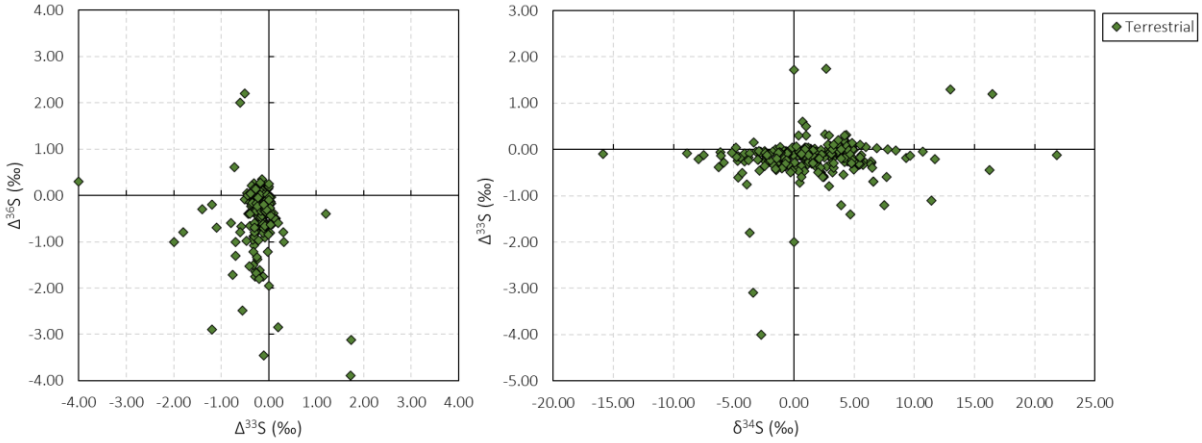

Figure 7.2. Compiled isotopic signatures of terrestrial sulfide minerals from this thesis and literature. A. $\Delta^{36}S$ vs. $\Delta^{33}S$, B. $\Delta^{33}S$ vs. $\delta^{34}S$. Literature data from Hofmann et al. (2009), Guy et al. (2012, 2014), Maynard et al. (2013).

Fractionation processes

Many of the grains within the diamictite and fluvial samples showed isotopic compositions consistent with MSR, showing that this was an active and geochemically important fractionation process within terrestrial environments during the Archean. The isotopic composition of paleosol hosted sulfide minerals, however, was not consistent with MSR, showing that other fractionation processes were also active within these environments. These fractionation processes could not be identified at this time and further research is required.

Comparing the isotopic composition of terrestrial and marine samples

When the isotopic composition of the terrestrial and marine samples analyzed in this thesis are compared, there is some overlap in that both types of samples preserve an MDF sulfur component. However, the samples differ in that the terrestrial samples show negative $\Delta^{33}S$ values consistent with preservation of MIF sulfate and that marine samples show positive $\Delta^{33}S$ signatures consistent with preservation of MIF elemental sulfur (Figure 7.3). This indicates that MIF sulfate was preferentially preserved within terrestrial sediments and that MIF elemental sulfur was preferentially preserved within marine sediments. When the greater sulfur isotope record is considered, this observation largely holds true, with terrestrial samples consistently showing negative $\Delta^{33}S$ values and the majority of marine samples showing positive $\Delta^{33}S$ values (Figure 7.4). In particular, marine clastic sedimentary rocks, such as shales and siltstones, are dominated by positive $\Delta^{33}S$ signatures (e.g. Ono et al., 2003; Thomazo et al., 2009; Izon et al., 2015). Where negative $\Delta^{33}S$ values are observed for marine samples, they are commonly found in barite or sulfide minerals deposited within marine hydrothermal environments, such as VMS deposits and banded iron formations (BIF), where the sulfate was likely fixated through high temperature thermochemical sulfate reduction (TSR) involving Fe^{2+} (Shanks et al., 1981; Shanks and Seyfried, 1987; Alt, 1995). Less commonly, negative $\Delta^{33}S$ values are observed within sulfide minerals hosted by sedimentary rocks which precipitate directly from seawater, such as limestones and dolomites, where the sulfate is fixated through MSR (Farquhar et al., 2013; Zhelezinskaia et al., 2014; Eickmann et al., 2018).

Possible reasons for the observed differences

The next logical question to ask is why this dichotomy would exist; *why do terrestrial sedimentary rocks only preserve MIF sulfate and why do marine sedimentary rocks favour preservation of MIF elemental sulfur?* Previously, this has been attributed to differences in solubility between the two types of MIF sulfur aerosols (Maynard et al., 2013). It may also possibly due to factors such as preferential accumulation of certain aerosols within particular environments and the mechanisms by which these aerosols are transformed into sulfide and incorporated into sulfide minerals. These possibilities are discussed below.

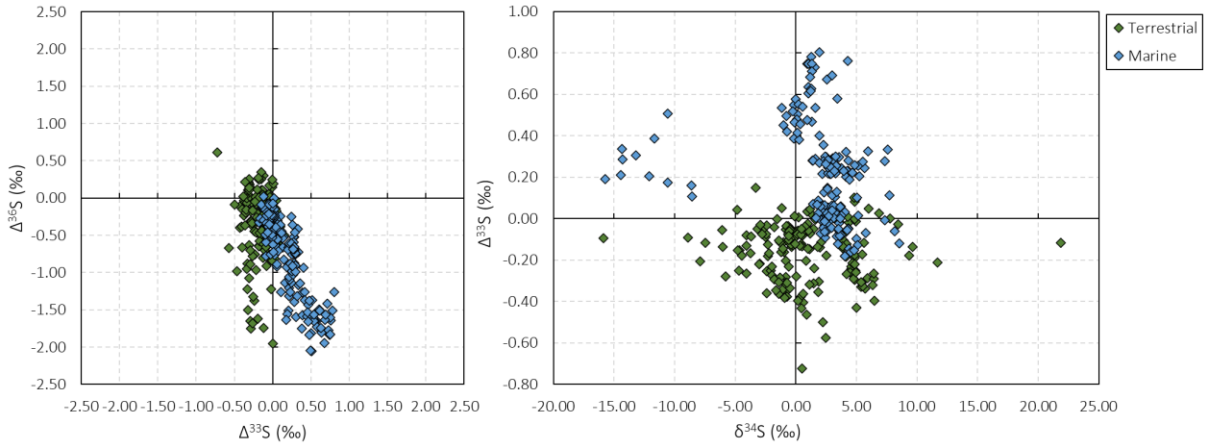

Figure 7.3. Comparison of the isotopic composition of the terrestrial and marine samples from this thesis. A. $\Delta^{36}S$ vs. $\Delta^{33}S$, B. $\Delta^{33}S$ vs. $\delta^{34}S$. Excluded from these plots are detrital grains from the diamictite samples that were determined to be from a VMS deposit, sulfide minerals from the Cooper Lake and Crown Lava paleosols, sulfide minerals from the units underlying and overlying paleosols, detrital grains from the fluvial samples determined to be igneous or hydrothermal in origin and epigenetic grains from the fluvial samples.

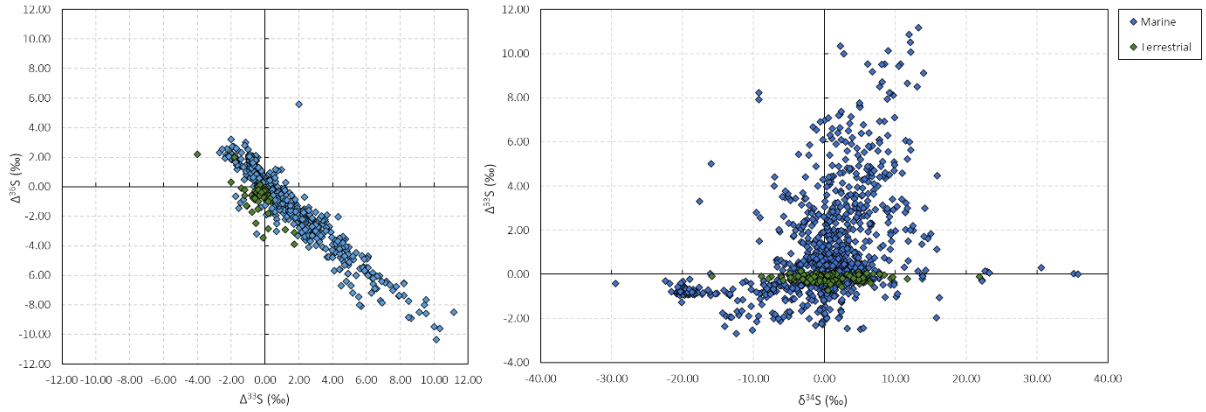

Figure 7.4. Comparison of the isotopic composition of terrestrial and marine samples from literature. A. $\Delta^{36}S$ vs. $\Delta^{33}S$, B. $\Delta^{33}S$ vs. $\delta^{34}S$. Data from Mojzsis et al. (2003); Ono et al. (2003, 2009); Ohmoto et al. (2006); Kamber and Whitehouse, (2007); Kaufman et al., (2007); Patridge et al. (2008); Hofmann et al. (2009); Shen et al. (2009); Thomazo et al. (2009); Guy et al. (2012, 2014); Zerkle et al. (2012); Farquhar et al. (2013); Zhelezinskaia et al. (2014); Izon et al. (2015); Eickmann et al. (2018).

As mentioned in Chapters 3 and 5, Maynard et al. (2013) proposed that terrestrial sedimentary rocks preferentially preserved MIF sulfate due to the greater solubility of sulfate in comparison to elemental sulfur. Under this hypothesis, sulfate, dissolved in rainwater, soaked into terrestrial sediments and was subsequently reduced and incorporated into sulfide minerals. In contrast, due to the relative insolubility of elemental sulfur, the MIF elemental sulfur aerosol remained at the surface, where erosion resulted in it being transported to the oceans and preserved within marine sedimentary rocks. However, the results of Chapters 3 and 5 indicate that this difference in solubility cannot fully explain the observed dichotomy. In regards to the results of Chapter 3, if the MIF elemental sulfur were residing at the

continental surface, it would have been collected in the subglacial sediments as the glacier moved across the continent. If solubility were the only barrier to this aerosol being preserved, it would be expected that it would be free to be incorporated into sulfide minerals once the subglacial sediments were deposited in the sedimentary basin. However, none of the analyzed diagenetic pyrite grains within the diamictite samples showed positive $\Delta^{33}S$ signatures consistent with preservation of MIF elemental sulfur. Similarly, none of the diagenetic pyrite within the fluvial sedimentary samples analyzed in Chapter 5 showed positive $\Delta^{33}S$ values. It would have been expected that at least a portion of the eroded MIF elemental sulfur would have been transported to the oceans via streams and rivers and that during this transport it would have available to be incorporated into diagenetic pyrite within fluvial sediments. These results indicate that whilst the difference in solubility between the two MIF aerosols may have contributed to preferential preservation within different environments, other factors play a significant role.

The second possibility relates to preferential accumulation of the MIF elemental sulfur aerosol within certain locations and the mechanisms by which the two MIF aerosols are incorporated into sulfide minerals. It expands on a hypothesis previously proposed by Farquhar et al. (2013). Under this hypothesis, the MIF elemental sulfur aerosol preferentially accumulated within depositional basins proximal to sources of atmospheric sulfur gases due to the short atmospheric residence time of elemental sulfur. Within these basins, the elemental sulfur reacted with small amounts of biogenic sulfide to form polysulfides and these polysulfides subsequently reacted with iron sulfide to form pyrite via the mechanisms described by Luther (1991) and Schoonen and Barnes (1991). The relative proportion of MIF sulfate-derived sulfide to MIF elemental sulfur-derived sulfide is proposed to have been low in these environments, resulting in pyrite carrying positive $\Delta^{33}S$ values. In contrast, pyrite showing negative $\Delta^{33}S$ values is proposed to have formed in environments or during times where MSR or TSR was more active and there was a higher proportion of MIF sulfate-derived sulfide. To extend this hypothesis to cover the dichotomy between marine and terrestrial samples, the prevalence of MSR within terrestrial sediments and relatively low amounts of MIF elemental sulfur within these sediments would have resulted in high levels of MIF sulfate-derived sulfide and, consequently, dominance of pyrite with negative $\Delta^{33}S$ values. However, within marine sediments, where the MIF elemental sulfur had accumulated and MSR or TSR was less active, there were high levels of MIF elemental sulfur-derived sulfide, resulting in dominance of pyrite with positive $\Delta^{33}S$ values. This hypothesis is able to

more fully explain the observed dichotomy and so is the preferred explanation. It is acknowledged, however, that further investigation of the mechanisms by which MIF elemental sulfur was incorporated into pyrite would be beneficial.

Limitations of the results

The first limitation of this work is that the vast majority of the terrestrial samples were collected from the same locality, the Kaapvaal Craton. Additionally, the previous work completed on terrestrial samples also analyzed samples collected from the Kaapvaal Craton (Hofmann et al., 2009; Guy et al., 2012, 2014; Maynard et al., 2013). Whilst this has provided a good understanding of the isotopic composition of Archean terrestrial sulfur reservoirs in this locality, it is yet to be determined if the observed isotopic composition is representative of all Archean terrestrial sulfur reservoirs.

Second, within Chapters 3, 4 and 6, difficulties were encountered in determining the paragenesis of some or most of the analyzed sulfide mineral grains. This does place some uncertainty around the some of the interpretations provided in those chapters. In particular, the lack of knowledge around how a diagenetic sulfide grain would form within a paleosol profile or whether it would form at all, impacted the author's ability to interpret the paragenesis of the sulfide grains analyzed within that chapter. As did the scarcity of trace element data available from sulfide minerals hosted by igneous rocks.

Third, some of the chapters could have benefited from analysis of more samples and collection of more data. The amount of data collected from the diamictite samples analyzed in Chapter 3 was quite limited (due to scarcity of sulfide grains) and that study could have benefited from analysis of more samples from both that particular diamictite and other Archean diamictites. Similarly, collection of new samples from the Crown Lava and Cooper Lake paleosols from within the known zones of sulfur enrichment would have beneficial in constraining the isotopic composition of paleosol-hosted sulfide minerals.

Directions for future work

Possibly the most interesting results from this thesis were obtained during analysis of pyrite hosted by the shallow marine Roodepoort Formation of the West Rand Group (Chapter 6). These samples appeared to show evidence for a period of oxygenation where MIF sulfur isotope signatures are absent from the rock record. Additionally, there was also evidence that the steepened MIF $\Delta^{36}S/\Delta^{33}S$ array observed within Mesoarchean samples may be due to secondary biological fractionation of MIF elemental sulfur, rather than a change in

atmospheric chemistry, as previously proposed (Farquhar et al., 2007). Both of these observations are of great interest to the Mesoarchean sulfur cycle and the chemistry of the Mesoarchean atmosphere and are worthy of further investigation.

The apparent period of oxygenation could initially be investigated further through detailed sulfur isotope analysis of sulfide minerals hosted by the sedimentary units underlying the Roodepoort Formation. Previous analysis of the trace element compositions of sulfide minerals from these units revealed elevated concentrations of the redox sensitive trace elements selenium and molybdenum, which was interpreted to represent elevated atmospheric O_2 (Large et al., 2014). Therefore, the isotopic signatures of sulfide minerals hosted by these rocks are of great interest. Whilst there is sulfur isotope data available from these rocks (Farquhar et al., 2007; Guy et al., 2012), the amount of four sulfur isotope data is relatively scarce and therefore there is room for further analysis to occur. This further analysis is important as it has the potential to provide new information regarding the cause of the Mesoarchean minimum in $\Delta^{33}S$ and $\Delta^{36}S$ values and whether it was caused by an increase in atmospheric O_2, as suggested by Ono et al. (2006b).

In terms of the steepened $\Delta^{36}S/\Delta^{33}S$ array being a product of secondary microbial action, further high resolution four sulfur isotope analysis of Mesoarchean samples would be beneficial in confirming the results and interpretation presented in this thesis. It is suggested that this analysis begin with samples collected from the same units as analyzed in Farquhar et al. (2007), as that study returned broadly similar results as to this thesis, however with less data and a different interpretation. This could then be followed by analysis of Mesoarchean samples from other localities to determine whether this was a localized or global phenomenon. This would provide new information regarding the role of microbes within the Mesoarchean sulfur cycle and whether the Mesoarchean was in fact a time of dynamic atmospheric chemistry.

Detailed studies of the trace element compositions of pyrite hosted by a variety of rock types are also needed. Currently, the guidelines used to determine if pyrite within sedimentary rocks is syngenetic/diagenetic come from a paper which examined pyrite hosted by black shales (Gregory et al., 2015a). Whilst this paper is useful, the earlier work of Guy et al. (2010) indicated that pyrite formed within different depositional environments and hosted by different sedimentary rocks types can display different trace element compositions. Therefore, the guidelines set out by Gregory et al. (2015a) may not be applicable to all

syngenetic/diagenetic pyrite. Expanding the current data base and establishing the trace element compositions of syngenetic/diagenetic pyrite from other sedimentary environments outside of black shales would be beneficial for future studies which require determination of pyrite paragenesis.

7.3 Conclusions

Despite the large amount of multiple sulfur isotope data gathered from Archean sulfide and sulfate minerals, only a very small portion of this data had been gathered from terrestrial environments. This left the isotopic composition of Archean terrestrial sulfur reservoirs largely undefined and, consequently, the current understanding of the Archean sulfur cycle was incomplete. Similarly, only a limited amount of well-constrained four sulfur isotope data was available from Mesoarchean samples, limiting the interpretation of unusual isotopic trends observed during this era. This thesis extended the limited work completed on the sulfur isotope composition of terrestrial sulfide minerals and examined the differences between the compositions of these sulfide minerals and those hosted by marine sediments. Additionally, it greatly expanded the available amount of Mesoarchean four sulfur isotope data, allowing for re-examination of the Mesoarchean sulfur isotope data record and providing new insights into why the data from samples of this era differs from that of samples from the other Archean eras. The following conclusions can be made:

- Archean terrestrial sulfur reservoirs were comprised of a combination of MIF sulfate and MDF sulfur. This confirms the earlier hypothesis of Maynard et al. (2013) that Archean terrestrial sedimentary rocks contained a pool of sulfur with negative $\Delta^{33}S$ that could be important for balancing the bias towards positive $\Delta^{33}S$ observed within the current data record. Additionally, within these environments, MSR was established to be an active and geochemically important process, providing further evidence for the antiquity of sulfate reducing microbes.
- The terrestrial and marine samples analyzed for this thesis showed distinctly different isotopic compositions; the terrestrial samples showed negative $\Delta^{33}S$ values consistent with preservation of MIF sulfate and the marine samples showed positive $\Delta^{33}S$ values consistent with preservation of MIF elemental sulfur. This observation holds when the greater sulfur isotope record is considered. This dichotomy is proposed to be due to the different MIF aerosols preferentially accumulating in different areas and the different mechanisms by which these aerosols are transformed to sulfide and incorporated into pyrite.

- The marine samples analyzed for this thesis preserve evidence for a period of increased atmospheric oxygen during the Mesoarchean, during which MIF sulfur isotope signatures were minimal if not absent from the rock record. This provides new evidence that the Mesoarchean minimum in $\Delta^{33}S$ and $\Delta^{36}S$ values could be due to a transient increase in atmospheric oxygen. The isotopic signatures of terrestrial samples also indicates that the Mesoarchean minimum in $\Delta^{33}S$ and $\Delta^{36}S$ values is related to dilution of MIF sulfur species by MDF sulfur species, possibly related to oxidative weathering during this period of increased atmospheric oxygen and/or the action of other mechanisms.
- The marine samples also showed that the steepened Mesoarchean MIF $\Delta^{36}S/\Delta^{33}S$ array observed within South African sedimentary rocks may be due to secondary microbial fractionation rather than a change in atmospheric chemistry.

References

Alt, J. C. (1995). Sulfur isotopic profile through the oceanic crust – sulfur mobility and seawater-crustal sulfur exchange during hydrothermal alteration. Geology 23: 585 – 588. doi: 10.1130/0091-7613(1995)023<0585:SIPTTO>2.3.CO;2

Altuhafi, F., Baudet, B. A. (2011). A hypothesis on the relative roles of crushing and abrasion in the mechanical genesis if a glacial sediment. Engineering Geology 120: 1 – 9. doi: 10.1016/j.enggeo.2011.03.002

Anbar, A. D., Duan, Y., Lyons, T. W., Arnold, G. L., Kendall, B., Creaser, R. A., Kaufman, A. J., Gordon, G. W., Scott, C., Garvin, J., Buick, R. (2007). A whiff of oxygen before the Great Oxidation Event? Science 317: 1903 – 1906. doi: 10.1126/science.1140325

Aoyama, A., Ueno, Y. (2017). Multiple sulfur isotope constraints on microbial sulfate reduction below an Archean seafloor hydrothermal system. Geobiology 16(2): 107 – 120. doi: 10.1111/gbi.12268

Armstrong, R. A., Compston, W., Retief, E. A., Williams, I. S., Welke, H. J. (1991). Zircon ion microprobe studies bearing on the age and evolution of the Witwatersrand triad. Precambrian Research 53: 243 – 266. doi: 10.1016/0301-9268(91)90074-K

Arnold, R. G. (1967). Range in composition and structure of 82 natural terrestrial pyrrhotites. The Canadian Mineralogist 9: 31 – 50.

Awramik, S. M., Buchheim, H. P. (2009). A giant late Archean lake system: The Meentheena Member (Tumbiana Formation: Fortescue Group), Western Australia. Precambrian Research 174: 215 – 240. doi: 10.1016/j.precamres.2009.07.005

Babechuk, M. G., Weimer, N. E., Kleinhanns, I. C., Eroglu, S., Swanner, E. D., Kenny, G. G., Kamber, B. S., Schoenberg, R. (2019). Pervasively anoxic surface conditions at the onset of the Great Oxidation Event: New multi-proxy constraints from the Cooper Lake paleosol. Precambrian Research 323: 126 – 163. doi: 10.1016/j.precamres.2018.12.029

Bajwah, Z. U., Seccombe, P. K., Offler, R. (1987). Trace element distribution, Co:Ni ratios and genesis of the Big Cadia iron-copper deposit, New South Wales, Australia. Mineralium Deposita 22: 292 – 300. doi: 10.1007/BF00204522

Bak, F., Pfennig, N. (1987). Chemolithotrophic growth of Desulfvibrio sulfodismutans sp. nov. by disproportionation of inorganic sulfur compounds. Archives of Microbiology 147(2): 184 – 189. doi: 10.1007/BF00415282

Baroni, M., Thiemens, M. H., Delmas, R. J., Savarino, J. (2007). Mass-independent sulfur isotopic compositions in stratospheric volcanic eruptions. Science 315: 84 – 87. doi: 10.1126/science.1131754

Barton, E. S., Hallbauer, D. K. (1996). Trace-element and U-Pb isotope compositions of pyrite types in the Proterozoic Black Reef, Transvaal Sequence, South Africa: Implications on genesis and age. doi: 10.1016/S0009-2541(96)00075-7

Beaudoin, G., Taylor, B. E., Rumble, D., Thiemens, M. (1994). Variations in the sulfur isotope composition of troilite from the Cañon Diablo iron meteorite. Geochimica et Cosmochimica Acta 58: 4253 – 4255. doi: 10.1016/0016-7037(94)90277-1

Bekker, A., Holland, H. D., Wang, P. L., Rumble, D., Stein, H. J., Hannah, J. L., Coetzee, L. L., Beukes, N. J. (2004). Dating the rise of atmospheric oxygen. Nature 427: 117 – 120.

Bekker, A., Barley, M. E., Fiorentini, M. L., Rouxel, O .J., Rumble, D. (2009). Atmospheric sulfur in Archean komatiite-hosted nickel deposits. Science 326: 1086 – 1089. doi: 10.1126/science.1177742

Bennett, G., Leahy, E. J., Walmsley, J. (1990). Sault Ste. Marie resident geologist's report for 1989. In: Fenwick, K. G., Giblin, P. E., Pitts, A. E. (Eds.) Report of Activities 1989, Resident Geologists, Ontario Geological Survey, pp. 205 – 215.

Bennett, G. (2006). The Huronian Supergroup between Sault Ste. Marie and Elliot Lake. Field Trip Guidebook. Institute on Lake Superior Geology 52: 1 – 65.

Bennett, G., Dressler, B. O., Robertson, J. A. (1991). The Huronian Supergroup and associated intrusive rocks. In: Thurston, P. C., Williams, H. R., Sutcliffe, R. H., Stott, G. M. (Eds.) Geology of Ontario. Ontario Ministry of Northern Development and Mines, Toronto, pp. 549 – 591

Berner, R. A. (1970). Sedimentary pyrite formation. American Journal of Science 268: 1 -23. doi: 10.2475/ajs.268.1.1

Berner, Z. A., Puchelt, H., Nöltner, T., Kramar, U. T. Z. (2013). Pyrite geochemistry in the Toarcian Posidonia Shale of south-west Germany: Evidence for contrasting trace-element patterns of diagenetic and syngenetic pyrites. Sedimentology 60: 548 – 573. doi: 10.1111/j.1365-3091.2012.01350.x

Beukes, N. J. (1995). Stratigraphy and basin analysis of the West Rand Group with special reference to prospective areas for placer gold deposits. Unpublished report, Rand Afrikaans University (University of Johannesburg), pp 117.

Beukes, N. J., Cairncross, B. (1991). A lithostratigraphic-sedimentological reference profile for the Late Archean Mozaan Group, Pongola Supergroup: Application to sequence stratigraphy and correlation with the Witwatersrand Supergroup. South African Journal of Geology 94(1): 44 – 69.

Bolhar, R., Van Kranendonk, M. J. (2007). A non-marine depositional setting for the northern Fortescue Group, Pilbara Craton, inferred from trace element geochemistry of stromatolitic carbonates. Precambrian Research 155: 229 – 250. doi: 10.1016/j.precamres.2007.02.002

Bontognali, T., Sessions, A. L., Allwood, A. C., Fischer, W. W., Grotzinger, J. P., Summons, R. E., Eiler, J. M. (2012). Sulfur isotopes of organic matter preserved in 3.45-billion-year-old stromatolites reveal microbial metabolism. Proceedings of the National Academy of Science 109(38): 15146 – 15151. doi: 10.1073/pnas.1207491109

Bouyon, A., Cartigney, P., Avila, J. N., Rego, E. S., Rossignol, C., Philippot, P. Trindade, R. I., Huhn, S. R. (2018). Multiple sulfur isotope record from the Precambrian of South America shows an unusual trend. Abstract V31B-04, presented at the 2018 American Geophysical Union Fall Meeting, Washington, D. C., 10 – 14 December.

Bralia, A., Sabatini, G., Troja, F. (1979). A revaluation of the Co/Ni ratio in pyrite as geochemical tool in ore genesis problems. Mineralium Deposita 14(3): 353 – 374. doi: 10.1007/BF00206365

Buick, R. (1992). The antiquity of oxygenic photosynthesis: Evidence from stromatolites in sulfate-deficient Archean lakes. Science 225: 74 – 77. doi: 10.1126/science.11536492

Cabral, R. A., Jackson, M. G., Rose-Koga, E. F., Koga, K. T., Whitehouse, M. J., Antonelli, M. A., Farquhar, J., Day, J. M. D., Hauri, E. H. (2013). Nature 496: 490 – 493. doi: 10.1038/nature12020

Cambel, B., Jarkovsky, J. (1969). Geochemistry of pyrrhotite of various genetic types. Komensky University, Bratislava.

Canfield, D. E. (2001a). Isotope fractionation by natural populations of sulfate-reducing bacteria. Geochimica et Cosmochimica Acta 65(7): 1117 – 1124. doi: 10.1016/S0016-7037(00)00584-6

Canfield, D. E. (2001b). Biogeochemistry of sulfur isotopes. Reviews in Mineralogy and Geochemistry 43(1): 607 – 636. doi: 10.2138/gsrmg.43.1.607

Canfield, D. E., Raiswell, R. (1999). The evolution of the sulfur cycle. American Journal of Science 299: 697 – 723. doi: 10.2475/ajs.299.7-9.697

Canfield, D. E., Raiswell, R., Westrich, J. T., Reaves, C. M., Berner, R. A. (1986). The use of chromium reduction in the analysis of reduced inorganic sulphur in sediments and shales. Chemical Geology 54: 149 – 155. doi: 10.1016/0009-2541(86)90078-1

Canfield, D. E., Teske, A. (1996). Late Proterozoic rise in atmospheric oxygen concentration inferred from phylogenetic and sulfur-isotope studies. Nature 382: 127 – 132.

Canfield, D. E., Thamdrup, B. (1994). The production of ^{34}S-depleted sulfide during bacterial disproportionation of elemental sulfur. Science 266: 1973 – 1975. doi: 10.1126/science.11540246

Canfield, D. E., Thamdrup, B., Fleisher, S. (1998). Isotope fractionation and sulfur metabolism by pure and enrichment cultures of elemental sulfur-disproportionating bacteria. Limnology Oceanology 43(2): 253 – 264. doi: 10.4319/lo.1998.43.2.0253

Card, K. D. (1978). Geology of the Sudbury-Manitoulin area, districts of Sudbury and Manitoulin. Ontario Geological Survey Report 166: 1 – 238.

Carstens, H. (1985). Early diagenetic cone-in-cone structures in pyrite concretions. Journal of Sedimentary Petrology 55(1): 105 – 108. doi: 10.1036/212F8625-2B24-11D7-8648000102C1865D.

Carstens, H. (1986). Displacive growth of authigenic pyrite. Journal of Sedimentary Research 56(2): 252 – 257. doi: 10.1306/212F88D7-8648000102C1865D

Cates, N. L. (2009). Petrogenic histories of pre-3750 Ma supracrustal rocks (Akila Association, West Greenland and Nuvvuatittuq Supracrustal Belt, Quebec, Canada). PhD Thesis (unpublished), University of Colorado.

Cates, N. L., Mojzsis, S. J. (2006). Chemical and isotopic evidence for widespread Eoarchean metasedimentary enclaves in southern West Greenland. Geochimica et Cosmochimica Acta 71: 5862 – 5875. doi: 10.1016/j.gca.2006.05.014

Catuneanu, O. (2001). Flexural partitioning in the Late Archaean Witwatersrand foreland system, South Africa. Sedimentary Geology 141 – 142: 95 – 112. doi: 10.1016/S0037-0738(01)00070-7

Chaussidon, M., Albarede, F., Sheppard, S. M. F. (1987). Sulphur isotope heterogeneity in the mantle from ion microprobe measurements of sulfide inclusions in diamonds. Nature 330: 242 – 244.

Chaussidon, M., Albarede, F., Sheppard, S. M. F. (1989). Sulphur isotope variations in the mantle from ion microprobe analysis of micro-sulfide inclusions. Earth and Planetary Science Letters 92: 144 – 156. doi: 10.1016/0012-821X(89)90042-3

Claypool, G. E., Mancini, E. A. (1989). Geochemical relationships of petroleum in Mesozoic reservoirs to carbonate source rocks of Jurassic Smackover Formation, southwestern Alabama. American Association of Petroleum Geologists Bulletin 73: 904 – 924.

Claire, M. W., Kasting, J. F., Domagal-Goldman, S. D., Stüeken, E. E., Buick, R., Meadows, V. S. (2014). Modelling the signature of sulfur mass-independent fractionation produced in the Archean atmosphere. Geochimica et Cosmochimica Acta 141: 365 – 380. doi: 10.1016/j.gca.2014.06.032

Coffey, J. M., Flannery, D. T., Walter, M. R., George, S. C. (2013). Sedimentology, stratigraphy and geochemistry of a stromatolite biofacies in the 2.72 Ga Tumbiana Formation, Fortescue Group, Western Australia. Precambrian Research 236: 282 – 296. doi: 10.1016/j.precamrest.2013.07.021

Corfu, F., Andrews, A. J. (1986). A U-Pb age for mineralized Nipissing diabase, Gowganda, Ontario. Canadian Journal of Earth Science 23: 107 – 109. doi: 10.1139/e86-011.

Craig, J. R., Vokes, F. M., Solberg, T. N. (1998). Pyrite: Physical and chemical textures. Mineralium Deposita 34: 82 – 101. doi: 10.1007/s001260050

Crockford, P. W., Cowie, B. R., Johnston, D. T., Hoffman, P. F., Sugiyama, I., Pellerin, A., Bui, T. H., Hayles, J., Halverson, G. P., Macdonald, F. A., Wing, B. A. (2016). Tripe oxygen and multiple sulfur isotope constraints on the evolution of the post-Marinoan sulfur cycle. Earth and Planetary Science Letters 435: 74 – 83. 10.1016/j.epsl.2015.12.017

Crowe, S. A., Dossing, L. N., Beukes, N. J., Bau, M., Kruger, S. J., Frei, R., Canfield, D. E. (2013). Atmospheric oxygenation three billion years ago. Nature 501: 535 – 539. doi: 10.1038/nature12426

Crowe, S. A., Paris, G., Katsev, S., Jones, C., Kim, S., Zerkle, A., Nomosatryo, S., Fowle, D. A., Adkins, J. F., Sessions, A. L., Farquhar, J., Canfield, D. E. (2014). Sulfate was a trace constituent of Archean seawater. Science 346: 735 – 739. doi: 10.1126/science.1258966

Crowe, D. E., Vaughan, R. G. (1996). Characterisation and use of isotopically homogenous standards for in situ laser microprobe analysis of $^{34}S/^{32}S$ analysis. American Mineralogist 81: 187 – 193. doi: 10.2138/am-1996-1-223

Cui, H., Kitajima, K., Spicuzza, M. J., Fournelle, J. H., Ishida, A., Brown, P. E., Valley, J. W. (2018). Searching for the great oxidation event in North America: A reappraisal of the Huronian Supergroup by SIMS sulfur four-isotope analysis. Astrobiology 18(5): 519 – 538. doi: 10.1089/ast.2017.1722

Cypionka, H., Smock, A. M., Bottcher, M. E. (1998). A combined pathway of sulfur compound disproportionation in Desulfovivrio desulfuricans. FEMS Microbiology Letters 166(2): 181 – 186. doi: 10.1111/j.1574-6968.1998.tb13888.x

Danyushevsky, L., Robinson, P., Gilbert, S., Norman, M., Large, R., McGoldrick, P., Shelley, M. (2011). Routine quantitative multi-element analysis of sulfide minerals by laser ablation ICP-MS: Standard development and consideration of matrix effects. Geochemistry: Exploration, Environment, Analysis 11: 51 – 60. doi: 10.1144/1467-7873/09-244

de Hoog, J. C. M., Taylor, B. E., van Bergen, M. J. (2001). Sulphur isotope systematics of basaltic lavas from Indonesia: Implications for the sulphur cycle in subduction zones. Earth and Planetary Science Letters 189: 237 – 252. doi: 10.1016/S0012-821X(01)00355-7

Demeter, J., Brüchert, V., Habicht, K. S., Kuever, J. (2001). Diversity of sulfur isotope fractionations by sulfate reducing prokaryoates. Applied Environmental Microbiology 67: 888 – 894. doi: 10.1128/AEM.67.2.888-894.2001

Depiné, M., Frimmel, H. E., Emsbo, P., Koenig, A. E., Kern, M. (2013). Trace element distribution in uraninite from Mesoarchean Witwatersrand conglomerates (South Africa) supports placer model and magmatogenic source. Mineralium Deposita 48: 423 – 435. doi: 10.1007/s00126-013-0458-3

Dimroth, E. (1979). Significance of diagenesis for the origin of Witwatersrand-type uraniferous conglomerates. Philosophical Transactions of the Royal Society of London A291: 277 – 287. doi: 10.1098/rsta.1979.0026

Ding, T., Valkiers, S., Kipphardt, H., De Bièvre, P., Taylor, P. D. P., Gonfiantini, R., Krouse, R. (2001). Calibrated sulfur isotope abundance ratios of three IAEA sulfur isotope reference materials and V-CDT with a reassessment of the atomic weight of sulfur. Geochimica et Cosmochimica Acta 65(15): 2433 – 2437. doi: 10.1016/S0016-7307(01)00611-1

Domagal-Goldman, S. D., Kastin, J. F., Johnston, D. T., Farquhar, J. (2008). Organic haze, glaciations and multiple sulfur isotopes in the Mid-Archean era. Earth and Planetary Science Letters 269: 29 – 40. 10.1016/j.epsl.2008.01.040

Edwards, A. B. (1947). Textures of the ore minerals and their significance. Australasian Institute of Mining and Metallurgy, Melbourne, pp. 166

Eickmann, B., Hofmann, A., Wille, M., Bui, T. H., Wing, B. A., Schoenberg, R. (2018). Isotopic evidence for oxygenated Mesoarchean shallow oceans. Nature Geoscience 11: 133 – 138. doi: 10.1038/s41561-017-0036-x

Eldridge, C. S., Compston, W., Williams, I. S., Harris, J. W., Bristow, J. W. (1991). Isotope evidence for the involvement of recycled sediments in diamond formation. Nature 353: 649 – 653.

Els, B. G. (1998). The auriferous late Archean sedimentation systems of South Africa: unique palaeo-environmental conditions? Sedimentary Geology 120(1-4): 205 – 224. doi: 10.1016/S0037-0738(98)00033-5

Elworthy, T., Eglington, B. M., Armstrong, R. A., Moyes, A. B. (2000). Rb-Sr isotope constraints on the timing of late to post-Archean tectonometamorphism affecting the southeastern Kaapvaal Craton. Journal of African Earth Sciences 30(3): 641 – 650. doi: 10.1016/S0899-5362(00)00043-9

England, G. L., Rasmussen, B., Krapez, B., Groves, D. I. (2001). The origin of uraninite, bitumen nodules and carbon seams in Witwatersrand gold-uranium-pyrite ore deposits, based on a Permo-Triassic analogue. Economic Geology 96: 1907 – 1920. doi: 10.2113/gsecongeo.96.8.1907

England, G. L., Rasmussen, B., Krapez, B., Groves, D. I. (2002). Paleoenvironmental significance of rounded pyrite in siliciclastic sequences of Late Archean Witwatersrand Basin: Oxygen deficient atmosphere or hydrothermal alteration? Sedimentology 49: 1133 – 1156. doi 10.1046/j.1365-3091.2002.00479.x

Endo, Y. (1975). Morphological features and growth process of dendritic pyrite from Ani mine, Akita Prefecture. Prof. T. Takeuchi Memorial Volume: 15 – 18.

Eriksson, K. A., Turner, B. R., Vos, R. G. (1981). Evidence of tidal processes from the lower part of the Witwatersrand Supergroup, South Africa. Sedimentary Geology 29: 309 – 325. doi: 10.1016/0037-0738(81)90078-6.

Farquhar, J., Bao, H. M., Theimens, M. (2000). Atmospheric influence of Earth's earliest sulfur cycle. Science 289(5480): 756 – 758. doi: 10.1126/science.289.5480.756

Farquhar, J., Cliff, J., Zerkle, A. L., Kamyshny, A., Poulton, S. W., Claire, M., Adams, D., Harms, B. (2013). Pathways for Neoarchean pyrite formation constrained by mass-independent sulfur isotopes. Proceedings of the National Academy of Science 110(44): 17638 – 17643.

Farquhar, J., Johnston, D. T., Wing, B. A., Habicht, K. S., Canfield, D. E., Aireau, S. A., Thiemens, M. H. (2003). Multiple sulfur isotopic interpretations of biosynthetic pathways: Implications for biological signatures in the sulfur isotope record. Geobiology 1: 15 – 27. doi: 10.1046/j.1472-4669.2003.00007.x

Farquhar, J., Peters, M., Johnston, D. T., Strauss, H., Masterson, A., Wiechert, U., Kaufman, A. J. (2007). Isotopic evidence for Mesoarchean anoxia and changing atmospheric sulphur chemistry. Nature 449: 706 – 709. doi: 10.1038/nature06202

Farquhar, J., Savarino, J., Airieau, S., Thiemens, M. H. (2001). Observation of wavelength-sensitive mass-independent sulfur isotope effects during SO_2 photolysis: Implications for the early atmosphere. Journal of Geophysical Research 106(E12): 32829 – 32839. doi: 10.1029/2000JE001437

Farquhar, J., Wing, B. A. (2003). Multiple sulfur isotopes and the evolution of the atmosphere. Earth and Planetary Science Letters 213: 1 – 13. doi: 10.1016/S0012-821X(03)00296-6

Farquhar, J., Wing, B. A. (2005). The terrestrial record of stable sulphur isotopes: a review of the implications for evolution of Earth's sulphur cycle. Geological Society of London, Special Publications 248: 167 – 177. doi: 10.1144/GSL.SP.2005.248.01.09

Farquhar, J., Wing, B. A., McKeegan, K. D., Harris, J. W., Cartigny, P., Thiemens, M. H. (2002). Mass-independent sulfur of inclusions in diamond and sulfur recycling on Early Earth. Science 298: 2369 – 2372. doi: 10.1126/science.1078617

Feather, C. E., Koen, G. M. (1975). The mineralogy of the Witwatersrand reefs. Minerals Science and Engineering 7(3): 189 – 244.

Fike, D. A., Finke, N., Zha, J., Blake, G., Hoehler, T. M., Orphan, V. J. (2009). The effect of sulfate concentration on (sub)millimeter-scale sulfide $\delta^{34}S$ in hypersaline cyanobacterial mats over the diurnal cycle. Geochimica et Cosmochimica Acta 73: 6187 – 6204. doi: 10.1016/j.gca.2009.07.006

Finster, K., Liesack, W., Thamdrup, B. (1998). Elemental sulfur and thiosulfate disproportionation by desulfocapsa sulfoexigens sp. nov., a new anaerobic bacterium isolated from marine surface sediment. Applied and Environmental Microbiology 64: 119 – 125.

Fleet, M. E., Chryssoulis, S. L., Maclean, P. J., Davidson, R., Weisner, C. G. (1993). Arsenian pyrite from gold deposits: Au and As distribution investigated by SIMS and EMP, and colour staining and surface oxidation by XPS and LIMS. Canadian Mineralogist 31: 1 – 17.

Forrest, J., Newman, L. (1977). AG-110 microgram sulfate analysis for short time resolution of ambient levels of sulfur aerosol. Analytical Chemistry 49: 1579 – 1584. doi: 10.1021/ac50019a030

Frimmel, H. E. (2005b). Archean atmospheric evolution: Evidence from the Witwatersrand gold fields, South Africa. Earth Science Reviews 70: 1 – 46. doi: 10.1016/j.earscirev.2004.19.003

Frimmel, H. E., Groves, D. I., Kirk, J., Ruiz, J., Chesley, J., Minter, W. E. L. (2005a). The formation and preservation of the Witwatersrand Gold Fields, the World's largest gold province. In: Hedenquist, J. W., Thompson, J. F. H., Goldfarb, R. J., Richards, J. P. (eds) Economic Geology 100th Anniversary Volume, Society of Economic Geologists, Littleton, pp 769 – 797.

Frimmel, H. E., LeRoex, A. P., Knight, J., Minter, W. E. L. (1993). A case study of the postdepositional alteration of the Witwatersrand Basal Reef gold placer. Economic Geology 88: 249 – 265. doi: 10.2113/gsecongeo.88.2.249

Frimmel, H. E., Mineter, W. E. L. (2002). Recent developments concerning the geological history and genesis of the Witwatersrand gold deposits, South Africa. Society of Economic Geologists Special Publication 9: 17 – 45. doi: 10.5382/SP.09.02

Füchtbauer, H., Müller, G. (1970). Sedimente und sedimentgesteine: Stuttgart, Schweizerbarth Verlag, 726p.

Gallagher, M., Whitehouse, M. J., Kamber, B. S. (2017). The Neoarchean surficial sulphur cycle: An alternative hypothesis based on analogies with 20th-century atmospheric lead. Geobiology 15(3): 385 – 400. doi: 10.1111/gbi.122234

Gehrisch, W., Maucher, A. (1975). Sulfur isotope and trace element analyses from the Sultijelma Ore Bodies, Northern Norway. Mineralium Deposita 10: 57 – 69. doi: 10.1007/BF00207461

George, L. L., Cook, N. J., Ciobanu, C. L. (2016). Partitioning of trace elements in co-crystallized sphalerite-galena-chalcopyrite hydrothermal ores. Ore Geology Reviews 77: 97 – 116. doi: 10.1016/j.oregeorev.2016.02.009

Gibson, R. L., Jones, M. Q. W. (2002). Late Archean to Paleoproterozoic geotherms in the Kaapvaal Craton, South Africa: Constraints on the thermal evolution of the Witwatersrand Basin. Basin Research 14: 169 – 181. doi: 10.1046/j.1365-2117.2002.00168.x

Gonfiantini, R., Stichler, W., Rozanski, K. (1993). Standards and intercomparison materials distributed by the International Atomic Energy Agency for stable isotope measurements. Reference and intercomparison materials for stable isotope of light elements. Proceedings of a consultants meeting, Vienna, 1-3 December 1993, pp. 13-30.

Goldhaber, M. B., Kaplan, I. R. (1975). Controls and consequences of sulfate reduction rates in recent marine sediments. Soil Science 119: 42 – 55.

Gomes, M. L., Hurtgen, M. T. (2015). Sulfur isotope fractionation in modern euxinic systems: Implications for paleoenvironmental reconstructions of paired sulfate-sulfide isotope records. Geochimica et Cosmochimica Acta 157: 39 – 55. doi: 10.1016/j.gca.2015.02.031

Gosh, R., Baidya, T. K. (2017). Mesoarchean BIF and iron ores of the Badampahar greenstone belt, Iron Ore Group, East Indian Shield. Journal of Asian Earth Sciences 15: 25 – 44. doi: 10.1016/j.jseas.2017.10.003

Grandstaff, D. E., Edelman, M. J., Foster, R. W., Zbinden, E., Kimberley, M. M. (1986). Chemistry and mineralogy of Precambrian paleosols at the base of the Dominion and Pongola Groups (Transvaal, South Africa). Precambrian Research 32: 97 – 131. doi: 10.1016/0301-9268(86)90003-3

Gregory, D. D., Large, R. R., Halpin, J. A., Baturina, E. L., Lyons, T. W., Wu, S., Danyushevsky, L., Sack, P. J., Chappez, A., Maslennikov, V. V., Bull, S. W. (2015a). Trace element content of sedimentary pyrite in black shales. Economic Geology 110: 1389 – 1410. doi: 10.2113/econgeo.110.6.1389

Gregory, D. D., Large, R. R., Halpin, J. A., Steadman, J. A., Hickman, A. H., Ireland, T. R., Holden, P. (2015b). The chemical conditions of the late Archean Hamersley basin inferred from whole rock and pyrite geochemistry with $\Delta^{33}S$ and $\delta^{34}S$ isotope analysis. Geochemica et Cosmochimica Acta 149: 223 – 250. doi: 10.1016/j.gca.2014.10.023

Gregory, D. D., Mukherjee, I., Olson, S. L., Large, R. R., Danushevsky, L. V., Stepanov, A. S., Avila, J. N., Cliff, J., Ireland, T. R., Raiswell, R., Olin, P. H., Maslennikov, V. V., Lyons, T. W. (2019). The formation mechanisms of sedimentary pyrite nodules determined by trace element and sulfur isotope microanalysis. Geochimica et Cosmochimica Acta 259: 53 – 68. doi: 10.1016/j.gca.2019.05.035

Gutzmer, J., Nhleko, N., Beukes, N. J., Pickard, A., Barley, M. E. (1999). Geochemistry and ion microprobe (SHRMP) age of a quartz porphyry sill in the Mozaan Group: Geochronological implication for the Pongola and the Witwatersrand Supergroups. South African Journal of Geology 102: 139 – 146.

Guy, B.M., Beukes, N. J., Gutzmer, J. (2010). Paleoenvironmental controls of the texture and chemical composition of pyrite from the non-conglomeratic rocks of the Mesoarchean Witwatersrand Supergroup, South Africa. South African Journal of Geology 113.2: 195 – 228. doi: 10.2113/gssajg.113.2.195

Guy, B.M., Ono, S., Gutzmer, J., Lin, Y., Fogel, M. L., Beukes, N. J. (2012). A multiple sulfur and organic carbon isotope record from non-conglomeratic sedimentary rocks of the Mesoarchean Witwatersrand Supergroup, South Africa. Precambrian Research 219: 208 – 231. doi: 10.1016/j/precamres.2012.06.018

Guy, B. M., Ono, S., Gutzmer, J., Lin, Y., Beukes, N. J. (2014). Sulfur sources of sedimentary "buckshot" pyrite in the auriferous conglomerates of the Mesoarchean Witwatersrand and Ventesdorp Supergroups, Kaapvaal Craton, South Africa. Mineralium Deposita 49: 751 – 775. doi: 10.1007/s00126-014-0518-3

Habicht, K. S., Canfield, D. E. (2001). Isotope fractionation by sulfate-reducing natural populations and the isotopic composition of sulfide in marine environments. Geology 29: 555 – 558. doi: 10.1130/0091-7613(2001)029<0555

Habicht, K. S., Canfield, D. E., Rethmeier, J. (1998). Sulfur isotope fractionation during bacterial reduction and disproportionation of thiosulfate and sulfite, Geochimica et Cosmochimica Acta 62: 2585 – 2595. doi: 10.1016/S0016-7037(98)00167-7

Habicht, K. S., Gade, M., Thamdrup, B., Berg, P., Canfield, D. E. (2002). Calibration of sulfate levels in the Archean ocean. Science 298: 2372 – 2374. doi: 10.1126/science.1078265

Halderson, S. (1981). Grain-size distribution of subglacial till and its relation to glacial crushing and abrasion. Boreas 10(1): 91 – 105. doi: 10.1111/j.1502-3885.1981.tb00472.x

Halderson, S. (1983). Mineralogy and geochemistry of basal till and their relationship to till-forming processes. Norsk Geologisk Tidsskrift 63: 15 – 25.

Halevy, I., Johnston, D. T., Schrag, D. P. (2010). Explaining the structure of the Archean mass-independent sulfur isotope record. Science 329: 204 – 207. doi: 10.1126/science.1190298

Hallbauer, D. K. (1986). The mineralogy and geochemistry of Witwatersrand pyrite, gold, uranium and carbonaceous matter. In: Anhaeusser C. R., Maske, S. (eds) Mineral Deposits of Southern Africa. Geological Society of South Africa, Johannesburg, pp. 731 – 752.

Hao, J., Sverjensky, D. A., Hazen, R. M. (2019). Redox states of Archean surficial environments: The importance of $H_{2,g}$ instead of $O_{2,g}$ for weathering reactions. Chemical Geology 521: 49 – 58. doi: 10.1016/j.chem.geo.2019.05.022

Haqq, J. D., Domagal-Goldman, S. D., Kasting, P. J., Kasting, J. F. (2008). A revised, hazy methane greenhouse for the Archean Earth. Astrobiology 8(6): 1127 – 1137. doi: 10.1089/ast.2007.0197

Harrison, A. G., Thode, H. G. (1958). Mechanisms of bacterial reduction of sulfate from isotope fractionation studies. Transactions of the Faraday Society 53: 84 – 92.

Hawley, J. E., Nichol, I. (1961). Trace elements in pyrite, pyrrhotite and chalcopyrite of different ores. Economic Geology 56: 467 – 487. doi: 10.2113/gsecongeo.56.3.467

Hegner, E., Kröner, A., Hofmann, A. W. (1984). Age and isotope geochemistry of the Archean Pongola and Usushwana suites in Swaziland, southern Africa: A case for crustal contamination of mantle-derived magma. Earth and Planetary Science Letters 70: 267 – 279. doi: 10.1016/0012-821X(84)90011-6.

Herzig, P. M., Hannington, M. D., Arribas, A. Sulfur isotopic composition of hydrothermal precipitates from the Lau back-arc: Implications for magmatic contributions to seafloor hydrothermal systems. Mineralium Deposita 33: 226 – 237. doi: 10.1007/s001260050

Hirdes, W., Saager, R. (1983). The Proterozoic Kimberley Reef placer in the Evander Goldfields, Witwatersrand, South Africa. Monograph Series on Mineral Deposits. 20, Gebrudewr Borntraeger, pp 101.

Hoefs, J., Nielson, H., Schidlowski, M. (1968). Sulfur isotope abundances in pyrite from the Witwatersrand Conglomerates. Economic Geology 63: 975 – 977. doi: 10.2113/gsecongeo.63.8.975

Hoffman, P. F. (1989). Precambrian geology and tectonic history of North America. In: Bally, A. W., Palmer, A. R. (Eds.), The Geology of North America – An Overview. The Geological Society of America, pp 447 – 512.

Hofmann, A., Kroner, A., Xie, H., Hegner, E., Belyanin, G., Kramers, J., Bolhar, R., Slabunov, A. Reihardt, J., Horvath, P. (2015). The Nhlangano gneiss dome in south-west Swaziland – A record of crustal destabilization of the eastern Kaapvaal craton in the Neoarchean. Precambrian Research 258: 109-132. doi: 10.1016/j.precamres.2014.12.008

Hofmann, A., Bekker, A., Rouxel, O., Rumble D., Master, S. (2009). Multiple sulphur and iron isotope composition of detrital pyrite in Archaean sedimentary rocks: A new tool for provenance analysis. Earth and Planetary Science Letters 286: 436 – 445. doi: 10.1016/j.epsl.2009.07.008

Holland, H. D., Beukes, N. J. (1990). A paleoweathering profile from Griqualand West, South Africa: Evidence for a dramatic rise in atmospheric oxygen between 2.2 and 1.9 bybp. American Journal of Science 290(A): 1 – 84.

Holland, H. D., Zbinden, E. A. (1988). Paleosols and the evolution of the atmosphere: Part I. In: Lemann, A., Meybeck, M. (Eds.). Physical and Chemical Weathering in Geochemical Cycles. Kluwer Academic Publishers, Dordrecht, The Netherlands. pp. 61 – 82.

Huerta-Diaz, M. A., Morse, J. W. (1992). Pyritization of trace metals in anoxic marine sediments. Geochimica et Cosmochimica Acta 56: 2681 – 2702. doi: 10.1016/0016-7037(92)90353-K

Hulston, J. R., Thode, H. G. (1965a). Variations in the S^{33}, S^{34} and S^{36} contents of meteorites and their relation to chemical and nuclear effects. Journal of Geophysical Research 70: 3475 - 3484. doi: 10.1029/JZ07i014p03475

Hulston, J. R., Thode, H. G. (1965b). Cosmic ray produced S^{33} and S^{36} in the metallic phase of iron meteorites. Journal of Geophysical Research 70: 4435 – 4442. doi: 10.1029/JZ0i018p04435

Ickert, R. B., Hiess, J., Williams, I. S., Holden, P., Ireland, T. R., Lanc, P., Schram, N., Foster, J. J., Clement, S. W. (2008). Determining high precision in situ oxygen isotope ratios with a SHRIMP II: Analyses of MPI-DING silicate-glass reference materials and zircon from contrasting granites. Chemical Geology 257: 114 – 128. doi: 10.1016/j.chemgeo.2008.08.024

Izon, G., Zerkle, A., L., Zhelezinskaia. I., Farquhar, J., Newton, R. J., Poulton, S. W., Eigenbrode, J. L., Claire, M. W. (2015). Multiple oscillations in Neoarchean atmospheric chemistry. Earth and Planetary Science Letters 431: 264 – 273. doi: 10.1016/j.epsl.2015.09.018

Jamieson, J. W., Wing, B. A., Farquhar, J., Hannington, M. D. (2013). Neoarchean seawater sulfate concentrations from sulphur isotopes in massive sulfide ore. Nature Geoscience 6: 61 – 64. doi: 10.1038/ngeo01647

Jamieson, J. W., Wing, B. A., Hannington, M. D., Farquhar, J. (2006). Evaluating isotopic equilibrium among sulfide mineral pairs in Archean ore deposits: Case study from the Kidd Creek VMS deposit, Ontario, Canada. Economic Geology 101: 1055 – 1061. doi: 10.2113/gsecongeo.101.5.1055

Janecky, D. R., Shanks, W. C. (1988). Computational modelling of chemical and sulfur isotopic reaction processes in seafloor hydrothermal systems: Chimneys, massive sulfides, and subjacent alteration zones.

Johnson, J. E., Gerpheide, A., Lamb, M. P., Fischer, W. W. (2014). O_2 constraints from Paleoproterozoic detrital pyrite and uraninite. GSA Bulletin 126(5-6): 813 – 830. doi: 10.1130/B30949.1

Johnston, D. T., Farquhar, J., Canfield, D. E. (2007). Sulfur isotope insights into microbial sulfate reduction: When microbes meet models. Geochimica et Cosmochimica Acta 71: 3929 – 3947. doi: 10.1016/j.gca.2007.05.008

Johnston, D. T., Farquhar, J., Habicht, K. S., Canfield, D. E. (2008). Sulphur isotopes and the search for life: Strategies for identifying sulphur metabolisms in the rock record and beyond. Geobiology 6: 425 – 435. doi: 10.1111/j.1472.2008.00171.x

Johnston, D. T., Farquhar, J., Wing, B. A., Kaufman, A. J., Canfield, D. E., Habicht, K. S. (2005b). Multiple sulfur isotope fractionations in biological systems: A case study with sulfate reducers and sulfur disproportionators. American Journal of Science 305: 645 – 660. doi: 10.2475/ajs.305.6-8.645

Johnston, D. T., Poulton, S. W., Fralick, P. W., Wing, B. A., Canfield, D. E., Farquhar, J. (2006). Evolution of the oceanic sulphur cycle at the end of the Paleoproterozoic. Geochimica et Cosmochimica Acta 70(23): 5723 – 5739. doi: 10.1016/j.gca.2006.08.001

Johnston, D. T., Wing, B. A., Farquhar, J., Kaufman, A. J., Strauss, H., Lyons, T. W., Kah, L. C., Canfield, D. E. (2005a). Active microbial disproportionation in the Mesoproterozoic. Science 310: 1477 – 1479. doi: 10.1126/science.1117824

Jones, G. E., Starkey, R. J. (1957). Fractionation of isotopes of sulfur by micro-organisms and their role in deposition of native sulfur. Journal of Applied Microbiology 5: 111 – 115.

Jorgenson, B. B. (1977). The sulfur cycle of a coastal marine sediment (LimFjorden, Denmark). Limnology and Oceanography 22: 814 – 832. doi: 10.4319/lo.1977.22.5.0814

Jørgenson, B. B., Zawacki, L. X., Jannasch, H. W. (1990). Thermophilic bacterial sulfate reduction in deep-sea sediments at the Guaymas Basin hydrothermal vent site. Deep-sea Research 37: 695 – 710. doi: 10.1016/0198-0149(90)90099-H

Kamber, B. S., Whitehouse, M. J. (2007). Microscale sulphur isotope evidence for sulphur cycling in the late Archean shallow ocean. Geobiology 5: 5 – 17. doi: 10.111/j.1472-4669.2006.00091.x

Kamo, S. L., Davis, D. W., de Wit, M. J. (1990). U-Pb geochronology of Archean plutonism in the Baberton region, South Africa: 800 Ma of crustal evolution (abs). 7th International Conference of Geochronology, Cosmochronology and Isotope Geology, p. 53.

Kamo, S. L., Reimold, W. U., Shirey, S. B. (1996). A 2.023 Ga age for the Vredefort impact event and a first report of shock metamorphosed zircons in pseudotachylitic breccias and granophyre. Earth and Planetary Science Letters 144: 369 – 388. doi: 10.1016/S0012-821X(96)00180-X

Kaplan, I. R., Rittenberg, S. C. (1962). Fractionation of isotopes in relation to the problem of elemental sulphur transport by micro-organisms. Nature 194: 1098 – 1099.

Kaufman, A. J., Johnston, D. T., Farquhar, J., Masterson, A. L., Lyons, T. W., Bates, S., Anbar, A. B., Arnold, G. L., Garvin, J., Buick, R. (2007). Late Archean biospheric oxygenation and atmospheric evolution. Science 317: 1900 – 1903. doi: 10.1126/science.1138700

Ketchum, K. Y., Heaman, L. M., Bennett, G., Hughes, D. H. (2013). Age, petrogenesis and tectonic setting of the Thessalon volcanic rocks, Huronian Supergroup, Canada. Precambrian Research 233: 144 – 172. doi: 10.1016/j.precamres.2013.04.009

Kimberley, M. M., Grandstaff, D. E. (1986). Profiles of elemental concentrations in Precambrian paleosols on basaltic and granitic parent materials. Precambrian Research 32: 133 – 154. doi: 10.1016/0301-9268(86)90004-5

King, J. J. (2013). A vapour-dominated high-sulphidation system. Geology, alteration and mineralization of the hypogene Au (Ag-Cu) Bowone and Binebase deposits, Sangihe Island, Indonesia. Unpublished masters thesis, McGill University, Montreal, Quebec, pp. 148.

Kiyosu, Y. (1980). Chemical reduction and sulfur isotope effects of sulfate by organic matter under hydrothermal conditions. Chemical Geology 30: 47 – 56. doi: 10.1016/0009-2541(80)90115-1

Koehler, M. C., Buick, R., Kipp, M. A., Stüeken, E. E., Zaloumis, J. (2018). Transient surface ocean oxygenation recorded in the ~2.66 Ga Jeerinah Formation, Australia. Proceedings of the National Academy of Science 115(35): 7711 – 7716. doi: 10.1073/pnas.1720820115

Koglin, N., Frimmel, H. E., Minter, W. E. L., Bratz, H. (2010). Trace element characteristics of different pyrite types in Mesoarchaean to Palaeoproterozoic placer deposits. Mineralium Deposita 45: 259 – 280. doi: 10.1007/s00126-009-0272-0

Kositcin, N., McNaughton, N. J., Griffin, B. J., Fletcher, I.R., Groves, D. I., Rasmussen, B. (2003). Textural and geochemical discrimination between xenotime of different origin in the Archaean Witwatersrand Basin, South Africa. Geochimica et Cosmochimica Acta 67: 709 – 731. doi: 10.1016/S0016-7037(02)01169-9

Kositcin, N., Krapez, B. (2004). Relationship between detrital zircon age-spectra and the tectonic evolution of the Late Archean Witwatersrand Basin, South Africa. Precambrian Research 129: 141 – 168. doi: 10.1016/j.precamres.2003.10.011

Kriewaldt, M., Ryan, G. R. (1967). Western Australia Geological Survey 1: 250,000 Geological Series, Pyramid Explanatory Notes: Sheet SF/50-7. pp. 1-39.

Krogh, T. W., Davis, D. W., Corfu, F. (1984). Precise U-Pb zircon and badelleyite ages for the Sudbury area. In: Pye, E. G., Naldrett, A. J., Giblin, P. E. (Eds.). The Geology and Ore Deposits of the Sudbury Structure. Ontario Geological Survey pp. 431 – 446.

Krouse, H. R., Coplen, T. B. (1997). Reporting of relative sulfur isotope-ratio data. Pure and Applied chemistry 69: 293 – 295. doi: 10.1351/pac199769020293

Krupp, R., Oberthur, T., Hirdes, W. (1994). The early Precambrian atmosphere and hydrosphere: Thermodynamic constraints from mineral deposits. Economic Geology 89: 1581 – 1598. doi: 10.2113/gsecongeo.89.7.1581

Kurzweil, F., Claire, M., Thomazo, C., Peters, M., Hannington, M., Strauss, H. (2013). Atmospheric sulfur rearrangement 2.7 billion years ago: Evidence for oxygenic photosynthesis. Earth and Planetary Science Letters 366: 17 – 26. doi: 10.1016/j.epsl.2013.01.028

Labidi, J., Cartigny, P., Birck, J., Assayag, N., Bourrand, J. (2012). Determination of multiple sulphur isotopes in glasses: A reappraisal of the MORB $\delta^{34}S$. Chemical Geology 334: 189 – 198. doi: 10.1016/j.chemgeo.2012.10.028

LaFlamme, C., Martin, L., Jeon, H., Reddy, S. M., Selvaraja, V., Caruso, S., Bui, T. H., Roberts, M. P., Voute, F., Hagemann, S., Wacey, D., Littman, S., Wing, B., Fiorentini, M., Kilburn, M. R. (2016). In situ multiple sulfur isotope analysis by SIMS of pyrite, chalcopyrite, pyrrhotite, and pentlandite to refine magmatic ore genetic models. Chemical Geology 44: 1 – 15. doi: 10.1016/j.chemgeo.2016.09.032

Lambert, I. B., Donnelly, T. H., Dunlop, J. S. R., Groves, D. I. (1978). Stable isotopic composition of early Archaean sulfate deposits of probable evaporitic and volcanogenic origins. Nature 276: 807 – 811.

Large, R. R., Halpin, J. A., Danyushevsky, L. V., Maslennikov, V. V., Bull, S. W., Long, J. A., Gregory, D. D., Lounejeva, E. Lyons, T. W., Sack, P. J., McGoldrick, P. J., Calver, C. R.

(2014). Trace element content of sedimentary pyrite as a new proxy for deep-time ocean-atmosphere evolution. Earth and Planetary Science Letters 389: 209 – 220. doi: 10.1016/j.epsl.2013.12.020

Large, R. R., Maslennikov, V. V., Robert, F., Danushevsky, L. V., Chang, Z. S. (2007). Multistage sedimentary and metamorphic origin of pyrite and gold in the giant Sukhoi Log deposit, Lena gold province, Russia. Economic Geology 102: 1233 – 1267. doi: 10.2113/gsecongeo.102.7.1233

Large, R. R., Meffre, S., Burnett, R., Guy, B., Bull, S., Gilbert S., Goemann, K., Danyushevsky, L. V. (2013). Evidence for an intrabasinal source and multiple concentration processes in the formation of the Carbon Leader Reef, Witwatersrand Supergroup, South Africa. Economic Geology 108: 1 – 28. doi: 10.2113/econgeo.108.6.1215

Lasaga, A. C., Otake, T., Watanabe, Y., Ohmoto, H. (2008). Anomalous fractionation of sulfur isotopes during heterogenous reactions. Earth and Planetary Science Letters 268: 225 – 238. doi: 10.1016/j.epsl.2008.01.016

Li, S., Junkin, W. D., Gaschnig, R. M., Ash, R. D., Piccoli, P. M., Candela, P. A., Rudnick, R. L. (2019) Molybdenum contents of sulfides in ancient glacial diamictites: Implications for molybdenum delivery to the oceans prior to the Great Oxidation Event. Geochemica et Cosmochimica Acta. doi: 10.1016/j.gca.2019.09.011

Lin, Y., Sim, S. M., Ono, S. (2011). Multiple-sulfur isotope effects during photolysis of carbonyl sulfide. Atmospheric Chemistry and Physics 11: 10283 – 10292. doi: 10.5194/acp-11-10283-2011

Loftus-Hills, G., Solomon, M. (1967). Cobalt, nickel and selenium in sulfides as indicators of ore genesis. Mineralium Deposita 2(3): 228 – 242. doi: 10.1007/BF00201918

Long, D. G. F. (2004). The tectonostratigraphic evolution of the Huronian basement and the subsequent basin fill: Geological constraints on impact models of the Sudbury event. Precambrian Research 129: 203 – 223. doi: 10.1016/j.precamres.2003.10.003

Luhr, J. F., Logan, A. V. (2002). Sulfur isotope systematics of the 1982 El Chichón trachyandesite: An ion microprobe study. Geochimica et Cosmochimica Acta 66: 3303 – 3316. doi: 10.1016/S0016-7037(02)00931

Luther, G. W. (1991). Pyrite synthesis via polysulfide compounds. Geochimica et Cosmochimica Acta 55(10): 2839 – 2849. doi: 10.1016/0016-7037(91)90449-F

Machel, H. G. (1998). Gas souring by thermochemical sulfate reduction at 140°C: discussion. American Association of Petroleum Geologists Bulletin 82(10): 1870 – 1873.

Machel, H. G. (2001). Bacterial and thermochemical sulfate reduction in diagenetic settings – old and new insights. Sedimentary Geology 140: 143 – 175. doi: 10.1016/S0037-0738(00)00176-7

Macnamara, J., Fleming, W., Szabo, A., Thode, H. G. (1951). The isotopic composition of igneous sulphur and the primordial abundance of the terrestrial sulphur isotopes. Canadian Journal of Chemistry 30: 73 – 76.

Marini, L., Moretti, R., Accornero, M. (2011). Sulfur isotopes in magmatic-hydrothermal systems, melts and magmas. Reviews in Mineralogy and Geochemistry 73: 423 – 492. doi: 10.2138/rmg.2011.73.14

Martin, J., Nirel, P., Thomas, A. (1987). Sequential extraction techniques: Promises and problems. Marine Chemistry 22: 313 – 341. doi: 10.1016/0304-42-3(87)90017-X

Matthews, P. E. (1967). The pre-Karroo formations of the White Umfolozi Inlier, Northern Natal. Transactions of the Geological Society of South Africa 70: 257 – 272.

Maynard, J. B. (1992). Chemistry of modern soils as a guide to interpreting Precambrian paleosols. Journal of Geology 100: 279 – 289. doi: 10.1086/629632

Maynard, J. B., Sutton, S. J., Rumble III, D., Bekker, A. (2013). Mass-independently fractionated sulphur in Archean paleosols: A large reservoir of negative $\Delta^{33}S$ anomaly on the early Earth. Chemical Geology 362: 74 – 81. doi: 10.1016/j.chemgeo.2013.09.011

McClay, K. R., Ellis, P. G. (1983). Deformation and recrystallisation of pyrite. Mineralogical Magazine 47: 527 – 538.

McLachlan, D. Jr., Carlson, A. (1952). Some factors in the growth of crystals: Part II. Dendritic growth. University of Utah Engineering Experiment Station Bulletin 57: 24 – 28.

Meier, D. L., Heinrich, C. A., Watts, M. A. (2009). Mafic dykes displacing Witwatersrand gold reefs: Evidence against metamorphic-hydrothermal ore formation. Geology 37: 607 – 610. doi: 10.1130/G25657A.1

Meyer, F. M., Robb, L. J., Oberthur, T., Saager, R., Stupp, H. D. (1990). Cobalt, nickel and gold in pyrite from primary gold deposits and Witwatersrand reefs. South African Journal of Geology 93: 70 – 82.

Mishima, K., Yamazaki, R., Satish-Kumar, M., Ueno, Y., Hokado, T., Toyoshima, T. (2017). Multiple sulfur isotope geochemistry of Dharwar Supergroup, southern India: Late Archean record of changing atmospheric chemistry. Earth and Planetary Science Letters 464: 69 – 83. doi: 10.1016/j.epsl.2017.02.007

Mojzsis, S. J. Sulphur on early Earth. In: Earth's Oldest Rocks (Van Kronendonk, M. J., Smithies, R. H., Bennet, V. Eds.). Developments in Precambrian Geology 15: 923 – 970. doi: 10.1016/S0166-2635(07)15075-1

Mojzsis, S. J., Coath, C. D., Greenwood, J. P., McKeegan, Harrison, T. M. (2003). Mass-independent isotope effects in Archean (2.3 to 3.8 Ga) sedimentary sulfides determined by ion microprobe analysis. Geochimica et Cosmochimica Acta 67: 1635 – 1658. doi: 10.1016/S0016-7037(03)00059-0

Montzka, S. A., Calvert, P., Hall, B. D., Elkins, J. W., Conway, T. J., Tans, P. P., Sweeney, C. (2007). On the global distribution, seasonality, and budget of atmospheric carbonyl sulfide (COS) and some similarities to CO_2. Journal of Geophysical Research 112: 1 – 15. doi: 10.1029/2006JD007665

Mook, W. G. (2001). Environmental isotopes in the hydrological cycle: Principles and applications. Technical Documents in Hydrogeology 6(39).

Mossman, D. J., Nagy, B., Davis, D. W. (1993). Hydrothermal alteration of organic matter in uranium ores, Elliot Lake Canada: Implications for selected organic-rich deposits. Geochimica et Cosmochimica Acta 57: 3251 – 3259. doi: 10.1016/0016-7037(93)90538-8

Muller, E., Philipott, P., Rollion-Bard, C., Cartigny, P. (2016). Multiple sulfur isotope signatures in Archean sulfates and their implications for the chemistry and dynamics of the early atmosphere. Proceedings of the National Academy of Science 113: 7432 – 7437. doi: 10.1073/pnas.1520522113

Muller, E., Philipott, P., Rollion-Bard, C., Cartigny, P., Assayag, N. Marin-Carbonne, J., Monhan, M. R., Sarma, D. S. (2017). Primary sulfur isotope signatures preserved in high-grade Archean barite deposits of the Sargur Group, Dharwar Craton, India. Precambrian Research 295: 38 – 47. doi: 10.1016/j.precamres.2017.04.029

Murakami, T., Utsunomiya, S., Imazu, Y., Prasad, N. (2001). Direct evidence of late Archean to early Proterozoic anoxic atmosphere from a product of 2.5 Ga old weathering. Earth and Planetary Science Letters 184: 523 – 528. doi: 10.1016/S0012-821X(00)00344-7

Mukhopadhyay, J., Crowley, Q. G., Ghosh, S., Ghosh, G., Chakrabarti, K., Misra, B., Heron, K., Bose, S. (2014). Oxygenation of the Archean atmosphere: New paleosol constraints from eastern India. Geology 42(10): 923 – 926. doi: 10.1130/G36091.1

Murowchick, J., Barnes, H. L. (1987). Effects of temperature and degree of supersaturation on pyrite morphology. American Mineralogist 72: 1241 – 1250.

Nabhan, S., Marin-Carbonne. J., Heubeck, C. (2018). Tracing metabolic pathways of Archean microbial communities. EPSC Abstracts, Vol. 12, EPSC2018-676.

Nabhan, S., Weidenbeck, M., Milke, R., Heubeck, C. (2016). Biogenic overgrowth on detrital pyrite in ca. 3.2 Ga Archean paleosols. Geology 44(9): 763 – 766. doi: 10.1130/G38090.1

Nesbitt, H. W., Young, G. M. (1982). Early Proterozoic climates and plate motions inferred from major element chemistry of lutites. Nature 299: 715 – 717.

Nesbitt, H. W., Young, G. M. (1996). Petrogenesis of sediments in the absence of chemical weathering. Effects of abrasion and sorting on bulk composition and mineralogy. Sedimentology 43: 341 – 358. doi: 10.1046/j.1365-3091.1996.d01-12.x

Newman, L., Krouse, H. R., Grinenko, V. A. (1991). Chapter 5: Sulphur isotope variations atmosphere. In: Krouse, H. R., Grinenko, V. A. (eds). Stable isotopes in the assessment of natural and anthropogenic sulphur in the environment, volume 43 of SCOPE, John Wiley and Sons, New York, pp. 133 – 176.

Nhleko, N. (2003). The Pongola Supergroup in Swaziland. PhD Thesis (unpublished), Rand Afrikaans Univeristy.

Nicolaysen, L. O., Burger, A. J., Liebenberg, W. R. (1962). Evidence for the extreme age of certain minerals from the Dominion Reef conglomerates and the underlying granite in the western Transvaal. Geochimica et Cosmochimica Acta 26: 15 – 23. doi: 10.1016/0016-7037(62)90003-0

Nielson, H., Pilot, J., Grinenko, L. N., Grinenko, V. A., Lein, A. Y., Smith, J. W., Pankina, R. G. (1991). Lithospheric sources of sulfur. In: Stable isotopes in the assessment of natural and anthropogenic sulfur in the environment. Krouse, H. R., Grinenko, V. A. (eds). SCOPE 43, J Wiley and Sons, p 65 – 132.

Norman, M., Robinson, P., Clark, D. (2003). Major and trace-element analysis of sulfide ores by laser-ablation ICP-MS, solution ICP-MS, and XRF: New data on international reference materials. The Canadian Mineralogist 41: 293 – 305. doi: 10.2113/gscanmin.41.2.293

Ohmoto, H., Goldhaber, M. B. (1997). Sulfur and carbon isotopes. In: Barnes, H. L. (ed.), Geochemistry of hydrothermal ore deposits. John Wiley and Sons, New York, pp. 517 – 611.

Ohmoto, H., Watanabe, Y., Ikemi, H., Poulson, S. R., Taylor, B. E. (2006). Sulphur isotope evidence for an oxic Archean atmosphere. Nature 442: 908 – 911.

Ono, S., Beukes, N. J., Rumble, D. (2009). Origin of two distinct multiple sulphur isotope compositions of pyrite in the 2.5 Ga Klein Naute Formation, Griqualand West Basin, South Africa. Precambrian Research 169: 48 – 57. doi: 10.1016/j.precamres.2008.10.012

Ono, S., Beukes, N. J., Rumble, D., Fogel, M. L. (2006b). Early evolution of atmospheric oxygen from multiple-sulfur and carbon isotope records of the 2.9 Ga Mozaan Group of the Pongola Supergroup, Southern Africa. South African Journal of Geology 109(1-2): 97 – 108. doi: 10.2113/gssajg.109.1-2.97

Ono, S., Eigenbrode, J. L., Pavlov, A. A., Kharecha, P., Rumble III, D., Kasting, J. F., Freeman, K. H. (2003). New insights into the Archean sulfur cycle from the Hamersley Basin, Australia. Earth and Planetary Science Letters 213: 15 – 30. doi: 10.1016/S0012-821X(03)00295-4

Ono, S., Shanks III, W. C., Rouxel, O. J., Rumble, D. (2007). S-33 constraints on the seawater sulfate contribution in modern seafloor hydrothermal vent sulfides. Geochimica et Cosmochimica Acta 71: 1170 – 1182. doi: 10.1016/j.gca.2006.11.017

Ono, S., Wing, B., Johnston, D., Farquhar, J., Rumble III, D. (2006a). Mass-dependent fractionation of quadruple stable sulfur isotope system as a new tracer of sulfur biogeochemical cycles. Geochimica et Cosmochimica Acta 70: 2238 – 2252. doi: 10.1016/j.gca.2006.01.022

Ossa Ossa, F., Hofmann, A., Spangenberg, J. E., Poulton, S. W., Stüeken, E. E., Schoenberg, R., Eickmann, B., Wille, M., Butler, M., Bekker, A. (2019). Limited oxygen production in the Mesoarchean ocean. Proceedings of the National Academy of Science 116(14): 6647 – 6652. doi: 10.1073/pnas.1818762116

Ossa Ossa, F., Hofmann, A., Vidal, O., Kramers, J. D., Belyanin, G., Cavalazzi, B. (2016). Unusual manganese enrichment in the Mesoarchean Mozaan Group, Pongola Supergroup, South Africa. Precambrian Research 281: 414 – 433. doi: 10.1016/j.precamres.2016.06.009

Packer, B. M. (1990). Sedimentology, paleontology and isotope-geochemistry of selected formations in the 2.7 billion-year-old Fortescue Group, Western Australia. PhD Thesis (unpublished), University of California, Los Angeles.

Palmer, J. A., Phillips, G. N., McCarthy, T. S. (1989). Paleosols and their relevance to Precambrian atmospheric compositions. Journal of Geology 97(1): 77 – 92. doi: 10.1086/629282

Papineau, D., Mojzsis, S. J., Coath, C. D., Karhu, J. A., McKeegan, K. D. (2005). Multiple sulfur isotopes of sulfides from sediments in the aftermath of Paleoproterozoic glaciations. Geochimica et Cosmochimica Acta 69: 5033 – 5060. doi: 10.1016/j.gca.2005.07.005

Papineau, D., Mojzsis, S. J., Schmitt, A. K. (2007). Multiple sulfur isotopes from Paleoproterozoic Huronian interglacial sediments and the rise of atmospheric oxygen. Earth and Planetary Science Letters 255: 188 – 212. doi: 10.1016/j.epsl.2006.21.015

Partridge, M. A., Golding, S. D., Baublys, K. A., Young, E. (2008). Pyrite paragenesis and multiple sulfur isotope distribution in the late Archean and early Proterozoic Hamersley Basin sediments. Earth and Planetary Science Letters 272: 41 – 49. doi: 10.1016/j.epsl.2008.03.051

Paton, C., Hellstrom, J., Paul, B., Woodhead, J., Hergt, J. (2011). Iolite: Freeware for the visualisation and processing of mass spectromic data. Journal of Analytical Atomic Spectroscopy 26: 2508 – 2518. doi: 10.1039/clja10172b

Pavlov, A. A., Kasting, J. F. (2002). Mass-independent fractionation of sulfur isotopes in Archean sediments: strong evidence for an anoxic Archean atmosphere. Astrobiology 2(1): 27 – 41. doi: 10.1089/15311072753621321

Peterson, E. C., Mavrogenes, J. A. (2014). Linking high-grade gold mineralisation to earthquake-induced fault-valve processes in the Porgera gold deposit, Papua New Guinea. Geology 42: 383 – 386. doi: 10.1130/G35286.1

Postgate, J. R. The sulfate-reducing bacteria 2nd edition. (1984). Cambridge University Press, Cambridge, pp. 208.

Poujel, M., Robb, L. J., Anhaeusser, C. R., Gericke, B. (2003). A review of the geochronological constraints on the evolution of the Kaapvaal Craton, South Africa. Precambrian Research 127: 181 – 213. doi: 10.1016/S0301-9268(03)00187-6

Poujel, M., Robb, L. J., Respaut, J. P. (1999). U-Pb and Pb-Pb isotopic studies relating to the origin of gold mineralisation in the Evander Goldfield, Witwatersrand Basin, South Africa. Precambrian Research 95: 167 – 185. doi: 10.1016/S0301-9268(98)00111-9

Philippot, P., Avila, J. N., Killingsworth, B. A., Tessalina, S., Baton, F., Caquineau, T., Muller, E., Pecoits, E., Cartigny, P., Lalonde, S. V., Ireland, T. R., Thomazo, C., van Kronendonk, M. J., Busigny, V. (2018). Globally asynchronous sulphur isotope signals require re-definition of the Great Oxidation Event. Nature Communications 9: 2245. doi: 10.1038/s4167-0.18-0.4621.

Philippot, P., Zuilen, M. V., Rollion-Bard, C. (2012). Variations in atmospheric sulphur chemistry on early Earth linked to volcanic activity. Nature Geoscience 5: 668 – 674. doi: 10.1038/NGEO1534

Philippot, P., Zuilen, M. V., Lepot, K., Thomazo, C., Farquhar, J., Van Kronendonk, M. J. (2007). Early Archean microorganisms preferred elemental sulfur, not sulfate. Science 317: 1534 – 1537. doi: 10.1126/science.1145861

Phillips, G. N., Meyers, R. E., Palmer, J. A. (1987). Problems with the placer model for Witwatersrand gold. Geology 15: 1027 – 1030. doi: 10.1130/0091-7613(1987)15<1027:PWTPMF>2.0.CO;2

Planavsky, N. J., Asael, D., Hofmann, A., Reinhard, C. T., Lalonde, S. V., Knudsen, A., Wang, X., Ossa Ossa, F., Pecoits, E., Smith, A. J. B., Beukes, N. J., Bekker, A., Johnson, T. M., Konhauser, K. O., Lyons, T. W., Rouxel, O. J. (2014). Evidence for oxygenic photosynthesis half a billion years before the Great Oxidation Event. Nature Geoscience 7: 283 – 286. doi: 10.1038/NGEO2122

Price, B. J. (1972). Minor elements in pyrites from the Smithers Map Area, B. C. and exploration applications of minor element studies. Masters Thesis (unpublished), University of British Columbia, Canada.

Rantzch, U., Gauert, C. D. K., Van der Westhuizen, W. A., Duhamel, I., Cuney, M., Beukes, G. J. (2011). Mineral chemical study of U-bearing minerals from the Dominion Reefs, South Africa. Mineralium Deposita 46(2): 187 – 196. doi: 10.1007/s00126-010-0317-4

Ramdohr, P. (1958). New observations on the ores of the Witwatersrand in South Africa and their genetic significance. Transactions of the Geological Society of South Africa 61: 1 – 50.

Rasmussen, B., Buick, R. (1999). Redox state of the Archean atmosphere: evidence from detrital heavy minerals in ca 3250 – 2750 Ma sandstones from the Pilbara Craton, Australia. Geology 27: 115 – 118. doi: 10.1130/0091-7613(1999)027<0115:RSOTAA>2.3.CO;2

Rasmussen, B., Fletcher, I. R., Muhling, J. R., Mueller, A. G., Hall, G. C. (2007). Bushveld-aged fluid flow, peak metamorphism, and gold mobilization in the Witwatersrand basin, South Africa: Constraints from in situ SHRIMP U-Pb dating of monazite and xenotime. Geology 35(10): 931 – 934. doi: 10.1130/G23588A.

Reimer, T. O., Mossman, D. J. (1990). Sulfidization of the Witwatersrand black sands: From enigma to myth. Geology 18: 426 – 429. doi: 10.1130/0091-7613(1990)018<0426:SOWBSF>2.3.CO;2

Reinhard, C. T., Planavsky, N. J., Lyons, T. W. (2013). Long-term sedimentary recycling of rare sulphur isotope anomalies. Nature 497: 100 – 103. doi: 10.1038/nature12021

Rickard, D. T. (1975). Kinetics and mechanism of pyrite formation at low temperatures. American Journal of Science 275: 636 – 652. doi: 10.2475/ajs.275.6.636

Robb, L. J., Davis, D., Kamo, S. L., Meyer, F. M. (1992). Ages of altered granites adjoining the Witwatersrand basin with implications for the origin of gold and uranium. Nature 357: 677 – 680.

Robinson, B. K. (1995). Sulphur isotope standards. In: Reference and intercomparison materials for stable isotopes of light elements. IAEA-TECDOC-825. pp. 39-45.

Robinson, B. W. (1993). Sulfur isotope standards. Reference and intercomparison materials for stable isotopes of light elements. Proceedings of a consultants meeting, Vienna, 1-3 December, 1993, pp. 13-30.

Rocholl, A. (1998). Major and trace element composition and homogeneity of microbeam reference material: Basalt glass USGS BCR-2G. Geostandards Newsletter 22: 33 – 45. doi: 10.1111/j.1751-908X.1998.tb00543.x

Roerdink, D. L., Mason, P. R. D., Whitehouse, M. J., Brouwer, F. M. (2016). Reworking of atmospheric sulfur in a Paleoarchean hydrothermal system at Londozi, Babertone Greenstone Belt, Swaziland. doi: 10.1016/j.precamres.2016.05.007

Romero, A. B., Thiemens, M. H. (2003). Mass-independent sulphur isotopic compositions in present-day sulfate aerosols. Journal of Geophysical Research – Atmospheres 108(D16): 4524. doi: 10.1029/2003/D003660

Rudolph, R. N., Inn, E. C. Y. (1981). OCS photolysis and absorption in the 200 – to 300-nm region. Journal of Geophysical Research 86: 9891 – 9894. doi: 10.1029/JC086iC10p09891

Rye, R., Holland, H.D. (1998). Paleosols and the evolution of atmospheric oxygen: A critical review. American Journal of Science 298: 621 – 672. doi: 10.2475/ajs.298.8.621

Rye, R. O., Luhr, J. F., Wasserman, M. D. (1984). Sulfur and oxygen isotope systematics of the 1982 eruptions of El Chichón volcano, Chiapas, Mexico. Journal of Volcanology and Geothermal Research 23: 109 – 123. doi: 10.1016/0377-0273(84)90058-1

Saager, R. (1970). Structures in pyrite from the Basal Reef in the Orange Free State gold-field. Transcripts of the Geological Society of South Africa 73: 29 – 46.

Sagemann, J., Jørgensen, B. B., Greef, O. (1998). Temperature dependence and rates of sulfate reduction in cold sediments of Svalbard, Arctic Ocean. Geomicrobiology Journal 15(2): 85 – 100. doi: 10.1080/01490459809378067.

Sakai, H., Des Marais, D. J., Ueda, A., Moore, J. G. (1984). Concentrations and isotopic ratios of carbon, nitrogen and sulfur in ocean-floor basalts. Geochimica et Cosmochimica Acta 48: 2433 – 2442. doi: 10.1016/001607037(84)90295-3

Sakuari, R., Ito, M., Ueno, Y., Kitajima, K., Maruyama, S. (2005). Facies architecture and sequence stratigraphic features of the Tumbiana Formation in the Pilbara Craton, northwestern Australia: Implications for depositional environments of oxygenic stromatolites during the late Archean. Precambrian Research 138: 255 – 273. doi: 10.1016/j.precamres.2005.05.008

Salles-Martinez, J. (1996). Concretion morphology, classification and genesis. Earth Science Reviews 41: 177 – 210. doi: 10.1016/S0012-8252(96)0002-0

Sansjofre, P., Cartigny, P., Trindade, R. I. F., Nogueira, A., C. R., Agrinier, P., Ader, M. (2016). Multiple sulfur isotope evidence for massive oceanic sulfate depletion in the aftermath of Snowball Earth. Nature Communications 7: 12912. doi: 10.1038/ncomms12192

Savarino, J., Romero, A., Cole-dai, J., Bekki, S., Thiemens, M. H. (2003). UV induced mass-independent sulfur isotope fractionation in stratospheric volcanic sulfate. Geophysical Research Letters 30(21): 1 – 4. doi: 10.1029/2003GL018134

Schaefer, B. F., Pearson, D. G., Rogers, N. W., Barnicoat, A. C. (2010). Re-Os isotope and PGE constraints on the timing and origin of gold mineralization in the Witwatersrand Basin. Chemical Geology 276: 88 – 94. doi: 10.1016/j.chemgeo.2010.06.001

Schoonen, M. A. A., Barnes, H. L. (1991). Reactions forming pyrite and marcasite from solution: II. Via FeS precursors below 100 °C. Geochimica et Cosmochimica Acta 55: 3491 – 3504. doi: 10.1016/0016-7307(91)90123-M

Schmitz, M. D., Bowring, S. A., de Wit, M. J., Gartz, V. (2004). Subduction and terrane collision stabilize the western Kaapvaal craton tectosphere 2.9 billion years ago. Earth and Planetary Science Letters 222: 363 – 376. doi: 10.1016/j.epsl.2004.03.036

Scoates, J. S., Friedman, R. M. (2008). Precise crystallisation age of the platiniferous Merensky Reef, Bushveld Complex, South Africa, by the U-Pb zircon chemical abrasion ID-TIMS technique. Economic Geology 103: 465 – 471.

Seal, R. R. (2006). Sulfur isotope geochemistry of sulfide minerals. Reviews in Mineralogy and Geochemistry 61: 633 – 677.

Shaheen, R., Abaunza, M. M., Jackson, T. L., McCabe, J., Savarino, J., Thiemens, M. (2014). Large sulfur-isotope anomaly in nonvolcanic sulfate aerosol and its implications for the Archean atmosphere (Supplementary Information). Proceedings of the National Academy of Science 111(33): 11979 – 11983. doi: 10.1073/pnas.1406315111

Shanks, W. C., Bischoff, J. L., Rosenbauer, R. J. (1981). Sea-water sulfate reduction and sulfur isotope fractionation in basaltic systems – interaction of seawater with fayalite and magnetite at 200 – 350 °C. Geochimica et Cosmochimica Acta 45: 1977 – 1995. doi: 10.1016/0016-7037(81)90054-5

Shanks, W. C., Seyfried, W. E. (1987). Stable isotope studies of vent fluids and chimney minerals, Southern Juan de Fuca Ridge: Sodium metasomatism and seawater sulfate reduction. Journal of Geophysical Research 92: 11387 – 11399. doi: 10.1029/JB092iB11p11387

Sharp, M., Gomez, B. (1986). Processes of debris comminution in the glacial environment and implications for quartz sand-grain micromorphology. Sedimentary Geology 46(1-2): 33 – 47. doi: 10.1016/0037-0738(86)90004-7

Shemansky, D. E. (1972). CO_2 extinction coefficient 1700-3000 Å. The Journal of Chemical Physics 56(4): 1582 – 1587. doi: 10.1063/1.1677408

Shen, Y., Buick, R., Canfield, D. E. (2001). Isotopic evidence for microbial sulfate reduction in the early Archaean era. Nature 410: 77 – 81. doi:

Shen, Y., Farquhar, J., Masterson, A., Kaufman, A. J., Buick, R. (2009). Evaluating the role of microbial sulfate reduction in the early Archean using quadruple isotope systematics. Earth and Planetary Science Letters 279: 383 – 391. doi: 10.1016/j.epsl.2009.01.018

Sidhu, K. S., Csizmadia, I. G., Strausz, O. P., Gunning, H. E. (1966). The reactions of sulfur atoms. VII. The ultraviolet spectrum, the photolysis, and the mercury sensitization of carbonyl sulfide. Journal of the American Chemical Society 11: 2412 – 2417. doi: 10.1021/ja00963a009

Sim, M. S., Ogata, H., Lubitz, W., Adkins, J. F., Sessions, A. L., Orphan, V. J., McGlynn, S. E. (2019). Role of APS reductase in biogeochemical sulfur isotope fractionation. Nature Communications 10(44): 1 – 9. doi: 10.1039/s41467-018-07878-4

Smith, J. W. (2000). Isotopic fractionations accompanying sulfur hydrolysis. Geochemical Journal 34: 95 – 99. doi: 10.2343/geochemj.34.95

Song, G. X., Cook, N. J., Wang, L., Qin, K. Z., Ciobanu, C. L., Li, G. M. (2019). Gold behaviour in intermediate sulfidation epithermal systems: a case study from the Zhengguang gold deposit, Heilongjiang Province, NE-China. Ore Geology Reviews 106: 446 – 462. doi: 10.1016/j.oregeorev.2019.02.001

Stüeken, E. E., Buick, R., Anbar, A. D. (2015). Selenium isotopes support free O_2 in the latest Archean. Geology 43(3): 259 – 262. doi: 10.1130/G36218.1

Surkov, A. V., Bötcher, M. E., Kuever, J. (2012). Sulphur isotope fractionation during the reduction of elemental sulphur and thiosulfate by Dethiosulfovibrio spp. Isotopes in Environmental and Health Studies 48(1): 65 – 75. doi: 10.1080/10256016.2011.626525

Sutton, S. J., Maynard, J. B. (1992). Multiple alteration events in the history of a sub-Huronian regolith at Lauzon Bay, Ontario. Canadian Journal of Earth Science 29: 432 – 445. doi: 10.1139/e92-038

Sutton, S. J., Ritger, S. D., Maynard, J. B. (1990). Stratigraphic control of chemistry and mineralogy in metamorphosed Witwatersrand quartzites. Journal of Geology 98(3): 329 – 341. doi: 10.1086/629408

Sykora, S., Cooke, D. R., Meffre, S., Stephanov, A. S., Gardner, K., Scott, R., Selley, D., Harris, A. C. (2018). Evolution of pyrite trace element compositions from porphyry-style and epithermal conditions at the Lihir gold deposit: Implications for ore genesis and mineral processing. Economic Geology 113: 193 – 208. doi: 10.5382/econgeo.2018.4548

Tada, A., Ueno, Y., Taka, K., Yoshida, N. (2008). Quadruple sulfur isotope fractionation of microbial sulphur reduction in pure culture. Proceedings of Japanese Geoscience Union Meeting, Chiba City. Abstract C203-P006.

Tankard, A. J., Jackson, M. P. A., Eriksson, K. A., Hobday, D. K., Hunter, D. R., Minter, W. E. L. (1982). Crustal evolution of Southern Africa, 3.8 billion years of Earth history. Springer-Verlag, New York, 523 p.

Taylor, K. G., Macquaker, J. H. S. (2000). Early diagenetic pyrite morphology in a mudstone-dominated succession: The low Jurassic Cleveland Ironstone Formation, eastern England. Sedimentary Geology 131: 77 – 86. doi: 10.1016/S0037-0738(00)00002-6

Thamdrup, B., Finster, K., Fossing, H., Hansen, J. W., Jørgensen, B. B. (1994). Thiosulfate and sulfite distribution in porewater marine sediments related to manganese, iron and sulfur geochemistry. Geochimica et Cosmochimica Acta 58: 67 – 73. doi: 10.1016/0016-7037(94)90446-4

Thode, H. G., Kleerekoper, H., McElcheran, D. (1951) Isotope fractionation in bacterial fractionation of sulfate. Research 4: 581 – 582.

Thode, H. G., Monster, J., Dunford, H. B. (1961). Sulfur isotope geochemistry. Geochimica et Cosmochimica Acta 25(3): 159 – 174. doi: 10.1016/0016-7037(61)90074-6.

Thomas, H. V., Large, R. R., Bull, S. W., Maslennikov, V., Berry, R. F., Fraser, R., Froud, S., Moye, R. (2011). Pyrite and pyrrhotite textures and composition in sediments, laminated quartz veins and reefs at Bendigo gold mine, Australia: Insights for ore genesis. Economic Geology 106: 1- 31. doi: 10.2113/econgeo.106.1.1

Thomassot, E., Cartigny, P., Harris, J. W., Lorand, J. P., Rollion-Bard, C., Chaussidon, M. (2009). Metasomatic diamond growth: A multi-isotope (^{13}C, ^{15}N, ^{33}S, ^{34}S) of sulfide inclusions and their host diamonds from Jwaneng (Botswana). Earth and Planetary Science Letters 282: 79 – 90. doi: 10.1016/j.epsl.2009.03.001

Thomazo, C., Ader, M., Farquhar, J., Philippot, P. (2009). Methanotrophs regulated atmospheric sulfur isotope anomalies during the late Archean (Tumbiana Formation, Western Australia). Earth and Planetary Science Letters 279: 65 – 75. doi: 10.1016/j.epsl.2008.12.036

Thorne, A. M., Trendall, A. F. (2001). Geology of the Fortescue Group, Pilbara Craton, Western Australia. In: Bulletin of the Geological Survey of Western Australia 144.

Torssander P. (1989). Sulfur isotope ratios of Icelandic rocks. Contributions to Mineralogy and Petrology 102: 18 – 23. doi: 10.1007/BF01160187

Trudinger, P. A., Chambers, L. A., Smith, J. W. (1985). Low temperature sulfate reduction: biological versus abiological. Canadian Journal of Earth Sciences 22: 1910 – 1918. doi: 10.1139/e85-207

Ueda, A., Sakai, H. (1984). Sulfur isotope study of Quarternary volcanic rocks from the Japanese island arc. Geochimica et Cosmochimica Acta 44: 579 – 587. doi: 10.1016/0016-7037(84)90037-1

Ueno, Y., Ono, S., Rumble III, D., Maruyama, S. (2008). Quadruple sulfur isotope analysis of ca. 3.5 Ga Dresser Formation: New evidence for microbial sulfate reduction in the early Archean. Geochimica et Cosmochimica Acta 72: 5675 – 5691. doi: 10.1016/j.gca.2008.08.026

Ueno, Y., Johnson, M. S., Danielache, S. O., Eskebjerg, C., Pandey, A. Yoshida, N. (2009). Geological sulfur isotopes indicate elevated OCS in the Archean atmosphere, solving faint young sun paradox. Proceedings of the National Academy of Science 106(35): 14784 – 14789. doi: 10.1073/pnas.0903518106

Urey, H. C. (1947). The thermodynamic properties of isotopic substances. Journal of the Chemical Society 1947: 562 – 581.

Utsunomiya, S., Murakami, T., Nakada, M., Kasama, T. (2003). Iron oxidation state of a 2.45-Byr-old paleosol developed on mafic volcanics. Geochimica et Cosmochimica Acta 67(2): 213 – 221. doi: 10.1016/S0016-7037(02)01083-9

Utter, T. (1978). Morphology and geochemistry of different pyrite types from the upper Witwatersrand system of the Klerksdorp goldfield, South Africa. Geologische Rundschau 67(2): 774 – 804. doi: 10.1007/BF01802816

Utter, T. (1980). Rounding of ore particles from the Witwatersrand Gold and Uranium deposit (South Africa) as an indicator of their detrital origin. Journal of Sedimentary Research 50(1): 71 – 76. doi: 10.1036/212F7969-2B24-11D7-8648000102C1865D

Van Niekerk, C. B., Burger, A. J. (1969). Lead isotopic data relating to the age of the Dominion Reef Lava. South African Journal of Geology 72(2): 37 – 45.

von Brunn, V., Gold, D. J. C. (1993). Diamictite in the Archean Pongola sequence of southern Africa 16(3): 367 – 374. doi: 10.1016/0899-5362(93)90056-V

von Brunn, W., Hobday, D. K. (1976). Early Precambrian tidal sedimentation in the Pongola Supergroup of South Africa. Journal of Sedimentary Petrology 46: 670 – 679. doi: 10.1306/212F7022-2B24-11D7-8648000102C1865D

Wacey, D., McLoughlin, N., Whitehouse, M. J., Kilburn, M. R. (2010). Two coexisting sulfur metabolisms in a ca. 3400 Ma sandstone. Geology 38(12): 1115 – 1118. doi: 10.1130/G31329

Walter, M. R. (1983). Archean stromatolites: Evidence of the Earth's earliest benthos. In: Schopf J. W., Earth's earliest biosphere: Its origin and evolution. Princeton University Press, Princeton.

Wang, X., Planavsky, N. J., Hofmann, A., Saupe, E. E., De Corte, B. P., Philippot, P., LaLonde, S. V., Jemison, N. E., Zou, H., Ossa Ossa, F., Rybacki, K., Alfimova, N., Larson, M. J., Tsikos, H., Fralick, P. W., Johnson, T. W., Knudsen, A. C., Reinhard, C. T.,

Konhauser, K. O. (2018). A Mesoarchean shift in uranium isotope systematics. Geochimica et Cosmochimica Acta 238: 438 – 452. doi: 10.1016/j.gca.2018.07.024

Watanabe, Y., Farquhar, J., Ohmoto, H. (2009). Anomalous fractionations of sulfur isotopes during thermochemical sulfate reduction. Science 324: 370 – 373. doi: 10.1126/science.1169289

Watchorn, M. F. (1991). The significance of marine modification in some Witwatersrand placers – an example from the Lower Witwatersrand, West Rand Group. South African Journal of Geology 94(5-6): 333 – 339.

Watchorn, M. B. (1980). Fluvial and tidal sedimentation in the 3000 Ma Mozaan Basin, South Africa. Precambrian Research 13: 27 – 42. doi: 10.1016/0301-9268(80)90057-1

Watchorn, M. B., Armstrong, N. V. (1981). Contemporaneous sedimentation and volcanism at the base of the early Precambrian Nsuze Group, South Africa. Transactions of the Geological Society of South Africa 83: 231 – 238.

Watts, S. F. (2000). The mass budgets of carbonyl sulfide, dimethyl sulfide, carbon disulfide and hydrogen sulfide. Atmospheric Environment 34: 761 – 779. doi: 10.1016/S1352-2310(99)0034208

Weilers, B. F. (1990). A review of the Pongola Supergroup and its setting on the Kaapvaal Craton. Economic Geology Research Unit Information Circular No. 228. University of the Witwatersrand.

Whitehall, A. R., Ono. S. (2012). Excitation band dependence of sulfur isotope mass-independent fractionation during photochemistry of sulfur dioxide using broadband light sources. Geochimica et Cosmochimica Acta 94: 238 – 253. doi: 10.1016/j.gca.2012.06.014

Whitehouse, M. J., Kamber, B. S., Fedo, C. M., Lepland, A. (2005). Integrated Pb and S-isotope investigation of sulfide minerals from the early Archean of south-west Greenland. Chemical Geology 222: 112 – 131. doi: 10.1016/j.chemgeo.2005.06.004

Wiliford, K. H.,, Ushikubo, T., Lepot, K., Kitajima, K., Hallmann, C., Spicuzza, M. J., Kozdon, R., Eigenbrode, J. L., Summons, R. E., Valley, J. W. (2016). Carbon and sulfur isotopic signatures of ancient life and environment at the microbial scale: Neoarchean shales and carbonates. Geobiology 14: 105 – 128. doi: 10.1111/gbi.121163

Wille, M., Kramers, J. D., Nägler, T. F., Beukes, N. J., Schröder, S., Meisel, T. H., Lacassie, J. P., Voegelin, A. R. (2007). Evidence for a gradual rise of oxygen between 2.6 and 2.5 Ga from Mo isotopes and Re-PGE signatures in shales. Geochimica et Cosmochimica Acta 71: 2417 – 2435. doi: 10.1016/j.gca.2007.02.019

Wing, B. A., Farquhar, J. (2015). Sulfur isotope homogeneity of lunar mare basalts. Geochimica et Cosmochimica Acta 170: 266 – 280. doi: 10.1016/j.gca.2015.09.003

Woodruff, L. G., Shanks, W. C. (1988). Sulfur isotope study of chimney minerals and vent fluids from 21 °N, East Pacific Rise – hydrothermal sulfur sources and disequilibrium sulfate reduction. Journal of Geophysical Research 93: 4562 – 4572. doi: 10.1029/JB093iB05p04562

Wronkiewicz, D. J., Condie, K. C. (1989). Geochemistry and provenance of sediments from the Pongola Supergroup, South Africa: Evidence for a 3.0 Ga-old continental craton. Geochimica et Cosmochimica Acta 53: 1537 – 1549. doi: 10.1016/0016-7037(89)90236-6

Yamaguchi, K. E., Johnson, C. M., Beard, B. I., Beukes, N. J., Gutzmer, J., Ohmoto, H. (2007). Isotopic evidence for iron mobilization during Paleoproterozoic lateritization of the Hekpoort paleosol profile from Gaborone, Botswana. Earth and Planetary Science Letters 256: 577 – 587. doi: 10.1016/j.epsl.2007.02.010

Young, G. M. (2015). Did prolonged two-stage fragmentation of the supercontinent Kenorland lead to arrested orogenesis on the southern margin of the Superior province? Geoscience Frontiers 6: 419 – 435. doi: 10.1016/j.gsf.2014.04.003

Young, G. M., Long, D. G. F., Fedo, C. M., Nesbitt, H. W. (2001). Paleoproterozoic Huronian basin: product of a Wilson cycle punctuated by glaciations and a meteorite impact. Sedimentary Geology 141 – 142: 233 – 254. doi: 10.1016/S0037-0738(01)00076-8

Young, G. M., von Brunn, V., Gold, D. J. C., Minter, W. E. L. (1998). Earth's oldest reported glaciation: Physical and chemical evidence from the Archean Mozaan Group (~2.9 Ga) of South Africa. The Journal of Geology 106: 523 – 538. doi: 10.1086/516039

Zerkle, A. L., Claire, M. W., Domagal-Goldman, S. D., Farquhar, J., Poulton, S. W. (2012). A bistable organic-rich atmosphere on the Neoarchean Earth. Nature Geoscience 5: 359 – 363.

Zhang, F., Zhu, X., Yan, B., Kendall, B., Peng, X., Li, J., Algeo, T. J., Romaniello, S. (2015). Oxygenation of a Cryogenian ocean (Nanhua Basin, South China) revealed by pyrite Fe isotope compositions. Earth and Planetary Science Letters 429: 11 – 19. doi: 10.1016/j.epsl.2015.07.021

Zhao, B. (1998). A mineralogical and geochemical study of alteration associated with the Ventesdorp Contact Reef in the Witwatersrand Basin. PhD Thesis (unpublished), University of the Witwatersrand, South Africa.

Zhelezinskaia, I., Kaufman, A. J., Farquhar, J., Cliff, J. (2014). Large sulfur isotope fractionations associated with Neoarchean microbial sulfate reduction. Science 346(6120): 742 – 744. doi: 10.1126/science.1256211

Appendix

Table A.1. Variations in sulfur concentrations through the Crown Lava and Cooper Lake paleosol profiles. From Maynard et al. (2013).

Stratigraphic Depth (m)	Depth below top of profile (m)	Sulfur concentrations (ppm)
	Crown Lava Paleosol	
1183.34	0	490
1183.37	0.03	540
1183.4	0.06	730
1183.43	0.09	525
1183.46	0.12	138
1183.49	0.15	239
1183.9	0.56	1293
1185.8	2.46	623
1186.2	2.86	496
1186.8	3.46	305
1188.3	4.96	147
	Cooper Lake Paleosol	
-	0.05	90
-	0.15	60
-	0.5	90
-	0.5	80
-	0.75	1500
-	1.5	1800
-	2.5	660
-	2.5	1600
-	2.5	750
-	3	220
-	3.2	1400
-	3.5	910
-	4	800
-	5	800

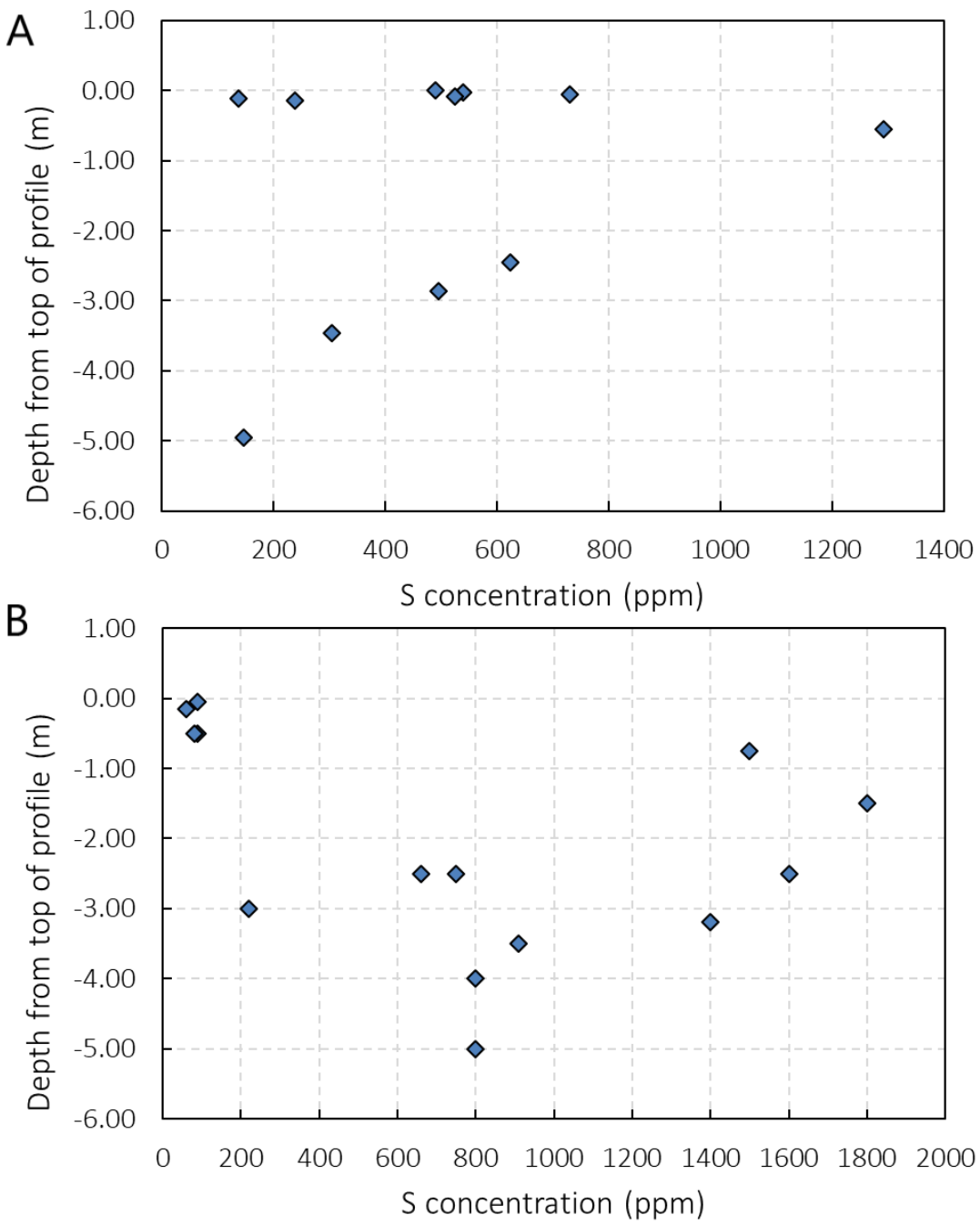

Figure A1. Variations in sulfur concentrations through the Crown Lava and Cooper Lake paleosols (Chapter 4). A. Crown Lava paleosol, B. Cooper Lake paleosol. Note sulfur enrichment in upper section of both paleosol profiles.

Equations A.1 and A.2 show the modified lambda equations used to calculate the lambda values for Chapter 6. Here, the mean $\delta^{3x}S$ values for a set of sulfide minerals are substituted into equations 6.1 and 6.2.

$$^{33}\lambda = \frac{ln\left(1+\frac{\delta^{33}S_{sulfide\ mean}}{\delta^{34}S_{sulfide\ mean}}\right)}{\ln\left(1+\frac{\delta^{34}S_{sulphide\ mean}}{1000}\right)} \quad \text{(A.1)}$$

$$^{36}\lambda = \frac{ln\left(1+\frac{\delta^{36}S_{sulfide\ mean}}{\delta^{34}S_{sulfide\ mean}}\right)}{ln\ (1+\frac{\delta^{34}S_{sulphide\ mean}}{1000})} \quad \text{(A.2)}$$

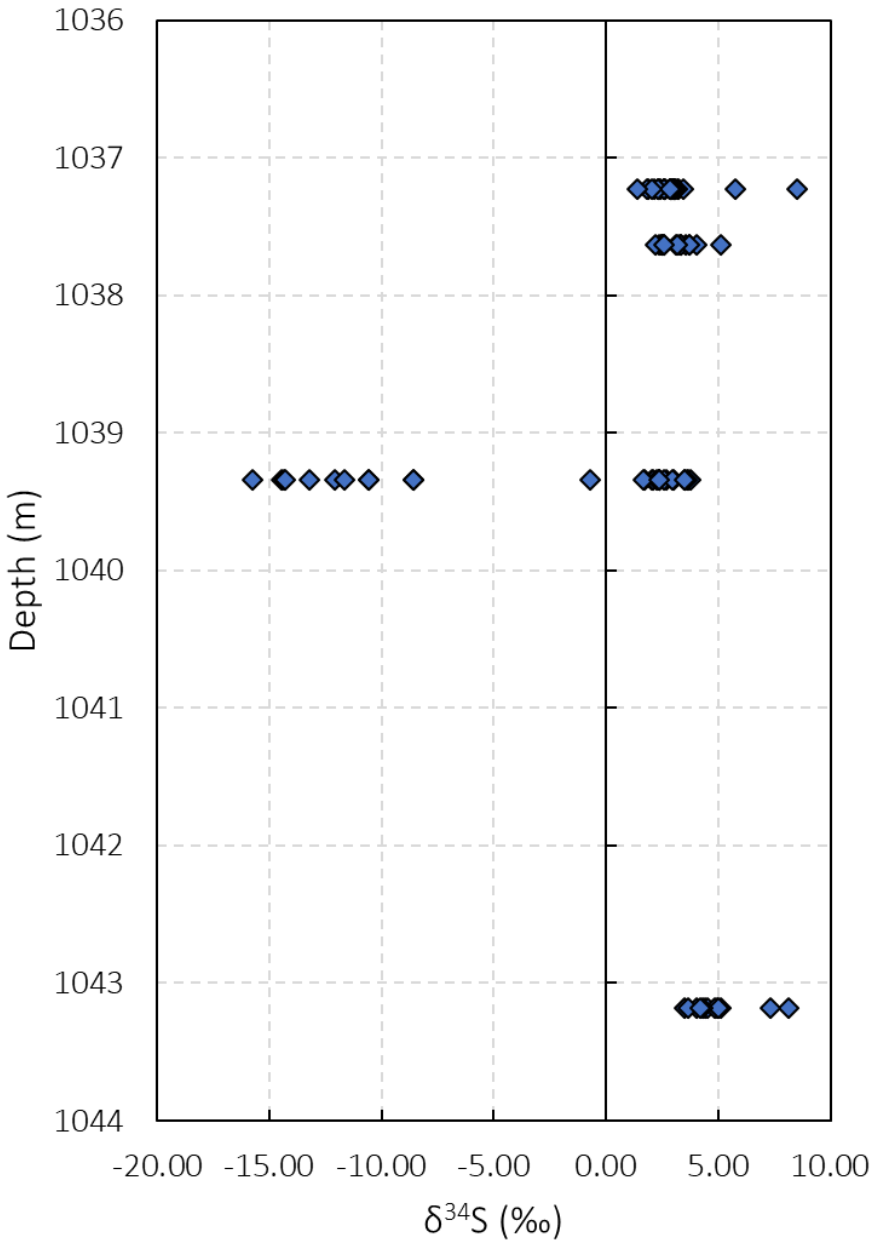

Figure A.2. Plot of depth vs. $\delta^{34}S$ for pyrite grains from the Roodepoort Formation (Chapter 6). Note that $\delta^{34}S$ does not correlate with depth.